DISS. ETH NO. 30369

SEISMIC BEHAVIOR, PERFORMANCE AND DESIGN OF REINFORCED CONCRETE SHEAR WALLS WITH LOW ASPECT RATIOS

A thesis submitted to attain the degree of

DOCTOR OF SCIENCES

(Dr. sc. ETH Zurich)

presented by

DIEGO MARTÍN PIZARRO POHL

Master in Engineering Sciences, Pontificia Universidad Católica de Chile

born on 18.05.1990

accepted on the recommendation of

Prof. Dr. Božidar Stojadinović

Prof. Dr. Matías Hube

Prof. Dr. Dawn Lehman

2024

ACKNOWLEDGEMENTS

I want to express my deepest gratitude to Prof. Bozidar Stojadinovic for allowing me to join his research group. He was a great advisor, being really generous in transferring all his knowledge, experience, and fun stories to us. Thanks to Professors Matias Hube and Dawn Lehman for their time to review my thesis, and for their feedback and nice discussion during my doctoral dissertation.

I want to thank the members of the Chair of Structural Dynamics and Earthquake Engineering. I am grateful to share my time with great and interesting people: Milan, Andreia, Lukas, Nikola, Safak, Constantinos, Nikos, Sergio, and Nora. It was great to share with you these years. The group was great, and I enjoyed talking and laughing with you. I worked close to Milan, as we spent many hours in the lab figuring out how to run the MAST, installing the specimens, and running the tests. Thanks to Margaretha and Nicole for their help during my time in Zurich.

The work in the lab is tough but can be fun with the right people. I was lucky to work with a great and competent team who made me enjoy my time in the lab. Thanks to Pius, Christoph, Dominik, Tomi, Andy and Martin for all their support and expertise. The specimens were built by the company Stüssi, who gave us all the facilities to go there to instrument the reinforcement bars or to take pictures of the process. Every time Milan and I went there, we had a lot of fun with the team, even being invited to some barbeques. I extend my gratitude to the team from Stüssi, especially to Raphael Zwahlen who was our main contact. Thanks to Matteo Dozio and Julian Lutz, who gave me plenty of support during the experimental campaign, becoming experts in postensioning and grinding cylinders. Thanks to the visiting members of our Chair: Larisa Garcia-Ramonda and Nicolas Tapia for their help in the first set of my specimens. I am thankful for the funding from the Swiss National Science Foundation (SNSF, Grant 200021_184805) and ETH Zurich.

I had a great time during these five years in Zürich. It was fun to be a part of FC Wiedikon. The football club felt really like home to me, the team was great and fun, and we had some great games. And thanks to the Chilean community in Zurich, which made me feel at home with the asados.

Thanks to my wife Angela for coming with me to Zurich. She did a lot of sacrifice . I am really grateful for all your time, patience, and dedication. Thanks as well to my daughter Sofía, who was definitely a source of inspiration during my work. And thanks to my family in Chile for all their support.

Zürich, June 2024 Diego Pizarro

ABSTRACT

The state-of-practice seismic design methods, either prescriptive or performance-based, assume that flexure and shear are the predominant behavior modes of a typical structure. However, reinforced concrete squat shear walls, considered those with a shear-span ratio (M/VL_w) less than 1, could have a predominant shear or sliding-controlled behavior. Current guidelines for assessing existing structures, such as ACI 369-22, address that a wall could have flexure, shear, or sliding-controlled behavior. Still, they do not account for the possibility of transitioning from one behavior mode to another at large deformations.

This thesis aimed to experimentally study the boundaries of the transition of the shear and sliding-controlled behavior modes in reinforced concrete shear walls with shear-span ratios smaller than 1. Furthermore, it will investigate if the sliding failure could be considered ductile, define the onset drift ratio of sliding behavior, and characterize the damage progression of sliding failure. A series of real-scale quasi-static cyclic and hybrid simulation shear wall tests of identical geometry were conducted at the Multi-Axial Subassemblage Testing (MAST) facility at ETH Zürich to identify the influence of the axial load ratio, the longitudinal and transverse steel reinforcement ratios, and the loading protocol on the transition between shear and sliding-controlled behavior modes. The quasi-static cyclic tests considered four specimens: a reference specimen, a specimen with double the axial load, a specimen whose reinforcement ratios were both reduced, and a specimen whose transverse reinforcement ratio was reduced. Furthermore, two specimens of identical geometry but different axial load ratios were tested under hybrid simulation to complement and extend the results of the cyclic test and asses the influence of the loading protocol. In these hybrid simulations, a single-degree-of-freedom reference system was chosen to be consistent with the cyclic tests, where the physical substructure corresponded to the experimental specimen.

In the cyclic tests, two specimens had sliding failure. Initially, these specimens had a shear-controlled behavior, with shear deformations contributing more than 80% of the total deformations. However, when they reached a point identified as sliding initiation, the specimens transitioned to a sliding-controlled behavior. The post-peak strength hysteresis was characterized by peak forces of around 80% of the maximum peak strength and by significant sliding deformation at constant force levels. These specimens reached drift ratios up to 2% and remained stable under the applied axial load. The other two cyclically tested specimens experienced shear failures, either in diagonal compression or diagonal tension. They behaved in shear-controlled behavior during the entire test and reached a maximum drift ratio of 0.90%. The failures were brittle, with the specimens experiencing a sudden drop in resistance and height.

The hybrid simulation tests were conducted with a scaled 1995 Kobe JMA ground motion. The first tested

specimen with a lower axial load ratio had sliding failure. The behavior was similar to that of its cyclic reference specimen counterpart, transitioning from shear to sliding-controlled behavior after reaching the sliding initiation drift ratio. In contrast, the second tested specimen with a higher axial load experienced a shear diagonal compression, web concrete crushing, failure, similar to its cyclic counterpart. While the test protocol did not affect the failure mode, it affected the shape of the hysteresis loops.

The results showed that the axial load is a key parameter in determining the controlling behavior mode of low aspect ratio reinforced concrete shear walls. When the axial load ratio was doubled from 4-5% to 8-10%, the behavior of the tested shear walls changed: a lightly loaded wall changed its behavior from shear to sliding but continued to carry its axial load. In contrast, a heavily loaded wall retained its shear behavior mode until failure by diagonal crushing compression of concrete. The comparison with nominally identical shear walls tested using a conventional quasi-static cyclic test protocol revealed that the loading protocol did not affect the behavior and failure modes. Varying the reinforcement ratios will not change the behavior mode of a shear wall, but the proportion of transverse/longitudinal reinforcement ratios is relevant as it defines the shear and sliding strengths of the wall.

KURZFASSUNG

in der Praxis angewandten seismischen Bemessungsmethoden, seien es die konventionellen normierten Ansätze oder die leistungsbasierten Methoden, gehen davon aus, dass Biegung und Schub die vorherrschenden Verhaltensmodi eines typischen Tragwerks sind. Allerdings könnten Stahlbetonwände mit niedrigem Seitenverhältnis, definiert als gedrungene Wände mit einem Schubschlankheitsgrad (M/VL_w) kleiner als 1, ein überwiegend durch Schub oder Gleiten kontrolliertes Verhalten aufweisen. Aktuelle Richtlinien zur Überprüfung bestehender Tragwerke, wie beispielsweise die ACI 369-22, berücksichtigen, dass eine Wand ein Biege-, Schub- oder Gleitverhalten zeigen könnte. Sie berücksichtigen jedoch nicht die Möglichkeit, dass bei grossen Verformungen ein Übergang von einem Verhaltensmodus zu einem anderen stattfinden könnte.

Diese Arbeit zielt darauf ab, experimentell die Grenzen des Übergangs zwischen schub- und gleitkontrollierten Verhaltensmodi in Stahlbeton-Schubwänden mit einem Schubschlankheitsgrad kleiner als 1 zu untersuchen. Darüber hinaus wird untersucht, ob das Gleitversagen als duktil angesehen werden kann, das Einsetzen des Driftverhältnisses für Gleitverhalten definiert und die Schadensentwicklung bei Gleitversagen charakterisiert werden kann. Eine Reihe von grossmassstäblichen, quasi-statischen zyklischen und hybriden Simulationstests von Schubwänden identischer Geometrie wurden an der Multi-Axial Subassemblage Testing (MAST) Einrichtung der ETH Zürich durchgeführt, um den Einfluss des axialen Lastverhältnisses, der Längs- und Querbewehrungsverhältnisse sowie des Belastungsprotokolls auf den Übergang zwischen schub- und gleitkontrollierten Verhaltensmodi zu identifizieren. Die quasi-statischen zyklischen Tests umfassten vier Proben: eine Referenzprobe, eine Probe mit doppelter axialer Last, eine Probe, deren Bewehrungsverhältnisse beide reduziert wurden, und eine Probe, deren Querbewehrung reduziert wurde. Zusätzlich wurden zwei Proben mit identischer Geometrie, aber unterschiedlichen axialen Lastverhältnissen unter hybrider Simulation getestet, um die Ergebnisse der zyklischen Tests zu ergänzen und zu erweitern sowie den Einfluss des Belastungsprotokolls zu bewerten. Bei diesen hybriden Simulationen wurde ein Referenzsystem mit einem Freiheitsgrad gewählt, um die Konsistenz mit den zyklischen Tests zu gewährleisten, wobei die physikalische Substruktur der experimentellen Probe entsprach.

Bei den zyklischen Tests wiesen zwei Proben ein Gleitversagen auf. Anfänglich zeigten diese Proben ein schubkontrolliertes Verhalten, wobei die Schubverformungen mehr als 80% der Gesamtverformungen ausmachten. Als jedoch der Punkt, der als Beginn des Gleitens identifiziert wurde, erreicht wurde, wechselten die Proben zu einem gleitkontrollierten Verhalten. Die Hysterese nach der Festigkeitsspitze (Post-Peak) war durch Spitzenkräfte von etwa 80% der maximalen Spitzenfestigkeit und durch erhebliche Gleitverformungen bei konstanten Kraftniveaus gekennzeichnet. Diese Proben erreichten

Schiefstellungen von bis zu 2% und blieben unter der aufgebrachten Axiallast stabil. Die anderen beiden zyklisch getesteten Proben erlitten Schubversagen, entweder in Form von diagonalem Druck- oder Zugversagen. Sie verhielten sich während des gesamten Tests schubkontrolliert und erreichten eine maximale Schiefstellung von 0,90%. Die Versagen waren spröde, wobei die Proben einen plötzlichen Abfall des Widerstands und der Höhe erfuhren.

Die hybriden Simulationstests wurden mit einer skalierten Kobe-JMA-Bodenbewegung von 1995 durchgeführt. Die erste getestete Probe mit einem geringeren Axiallastverhältnis wies ein Gleitversagen auf. Das Verhalten war ähnlich wie das der zyklischen Referenzprobe und wechselte nach Erreichen der Gleitbeginn-Schiefstellung von einem schub- zu einem gleitkontrollierten Verhalten. Im Gegensatz dazu kam es bei der zweiten Probe mit höherer Axiallast zu einem Schubversagen durch diagonale Druckbeanspruchung, ähnlich wie bei der zyklisch geprüften Probe. Während das Prüfprotokoll keinen Einfluss auf den Versagensmodus hatte, wirkte es sich auf die Form der Hystereseschleifen aus.

Die Ergebnisse zeigten, dass die Axiallast ein entscheidender Parameter zur Bestimmung des dominierenden Verhaltensmodus von Stahlbeton-Schubwänden mit niedrigem Seitenverhältnis ist. Als das Verhältnis der Axiallast von 4-5% auf 8-10% verdoppelt wurde, änderte sich das Verhalten der getesteten Schubwände: Eine gering belastete Wand änderte ihr Verhalten von Schub auf Gleiten, trug jedoch weiterhin ihre Axiallast. Im Gegensatz dazu behielt eine stark belastete Wand ihr Schubverhalten bis zum Versagen durch diagonale Druckbeanspruchung des Betons bei. Der Vergleich mit nominell identischen Schubwänden, die mit einem konventionellen quasi-statischen zyklischen Testprotokoll getestet wurden, ergab, dass das Belastungsprotokoll keinen Einfluss auf das Verhalten und die Versagensmodi hatte. Die Variation der Bewehrungsgrade wird den Verhaltensmodus einer Schubwand nicht ändern, aber das Verhältnis von Quer- zu Längsbewehrung ist relevant, da es die Schub- und Gleitfestigkeiten der Wand bestimmt.

TABLE OF CONTENTS

CHAPTER 1

INTRODUCTION

1.1 Motivation

Earthquakes are natural hazards that can inflict significant damage on structures. The earthquakes of Turkey-Syria in 2023 and Haiti in 2010 have shown enormous social damage, both in casualties and housing, due to the collapse of structures. This raises the awareness that buildings must be designed, or retrofitted, to withstand the seismic demands that a specific location has to guarantee a safe response of our buildings under an earthquake.

The lateral resisting system of a structure carries the earthquake loads. A good example and commonly used system in seismic countries is reinforced concrete shear walls, which provide enough building stiffness and can carry gravity loads. Therefore, the lateral and vertical load systems are coupled. The practice and experience of Chile on earthquake resistance systems provide two configuration examples with shear walls: Office buildings have reinforced concrete core walls with special or intermediate resisting frames at the perimeter, whereas residential buildings have a significant amount of shear walls in orthogonal directions distributed along the floor plan, with a ratio between wall area and slab area of 1.5% to 3.5% [1, 2].

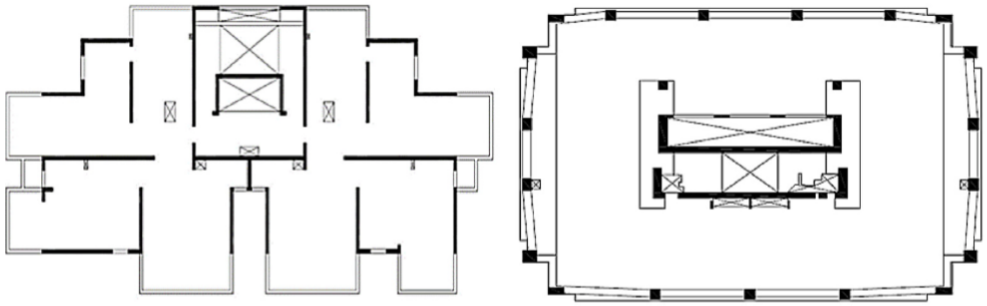

Figure 1.1: Typical Chilean wall lateral resistance system configuration (a) Residential building (b) Office building. From Lagos et al. [3].

Structures with reinforced concrete shear walls could have different failure modes, which depend of parameters of the walls such as the geometry, axial load, steel reinforcement arrangement or others. In particular, reinforced concrete shear walls are prone to develop the following failure modes:

- Flexure: This failure mode is associated to yielding of the vertical steel reinforcement in the plastic hinge region of a structure (Figure 1.2 (a)). This can lead to large compression stresses in the concrete of the opposite border, and without adequate confinement these concrete could spall and buckle the reinforcement bars. Appropriate confinement of the boundary element gives the flexure failure large ductility, which is seek to guarantee safety in seismic design of structures [4].

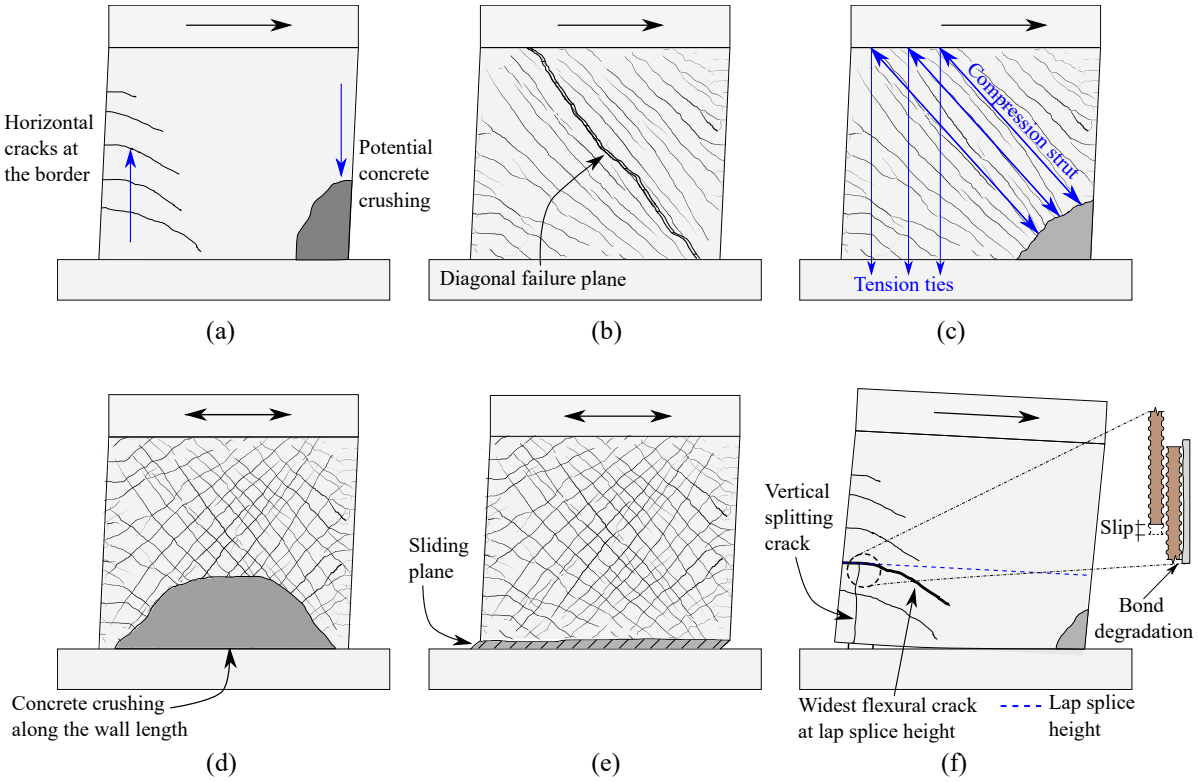

Figure 1.2: Failure modes in reinforced concrete shear walls (a) Flexure failure mode (b) Shear diagonal tension failure mode (c) Shear diagonal compression failure mode (d) Shear diagonal compression failure mode with concrete crushing across the length of the wall (e) Sliding failure mode (f) Rocking failure mode

- Shear Diagonal Tension: With insufficient horizontal distributed steel reinforcement, a corner to corner diagonal failure plane can develop along one or more of the shear diagonal cracks (Figure 1.2 (b)). Under sufficient deformations, the steel crossing the crack is responsible for transferring most of the shear stresses, and a brittle failure can develop if the reinforcement bars fracture [5].

- Shear Diagonal Compression: Large shear stresses can crush the concrete at the bottom or top of the diagonal strut if the wall have sufficient distributed steel reinforcement (Figure 1.2 (c)). Due to loss of concrete, the wall becomes vertically unstable and develops a brittle failure. The failure can progress from the strut of one direction to the other under load reversal, which can lead to damage across the entire wall's length (Figure 1.2 (d)) [5].

- Sliding shear: If there is enough shear reinforcement and concrete strength to block both shear failures, the walls could fail in sliding along a weak interface of the wall, usually expected at the cold joint with the foundation (Figure 1.2 (e)). If the vertical reinforcement yields with loading, upon load reversal it has to yield in compression to fully close the crack. If it does not, the crack width starts to accumulate until it generates a weak interface where sliding can occur. The damage of this failure is characterized by focused concrete spalling at the bottom of the specimen and dowel deformation or fracture of reinforcement bars crossing the sliding interface [5].

- Rocking: Slipping between two vertical reinforcement bars or loss of bond with the concrete could occur after successive tension and compression cycles, which could cause vertical splitting cracks that will reduce the load carrying capacity of the splice. The reinforcement bars of the splice might

lose contact with each other, resulting in incompatibility in transferring the lateral force, and the wall will not attain its full ultimate moment capacity [4]. This failure mode can also be caused by insufficient development length or anchorage of the vertical reinforcement bars in the foundation.

The lateral deformation of a wall can be decomposed into four behavior modes: flexure, shear, sliding, and rocking (associated with reinforcement bond-slip deformations), and they can lead to one of the previously mentioned failure modes. However, with increasing lateral deformation, a transition from one behavior mode to another, for instance, from flexure or shear to sliding, could occur. In particular, squat reinforced concrete walls, those with a shear-span ratio below 1, are prone to have shear or sliding-controlled behavior. Engineers who design a new structure or assess an existing one for seismic loads benefit from knowing the likely behavior mode of a given wall, but problems arise when the behavior mode boundaries are close to each other, making it hard to determine which behavior mode will dominate or if a mode transition will occur before failure.

The design and assessment of structures are guided by design codes, which are crafted by a group of engineering experts. Seismic codes provide guidelines for the design of earthquake-resisting systems, such as those explained before, with the aim to have minor damage under the called "design earthquake" and avoid collapse under large earthquakes. Current seismic design procedures can be classified into two groups: force-based and displacement-based. The force-method procedures, commonly used for the typical design of buildings, use a surrogate to determine the base shear coefficient consistent with the deformation capacity of the prototype structure. On the other hand, displacement-based procedures determine the maximum deformation a structure is expected to undergo and compare it to the deformation capacity of the prototype structure.

However, current state-of-the art seismic design procedures have shortcomings. First, the assumed deformations of the structures is purely flexural, and it does not consider other deformation or possible behavior modes such as shear and sliding. Second, the transformation between the structure and the surrogate is done with elastic properties, even when the structure is expected to behave inelastically. Finally, current seismic design procedures use the fundamental period to characterize the dynamic behavior of the prototype structure and surrogate, despite the fact that this dynamic response property changes when the strength of the structure changes during design.

The Swiss National Science Foundation (SNSF) project "Quasi-Dynamic Seismic Performance-Based Design Procedure" aimed to tackle those gaps in current design methods. The project was separated into three work packages. Andreia HA Da Silva [6] developed surrogate models for designing flexible rocking and sliding structures and proposed ductility-strength relations for a constant yield displacement seismic design procedure. Milan Kovarbasic and myself conducted the experimental part of the project. Milan Kovarbasic [7] experimentally studied the transition of the flexure and rocking-controlled behavior modes, and in this thesis, I present the third workload of the project, related to the experimental identification of the transition between the shear and sliding-controlled behavior modes.

1.2 Research objectives

The main objective of this thesis is to experimentally identify the transition between the sliding shear and diagonal shear-controlled behavior modes by conducting cyclic testing and hybrid simulation on squat-reinforced concrete shear walls with shear-span ratio smaller than 1.0. This research seeks to identify which parameters delineate the boundary between those behavior modes. Therefore, the experimental campaign will be designed with the behavior mode as the expected and primary outcome. Furthermore, this research will help to close the gap in the sliding shear failure mode knowledge:

- Investigate if the sliding shear failure, with the presence of axial load, could be considered ductile.
- Define the onset drift of the sliding shear behavior.
- Characterize the damage progression of the sliding shear failure.

1.3 Organization of the thesis

The dissertation is organized into six chapters:

- **Chapter 2: Literature review.** Presents the previous work that is relevant to understanding the thesis. First, it presents the effects involved in the sliding shear mechanism and then previous tests on reinforced concrete shear walls. It also shows how current design codes tackle the sliding shear and diagonal shear mechanism, and which formulas from scholars are being proposed to estimate the peak strength of squat RC walls. Finally, it describes a brief history and description of hybrid simulation.
- **Chapter 3: Experimental program.** This chapter describes how the experimental campaign was designed and conducted. The first section shows the decisions to select the specimens and the parameters to vary and describes the geometry, reinforcement and construction process of the specimens. It also describes the ETH MAST facility at which the tests were conducted, showing the hardware and control, and how the cyclic and hybrid simulation tests were implemented. To conclude, it describes the instrumentation and how the data acquired during the tests was post-processed.
- **Chapter 4: Cyclic tests.** Describes the results of the four specimens tested under cyclic loading. By varying the axial load ratio and the steel reinforcement arrangement, the four specimens exhibited different failure modes. The results are presented and discussed with the lateral resistance-drift hysteresis, cracks pattern and width, residual cracks and displacements that are valuable for post-earthquake damage assessment. The results gave key insights into the failure development and deformation capacity of the diagonal shear and sliding shear failures.
- **Chapter 5: Hybrid tests.** Focuses on the results of the two specimens tested under hybrid simulation. Chapter 5 is, therefore, an extension of the cyclic campaign, that allowed us to understand how the sliding shear and diagonal shear failure modes develop with a load pattern corresponding to a real seismic record of the 1995 Kobe earthquake in Japan. The specimens tested

under hybrid simulation had identical characteristics to two of those tested under cyclic loading, which allowed a direct comparison between the corresponding results.

- **Chapter 6: Discussion.** This section discusses the results of the cyclic and hybrid experimental campaign in terms of the influence of the axial load, steel reinforcement and test protocol. It discusses further the accuracy of the failure mode identification adopted by design codes [8] and explores new proposals based on machine learning. Finally, it presents a discussion of the sliding failure mode, which addresses the development of that failure mode at the system level and presents gaps that still need to be investigated.
- **Chapter 7: Conclusions.** Summarizes the conclusions from the presented research and presents future research directions.

The data that supports the findings of this thesis is publicly available at the ETH Research Collection [9, 10].

CHAPTER 2

LITERATURE REVIEW

2.1 Sliding shear mechanism

Sliding shear failure consists of a separation and relative displacement between two planes of a structural element that is considered monolithic. The slipping happens at a weak interface, which in reinforced concrete elements are cracks: either at a cold joint between elements. The sliding shear resistance along a crack is given by two effects: aggregate interlock and the dowel action of the steel reinforcement.

The aggregate interlock effect relates the crack displacements, opening δ_n and slipping δ_t to the shear τ_{ctnr} and normal σ_{ctnr} stresses that a crack can transfer [11]. Walraven [12, 13] developed the two-phase model (TPM), which derives the aggregate interlock stresses from the penetration forces of spherical aggregates into a rigid-perfectly plastic cement matrix. Walraven assumed a random distribution of aggregates in the cement matrix and considered the distribution of diameter sizes in the aggregates with a cumulative distribution p. The stresses at the crack interface are given in Equation 2.1, where $\sigma_{pu} = 6.39 f_{cc}^{0.56}$ (N/mm^2) is the cement matrix yielding strength, μ is the friction coefficient calibrated as 0.4, and A_n and A_t are coefficients that depend on the crack width, slip displacement, maximum aggregate diameter and the cumulative distribution of aggregate sizes in the cement matrix p.

$$\begin{aligned} \sigma_{cnr} &= -\sigma_{pu}(A_n - \mu A_t) \\ \tau_{cnr} &= \quad \sigma_{pu}(A_t + \mu A_n) \end{aligned} \tag{2.1}$$

Walraven proposed the TPM model in the early 80s, and the model has been extensively used in models to predict shear strength as the stress transfer mechanism, such as the Modified Compression Field Theory [14], and has been the base for the development of modern reinforced concrete design codes [15, 16].

Gambarova and Karakoc [17] proposed the rough crack model (RCM), developed after the proposal of Bazant and Gambarova [18], which had a novel formulation for aggregate interlock stresses in cracks based on an empirical model based on push-out tests, and Li, Maekawa and Okamura [19] proposed the Contact Density Model (CDM), which considers the asperity of the crack surface. A comparison of these two models and the TPM model can be found in Beck et al. [20].

The dowel action of the steel reinforcement is its capacity to transfer forces perpendicular to its longitudinal axis. According to Paulay, Park, and Phillips [21], three mechanisms are involved in the deformation of the reinforcement bars over the free length: bending, shear, and kinking. One of the widely used models for cyclic dowel action is the one of Vintzeleou and Tassios [22], in which the mechanical derivation is done by assuming similarities of the reinforcement bar-concrete to a pile-soil. They considered two failure modes: (1) crushing concrete of concrete and yielding of the bar and (2) concrete splitting.

The tests that have given insights into the behavior of sliding shear are push-off tests. The results of the push-off tests conducted by Mattock et al. [23–25] in the 70s are still the base of the friction strength expression used in ACI 318-19 [26]. The study of Davaadorj, Calvi and Stanton [27] provides a comprehensive database of many push-off and pull-off tests, and analyzes the accuracy of many of the strength models that have been proposed through the years. They suggest that the term related to cohesion, which is neglected by many approaches and even by ACI 318-19, should be adopted universally. Other types of tests have expanded the knowledge in cyclic shear loading in interfaces, such as Trost, Schuler and Stojadinovic [28] and Calvi, Bentz and Collins [29], who at the same time applied compression and tension, respectively.

2.2 Experimental research on squat reinforced concrete walls

Experimental tests of real-scale squat walls are the best way to generate data to help understand their behavior. Due to the equipment/setup required, preparation time, and the significant price of the specimens, these tests are scarce, with the experimental campaigns having a small number of specimens. Because of this, the global behavior of reinforced walls, development of peak strength formulas, or calibration of design codes must be done considering the conclusions of many experimental campaigns done throughout the years. There have been many scholars that have collected these tests in their databases, specifying many parameters but also their failure mode [30, 31], and the database published by Mangalathu et al. [32] is one of the few that includes specimens with sliding shear failure. This section presents experimental campaigns which contributed to understand the sliding shear failure or the behavior of reinforced concrete squat walls.

Paulay et al. [33] tested four walls to study if it was possible to get an adequate level of ductility on squat RC shear walls, and these are the tests commonly referenced as the first ones to study the sliding failure and the first one to describe it [5]. In this study, they forced the walls to fail either in flexure or sliding by providing enough horizontal reinforcement in their specimens to avoid diagonal tension failure. To study the transition between the flexure and sliding failure modes, they had one specimen with distributed shear reinforcement and boundary elements (Wall 1) and another one with extra diagonal bars from the bottom of the foundation to the top of the specimens (Wall 2).

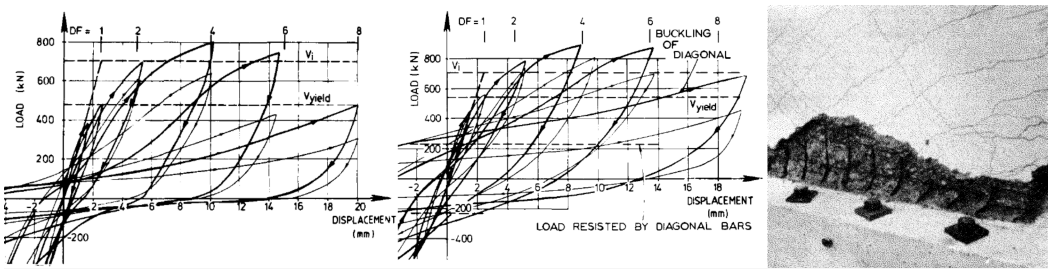

(a) (b) (c)

Figure 2.1: Load displacement curves of (a) Wall 1, and (b) Wall 2. (c) Sliding failure of Wall 1. Figures from Paulay et al. [33].

Specimen Wall 1 reached a ductility factor (DF) of 4, and at the second cycle of that displacement, the sliding deformations became considerable (Figure 2.1). The specimen reached a DF of 6, with sliding

contributing 65% of the total deformation. They assigned a DF of 4 to the specimen, not stated why, but it seems because, at DF of 6, the specimen lost more than 20% of the peak strength. On the other hand, Wall 2 did not fail in sliding shearbut could develop flexure deformations, and after a DF of 6, the diagonal bar buckled. The specimen could reach the maximum target DF of 8. Further analysis of their data showed that the specimen that failed in sliding shear had less energy dissipation capacity than Wall 2. Therefore, they characterized the sliding shear failure as a low-energy dissipation. They also tested two specimens with flanges, one of which also failed in sliding shear.

Salonikios et al. [34, 35] conducted tests on 11 RC squat walls to study their cyclic behavior, especially concerning the sliding shear failure and the role of inclined rebars in preventing it, and to assess the shear formula's validity of Eurocode 8 and ACI 318-19 codes. They tested specimens of aspect ratios and $M/V\ell_w$ of 1.0 and 1.5, but only the specimens of 1.0 aspect ratio are relevant for this thesis. Of their five squat specimens, two were reinforced with diagonal bars. In the other three specimens, LSW1 had 0.565% distributed shear reinforcement in both directions, LSW2 had 0.277%, and LSW3 was identical to LSW2 but with 7% of axial load ratio (ALR).

The three specimens, LSW1, LSW2, and LSW3, had sliding shear failure. Specimens LSW1 and LSW2, without axial load, had damage focused on the cold joint. Both specimens had similar levels of pinching even though there were differences in reinforcement, which is a strong indicator that the pinching was controlled by sliding shear. Specimen LSW3 also slid, but it showed larger concrete spalling and less hysteretic pinching due to the axial load. The specimens reinforced with diagonal bars restricted the sliding shear mechanism. The crack widths in the web were smaller than specimens without diagonal rebars, as the reinforcement crossed the cracks almost perpendicular, making it more efficient in tension.

The necessity of high-strength materials motivated researchers to study their effect on the peak strength and deformation of reinforced concrete shear walls. Cheng et al. [36] tested five squat specimens without axial load, and the specimens differed in the steel quality (400 MPa or 785 MPa), amount of distributed shear reinforcement, and spacing of hoops in the boundary elements. Four of their specimens had significant sliding contributions, reaching between 20%-40% of the total deformation. All the specimens had low sliding contributions at a low-level drift ratio. The specimens that were heavily reinforced in the web and had regular steel (H60 and H60x) slid after a 0.3% drift ratio, whereas a specimen with high-grade steel and mild reinforcement slid after a 0.75% drift ratio. In all specimens, though, the initiation of sliding coincided with the drifts at which the longitudinal reinforcement exceeded the yielding strain.

Scholars have conducted a series of tests to study the behavior of squat walls reinforced with normal and high strength steel, focused on the diagonal shear and sliding shear failure modes. Park et al. [37] tested eight specimens of $M/V\ell_w = 1$, 7% axial load and reinforced with 420 MPa and 550 MPa rebars. Although sliding at the base is not reported, slipping occurred at the shear diagonal crack and developed into a web crushing failure. An extension of the previously mentioned study is the one of Baek et al. [38], which tested twelve specimens with the same steel quality and axial load, but with $M/V\ell_w$ of 1 and 1.5. But as they assessed only the diagonal shear failure mode, the cold joint of the wall-foundation interface was moved 5 cm into the inside of the foundation, which blocked a potential sliding shear failure.

In the next set of tests, Baek et al. [39] studied the effect of high-strength steel (600 MPa) on the sliding

shear strength, as ACI 318-19 limits the yield strength on its formula to estimate the friction strength (Eq. 2.9). They tested 13 specimens with constant shear-span ($M/V\ell_w = 0.33$) and no axial load. They varied the amount and quality of steel, treatment and location of the cold joint, and presence of flanges. Between their specimens, the critical parameter that affected the transition between a sliding shear and a web-crushing failure was the treatment of the cold joint, especially between an untreated surface and an over-grooved one. With their results, they proposed new formulas for sliding shear, where they included an effective strain for the reinforcement bars. Kim and Park [40] then investigated the effect of flanges in diagonal shear and sliding shear failure modes in squat walls. They dedicated two specimens to study the sliding failure, which showed that walls with flanges can indeed slide and that the flanges contribute to the sliding strength. Finally, Kim and Park [41] studied the effect of 700 MPa strength reinforcement bars on the friction resistance of squat specimens with/without flanges. Even though they had similar conclusions to the previous studies, all their specimens slid, and in the specimens with flanges, the web failed in sliding shear while the flanges had punching failure.

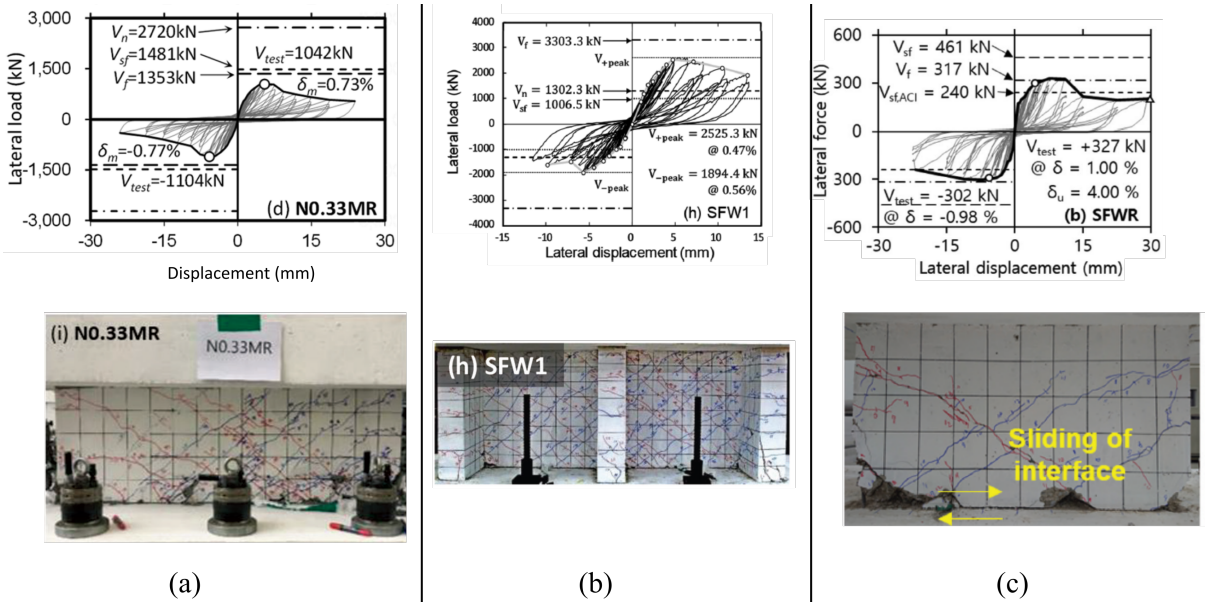

Figure 2.2: Load displacement curves and final state of specimens (a) N0.33MR of Baek et al. [39], (b) SFW1 of Kim et al. [40], and (c) SFWR of Kim and Park [41].

Other experimental campaigns had specimens with sliding shear failures. For instance, one specimen of Terzioglu et al. [42] slid, as it was the specimen with less vertical reinforcement and large web reinforcement. Hube et al. [43] studied thin squat reinforced concrete walls for low-rise constructions in specimens with a single layer of wire-weld-mesh as reinforcement. The specimen had considerable boundary reinforcement to avoid flexure failure. A reference specimen failed in a brittle diagonal tension manner, and a second specimen with similar geometry and web reinforcement but less boundary reinforcement failed in sliding shear. Finally, Barbachyn et al. [44] tested two squat walls ($M/V\ell_w$ = 0.52) with normal and high-strength steel that had sliding failure. All the previously mentioned specimens are reported to behave as diagonal shear-controlled specimens until the peak load (Fig. 2.3). After this point, the specimens had increasingly sliding deformations. Also note that almost all the specimens that failed in sliding shear were tested without axial load and that upon load reversal, the plateau that defines the sliding shear failure is at zero force.

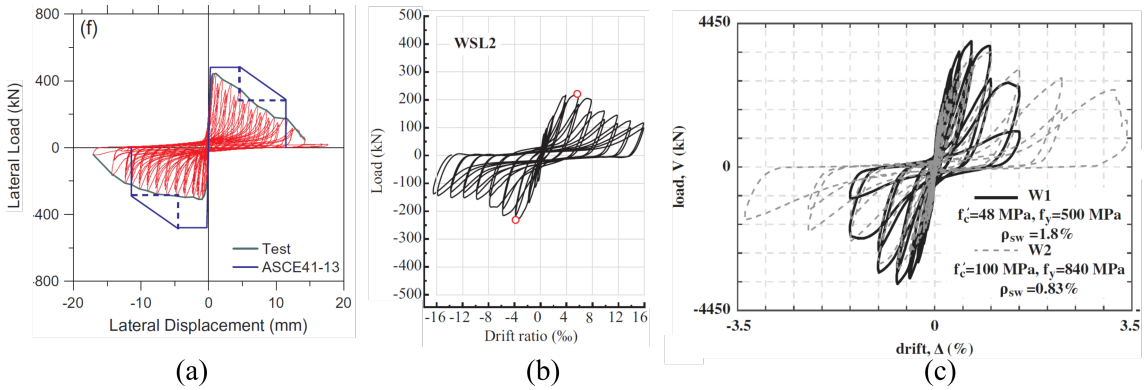

(a) (b) (c)

Figure 2.3: Load displacement curves of specimens (a) T3-S1 of Terzioglu et al. [42], (b) WSL2 of Hube et al. [43], and (c) W1 and W2 of Barbachyn et al. [44].

Two full-scale reinforced concrete buildings of 4-storeys were tested at the E-Defense shaking table in Japan [45]. The buildings had the same geometry, but one had regular reinforced concrete elements, whereas the other had pre-cast elements. One direction of the building had two frames as a lateral load-resisting system, and the other had two shear walls. The structures were subjected to the JMA-Kobe 1995 ground motion, with an increasing set of intensities: 10, 25, 50, and 100%. When the full intensity was applied, one shear wall had sliding shear failure, which showed that sliding could happen in actual structures with a realistic ground motion. This building has been a benchmark example for researchers who want to develop dynamic models of reinforced concrete elements. A group of researchers [46] used existing tools like ASCE/SEI 41-17 [47] to evaluate those guidelines with a series of real-scale shaking table tests. Because the sliding shear failure was not addressed in ASCE/SEI 41-17, the models could not predict the drift profile over the height of the building.

2.3 Squat shear walls in code provisions and guidelines

Design codes and guidelines provide a standard route for engineers to design and assess structures. They set up the rules of design: they define the load scenarios, the maximum strength of elements, limit the service deformations, orientate detailing aspects, etc. They have been calibrated with ongoing professional experience, evolving through the years. This section describes the guidelines for reinforced concrete of two principal codes, ACI 318-19 [26] and Eurocode 8 [15], which will help to understand the dimensions and detailing of the tested specimens and how buildings' walls are designed. Then, guidelines for assessing structures are described, explaining their significant implications in squat reinforced concrete shear walls.

2.3.1 ACI 318-19

Estimation of shear strength

ACI 318-19 has two different formulas to estimate the diagonal shear strength of shear walls. Chapter 11 describes the provision for ordinary walls, and chapter 21 provides seismic guidance for special walls.

- Chapter 11: The nominal diagonal shear strength is obtained as the sum of the contribution to the strength of the concrete (V_c) and the steel (V_s):

$$V_n = V_c + V_s \tag{2.2}$$

The value of d should be taken as $0.8\ell_w$. The contribution of the concrete if the wall is subjected to compression is calculated as:

$$V_c = 0.17\lambda\sqrt{f'_c}hd \tag{2.3}$$

For walls subjected to axial tension:

$$V_c = 0.17\left(1 + \frac{0.29N_u}{A_g}\right)\lambda\sqrt{f'_c}b_w d \tag{2.4}$$

In a more detailed manner, V_c can be calculated as the minimum of:

$$V_c = \min\left\{0.17\lambda\sqrt{f'_c}hd + \frac{N_u d}{4\ell_w}, \left(0.6\lambda\sqrt{f'_c} + \frac{\ell_w\left(1.25\lambda\sqrt{f'_c} + 0.2\frac{N_u}{\ell_w h}\right)}{\frac{M_u}{V_u} - \frac{\ell_w}{2}}\right)hd\right\} \tag{2.5}$$

The steel reinforcement contribution V_s is obtained as:

$$V_s = \frac{A_v f_y d}{s} \tag{2.6}$$

V_n is limited to $0.83\sqrt{f'_c}hd$. The minimum amount of horizontal web reinforcement ρ_t is 0.0025. The longitudinal web reinforcement shall not be less than:

$$\rho_\ell = \max\left(0.0025, 0.0025 + 0.5\left(2.5 - \frac{h_w}{\ell_w}\right)(\rho_t - 0.0025)\right) \tag{2.7}$$

- Chapter 18: The code has a different expression for shear walls resisting seismic loads. The nominal shear strength is given by:

$$V_n = A_{cv}(\alpha_c\lambda\sqrt{f'_c} + \rho_t f_y) \leq 0.83A_{cv}\sqrt{f'_c} \tag{2.8}$$

Where α_c accounts for the difference between the expected occurrence of flexure-shear cracking in slender walls and web-shear cracking in squat walls [48]. α_c = 3 for $h_w/\ell_w \leq 1.5$, is 2 for $h_w/\ell_w > 2$, and varies linearly between 3.0 and 2.0 for h_w/ℓ_w between 1.5 and 2.0. A_cv is the gross area of the concrete section bounded by the web thickness and length of the section in the direction of the considered shear forces.

Earthquake-resistant provisions of ACI 318-19 introduce extra requirements for the web reinforcement. The minimum web reinforcement for ρ_t and ρ_ℓ is 0.0025 (18.10.4.3). Additionally, if the wall's aspect ratio is less than 2.0, the longitudinal reinforcement ratio ρ_ℓ shall not be less than the transversal reinforcement ratio ρ_t.

Friction strength

Chapter 22 of ACI 318-19 provides expressions for the shear-friction strength (or sliding shear strength). These provisions were developed from the experimental studies of Mattock [23–25]. The shear friction nominal strength, V_n, shall be computed as:

$$V_n = \mu(A_{vf}f_y + N_u) \leq 0.2f'_c A_c \tag{2.9}$$

Where A_{vf} is the area of steel perpendicularly crossing the sliding interface, μ is the friction coefficient, which depends on the condition of the sliding surface, as shown in Table 2.1, A_c is the area of concrete resisting the shear transfer, and N_u is the compression force at the interface. The maximum yield steel stress is limited to 420 MPa.

Table 2.1: Friction coefficient. $\lambda = 1.0$ for normal-weight concrete; $\lambda = 0.75$ for light-weight concrete.

Contact surface condition	μ
Concrete placed monolithically	1.4λ
Concrete placed against hardened concrete with surface intentionally roughened	1.0λ
Concrete placed against hardened concrete not intentionally roughened	0.6λ
Concrete anchored to as-rolled structural steel by headed studs or by reinforcing bars	0.7λ

The shear friction strength is limited to:

$$V_n \leq \min(0.2f'_c, (3.3 + 0.08f'_c)A_c, 11A_c) \tag{2.10}$$

2.3.2 Eurocode 8

Eurocode 8 [15] explicitly defines diagonal compression, diagonal tension, and sliding shear as possible shear failure modes of squat walls, and provides for each of them expressions to estimate their strength.

The philosophy of strength reduction in Eurocode is different from ACI 318-19. The reduction factor is directly applied to the material strength rather than to the nominal strength. These reduced materials' strengths are called design values and their reduction factor is different for each material. This is why Eurocode expressions are defined in terms of f_{yd} (design value of steel yield strength) or f_{cd} (design value of concrete compressive strength) rather than f_y or f'_c. The reduction factor for the steel yield strength is 1.1, and for the concrete compressive strength is 1.5.

Diagonal compression failure of the web due to shear (Section 5.5.3.4.2)

The maximum strength related to diagonal compression of a shear wall is calculated with section 6.2.3 of Eurocode 2:

$$V_{RD,max} = \frac{b_w z \nu_1 f_{cd}}{\cot\theta + \tan\theta} \tag{2.11}$$

Where z, the lever arm, should be taken as $0.8L_w$, b_w is the thickness of the wall, ν_1 is a strength reduction factor that accounts for concrete cracked in shear (Equation 2.12), and θ is the strut angle, taken as 45^o.

$$\nu_1 = 0.6\left(1 - \frac{f_{ck}}{250}\right) \tag{2.12}$$

Diagonal tension failure of the web due to shear (Section 5.5.3.4.3)

Eurocode 8 has special provisions for squat walls, which are defined as those with a the shear-span (α_s = $M_{Ed}/(V_{Ed}\ell_w)$) below 2. The diagonal tension strength is the sum of the contribution of the strength

without shear reinforcement ($V_{Rd,c}$, defined in Section 6.2.2 of Eurocode 2 [15]) and the contribution of the horizontal distributed web steel reinforcement:

$$V_{Ed} \leq V_{Rd,c} + 0.75\rho_t f_{yd,t} b_w \alpha_s L_w \tag{2.13}$$

And the vertical reinforcement ratio (ρ_ℓ) should satisfy:

$$\rho_t f_{yd,t} b_w z \leq \rho_\ell f_{yd,\ell} b_w z + \min N_{Ed} \tag{2.14}$$

Sliding shear failure (Section 5.5.3.4.4)

Eurocode 8 calculates the sliding shear strength $V_{Rd,S}$ as the contribution of the dowel resistance of the vertical bars V_{dd}, the shear resistance of inclined bars V_{id}, and the friction resistance V_{fd}.

$$\begin{aligned} V_{dd} &= \min\left(1.3 \cdot \sum A_{sj} \cdot \sqrt{f_{cd} \cdot f_{yd}}, 0.25 \cdot f_{yd} \sum A_{sj}\right) \\ V_{id} &= \sum A_{si} \cdot A_{sj} \cdot \cos\varphi \\ V_{fd} &= \min\left(\mu \cdot \left[\left(\sum A_{sj} \cdot f_{yd} + N_{Ed}\right) \cdot \xi + \frac{M_{Ed}}{z}\right], 0.5\eta \cdot f_{cd} \cdot \xi \cdot \ell_w \cdot b_{wo}\right) \end{aligned} \tag{2.15}$$

Where μ is the friction coefficient (0.6 for smooth surfaces and 0.7 for rough ones), z is the internal lever arm, ξ is the normalized neutral axis depth, ℓ_w is the length of the wall, $\sum A_{sj}$ is the sum of the vertical bars' area, $\sum A_{si}$ is the sum of the diagonal bars' area, N_{Ed} the axial load at the interface, M_{Ed} is the moment at the interface, φ is the inclination angle of the diagonal reinforcement,and $\eta = 0.6(1 - f_{ck}/250)$. Note that V_{fd} is the most similar term to the ACI 318-19 provisions, but Eurocode 8 includes the effect of the moment in the sliding interface.

Eurocode 8 requires a minimum of diagonal reinforcement for squat walls. In the base, the friction resistance contributed by diagonal reinforcement V_{id} must be greater than half of the demand V_{Ed}.

2.3.3 ASCE/SEI 41-23

The standard ASCE/SEI 41-23: Seismic Evaluation and Retrofit of Existing Buildings [49] included new provisions for reinforced concrete shear walls. In particular, it provided new expressions for the yield and peak strength of walls controlled by diagonal shear, but more importantly, it included for the first time provisions for walls controlled by sliding shear behavior. The research behind the updates is explained in FEMA P-2208 [50]. The following subsections address the provisions for non-linear modeling of diagonal shear- and sliding shear-controlled walls according to ASCE/SEI 41-23.

Diagonal shear-controlled walls provisions

The revision to diagonal shear-controlled walls was conducted with a subset of 325 specimens that had diagonal shear or diagonal shear/flexure failures, tested mainly in quasi-static, reversed cyclic loading protocols.

The adopted force-deformation relation of diagonal shear-controlled walls is shown in Figure 2.4. It is characterized by a diagonal shear cracking point F, yield diagonal shear strength point B, a peak diagonal

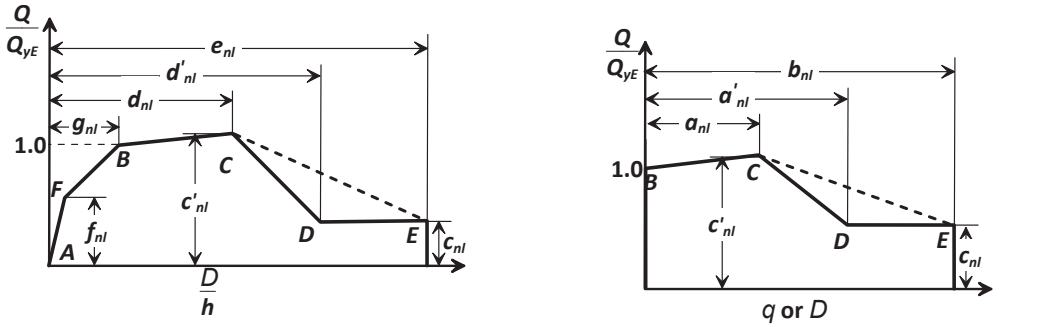

Figure 2.4: Generalized force-deformation relation for concrete elements or components. Adopted from ASCE/SEI 41-23 [49].

shear strength point C, and residual strength points D and E. The diagonal shear cracking strength of a wall or wall segment ($V_{CcrWallE}$) can be estimated as:

$$V_{CcrWallE} = \alpha_c \lambda \sqrt{f'_{cE}} A_{cv} \tag{2.16}$$

Where f'_{cE} is the expected compressive strength of the concrete, and A_cv is the gross area of the concrete section bounded by the web thickness and length of the section in the direction of the considered shear forces. α_c was previously defined in Eq. 2.8.

The yield diagonal shear strength $V_{CydWallE}$ is defined as:

$$V_{CydWallE} = \left(2.0 - \frac{V_{CWall318E}}{\omega_v V_{MCultE}}\right) V_{CWall318E} \tag{2.17}$$

The strength is lower and upper-bounded by $0.8V_{CWall318E}$ and $1.8V_{CWall318E}$, where $V_{CWall318E}$ is the diagonal shear strength calculated with Eq. 2.8, by using the expected values of the steel yield strength ($f_{yt,E}$) and concrete compressive strength (f'_{cE}). V_{MCultE} is the shear demand at the ultimate moment of a section, which can be obtained from a moment curvature analysis. ω_v is the shear dynamic amplification factor. The ultimate diagonal shear strength $V_{CultdWallE}$ shall be taken as $V_{CydWallE}$ multiplied by the factor c'_{nl}, defined in Table 7.4.1.1.2 of ASCE/SEI 41-23. For rectangular walls and with an axial load ratio below 10%, the value c'_{nl} equals to 1.1. The extra parameters defined in Figure 2.4 (a) are defined in Table 7.4.1.1.2 of ASCE/SEI 41-23.

Sliding shear-controlled walls provisions

The guidelines for non-linear modeling of sliding shear-controlled suggest using an interface element at the zone where sliding is expected to occur. The element is characterized by the force-deformation relation of Figure 2.4 (b). The force-deformation relations of a sliding shear-controlled wall are defined in terms of absolute displacements, rather than a normalized value such as the drift ratio. The force-deformation relation is characterized by the yield sliding shear strength at point B, the peak sliding shear strength at point C, and residual strength at points D and E. The force-deformation relation considers no slip at the sliding interface until the yield sliding shear strength is exceeded. Prior to the yield sliding shear strength, the response of the wall is captured by diagonal shear or flexure springs, which can be assumed to be linear. Therefore, ASCE/SEI 41-23 considers the sliding shear-controlled behavior of

walls as a two degree-of-freedom system. The calibration of the parameters of the new provisions was conducted with 71 sliding shear-controlled walls, in its vast majority without applied axial load. The yield sliding-shear strength is defined as: The yield diagonal shear strength $V_{CydWallE}$ is defined as:

$$V_{CfyWallE} = \left(2.0 - \frac{V_{CfyWallSE}}{\omega_v V_{MCyDE}}\right) V_{CfyWallSE} \tag{2.18}$$

The strength is lower and upper-bounded by $0.8V_{CfyWallSE}$ and $1.8V_{CfyWallSE}$, where $V_{CfyWallSE}$ is the sliding shear strength calculated with Eq. 2.9. There are two main differences with the provisions of ACI 318-19. First, the maximum steel yield stress allowed to estimate $V_{CfyWallSE}$ is 520 MPa instead of 420 MPa. Second, the values of the friction coefficient are:

- $\mu = 0.7$ for concrete cast monolithically or placed against hardened concrete that is intentionally roughened to a full amplitude of approximately 1/4 in.
- $\mu = 0.6$ for concrete placed against hardened concrete that is not intentionally roughened.

For flanged sections, the reinforcing steel crossing the interface, including the reinforcement within the effective flange width, can be included in A_{vf}. Finally, the peak strength of a sliding shear-controlled wall is 1.1 times the yield strength of point B (Eq. 2.18). The maximum allowed displacement for sliding shear-controlled walls is 3 inches, based on engineering judgment, as this behavior mode usually does not present axial failure.

2.3.4 FEMA 306

The document FEMA 306 [51] has the purpose of providing practical criteria and guidance for evaluating earthquake damage to buildings with concrete and masonry members acting as a primary lateral-force-resisting systems. FEMA 306 describes the residual damage that is expected in structural elements in terms of observable criteria like crack width, crack pattern, concrete spalling, residual damage, etc, for five levels of damage severity: insignificant, slight, moderate, heavy and extreme. For each level of severity and depending on the failure mode, FEMA 306 provides modification factors for the initial stiffness (λ_K), the peak strength (λ_Q) and the deformation acceptability limits (λ_D). Tables 2.2, and 2.4 provide the modification factors and description of damages for the behavior modes of shear diagonal tension, shear diagonal compression or web crushing and sliding shear, which are of interest in this thesis.

2.3.5 FEMA P58

FEMA P58: Seismic performance assessment of buildings, methodology and implementation had the objective to develop the next generation of performance-based seismic design procedures for new and existing buildings. It was a major work and its principal product was a series of volumes, background documentation and electronic material.

The third volume, Supporting Electronic Materials and Background Documentation [52], provides the document Damage States and Fragility Curves for Squat Reinforced Concrete Walls [53], which is a study of Gulec and Whittaker [54]. These documents summarize the development of fragility curves for low aspect ratio reinforced concrete walls. To this end, they assembled a family of damage states

Table 2.2: Component damage classification guide for a reinforced concrete wall with flexure/diagonal tension failure mode.

Severity	λ_K	λ_Q	λ_D	Description of damage
Insignificant	0.8	1.0	1.0	Shear cracks do not exceed 1/16 in (1.6 mm)
				Flexural crack widths do not exceed 3/16 in (4.7 mm)
				No significant spalling or vertical cracking
Slightly				Not used
Moderate	0.5	0.8	0.9	Shear crack widths do not exceed 1/8 in (3.2 mm)
				Flexural crack widths do not exceed 1/4 in (3.2 mm)
				Shear cracks exceed 1/16 in (1.6 mm), or limited spalling occurs at web or toe regions
				No buckled or fractured reinforcement
				No significant residual displacement
Heavy	0.2	0.3	0.7	Shear crack widths may exceed 1/8 in (3.2 mm), but do not exceed 3/8 in (9.5 mm). Higher cracking width is concentrated at one or more cracks
Extreme	-	-	-	Reinforcement has fractured
				Replace or enhance the structural element

Table 2.3: Component damage classification guide for a reinforced concrete wall with flexure/web crushing.

Severity	λ_K	λ_Q	λ_D	Description of damage
Insignificant				See Table 2.2
Slightly				Not used
Moderate				See Table 2.2
Heavy	0.2	0.3	0.7	Significant spalling of concrete in web, and
				No fractured reinforcement
Extreme	-	-	-	Heavy spalling and voids in web concrete, or significant residual displacement
				Replace or enhance the structural element

based on four methods of repair (MoR): Cosmetic repair (MoR-1), epoxy injection(MoR-2), partial wall replacement (MoR-3) and Wall replacement(MoR-4). Then, they assigned to each specimen of a database one method of repair depending on the damage observed and measured during the test. The parameters that they adopted, such as crack width or displacements, were the maximums measured and reported in the tests, therefore, it is a tool to analyze the data of cyclic tests rather than to provide post-earthquake damage identification parameters. In terms of sliding deformations, they assigned the sliding initiation of a wall as the worst damage state (Wall Replacement).

One crucial point was to associate each damage state with a particular drift ratio. In the case of sliding shear failure, the authors acknowledge that there is no agreement about the drift associated with the sliding shear failure, as some tests report the drifts related to sliding initiation and others to significant displacements. Thus, they defined supplemental criteria to identify the drift associated with the damage state Wall Replacement: (1) Residual drift exceeding 0.5%, and (2) Drift ratio associated with a wall strength less than 50% of the peak strength. For criteria (1), they associated the residual drift of 0.5%

Table 2.4: Component damage classification guide for a reinforced concrete wall with flexure/sliding shear.

Severity	λ_K	λ_Q	λ_D	Description of damage
Insignificant	0.8	1.0	1.0	No crack width exceed 3/16 in (4.7 mm) No shear cracks exceed 1/8 in (3.2 mm) No significant spalling or vertical cracking
Slight	0.6	1.0	1.0	Crack widths do not exceed 1/4 in (0.635) No shear cracks exceed 1/8 in (3.2 mm)
Moderate				Not used
Heavy	0.4	0.5	0.8	Development of a major horizontal flexural crack along the entire wall length, with some degradation of concrete along the crack, indicating that sliding has occurred. Possible small lateral offset at crack
Extreme	-	-	-	Significant lateral offset at sliding plane Replace or enhance the structural element

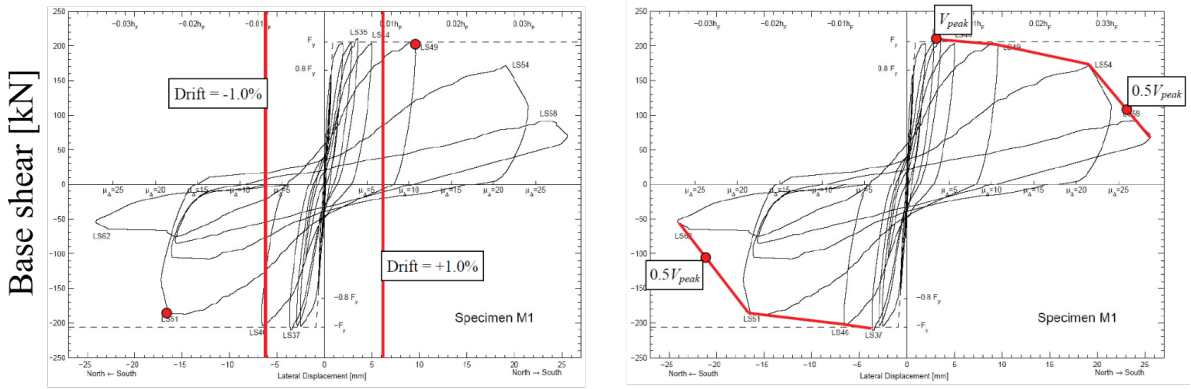

Figure 2.5: Criterias to define the sliding shear failure according to Gulec and Whittaker [54] (a) Criteria 1 (b) Criteria 2. Adopted from the third volume of FEMA P58 [52].

to a zero-force displacement intercept of 1% story drift ratio because the coda portion of the earthquake ground motions will re-center the displaced components. Figure 2.5 graphically shows the previously described criteria.

2.4 Estimation of peak shear strength of R/C squat walls

With the increasing number of squat shear wall tests, researchers have been proposing new formulas for estimating the peak shear strength using statistical regressions, machine learning, or other methods. This section presents selected formulas that have been proposed in the last years but are not yet included in codes or guidelines.

Gulec and Whittaker

Gulec and Whittaker proposed an equation for the peak diagonal shear strength of squat walls with a database of 227 walls [55] by doing a regression analysis, and studying the influence of parameters such as aspect ratio horizontal and vertical reinforcement ratios, concrete compressive strength, axial

force and vertical boundary element reinforcement ratio. Equation 2.19 shows the proposed formula for rectangular walls (in psi, in and lb).

$$V_n = \frac{1.5\sqrt{f'_c}A_{eff} + 0.25F_{vw} + 0.20F_{vbe} + 0.4P}{\sqrt{H_w/L_w}} \leq 10\sqrt{f'_c}A_w \tag{2.19}$$

Where A_w is the wall area, f'_c the compressive concrete strength, F_vw the force attributed to vertical web reinforcement (calculated as the product of the total area of vertical web reinforcement and the reinforcement yield stress), F_{vbe} is the force attributed to boundary element reinforcement (calculated as the product of the total area of vertical reinforcement yield stress), and P is the axial load. Interestingly, this formula dropped the contribution of the web horizontal reinforcement bars.

Moretti, Kono and Obara

They proposed an empirical equation based on a database of 414 reinforced concrete specimens [31]. The main characteristics that contribute to the diagonal shear strength of the walls are clearly defined, and are independent of each other. The formula assumes the contribution of the boundary elements V_{be} (Equation 2.21), the longitudinal V_v (Equation 2.22) and transversal V_h (Equation 2.23) reinforcement, the axial load V_N (Equation 2.24) and the compression strut V_{strut} (Equation 2.25). The peak shear strength is the sum of these contributions.

$$V_n = V_{be} + V_v + V_h + V_N + V_{strut} \tag{2.20}$$

$$V_{be} = 0.25\rho_{be}H_bB_b \min(f_{yL}, 700\text{ MPa})/\sqrt{H_w/L_w} \tag{2.21}$$

$$V_v = 0.3\rho_v b_w(0.8L_w - _b)f_{yv}/\sqrt{H_w/L_w} \tag{2.22}$$

$$V_h = 0.2\rho_h b_w(0.8\ell_w - H_b)\tan(\theta)f_{yh} \tag{2.23}$$

$$V_N = \frac{0.15N}{\sqrt{\frac{M}{VL_w}}} \tag{2.24}$$

$$V_{strut} = w_{strut}b_w f'_c\left(0.78 - \frac{f'_c}{200}\right)\frac{1}{\sqrt{M/VL_w} + 0.18}\cos(\theta) \tag{2.25}$$

Figure 2.20 shows the definition of the variables and the assumed diagonal strut by Moretti et al. The strut width is obtained from the expression for infills in RC frames of FEMA 306 [51] according to Equation 2.26.

$$w_{strut} = 0.175(\lambda H_o)^{-0.4}r_{inf} \tag{2.26}$$

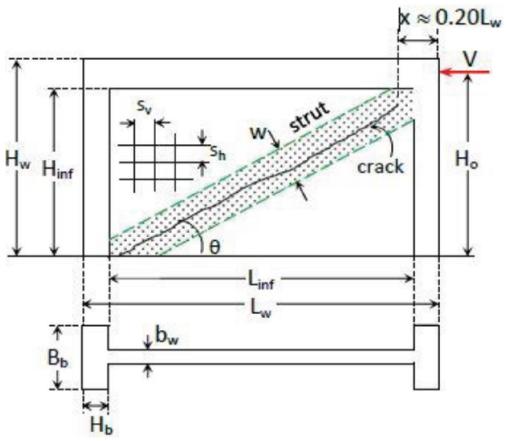

Figure 2.6: Wall characteristics and diagonal strut mechanism assumed by Moretti et al [31].

Where $I_{bc} = B_w H_b^3/12$ is the moment of inertia of the boundary columns. In the case of rectangular walls, $H_b = b_w/2$ for $\rho_{be} > 0$, or $H_b = b_w/4$ for $\rho_{be} = 0$, and $r_{inf} = \sqrt{L_w^2 + H^2}$

Matias Rojas-León

Matias Rojas-León et al. [56] proposed a formula by employing statistical and machine learning approaches with a database of more than 340 walls. The motivation of this work was to update the seismic shear strength formula of ACI 318-19 code, which has not changed in years even though extensive research and tests have been conducted in that time frame. The proposed formula is:

$$V_n = \alpha_c A'_g f'_c + \alpha_s(\rho_{sb} f_{ysb} + \rho_t f_{y,t}) A_{cv} \tag{2.27}$$

Where the values of α_c and α_s are:

$$\alpha_c = \frac{1}{100}\left(9\frac{\left(1+\frac{P_u}{A'_g f'_c}\right)^3}{\left(\frac{M_u}{V_u L_w}^{1/3}\right)} - 6\right) \tag{2.28}$$

$$\alpha_s = \frac{2}{5\left(\frac{M_u}{V_u L_w}\right)^{1/3}} \tag{2.29}$$

This formula accounts for the effects of the boundary longitudinal reinforcement (the ratio ρ_{sb} and yield stress f_{ysb}), the transverse web reinforcement (ρ_t and $f_{y,t}$), the axial load ratio $P_u/A'_g f'_c$, where A'_g is the gross area of the section, and the shear-span ratio. The formula does not include the contribution of the vertical web reinforcement as the term was dropped during the process of shrinking the initial guess formula.

2.5 Controlling behavior mode classification

As previously mentioned, reinforced concrete shear walls can have a flexure, diagonal shear, sliding shear, or rocking-controlled behavior. The behavior mode depends on parameters such as the geometry,

load conditions, reinforcement ratios, and axial load, among others. Some walls have a clearly defined controlling behavior mode, but some are close to the transition zone between two or more behavior modes. This section summarizes recent efforts to identify these transitions.

Abdullah [57] proposed a shear wall behavior mode classification calibrated with a dataset of more than 1000 specimens, which was adopted in the ACI 369.1-22 code [8]. This classification is based on the relative flexure, diagonal shear, and sliding shear strengths, which were demonstrated to be a good indicator of the possible failure mode compared to the database. The method is relatively simple as it computes the strengths with the expressions of ACI 318-19 [26]. Using the notation of Abdullah, the flexure strength $V_{@MyE}$ is obtained from a moment-curvature analysis, the sliding shear strength $V_{yE,f}$ is obtained with Equation 2.9 and the sliding shear strength $V_{yE,d}$ with Equation 2.3. The controlling behavior mode is then obtained according to Table 2.5, where ω_v is the dynamic amplification factor, which for experimental specimens is considered equal to 1. Note that the strength expressions of ACI 318-19, especially those related to friction and shear, are known to be conservative [31, 53], but this methodology showed that the ratios of Table 2.5 showed good agreement predicting the failure modes against the test database.

Table 2.5: Structural wall and wall segment controlling behavior classification according to ACI 369.1-22 [8].

Criteria		Expected controlling behavior
$V_{yE}/(\omega_v V_{@M_{yE}}) < 1.0$	$V_{yE,f}/V_{yE,d} < 1.0$	Sliding shear
	$V_{yE,f}/V_{yE,d} > 1.0$	Diagonal shear
$V_{yE}/(\omega_v V_{@M_{yE}}) > 1.0$		Flexure

An advantage of this method is that it can be graphically represented. By plotting the ratio $V_{yE,f}/V_{yE,f}$ in the x-axis and the $V_{yE}/V_{yE,f}$ ratio in the y-axis, the boundaries between the behavior modes are clearly defined. Figure 2.7 shows the diagram with the database specimens, where the red zone indicates a diagonal shear-controlled behavior, the yellow one a sliding shear-controlled behavior, and the blue one a flexure-controlled behavior. The friction coefficient considered for the sliding shear strength of the specimens plotted in Figure 2.7 was 0.6.

Trost, Schuler and Stojadinovic [58] proposed a behavior mode classification for squat walls based on non-linear analysis. The shear walls were modeled considering the flexure, diagonal shear, and sliding shear deformation in series, which means no interaction exists between them. The walls are subjected to a specific cyclic load protocol, and the behavior mode that reaches peak strength first is defined as the failure mode. Figure 2.8 shows the graphical representation of this behavior mode identification, where the boundaries are defined in terms of the axial load ratio and the geometrical aspect ratio.

Mangalathu et al. [32] studied using machine learning algorithms to identify the failure mode of walls. They used a database of 393 specimens, of which 152 had flexure failure, 96 had flexure-diagonal shear failure, 122 had diagonal shear failure, and 23 had sliding shear failure. The inputs for their database were the aspect ratio M/VL_w, wall length to wall thickness ratio, concrete compressive strength, vertical and horizontal reinforcement of the boundary elements and the web, yield strength of the steel reinforcement bars, the section gross area and the boundary elements area. Using different machine learning techniques,

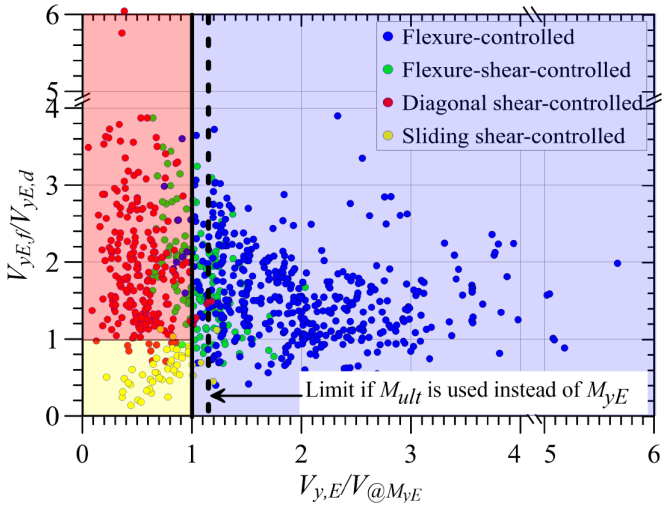

Figure 2.7: Graphical representation of the behavior mode diagram of Abdullah [57].

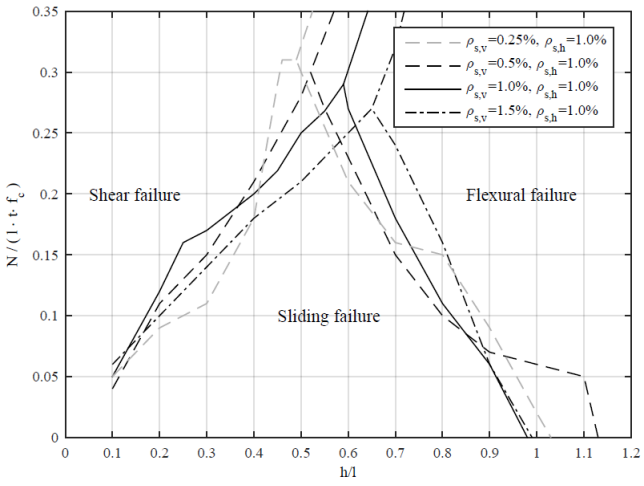

Figure 2.8: Graphical representation of the failure mode diagram Trost [28].

they reached an accuracy between 67%-86%, with random forest having the most considerable accuracy. Even though the dataset seems small for a machine learning algorithm, the exploration was interesting, and it showed that it could be a good methodology to predict the failure mode of the specimen. The accuracy of this model should increase with a larger number of walls, especially those with parameters not represented in the database, such as M/VL_w lower than one and sliding shear failure.

2.6 Hybrid simulation

Experimental tests in structural elements provide significant results in understanding the behavior of our structures. From them, we can understand the damage progression, failure modes, maximum deformation and strength, and calibrate models, and they are even the basis for design codes. The most common type of test is cycling testing, where a structure, part of it, or a single structural element is subjected to a predefined history of loads or displacements applied by actuators. The results of these tests allow us to obtain forces and deformations of the elements in a controlled manner and are the basis for calibrating hysteretic models that are used in research and practice.

The highest level of complexity is shaking table tests, where the whole building or part of it is subjected

to accelerations corresponding to a specific ground motion. These tests are dynamic and, therefore, consider inertial and damping effects, strain rate effects, etc. These tests provide the most accurate behavior of the structure, as each element has actual boundary conditions and connections with other parts of the structure. While cyclic tests can be conducted with at least one actuator with equipment that many laboratories around the globe have, shaking table tests need a complex arrangement of actuators and precise real-time control. Even though many shaking tables can test different ranges of scales, few can handle real-scale structures in the three translation degrees of freedom, such as the shaking table of the University of California at San Diego and the E-Defense shaking table in Japan.

Hybrid simulation is an experimental technique that studies the response of structures with a hybrid model consisting of numerical and physical subdomains [59]. The physical subdomain corresponds to a structure or part of it (substructure) represented by a specimen in an experimental setup 2.9. The numerical subdomain comprises an analytical model in a computer and includes the numerical integration of the dynamic system and the finite element model of the rest of the substructure. These two models exchange data continuously to simulate displacement, velocity, and acceleration time histories of the hybrid system [60]. Hybrid simulation allows the tests of more complex systems than the cyclic tests, as it can capture the interaction of the tested specimen with the rest of the structure and can be subjected to realistic ground motion instead of a pre-defined load protocol, and is simpler than a shaking table tests as the hybrid simulation does not need the entire structure to be tested, it can be conducted at low rates (quasi-dynamic) and the dynamic effects and rest of the structure is considered in the numerical model.

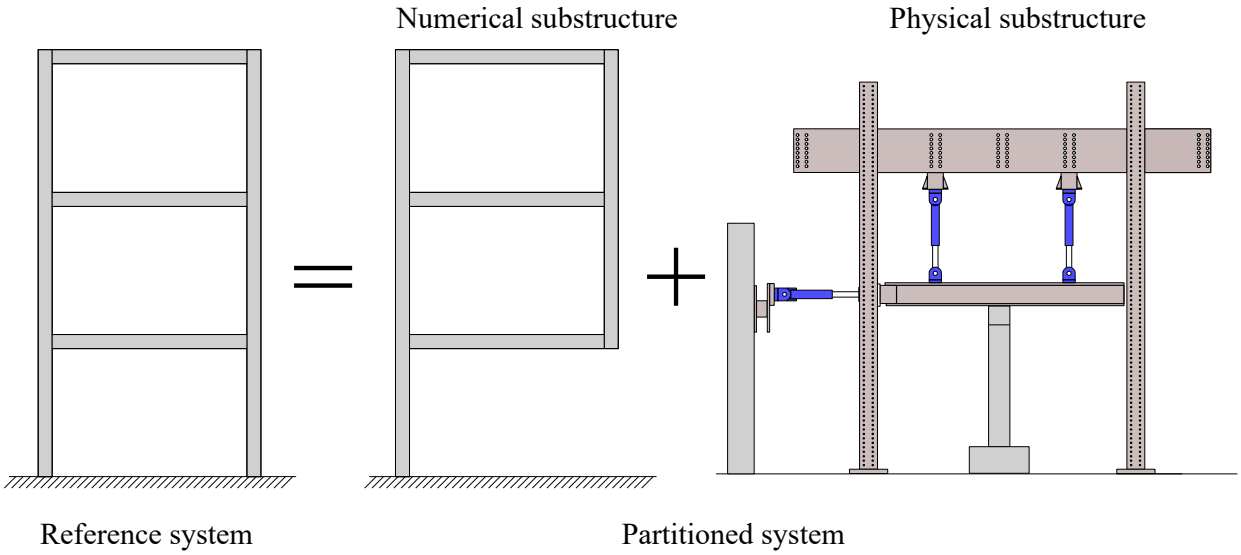

Figure 2.9: Reference system, numerical and physical substructure of a hybrid simulation test

Professor Nakashima wrote an article with a short history of the application of hybrid simulation in earthquake engineering [60], where he separates it into three stages. The first stage relates to the beginning of the application of hybrid simulation in earthquake engineering, which dates back to the early 70s in Japan. The hybrid simulation was developed as an alternative to shaking table and cyclic tests by Takanashi et al. [61]. In the words of Nakashima [60]: "The group has essentially expanded the capability of quasi-static tests so that the tests could be done with an actual displacement history and let the computer, in which the governing equations of motion are established, decide the history." The

group led by Takanashi was the first to come up with the concept and had to develop an architecture for hybrid simulation and integration schemes. The first concept included an implicit Newmark integration scheme [62], but it needed a constant estimation of the secant stiffness. They overcame this by using the explicit Central Difference Method [63], which was successfully implemented in two-story steel frame tests that showed the stability of the methodology [64].

These ideas were further developed in the 80s and '90s in Stage II, mainly from the work due to an alliance between the United States and Japan. One of the key milestones was the test of a real-scale 7-story reinforced concrete building [65]. This test showed the complications of hybrid simulation on a multi-degree-of-freedom (MDOF) system, and it was condensed to one DOF system assuming a triangular force distribution. Nevertheless, this test showed all the complexities of HS and paved the way for the development of HS in stage two. The main challenges developed during this stage were error propagation and suppression of errors [66, 67], substructuring approaches in hybrid simulation [68], and the start of real-time hybrid simulation [69].

An essential step in the current implementation of hybrid simulation has been the development of middlewares that allow the connection between finite element models and data acquisition systems in laboratories. Common middlewares used in hybrid simulation are OpenFresco [70] and UT-SIM Framework [71]. The most common is OpenFresco, a natural extension of OpenSees [72], but it allows connections with other finite element software. OpenFresco is an object-oriented software with different integration algorithms suitable for conducting hybrid simulation. OpenFresco has four classes that define the hybrid simulation: Experimental Element represents the physical portion of a model, Experimental Site relates to the laboratory where the specimen is tested and allows geographically distributed hybrid simulation [73], Experimental Setup defines the setup in which the specimen is tested, and Experimental Control provides the interface to connect with the data acquisition system.

Hybrid simulation needs experimental setups and controllers capable of transferring the displacement commands from the finite element model of the computer to a control point of the experimental specimen, which is usually the shared point with the linked DOFs between the numerical and experimental parts. Each setup consists of an arrangement of actuators and measuring devices, and the controller has to transform the actuator's DOFs into the compatible DOFs with the numerical sub-structure [74]; therefore, each setup has a transformation matrix from the actuator to the numerical DOFs domain or even more complex algebraic transformation [75]. The MAST Facilities (Multi-axial Subasemblage Testing) can control the six degrees of freedom from an arrangement of actuators included in the controller. Thus, the command displacements are sent directly to the control point. The University of Minnesota [76], Swinburne University of Technology [77], Polytechnique Montreal [78], ETH Zürich [79] count with MAST Facilities for structural engineering testing. These setups have attractive features for hybrid simulation, such as 6-DOF control and mixed-mode control that allow precise boundary condition control and multi-direction excitation.

Large-scale testing in hybrid simulation has its complexities, mainly due to the degrees of freedom with significant stiffness, such as axial deformation, because the actuators must apply a small increment in displacement that can be out of their precision. A way to overcome this issue is with a mixed-mode

control [80], in which some degrees of freedom are in displacement-control and others in force-control. As each time integration step results are given in displacements, the host computer must convert the displacement to a force command. Some hybrid simulation tests with mixed mode control have converted the displacement to forces with the axial stiffness and have been used in columns or frame tests [81–83], but so far not in walls which have much larger axial stiffness.

There are few hybrid simulation tests with real-scale reinforced concrete walls, as they need large forces and precise control of boundary conditions due to their large stiffness. Whyte and Stojadinovic [84] conducted a hybrid simulation test in squat specimens with large stiffness by including a high-resolution external sensor [85], but the test did not consider axial load. Fatemi et al. [86, 87] and Woods et al. [4] conducted tests by considering as experimental part the bottom story of an 8-story and 3-story building, respectively. Both tests used a similar setup with a tri-actuator arrangement that gives control over the three in-plane degrees of freedom. They controlled the displacement and rotations with high-definition encoders and kept an axial load constant during the test.

CHAPTER 3

EXPERIMENTAL PROGRAM

3.1 Specimens

3.1.1 Specimen design

The experimental campaign considered six specimens to study the transition between the shear and sliding-controlled behavior modes in real-scale walls. The small number of specimens made it important to select a range of diversity within them to study the boundary of those behavior modes. Sliding and shear-controlled behavior modes usually develop in squat specimens, and, therefore, the specimens need to have shear-span (M/VL_w) lower than one. The design, steel reinforcement detailing, and axial load ratio of the specimens should be consistent with a typical low-rise building configuration with squat shear walls as the lateral resisting system. The capacity of the laboratory also constrained the specimens, as the maximum capacity of the cranes was 20 tons, and the lateral force of the test facility, which will be described later, was 4000 kN. The force capacity is enough for real-scale specimens, and it was decided to use as much of it as possible.

Many parameters influence the behavior of shear walls. Still, as there were only six specimens, the parameters had to be reduced to a set that could help to get significant conclusions about the transition of the behavior modes. It was decided to keep the geometry of the specimens constant, with a cross-section of 3000x200 mm and a height of 2550 mm. The specimens also include a 4 m long foundation to connect to the strong floor and a top cap beam to connect to the test facility, both 500 mm in height.

The axial load ratio and the distributed steel reinforcement were selected as the design parameters. The axial load ratio is known to be a key parameter in sliding. It is well known that the sliding resistance of a frictional system is $F = \mu P$, where μ is the frictional coefficient and P is the axial load. The distributed steel reinforcement in the web significantly influences the type of shear failure: diagonal compression and tension. Additionally, to investigate the influence of load protocol, two hybrid simulation tests were planned. These two specimens were selected from the pool of specimens of the cyclic tests to compare their results.

The specimens were designed to straddle between the boundaries of the shear and sliding-controlled behavior modes following the previously described method of Abdullah [57]. To this end, the specimens were designed to have the ratio of their nominal sliding shear and diagonal shear strengths (V_{sl}/V_{sh}) between 0.8 and 1.2, and the ratio of the minimum of sliding shear and diagonal shear resistance and flexure strength ratio ($\min(V_{sl}/V_{sh})/V_{fl}$) to be less than 0.8 to avoid flexure failure. The nominal flexure strength was obtained with a moment-curvature analysis, the nominal shear strength V_{sh} with Equation 2.8, and the nominal sliding strength V_{sl} with Equation 2.9. The friction coefficient μ was equal to 0.8, as it showed good agreement with the results of the first two specimens. Table 3.1 shows the test matrix,

where the nominal strengths are tabulated, and Figure 3.1 graphically shows in which behavior mode zone each specimen is.

Table 3.1: Properties of the tested squat reinforced concrete shear wall specimens.

Specimen	f'_c [MPa]	P [kN]	ALR [%]	ρ_t [%]	ρ_ℓ [%]	V_{fl} [kN]	V_{sh} [kN]	V_{sl} [kN]	$\frac{V_{sl}}{V_{sh}}$	$\frac{min(V_{sl}, V_{sh})}{V_{fl}}$
SW01	34.6	900	4.34	0.523	0.523	2741	2451	2170	0.89	0.79
SW02	28.5	1800	10.53	0.523	0.523	3447	2370	2890	1.22	0.69
SW03	35.9	900	4.18	0.333	0.333	2241	1904	1764	0.93	0.79
SW04	42.4	1200	4.72	0.393	0.523	3045	2154	2410	1.12	0.71
HSW01	37.3	900	4.02	0.523	0.523	2741	2485	2170	0.87	0.79
HSW02	37.5	1800	8.00	0.523	0.523	3617	2487	2890	1.16	0.68

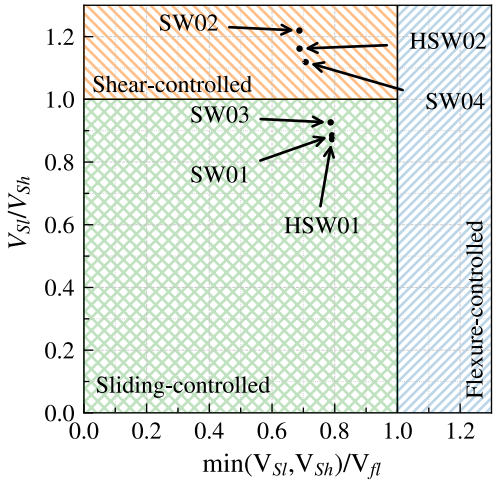

Figure 3.1: Behavior mode interaction diagram, considering $\mu = 0.8$ as a friction coefficient in Equation 2.9

Specimen SW01 was set as the reference specimen. It has distributed longitudinal and transverse reinforcement of 0.523% (double mesh of ϕ10@15), an axial load ratio of 4.41% ($P = 900$ kN). According to the controlling behavior mode classification, it should have sliding shear-controlled behavior. With respect to the reference specimen SW01, the changes on the other specimens were:

- Specimen SW02: The axial load was doubled to 1800 kN, which resulted in an ALR of 10.53%. By increasing the ALR, the wall moved to the diagonal shear-controlled zone.
- Specimen SW03: The transverse and longitudinal reinforcement ratios were reduced to 0.33%, which lowered both the sliding shear and diagonal shear strength. The objective was to approach the minimum reinforcement ratio for special walls in ACI 318-19 (ρ = 0.25%) without coming too close to the flexure-controlled zone. This specimen was, thus, in the sliding shear-controlled zone of Figure 3.1.
- Specimen SW04: Only the transverse reinforcement ratio was reduced, to keep the sliding shear strength equal to SW01, but lower the shear strength. This moved specimen SW04 into the diagonal shear-controlled zone of Figure 3.1. However, the concrete strength was much larger than the target of 30 MPa. To maintain an ALR level similar to specimens SW01 and SW03, the applied axial load

on specimen SW04 was increased to 1200 kN. This caused an increase in the maximum sliding strength that pushed specimen SW04 somewhat further from the sliding/shear boundary in Figure 3.1 than intended.

- Specimen HSW01 and HSW02: These two specimens are an extension of specimens SW01 and SW02, respectively. They have the same geometry, reinforcement, and respective axial loads but will be tested under hybrid simulation. Specimens HSW01 and HSW02 fall in the same controlling behavior mode in Fig. 3.1 as their cyclic counterpart. The parameter of interest in these two specimens is to see the influence of the load protocol in the controlling behavior and failure mode.

3.1.2 Specimen geometry and reinforcement

The specimens consisted of a foundation, a wall, and a top cap beam to facilitate the connection with the experimental setup. The wall panels had a cross-section of 3000x200 mm with a height of 2550 mm, plus a 500 mm thick foundation and top cap beam, as shown in Figure 3.2.

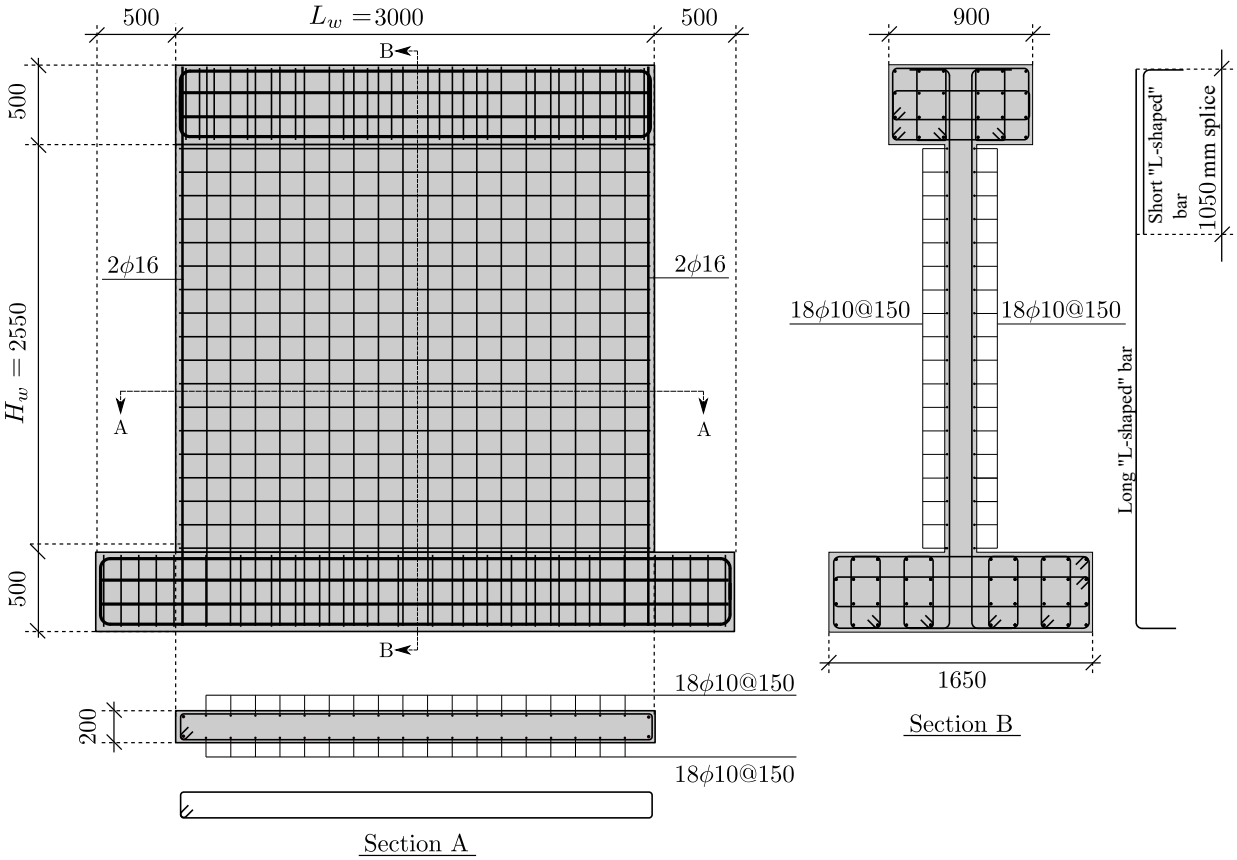

Figure 3.2: Specimen reinforcement and geometry of specimens SW01, SW02, HSW01 and HSW02.

Figure 3.2 shows the steel reinforcement layout of the specimens. The specimens do not consider boundary elements as they represent a medium-rise building. Following engineering practice, two longitudinal reinforcement bars of 16 mm diameter are specified in the borders to hook the transverse reinforcement correctly. The distributed reinforcement was detailed as two layers of steel. The transverse layer consists of stirrups closed with 135° hooks. The longitudinal reinforcement bars are L-shaped and start from the bottom until the top of the specimen. Additional shorter inverted L-shaped reinforcement

bars were placed from the top and spliced with the long ones. This configuration had two purposes: to facilitate the assembly of the reinforcement cage and to reinforce the cold joint between the wall panel and the top beam to force the possible sliding failure to occur at the bottom.

3.1.3 Specimen construction

The specimens were assembled and cast in the yard of a pre-fabricated concrete element company Stüssi AG, in the outskirts of Zürich, and then transported to the ETH Zürich Structures Laboratory. The company was in charge of providing the steel reinforcement and the concrete, and everything related to the construction, from assembling the reinforcement cage, building the formwork, and casting the concrete.

The specimens were constructed, imitating the state-of-practice as closely as possible. To this end, each part of the specimen (foundation, wall panel, and cap beam) was cast vertically and on different days. First, the foundation and wall reinforcement cages were assembled and placed in the form. Then, the foundation was cast. One or two days later, the top beam reinforcement was assembled, and the formwork of the wall was installed. The wall panel concrete was cast first, followed a few days later by the top beam. Figures 3.3, 3.4 and 3.5 show pictures of the construction sequence and Table 3.2 the dates on which each part of the specimens were cast, the day of the test and the day when the concrete cylinder samples were tested.

Table 3.2: Dates of specimens casting, tests, and concrete cylinder samples tests.

Specimen	Concrete casting dates			Specimen test	Concrete strength test
	Foundation	Wall	Top		
SW01	22.06.2022	27.06.2022	30.06.2022	28.07.2022	29.07.2022
SW02	16.05.2022	19.05.2022	25.05.2022	16.06.2022	20.06.2022
SW03	21.02.2023	24.02.2023	02.03.2023	24.03.2023	27.03.2023
SW04	21.03.2023	28.03.2023	04.04.2023	25.04.2023	24.04.2023
HSW01	31.05.2023	07.06.2023	21.06.2023	18.07.2023	11.07.2023
HSW02	28.07.2023	09.08.2023	14.08.2023	04.09.2023	30.08.2023

The interfaces between the parts were prepared as cold construction joints, simulating the actual construction site conditions to the closest possible extent. The vertical construction secures a realistic fluid concrete pressure on the cold construction joints, which gives a realistic bonding and cohesion [88]. Specifically, this interface was cleaned, freed of laitance, and roughened with high-pressure water jetting before the installation of the formwork for the wall panel. The cold joints reached a roughness between 3-5 mm, less than the 6 mm roughness of ACI 318-19 [26], but it complied with the rough interface requirements of Eurocode 2 [15] of 2-3 mm. The resulting friction coefficient could, then, be deemed realistic.

Figure 3.3: Assembled steel reinforcement.

Figure 3.4: Foundation casting.

Figure 3.5: Wall framework and concrete casting.

3.1.4 Materials

Concrete

The target concrete compression strength was 30 MPa, and therefore, a compression strength of 25 MPa was specified with an aggregate size of a maximum of 16 mm. The concrete was provided by the contractor. The specimens were cast 4 weeks before the target test date to have at least 28 days of age. Concrete samples of 300 mm height and 150 mm radius were taken from each section to get the maximum compression strength f_c' and the elastic modulus. Table 3.3 summarizes the obtained properties.

Table 3.3: Mechanical properties of concrete at the day of the test of each specimen.

Specimen	Wall		Foundation	Top beam
	f_c' [MPa]	E_c [MPa]	f_c' [MPa]	f_c' [MPa]
SW01	34.6	29868	34.1	41.7
SW02	28.5	32145	40.6	36.6
SW03	35.9	31504	43.7	50.1
SW04	42.4	35249	46.8	44.8
HSW01	37.3	32597	44.1	40.1
HSW02	37.5	33000	39.7	41.9

Steel reinforcement

The steel reinforcement was specified as B500B according to the Swiss code SIA262 [89], which is the standard practice in Swiss construction today. The requirements for this steel grade are: (1) the yield strength should be larger than 500 MPa, (2) the radio of ultimate-to-yield stress should be larger than 1.08, and (3) the strain at the ultimate tensile strength should be larger than 5%. The reinforcing steel used in all four specimens originated from the same batch, thus three reinforcing bars of each diameter were tested to get the stress-strain response diagrams shown in Figure 3.6. These stress-strain response curves are typical for Swiss B500B reinforcing steel. As the yield plateau is not pronounced, the yield strength was computed as the intersection between the strain-stress curve and a straight line starting at 0.2% with a slope equal to the measured elastic modulus.

3.2 ETH MAST Facility

3.2.1 Hardware and software

The tests were conducted at the MAST Facility at ETH Zürich (Figure 3.7). It combines ten actuators, two reaction walls, a modular steel crosshead, and a strong floor into an optimized machine that can handle a full-wise coupling between a numeral and physical sub-domain of a hybrid model. The Facility enables large-scale testing of various structural elements with two configurations: the long-arm configuration allows tests of small buildings, long reinforced concrete shear walls, or other large specimens, and the short-arm configuration allows tests with narrow profile specimens such as columns or bearings. While the long-arm configuration allows more space for the specimens and has a larger force capacity, the short configuration allows larger rotations.

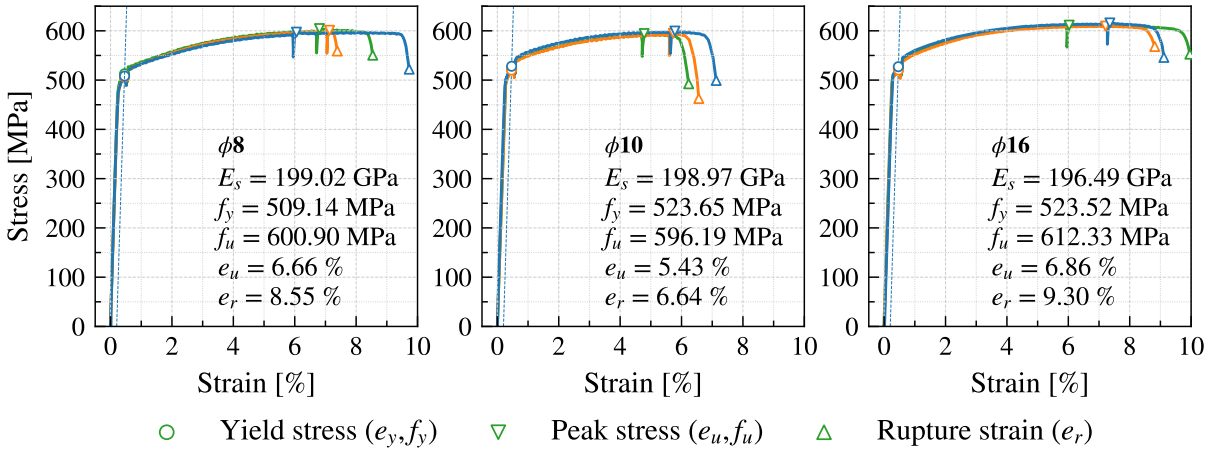

Figure 3.6: Steel reinforcement stress-strain curves and their mechanical characteristics. Notation: E_s: Steel elastic modulus; f_y: steel yield stress; e_y: steel yield strain; f_u: steel peak stress; e_u: steel strain at peak stress; e_r: steel rupture strain.

Figure 3.7: ETH MAST Facility with specimen SW04 installed in it.

The steel crosshead of the MAST transfers the loads from the ten actuators to the specimen. The total length is 15.12 m in the X direction and 11.52 m in the Y direction (Figure 3.8), with a total weight of 92 tons. The 1450 x 1600 mm cross-section is made out of plates of 40 mm thickness and interior stiffeners of 30 mm thickness every 600 mm. The ETHZ MAST Facility has two reinforced concrete reaction towers with a box section in opposite corners that transfer the loads from the actuators to the strong floor, transferring the loads to the foundations. The strong floor is a box girder with a top flange of 1000 mm to which the reaction walls, vertical actuators, and specimens are attached.

The ETH MAST facility has ten actuators: four in the vertical direction, four in the long direction, and two in the short direction, and Figure 3.8 shows their location and denomination. They apply the desired forces and displacements to the crosshead, which then transmits them to the specimen. The vertical actuators have a capacity of 2 MN each, whereas the horizontal actuators have each 1 MN, which gives a total capacity of 4000 kN of lateral load in the x-direction. All of the actuators have strokes of $\pm$600

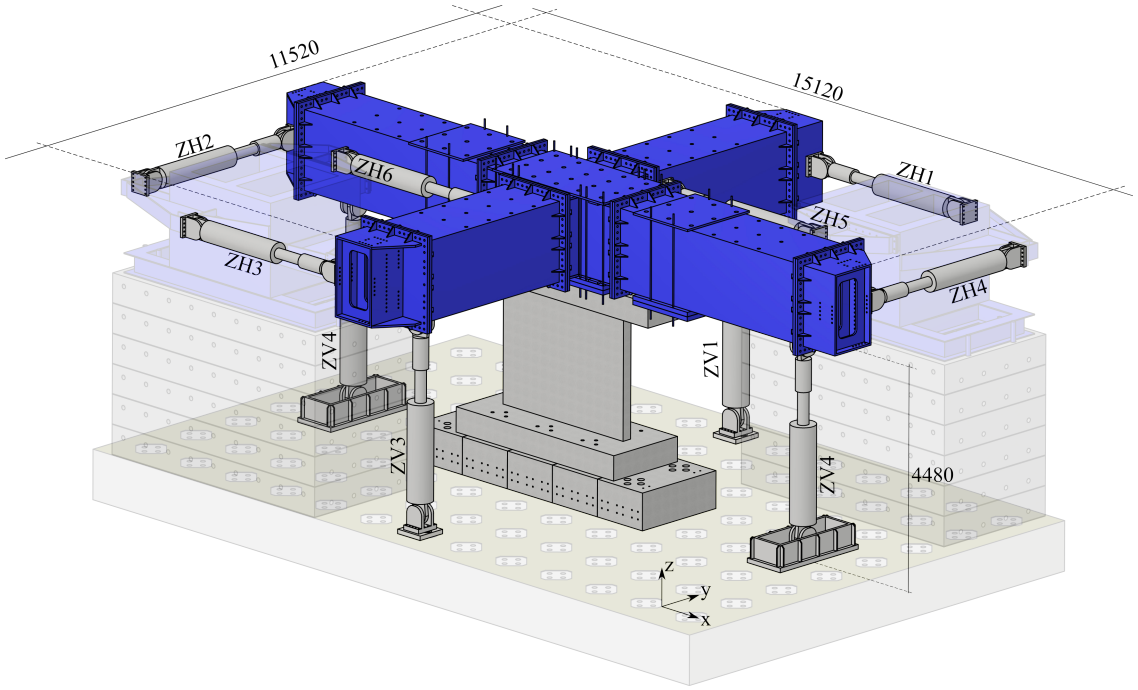

Figure 3.8: Long arm configuration of the ETH MAST facility's steel crosshead.

mm.

The commands and feedback are given to and obtained from the ETH MAST facility as displacement, forces, or mixed mode in the 6 DOFs at a control point. The control point can be spatially user-defined but, by default, is set at the center bottom flange of the steel crosshead. The ability to control the six DOFs means that the actuators must act simultaneously and coordinate to have the desired displacement or force at the control point. Figure 3.9 illustrates the control system.

The control of the ETH MAST can be divided into the modal and actuator domains. The command forces or displacements have to be transformed into instructions to the actuators so the crosshead moves in the desired manner. The link between these two domains is performed with two kinematic transformations, backward and forward, which are included in the feedback loop (Figure 3.9). The backward transformation calculates the actuator's servo valves to the crosshead coordinates. The backward kinematic transformation can be obtained analytically by calculating the deformation of the actuators in terms of the displacement of the control point (Swinburne University MAST [77]). On the other hand, the forward kinematic transformation takes as input the elongation and forces of the actuators and calculates the crosshead's position and angles. The forward transformation has ten equations, one for each actuator, and has to find six variables. Namely, many solutions satisfy the system, and, therefore, the one with the least square error is chosen, which is done numerically. With the solution of the forward transformation, the position, forces, and balance channels are obtained and sent to the PID controller.

3.2.2 Hybrid simulation architecture

The hybrid simulation process is implemented using a three-layer architecture [90]:

- A host computer, which runs the dynamic finite element and performs the numerical integration.
- Real-time Indel machine: Acts as a middleware between the host computer and the Inova Controller

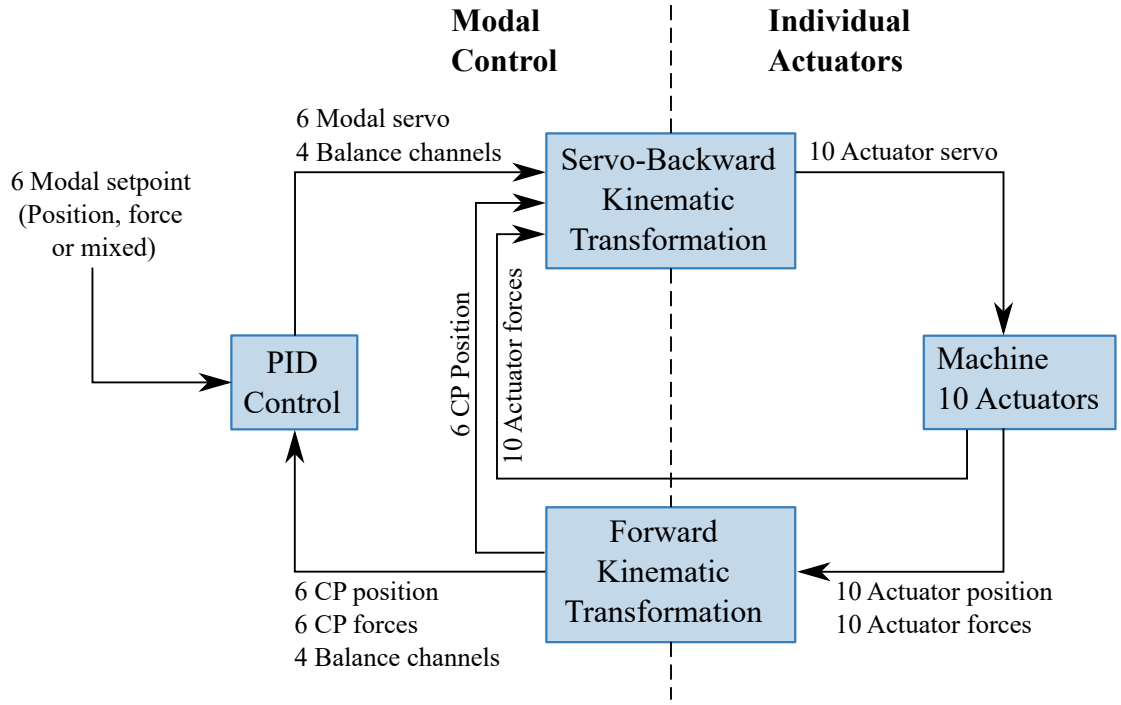

Figure 3.9: PID control loop of the ETH MAST Facility.

- Inova Controller: Previously described in Section 3.2, it sends and receives the signal from the Real-Time Indel machine to the ETH MAST facility. The Inova controller consists of a computer where the test is controlled and a real-time computer connected to the hardware.

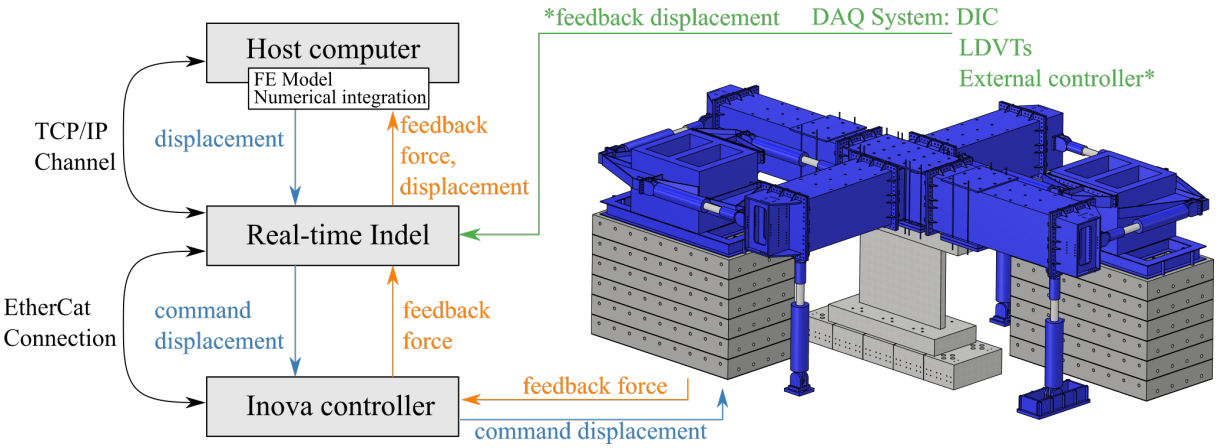

Figure 3.10: Hybrid simulation architecture.

Figure 3.10 illustrates the previously described architecture. One time step in this architecture would work like this: at a given time step, the host computer starts an integration step and computes the command displacement. Then, it sends it to the Real-Time Indel Machine via TCP/IP, and the latter sends it to the Inova Controller via the EtherCAT connection. The Inova controller receives the command displacement, transforms it to the actuator's domain with its kinematics transformation, and sends the signal to them. When the displacement is fully applied, the feedback force is sent by the same path to the host computer, which finalizes the time step and continues to the next one. Note that the host computer computes the command displacement at the control point, and because the Inova controller internally does the kinematics transformation, the system works as a NoTransfromation Setup [70]. This

architecture allows running tests that do not require feedback force, such as cyclic tests. In that case, only the displacement commands are sent, the forces are received in real-time but only to store their value, and they are not used to compute the displacement of the next step.

The data acquisition system can be connected directly to the Real-time Indel Machine. The advantage is that all the data is gathered in one computer and is, therefore, coordinated without the need for post-processing. In the case of DIC, the host computer can be coded to send trigger commands to the camera and, therefore, know the exact moment a picture was taken.

3.3 Cyclic tests implementation

Four of the specimens were tested under cyclic protocol. The specimens were subjected to a series of horizontal cycles along the specimen's strong axis. Each cycle was repeated twice to account for the degradation of the specimen, following the recommendations of ACI 374.2R-13 [91]. The code suggests estimating the amplitude of those cycles based on the yield displacement, but that parameter is hard to estimate for squat specimens. Thus, the loading protocol was defined in terms of the peak strength and capacity deformation obtained from Vector2 [92] models of the specimens. The first two series of cycles were conducted in force control due to the considerable stiffness of the specimens, and were conducted with force levels below the cracking force obtained from Vector2. From then on, the cycles were conducted in displacement control. The force-controlled cycles had amplitudes of 400 kN and 800 kN, which corresponded to 1/6 and 1/3 of the peak strength obtained in Vector2. Specimen SW03 had a lower peak strength, and therefore lower force levels of 350 kN and 700 kN were chosen. The other three specimens had the same force-controlled cycles.

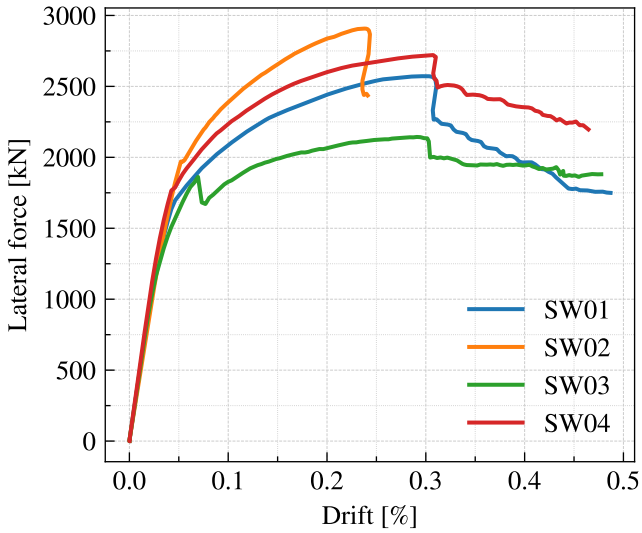

Figure 3.11: Pushover curve of the specimens obtained with the software Vector2.

According to the Vector2 models, the failure would trigger at around 7.6 mm. All the specimens had shear-controlled behavior and shear failure, as the software does not account for sliding deformations . An increase of 3 mm was chosen after each set of two cycles. Specimen SW02, the first tested specimen, had a deformation close to 1.5 mm in at the 800 kN amplitude, and it was decided to have amplitudes

of 3 mm, 4.5 mm, and 6 mm, and then do increases of 3 mm until a maximum top displacement of 36 mm. A cycle of 50 mm was added to the protocol if the specimen did not fail or collapse after the 36 mm cycles.

The load protocol programmed in the controller corresponds to the displacement commands sent to the Inova Controller, and due to the flexibility of the crosshead, the actual displacement at the control point would be less than the displacement command. Therefore, an infra-red target was installed at the control point to measure its actual displacement. The fact that the actual displacement depends on the loads of the actuators means that each specimen had a slightly different load protocol. Figure 3.12 shows the loading protocol applied to Specimen SW01, with the displacement measured with the infra-red target. The values of the amplitudes of each specimen are given in Chapter 4 with the results of the tests, along with the speed rates of each part of the test.

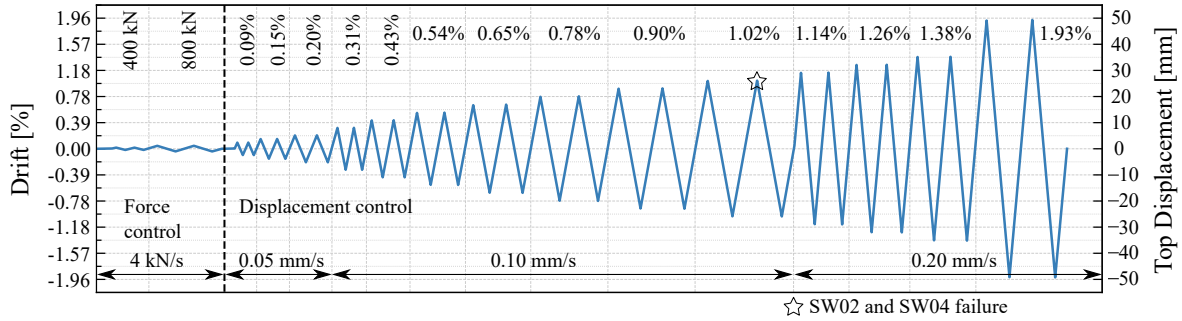

Figure 3.12: Quasi-static cyclic test protocol used in tests of specimens SW01, SW02, SW03 and SW04

The cyclic tests were run within the hybrid architecture framework of the ETH MAST Facility to coordinate them with the data acquisition system. The load protocol was programmed in a Simulink Model that sent the displacement commands to the Inova Controller via the Indel real-time Machine. The control point's displacements and forces were received as feedback but not used to update the load protocol. There was one Simulink model for the force-controlled section and one for the displacement-controlled section.

The control point of the tests was placed at the top of the wall, which is 2.55m above the wall foundation interface. The tests were run in an in-plane fixed-fixed condition, which means that the system could not rotate at the control point, and out-of-plane translation and rotations of the specimens were constrained. The specimens were allowed to move in the vertical axis, as this degree of freedom was force-controlled. These boundary conditions resulted in a target shear-span ratio of M/VL_w = 0.425, where L_w is the length of the wall, equal to 3000 mm. The system was in-plane statically indeterminate, which could cause a deviation in the target shear-span ratio depending on the redistribution of membrane stresses due to cumulative damage of the specimens during the tests.

At the beginning of the tests, the target axial load was applied according to the values of Table 3.1. Then, the Simulink Model related to the force-controlled cycles was loaded and run in the Indel real-time machine. Once the force-controlled cycles were finished, there was a waiting block to set up and load the displacement-controlled cycles Simulink model or modify the load pattern if necessary. Then, the displacement-controlled cycles were started, and the tests were run until the last cycles of 50 mm or until the failure of the specimens.

3.4 Hybrid simulation implementation

3.4.1 Hybrid reference system

The objective of the hybrid simulation tests was to see the influence of the loading protocol in the transition of shear and sliding-controlled behavior modes and extend the results obtained from the cyclic tests. As previously mentioned, cyclic tests allow for associate damage to a certain displacement, but they can not be associated with a specific seismic demand. The reference system of the hybrid simulation tests was chosen to be consistent with the system of the cyclic tests and to have comparable results. The hybrid simulation tests were conducted as pseudo-dynamic. Namely, the specimen was moving at a low speed such that the inertial forces of the system could be neglected, and thus, the test is not considered real-time.

The hybrid model corresponded to an in-plane single degree-of-freedom (DOF) system (Figure 3.13). The mass at the top of the structure has a horizontal DOF u_1, while its in-plane rotation is restrained. The structure was fully fixed at the bottom. Such a hybrid model was selected to be consistent with the specimen boundary conditions of the quasi-static cyclic tests. The hybrid model was subjected to a constant vertical load P applied at the top to simulate the gravity load as specified by Table 3.1. It had a seismic mass m of 180 tons and an elastic/initial horizontal stiffness k of 780 kN/mm giving the hybrid model a horizontal vibration period $T = 0.1$ seconds, and a viscous damping ratio of 3%. The hybrid was subjected to a horizontal ground motion applied at the base. The dynamic response of the hybrid model in the vertical direction was neglected.

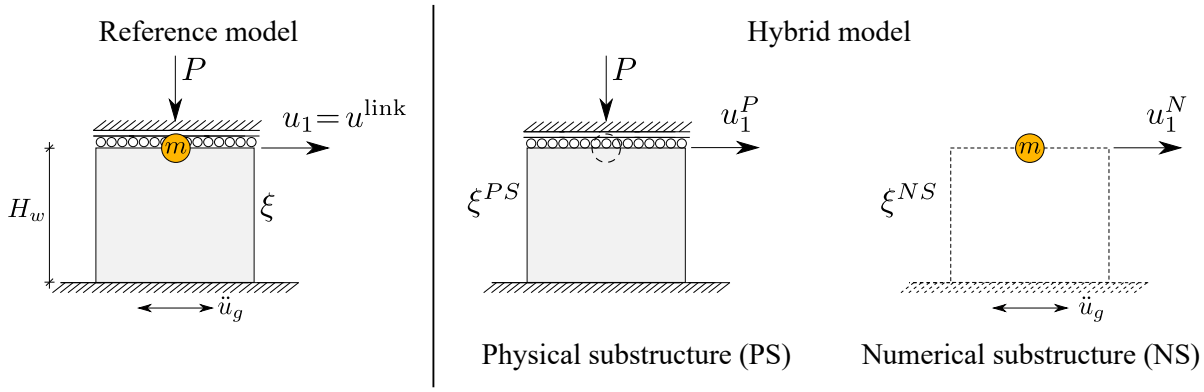

Figure 3.13: Hybrid simulation reference system

The hybrid model was divided into physical and numerical substructures. The physical substructure consisted of the shear wall specimen, the boundary conditions at the top and bottom, the gravity loads, and the vertical degree of freedom. The numerical substructure comprised the seismic mass and viscous damping ratio. The horizontal displacement of the top of the shear wall u_1 was the controlled degree of freedom of the hybrid model that linked the numerical and the physical substructures.

The hybrid model was subjected to the North-South component of the 1995 Kobe JMA ground motion record [93]. This seismic record was selected because Nagae et al. [45] used it in a shaking table test of a 4-story building where one reinforced concrete shear wall had a sliding failure, and because it produced significant displacement demands on the hybrid model without the need for large scaling

factors. Specimen HSW01 was subjected to the 1995 Kobe JMA ground motion scaled by 1.75, whereas specimen HSW02 was subjected to a sequence of excitations obtained by scaling the original 1995 Kobe JMA ground motion record by 1.75, 2.0, and 2.75. Only 20 seconds of the original ground motion record were used in the hybrid simulations (Figure 3.14). The original 0.02 second time step of this ground motion record was linearly interpolated to a 0.005 second time step to facilitate the stability of the hybrid model integration algorithm.

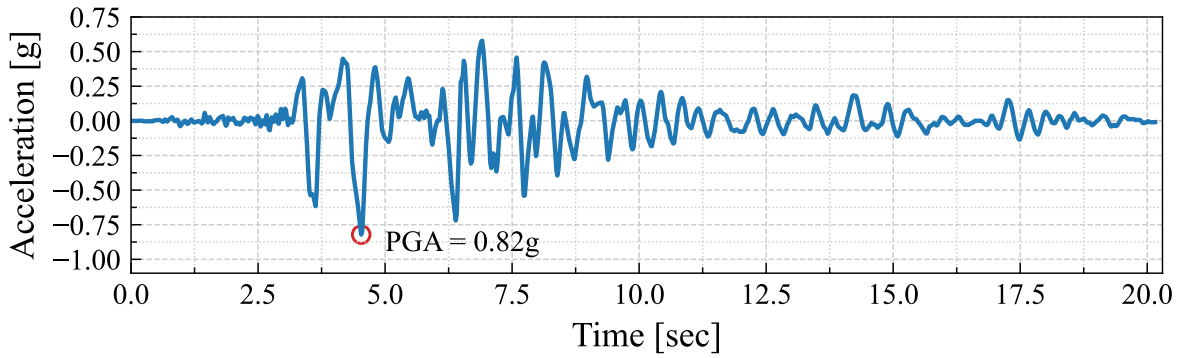

Figure 3.14: Kobe JMA 1995 seismic record

3.4.2 Numerical integration

The equation of motion that describes the dynamics of a structural system is:

$$\mathbf{M}\ddot{\mathbf{u}} + \mathbf{C}\dot{\mathbf{u}} + \mathbf{r}(\mathbf{u}) = \mathbf{f}(t) \tag{3.1}$$

Where $\mathbf{M}$, $\mathbf{C}$, $\mathbf{r}$ and $\mathbf{f}(t)$ denote the mass matrix, damping matrix, restoring force and external load vector, respectively. This equation of motion is solved by applying numerical time-stepping integration algorithms.

There are numerical algorithms suitable for hybrid simulation. Special care must be taken because it deals with an experimental element rather than a numerical one; therefore, stability is critical during the simulation. In this research, the partitioned numerical time integration algorithm described in Abbiati et al [94] was used, which is a combination of the Gravouil-Combescure Algorithm [95] with Localized-Lagrange Multipliers [96]. The numerical integration presented herein divides a structural system into n substructures, which for the reference system of Figure 3.13 correspond to two, denoted P for the Physical substructure and N for the Numerical substructure. The degree of freedom that links both substructures is $\mathbf{u}_{\text{Link}} = u_1$. Then, the method considers the coupled system of equations represented in Equation 3.2, in which each substructure has its equation of motion.

$$
\begin{cases}
\mathbf{M}^P\ddot{\mathbf{u}}^P + \mathbf{C}^P\dot{\mathbf{u}}^P + \mathbf{r}^P(\mathbf{u}^P) = \mathbf{f}^P(t) + \mathbf{L}^{P^T}\mathbf{\Lambda^P} \\
\mathbf{L}^P\dot{\mathbf{u}}^P + \overline{\mathbf{L}}^P\dot{\mathbf{u}}_{\text{Link}} = \mathbf{0}
\end{cases}
$$

$$
\begin{cases}
\mathbf{M}^N\ddot{\mathbf{u}}^N + \mathbf{C}^N\dot{\mathbf{u}}^N + \mathbf{r}^N(\mathbf{u}^N) = \mathbf{f}^N(t) + \mathbf{L}^{N^T}\mathbf{\Lambda^N} \\
\mathbf{L}^N\dot{\mathbf{u}}^N + \overline{\mathbf{L}}^N\dot{\mathbf{u}}_{\text{Link}} = \mathbf{0}
\end{cases}
\tag{3.2}
$$

$$
\overline{\mathbf{L}}^P\mathbf{\Lambda}^P + \overline{\mathbf{L}}^N\mathbf{\Lambda}^N = \mathbf{0}
$$

The link between the numerical and physical system DOFs $\mathbf{u}^P$-$\mathbf{u}^N$ and the link DOFs $\mathbf{u}_{\text{Link}}$ is given with the boolean matrices $\mathbf{L}^P$-$\mathbf{L}^N$ and $\overline{\mathbf{L}}^P$-$\overline{\mathbf{L}}^N$ and ensures velocity compatibility between the systems. Figure 3.15 shows the boolean matrices for the hybrid system. $\mathbf{\Lambda^P}$ and $\mathbf{\Lambda^N}$ are the Lagrange multiplier vectors of the physical and numerical substructure.

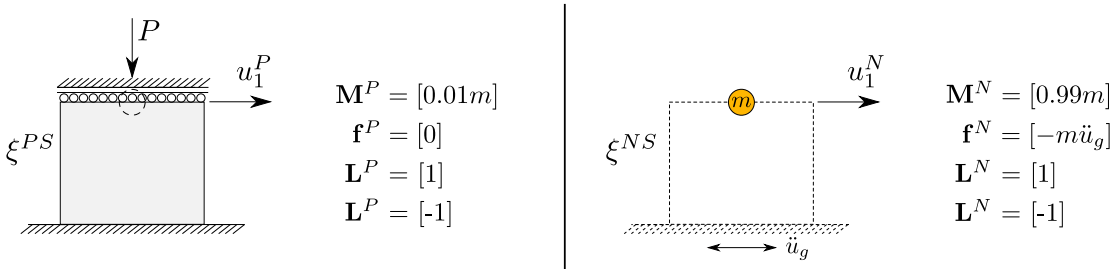

Figure 3.15: Matrices of the hybrid system

The system of equations is solved with an explicit Newmark integration method ($\gamma = 0.5$ and $\beta = 0$) in the form of predictor-corrector, shown in Figure 3.16. Some variables must be computed before the numerical integration, such as $\mathbf{D^P}$, $\mathbf{D^N}$ and the Steklov-Poitcaré operator $\mathbf{G}$, which are defined in Figure 3.16. The Newmark integration scheme solves each substructure independently as a free problem. At a given time step k, the algorithm first predicts a displacement and velocity for the physical ($\widetilde{\mathbf{u}}_k^{P,free}, \widetilde{\dot{\mathbf{u}}}_k^{P,free}$) and numerical ($\widetilde{\mathbf{u}}_k^{P,free}, \widetilde{\dot{\mathbf{u}}}_k^{N,free}$) substructure. The displacement predicted in the physical substructure is sent to the experimental specimen, receives the restoring force, and corrects the predicted physical displacement and velocity. The numerical substructure displacement prediction is sent to the numerical model, gets the numerical restoring forces, and corrects the numerical predictions. Because the integration scheme is explicit, the velocity prediction is corrected but not the displacement prediction as $\beta = 0$. The Lagrange multiplier vectors are calculated in the Hybrid Simulation Coordinator zone (Green zone in Figure 3.16), and finally, the coupled accelerations, velocities, and displacements are obtained.

The explicit Newmark integration algorithm is conditionally stable, with the stability limit of Equation 3.3, where T_n is the shortest natural period of the structure and Δt is the time step size of the integration method.

$$
\Delta t \leq \frac{T_n}{\pi} \tag{3.3}
$$

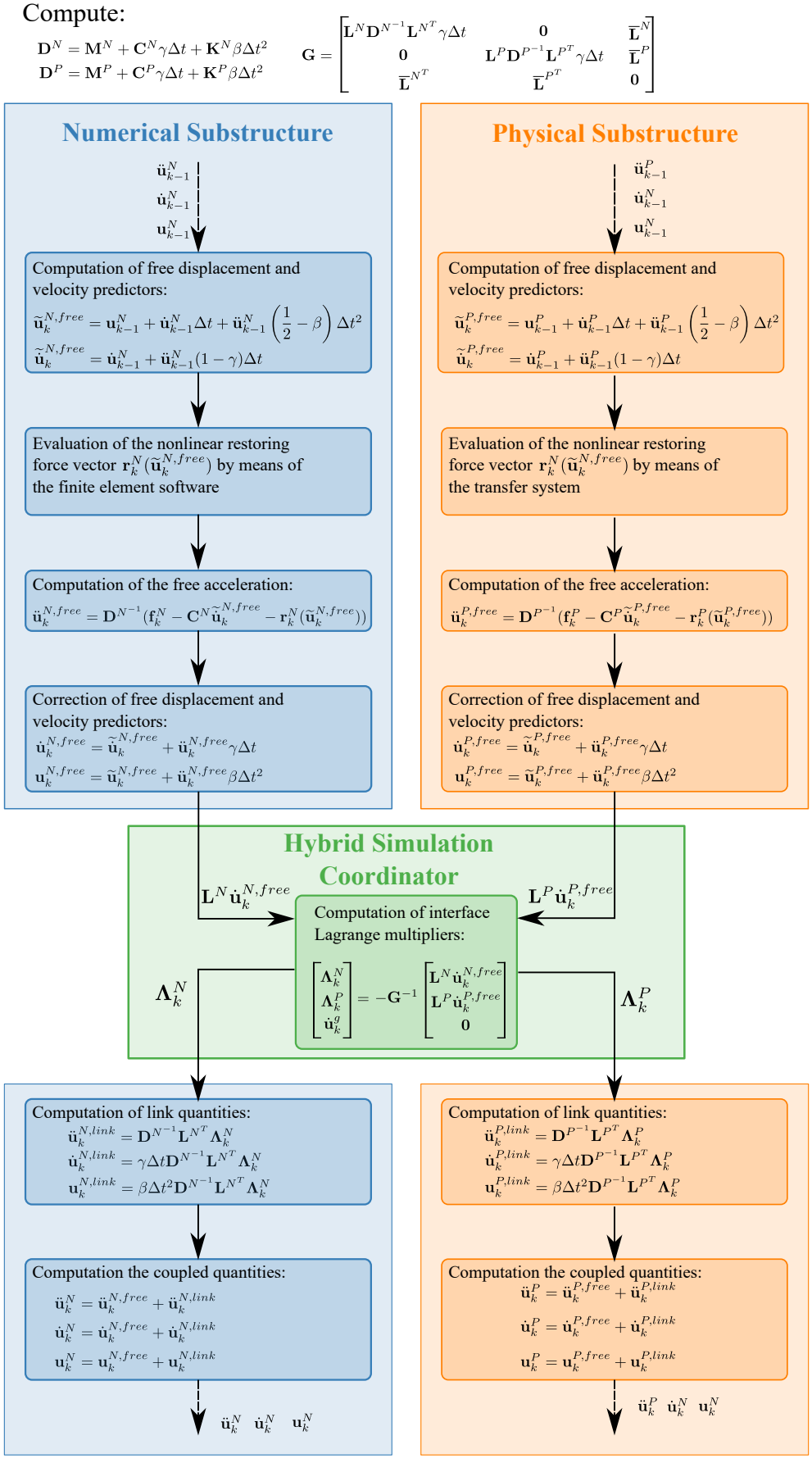

Figure 3.16: Numerical integration algorithm. Adapted from Abbiati et al. [94].

3.4.3 External sensor

The experience of the cyclic tests showed that the flexibility compensation did not fully eliminate the error between the command and measured displacement. Thus, it was decided to control the X displacement of the control point with an external sensor. The sensor was an analog magnetostrictive transducer, model LMRB 27 [97], with a stroke of $\pm$ 50 mm. The sensor was installed in a reference column fixed to the strong floor, and it was attached directly to the steel crosshead of the ETH MAST. The sensor was not connected directly to the specimen because potential cracks or sudden damage could provoke a control problem. The control point of the test was defined at the exact location as the external sensor, at the bottom flange of the steel crosshead. Because of the boundary conditions of the problem (no rotations on the top), the displacement of the crosshead's bottom core and the top of the wall panel should be similar. This was controlled during the tests.

The external sensor was not included at the Inova level of the hybrid architecture because of the complex kinematics transformations involved (Figure 3.10), but rather at the Indel Real-Time machine level. The problem is that the differential displacement obtained from the numerical model, $\Delta d = d_k - d_{k-1}$, is not the same as the differential displacement that has to be applied in the ETH MAST, $\Delta d_{MAST} = d_{MAST,k} - d_{MAST}$, because of the flexibility of the crosshead. Thus, the deformation was applied to the specimen in two steps. First, the integration algorithm computes the command displacement at a time step k and calculates the differential displacement of the hybrid model Δd. The host computer sends a command displacement to the MAST equal as $d_{\text{command}} = d_{MAST,k} + \Delta d$. Once applied, it checks if the feedback displacement from the external sensor is within a tolerance of 0.1 mm with the target displacement d_k. If it is, it goes to the next step. If it is not, the host computer sends displacements to the MAST until the external sensor measurement is within the 0.1 mm tolerance error with the command displacement. The procedure was done in these two steps because at minimal displacement increases, for instance, at the beginning of the test, any displacement would have complied with the tolerance due to small displacements. The top of the specimens moves vertically to the elongation of the materials, which could affect the signal of the external sensor. In this case, the expected vertical deformations were not considered an issue, but it would have been in case of a sudden drop of the specimen due to axial failure.

3.4.4 Python script

The hybrid model and the numerical integration were coded in a Python script. Indel has an usepackage, inco_32, with a series of classes that allows communication with Indel industrial automation systems. A GUI to control the hybrid simulation was coded in Python, that allowed to start the test and follow in real-time the displacement and force from the specimen. The GUI was coded with the library PyQt5, and it works as Object Oriented Programming, where the main Class is the HybridGUI (self coded). The most important functions of this class are:

- `numerical_integration`: It has the definition of the parameters of the hybrid simulation, such as masses, damping ratios, initial stiffness, and all the relevant parameters for the numerical integration. This is where the numerical integration takes place, and within the `for` loop that

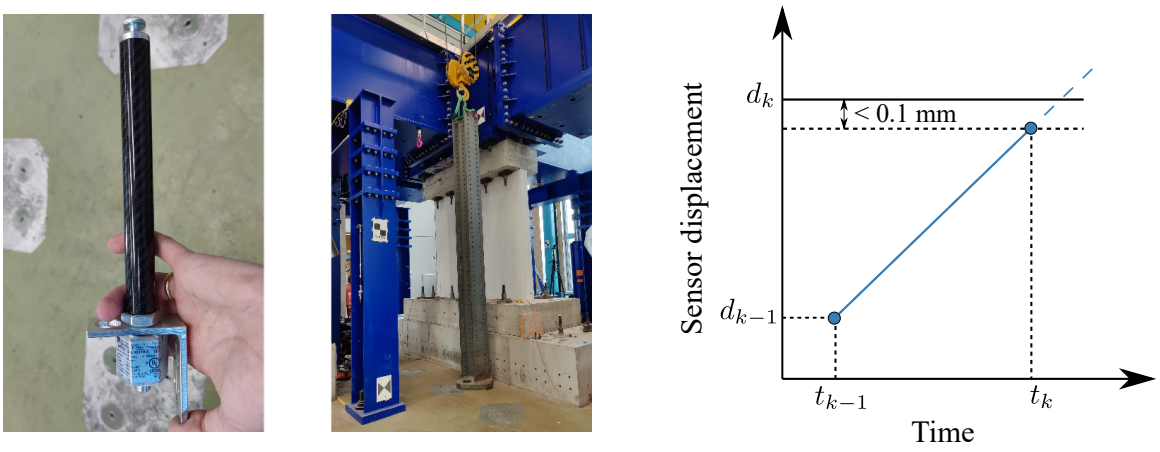

Figure 3.17: (a) Magnetoestrictive transducer (b) Reference column (c) .

includes the integration, it sends the displacement commands to Indel and receives the feedback forces.

- `apply_displacements`: It sends the displacement commands to Indel. It receives as input the command displacement obtained from the `numerical_integration` method and the displacement of the previous step. It calculates the steps that the machine needs to apply the displacements as a function of the test speed (0.05 mm/s) and the frequency that the commands are sent to Indel (10 Hz). It calculates the steps needed `steps = du/speed*rate` and creates a vector of displacements `apply_u = np.linspace(u1,u2,int(steps)+1)`. Then sends these displacements at a 0.1s rate with the function `inco_32.PutVariable()`.
- `read_forces()`: It reads the feedback forces from indel once the specimen reaches the command displacement.

The test started by applying the desired axial load (Table 3.1). Then, there is a waiting block, and the MAST waits until the Python script starts running. There is enough time to check instrumentation and other issues, and then the host computer begins to send the signals from the hybrid simulation. The tests were run until the end of the ground motion sequence or up to the specimen failure.

3.5 Instrumentation

- Digital image correlation (DIC): One side of the wall was speckled with 2 mm radius dots in a random pattern. The pictures were taken with a D810 Nikon Camera equipped with an AF-S NIKKOR 14–24 mm 1:2.8G ED lens. Two lights Elinchrom Style RX 1200 were flashed every time a picture was taken. The pictures were coordinated with the setup controller, taking pictures every 6 to 10 seconds and carefully including the peaks. The images were saved as raw files (.NEF) in high resolution.
- Optical tracking: The Optotrak Certus system of the company NDI is used to do the optical tracking. This system tracks the 3D displacements of LED targets in real time. Two optical trackers were needed to follow the LED targets Because of the distance of the tracker to the wall. Figure 3.18

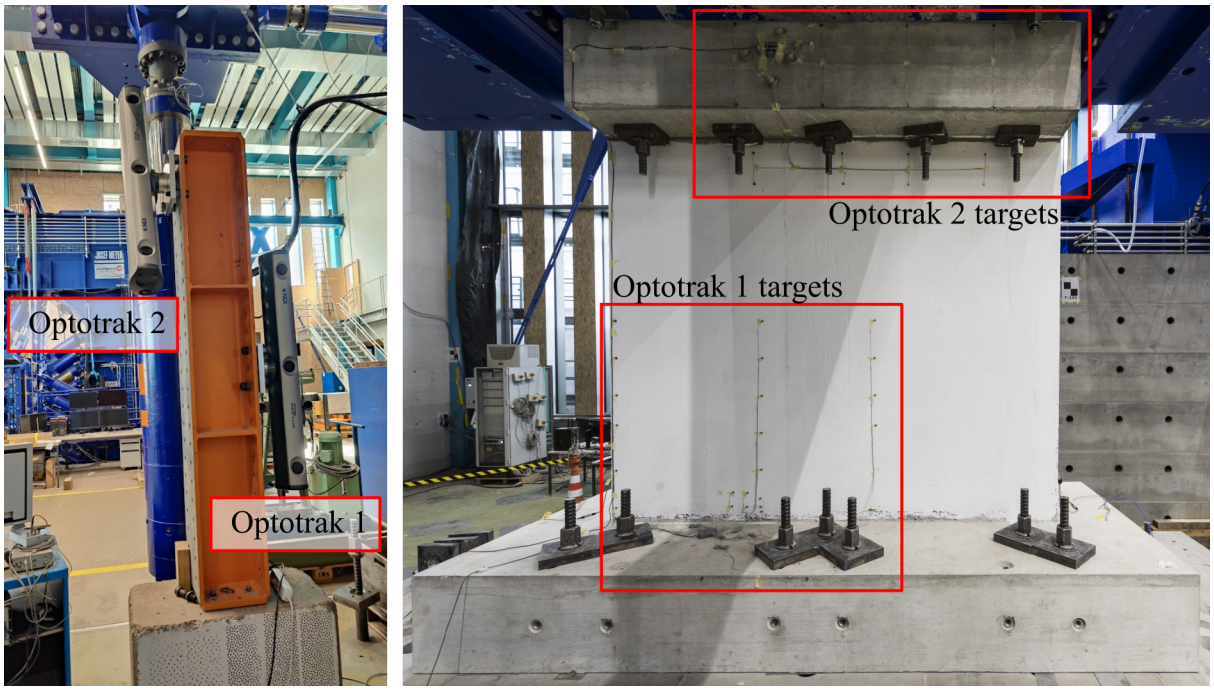

Figure 3.18: On the left: Position of the two cameras. On the right: NDI targets installed on the wall (Picture courtesy of Milan Rohrer).

shows the LED target configuration. The upper targets measure the displacement on the control point and any relative displacement between the MAST and the specimen. The LED targets in the bottom are to track the siding of the foundation with the ground floor, and the sliding of the cold joint. Many trackers were installed close to the interface to have redundancy as concrete spalling could make a target disappear.

The NDI system data collection was not synchronized with the MAST data acquisition. The data was collected at 1 Hz during the cyclic tests, and at 0.1 Hz during the hybrid simulation tests.

3.6 Data Post-Processing

The data obtained from the test had to be collated for the post-process. The ETH MAST collected raw data at 10 kHz, and that was reduced to 10 Hz for the plots and post-processing due to the length and size of the original files. The data acquired with the NDI Optotrak system was coordinated with the one of the ETH MAST by matching the peak displacement responses of each cycle, and it was linearly interpolated to get the same rate as the ETH MAST. The camera that took the DIC pictures was coordinated through the Indel machine, and therefore, each picture was associated to a specific displacement in the test.

As previously mentioned, the displacements that the ETH MAST measures overestimate the actual displacement at the control point. Therefore, the post-process and analysis of the displacement results was conducted with the displacement measured by the NDI Optotrak system at the control point. To obtain the drift ratio, the displacement was divided by the height of the specimen $H_w = 2550mm$. The moment at the base of the specimen, necessary to compute the shear-span ratio M/VL_w, was obtained from the forces and location of the ten actuators, as the moment computed by the MAST is given at the location of the control point. The effective height h_{eff} of the specimen, the point where the moment

diagram goes through zero, was calculated as:

$$h_{eff} = \frac{M_{bot}}{M_{bot} + M_{top}} \cdot H_w \tag{3.4}$$

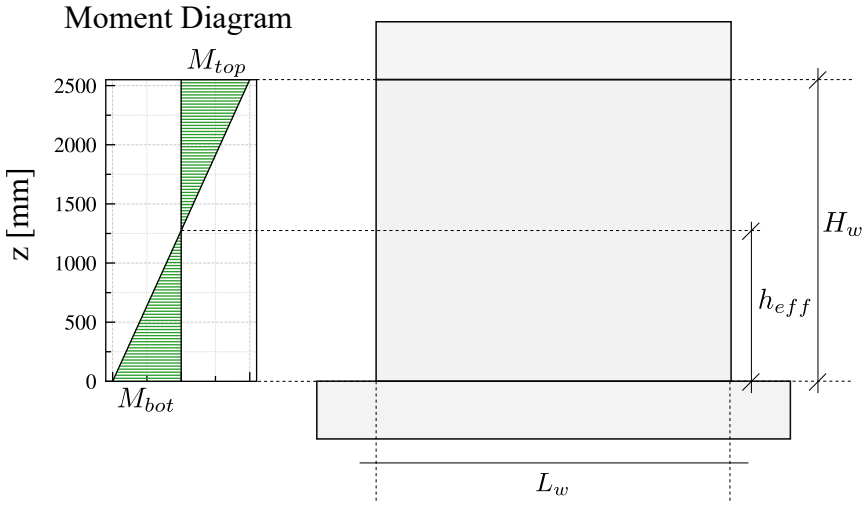

Figure 3.19: Moment diagram of a specimen and its effective height h_{eff}.

That value is presented in the discussion as it is an indicator of the development of damage to the specimen. The target value of h_{eff} during the tests was $0.5H_w$, which relates to a $M/VL_w = 0.425$, but it could shift up or downwards to membrane forces redistribution due to cracking or concrete spalling.

The initial stiffness of the specimens tested under cyclic testing was calculated from the force-controlled cycles at 400 kN. On the other hand, the secant stiffness at the cycle's peak displacement was obtained by considering the force and displacement at the peak point, and the force and displacement of a point 10 steps behind. The secant stiffness was then calculated with Equation 3.6. Thus, the values of initial stiffness and secant stiffness in the cycles of 400 kN could differ.

$$k_i = \frac{F_{max,400kN} - F_{min,400kN}}{d_{max,400kN} - d_{min,400kN}} \tag{3.5}$$

$$k_{sec} = \frac{F_j - F_{j-10}}{d_j - d_{j-10}} \tag{3.6}$$

The DIC pictures were post-processed with the software VIC-2D of the company Correlated Solution. The pictures were loaded into the software, along with a calibration and a reference picture, and then it calculated the displacement field of the specimens for each picture. For all the specimens, a subset of 29 and a step of 7 were selected. The software calculates the principal strains and the maximum shear strain. The results are then exported in MAT files for further post process. The crack pattern and crack width of the specimens were obtained with the Automatic Crack Detection and Measurement (ACDM), an open-source software developed by the Chair of Concrete Structures and Bridge Design at ETH Zurich [98, 99]. This software receives as input the displacement and strain outputs from VIC 2D.

The deformation of the specimens is a sum of the contributions of flexure, shear and sliding deformations. To identify the transition between them it is of interest to know how each of those modes contributed to the total displacement of the control point. The shear and flexure deformation components of the specimens were determined with the methodology of Hiraishi et al. [100] and Massone and Wallace [101], which was adopted for DIC results. Figure 3.20 shows the assumed deformation of a section of the wall panel.

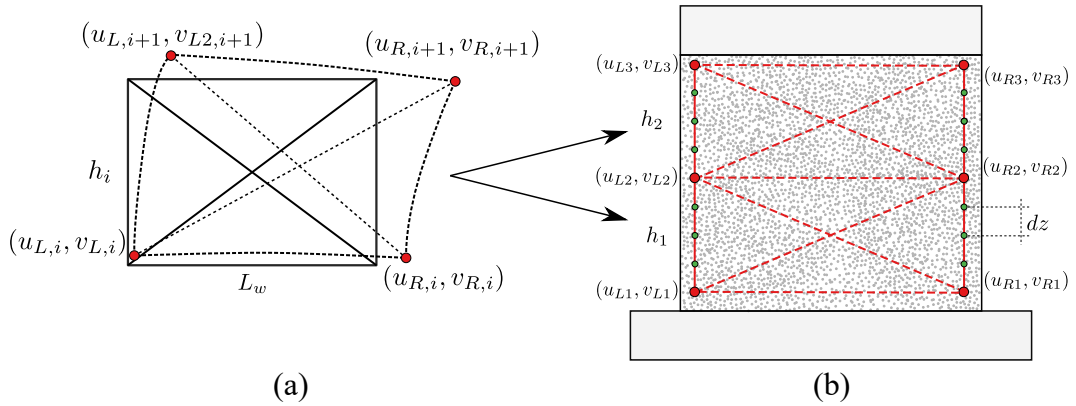

Figure 3.20: (a) Deformation of a shear wall subjected to lateral load (b) Arrangement of virtual transducers which divides the wall panel into two elements of (a).

The displacements needed to compute the specimen deformation contributions are commonly obtained from linear transducers arranged diagonally to measure shear deformations and vertically along the wall edges to measure rotations due to bending. In this case, virtual transducers were defined using DIC measurements, as shown in Figure 3.20 (b). An advantage is that there is a better resolution of the results, as many vertical transducers can be defined in terms of the vertical spacing of the results.

The flexure deformations are obtained with Equation 3.7, where the rotations are computed along the height of the wall by getting the difference in vertical displacement between points in opposite borders at the same horizontal level.

$$u_{flexure} = \int_0^{H_w} \theta_z dz \tag{3.7}$$

The shear deformation of each element of Figure 3.20 (a) is obtained from Equation 3.8, where the horizontal displacements u are computed from the DIC results. The total shear deformation is the contribution of the deformation of each defined element of height h_i. The flexure deformation of each section $u_{flexure,i}$ can be obtained by integrating the rotations with Equation 3.7, but integrating only within the height of the element.

$$u_{shear,i} = 0.5 \cdot (u_{R,i+1} + u_{L,i+1} - u_{R,i} - u_{L,i}) - u_{flexure,i} \tag{3.8}$$

The sliding displacements were obtained directly from the led target placed at 10 cm over the cold joint (Figure 3.18), which means that it also measures some contributions of shear and flexure, but they were

neglected.

CHAPTER 4

CYCLIC TESTS

4.1 Introduction

This chapter presents the results of the specimens tested under cyclic loading. Each specimen has its section where the results are presented in terms of their lateral force-drift hysteresis, damage progression, crack kinematics and deformation decomposition. All the forces and drift ratios presented in this section are related to the control point of the test, namely, the displacements obtained were divided by 2550 mm. Table 4.1 summarizes the drift ratios Δ, lateral force resistance V and shear-span M_{bot}/VL_w measured at important points of the four tests: when the first diagonal crack appeared, when maximum lateral resistance was attained and when the maximum drift ratio was attained.

Table 4.1: Measured drift ratios Δ, lateral force resistance V, and bottom and top shear-span ratios at three important points attained during the four tests. The resistance at the maximum drift of specimens SW01 and SW03 was taken at the second cycle of the last amplitude.

Specimen	Observed failure mode	k_i [kN/mm]	At first diagonal crack			At maximum strength			At maximum drift		
			Δ [%]	V [kN]	$\frac{M_{bot}}{VL_w}$	Δ [%]	V [kN]	$\frac{M_{bot}}{VL_w}$	Δ [%]	V [kN]	$\frac{M_{top}}{VL_w}$
SW01	Sliding	674	0.08	1090	0.48	0.65	2329	0.38	1.93	1263	0.35
			-0.06	-1108	-0.52	-0.54	-2413	-0.44	-1.93	-1070	-0.08
SW02	Shear	708	0.07	1050	0.63	0.72	2760	0.38	0.96	2410	0.39
			-0.08	-1460	-0.39	-0.75	-2990	-0.41	-1.00	-1180	-0.64
SW03	Sliding	904	0.10	1562	0.51	0.3	2194	0.40	1.95	810	0.15
			-0.11	-1615	-0.43	-0.31	-2156	-0.44	-1.95	-797	-0.19
SW04	Shear	939	0.06	1229	0.49	0.76	2830	0.42	1.01	1742	0.39
			-0.07	-1367	-0.45	-0.53	-2765	-0.43	-0.99	-2299	-0.35

4.2 Specimen SW01

Specimen SW01, the reference specimen, had 4.31% of ALR, 0.53% of longitudinal and transverse reinforcement ratio and was in the sliding zone of the controlling behavior mode interaction diagram (Figure 3.1. Figure 4.1 shows the lateral force-drift hysteresis and Table 4.2 presents the values of forces and shear-span ratio obtained at the peak of each cycle.

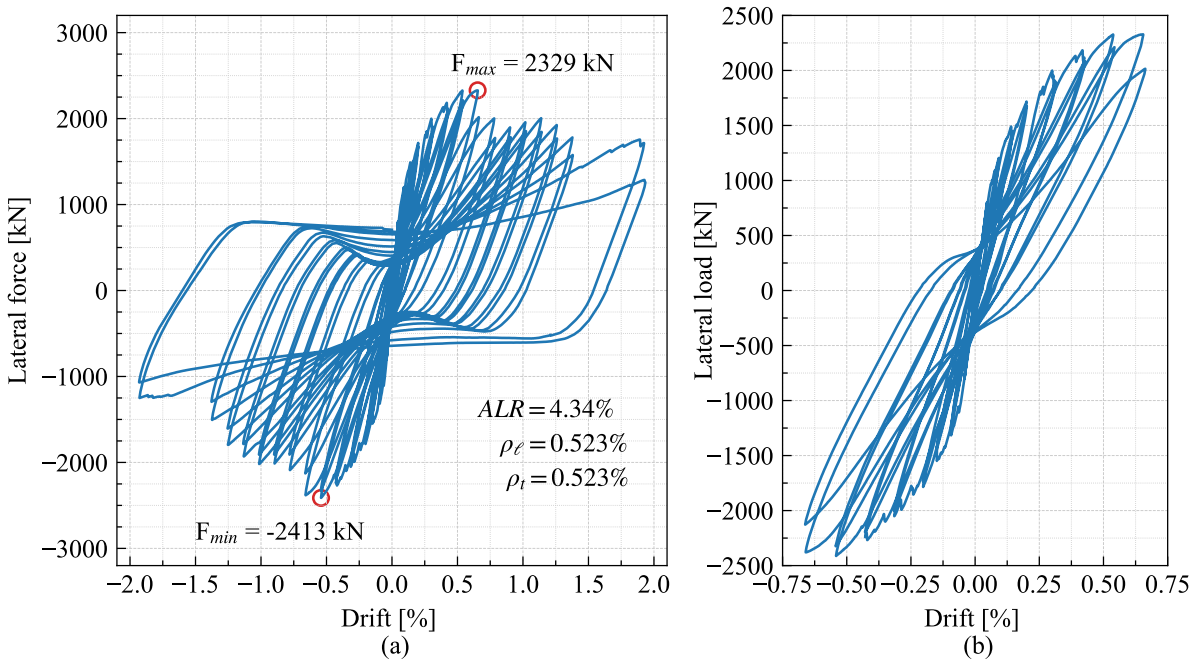

Figure 4.1: (a) Lateral force-drift hysteresis of specimen SW01 (b) Lateral force-drift hysteresis plotted until the sliding initiation.

Specimen SW01 had an uncracked behavior in the first two force-controlled cycles with an initial stiffness of 674 kN/mm. Between the start of the test and until a drift of 0.65%, the wall had essentially a shear-controlled behavior, as shown in Figure 4.1(b), characterized by low pinching and low energy dissipation. The first diagonal cracks formed at 0.08% and -0.06% drift ratio with a load resistance of 1090 kN and -1108 kN, respectively. The diagonal cracks spread with each increase in displacement: the new cracks can be identified in the lateral force-drift hysteresis as a subtle drop in the resistance of the specimen with increasing displacement. The crack pattern was fully developed at ± 0.42% drift ratio. The crack pattern was characterized by diagonal cracks inclined at approximately 50^o in both directions (Figure 4.2(a)) with a constant crack spacing of 200 mm. There are flexural cracks in the corners of the specimen as it was in a double fixed condition. The widest flexural crack formed in the top corners of the specimen, specifically at the height where the splice of the boundary reinforcement started. The width of the main diagonal crack (Figure 4.2 (b)) increased since its formation until it reached 1 mm at 0.65% drift ratio. The top vertical displacement showed an expected behavior for shear walls Figure 4.3(a). The specimens displaced up with an increase of horizontal displacement due to the elongation of the steel. At 0.65% drift ratio, the wall had 6 mm of vertical displacements.

The specimen had a peak strength level essentially at two drift ratios: at ± 0.54%, the specimen attained forces of 2323 kN and -2411 kN, and at ± 0.65%, it reached 2324 kN and -2378 kN. At 0.65% drift

Table 4.2: Lateral force resistance V and shear-span ratio M_{bot}/VL_w measured at the peak. The sub-index "1" and "2" refers to the first and second cycles of a given amplitude.

	Positive cycles					Negative cycles				
Δ	V_1 [kN]	$\frac{M_{bot1}}{VL_w}$	V_2 [kN]	$\frac{M_{bot2}}{VL_w}$	$\frac{V_2}{V_1}$	V_1 [kN]	$\frac{M_{bot1}}{VL_w}$	V_2 [kN]	$\frac{M_{bot2}}{VL_w}$	$\frac{V_2}{V_1}$
0.02	400	0.607	400	0.606	1.000	-400	0.494	-400	0.494	1.000
0.05	800	0.526	800	0.527	1.000	-800	0.477	-800	0.477	1.000
0.09	1202	0.485	1199	0.476	0.997	-1304	0.462	-1272	0.462	0.975
0.15	1444	0.488	1440	0.481	0.997	-1495	0.457	-1455	0.457	0.973
0.20	1717	0.470	1676	0.470	0.976	-1784	0.462	-1736	0.462	0.973
0.31	1889	0.453	1888	0.454	0.999	-2050	0.439	-2000	0.439	0.975
0.43	2115	0.434	2085	0.432	0.986	-2242	0.432	-2195	0.432	0.979
0.54	2323	0.416	2212	0.409	0.952	-2411	0.425	-2323	0.425	0.963
0.65	2324	0.392	2014	0.382	0.866	-2378	0.402	-2127	0.402	0.894
0.78	2000	0.368	1772	0.370	0.886	-2086	0.380	-1907	0.380	0.914
0.90	1895	0.366	1780	0.368	0.939	-2012	0.368	-1907	0.368	0.948
1.02	1956	0.362	1853	0.360	0.947	-2015	0.357	-1908	0.357	0.947
1.14	2002	0.352	1844	0.349	0.921	-1927	0.337	-1778	0.337	0.923
1.26	1923	0.341	1765	0.339	0.918	-1795	0.301	-1603	0.301	0.893
1.38	1781	0.330	1574	0.335	0.884	-1502	0.207	-1291	0.207	0.860
1.93	1712	0.337	1256	0.349	0.734	-1247	-0.031	-1068	-0.031	0.856

ratio, there was no concrete spalling in any zone of the wall panel and the only visible damage were the diagonal and flexural cracks, plus a horizontal flexure crack along the entire length of the wall-foundation cold construction joint. The pinching level at those drifts was quite different, as the loss of strength was 4.7% at 0.54% drift ratio and 13.4% at 0.65% drift ratio. At the drift ratio of 0.65%, the specimen had low secant stiffness (7 kN/mm), which suggests that the specimen was close to its maximum shear/flexure capacity (Figure 4.3(d)).

The drift ratio at 0.65% was the point considered as the initiation of the sliding mechanism at the wall-foundation interface, recognized by the high pinching level. The following cycles showed increasing and eventually considerable pinching of the force-drift hysteresis (Figure 4.2). The residual post-peak resistance of specimen SW01 between 0.65% and 1.3% drift ratios stabilized between 1750-2000 kN, about 20% below the peak resistance. At these displacement peaks, the specimen had a secant stiffness of 50-70 kN/mm, which means that the specimens could have reached larger forces if the displacement had not been reversed. There is a significant loss (7-10%) of strength within cycles of the same amplitude (Table 4.2) attributed to sliding. Interestingly, in the post-peak phase of the hysteresis at drift ratios between 0.65% and 1.3%, the cracks could not reach the maximum crack width of 1.06 mm. Figure 4.2(b) shows that the width remained below the peak of 1.06 mm, reaching a width of approximately 0.95 mm. The shape of the crack width curve is similar to the envelope of the hysteresis, as they both reach similar peaks after the peak strength. The fact that the specimen still had secant stiffness in the

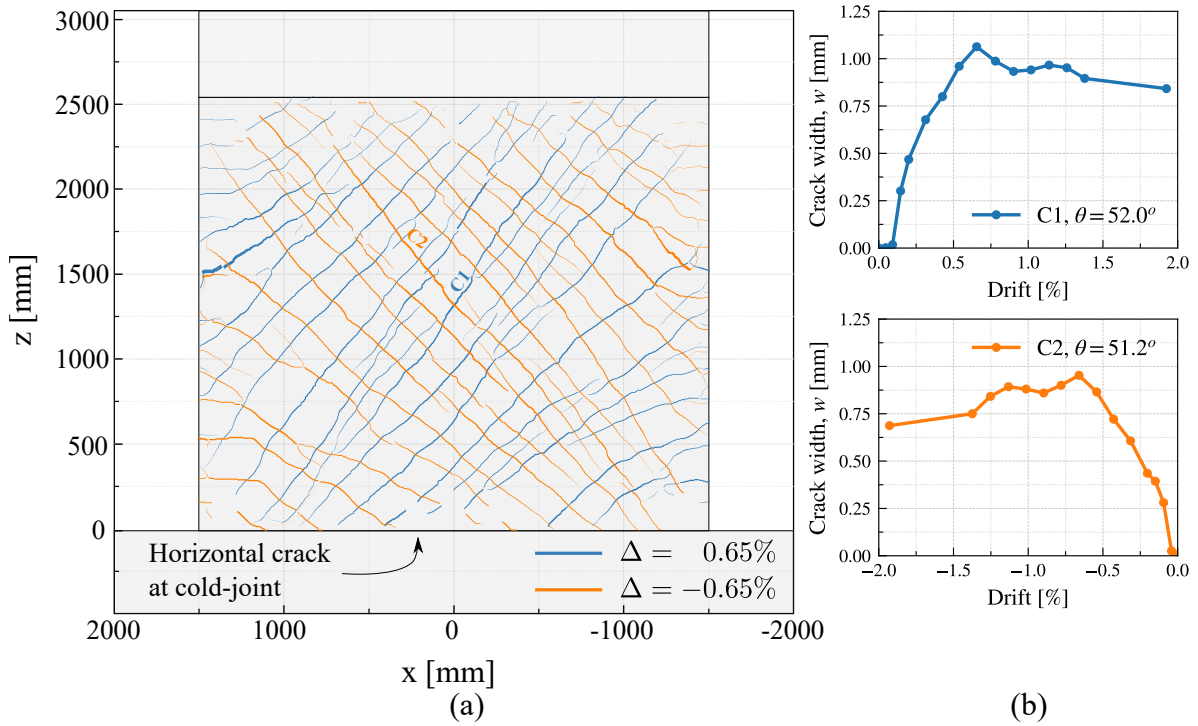

Figure 4.2: Crack pattern of specimen SW01

post-peak phase and that the crack width did not reach the peak-crack width suggests that the specimen did not engage the same level of shear and flexure as it did at the initiation of sliding drift ratio (0.65%).

Specimen SW01 exhibited a resistance plateau of about 750 kN at a zero-displacement point during each post-peak-resistance test cycle (Figure 4.1 (a)), which is typical of a sliding-controlled behavior. During this plateau, the sliding displacements and damage in the cold joint occurred. This plateau is evident at the load reversal of ±0.90% drift ratio, where it reached force levels of 250 kN and, after each displacement increment, the force of the plateau increased until it stabilized at a force of 750 kN. With the increasing amount of cycles, the length of the sliding plateaus increased due to degradation of the cold joint. Figure 4.3(c) shows the sliding displacement, where two effects can be observed: the sliding displacement increases with each increment of displacement, and the sliding contribution increases from the first to the second cycle of the same amplitude. These two effects happened because the sliding interface degraded in each sliding incursion [28].

Figure 4.4 shows the damage progression at the cold joint of Specimen SW01 due to sliding displacements. The first visible damage was a minor detachment of the concrete cover at the bottom corners of the wall during the 0.65% drift cycles. In the next test cycle to 0.78% drift ratio, that piece detached, while more cracks formed above the wall-foundation interface, indicating sliding damage. There was progressive concrete spalling along the wall-foundation joint in the following cycles due to sliding. The boundary reinforcing bars and the bottom transverse reinforcement stirrup became visible during the 1.02% drift ratio test cycles. The dowel-action of the reinforcement bars induced deformation of the boundary that became clearly visible during the subsequent test cycles to larger drift ratio amplitudes. Plastic elongation of the vertical reinforcement crossing the wall-foundation joint as well as the spalling and damage of the concrete changed the boundary condition at the bottom of the specimens. This can be appreciated from the decrease of the negative direction shear-span ratio

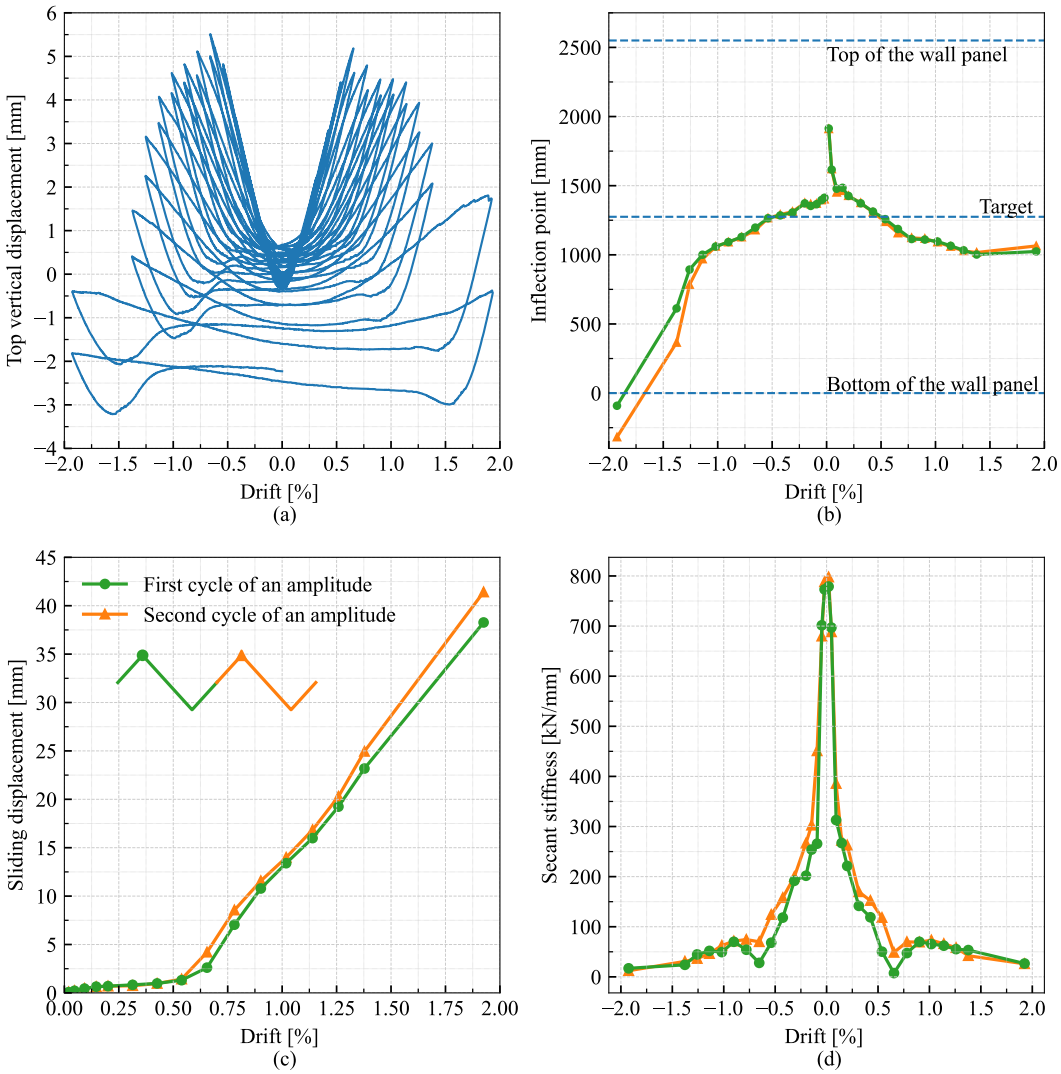

Figure 4.3: (a) Top growth of specimen SW01 (b) Position of the inflection point (c) Sliding displacement at the cold joint (d) Secant stiffness. The legend in plot (c) is valid for (b) and (d)

M_{bot}/VL_w in Table 4.2 from 0.44 to 0.08, which means that the specimen practically started to behave as a cantilever fixed at the top as Figure 4.3 (b) shows.

Unloading of specimen SW01 upon the reversal of displacement direction in each post-peak cycle was practically linear-elastic, a consequence of the elastic rebound of the segment of the wall above the, now sliding, cold joint. The measured unloading stiffness was 175 kN/mm, which was invariant with the drift amplitude. The unloading branch had only flexure and shear deformations, and the specimen started to slide once again when they reached the sliding plateaus. The drifts at which the residual sliding resistance in the opposite direction was attained do not differ substantially from the test cycle amplitude (Figure 4.1 (a)), indicating that specimens SW01 and SW03 have low displacement restoration capacities. Table 4.3 shows the values of residual sliding displacement, residual top displacement and residual crack width of the main diagonal crack. With an increasing number of cycles, the sliding residual displacement started to accumulate, reaching 1.47% drift ratio in SW01 after the last cycles. The increasing values of residual sliding displacements are due to the invariance of unloading stiffness: resistance force peaks had similar force levels, and with the same unloading stiffness the drift difference with the zero force

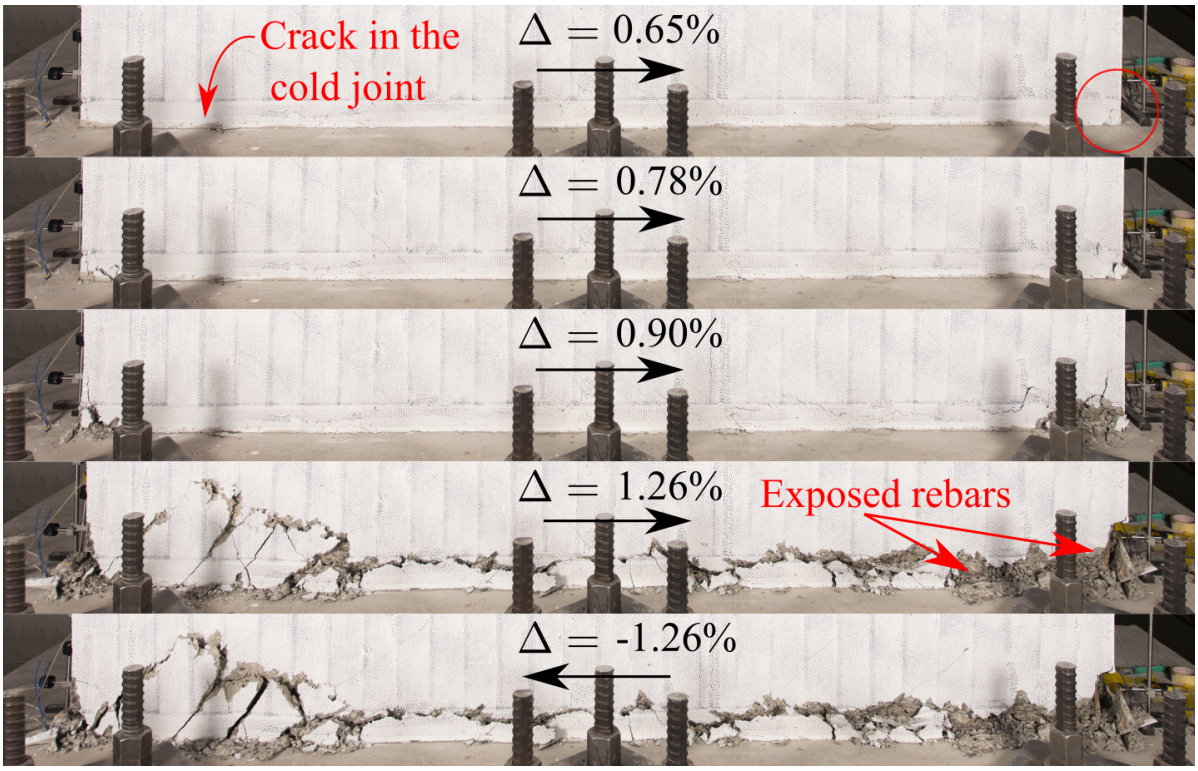

Figure 4.4: Specimen SW01 damage at the sliding interface

level is similar for each unloading branch. Note that the top residual displacement is relatively close to the sliding residual displacement, which indicates that there is a residual component of shear and flexure deformation, but mostly controlled by the previously attained sliding deformation during the loading of the specimen. This can be seen in the hysteresis curves of SW01 (Figure 4.1). Gulec and Whittaker [54] assumed the failure drift of sliding walls to the one associated with a 0.5% residual drift ratio at the top of the specimen. Specimens SW01 exceeded this residual drift ratio when it was unloaded from 0.90% drift ratio.

Table 4.3: The peak attained drift ratio Δ_{peak}, the residual sliding drift ratio Δ_{res}^{slid}, the residual top drift ratio (Δ_{res}) and residual crack width w_{res} (computed at zero force after each cycle peak) of the tested specimens in each test cycle. Only the positive drift values are shown. Rows in bold denote the test cycles when the peak strength of the respective specimen was attained.

Δ_{peak} [%]	Δ_{res}^{slid} [%]	Δ_{res} [%]	w_{res} [mm]	Δ_{peak} [%]	Δ_{res}^{slid} [%]	Δ_{res} [%]	w_{res} [mm]
0.09	0	0.02	-	0.78	0.23	0.34	0.26
0.15	0.01	0.02	0.19	0.9	0.38	0.49	0.24
0.2	0.01	0.03	0.21	1.02	0.49	0.59	0.23
0.31	0.01	0.05	0.2	1.14	0.59	0.69	0.2
0.43	0.01	0.08	0.22	1.26	0.72	0.85	0.24
0.54	0.01	0.1	0.24	1.38	0.88	0.97	0.43
0.65	**0.05**	**0.17**	**0.32**	1.93	1.47	1.54	0.25

The test of specimen SW01 was finished after the 1.93% drift ratio cycles because the specimen sliding behavior was repeatable. The specimen held the applied axial load throughout its test without showing

any signs of impending axial instability or loss of axial load carrying capacity. The shape of the post-peak force-drift hysteresis curves of specimen SW01 resembles those of friction-sliding seismic isolation devices. Note that the peak residual resistance of this specimen depended on the damage induced at the wall-foundation interface, thus, indirectly, on the applied cyclic test protocol. Namely, the attained residual resistance is expected to be different if the test protocol with incrementally increasing symmetric amplitudes is changed after the specimen attains its peak resistance to a protocol with an asymmetric or monotonic amplitude pattern. Figure 4.5 shows the final state of specimen SW01 is characterized by damage focused at the bottom, and the diagonal cracks can be observed by the human eye. The vertical steel reinforcement of specimen SW01 was heavily bent due to dowell deformations and the boundary reinforcement was buckled due to shortening of the specimen. There was no steel reinforcement bar fracture.

Figure 4.5: Final state of Specimen SW01

Specimens SW01 had a diagonal shear-controlled behavior before it attained their peak resistance. Diagonal shear deformation controlled the majority (70% to 90%) of the top displacement, and this level stayed until the sliding shear behavior mode was triggered. After this point, the sliding shear deformation contribution increased up 80% to 90% of the total top displacement. A more detailed investigation into the absolute values of the diagonal shear and sliding shear contributions of these walls shows the evolution of shear deformations (Figure 4.6 (a)). The diagonal shear and sliding shear deformations were computed at the same drift ratio as the deformation contribution, namely, only at the peaks of the first cycle of each amplitude. Post-peak diagonal shear deformations of SW01 reached values of 0.39-0.42% at the peak of each cycle. The fact that this level of shear was somewhat constant throughout the ranges of 0.78%-1.38% drift ratios was consistent with the behavior of the crack width (Figure 4.2) and the envelope of the lateral resistance-drift hysteresis (Figure 4.1 (a)).

After the point of reaching its maximum resistance, specimen SW01 transitioned from a shear and flexure to sliding-controlled behavior along the cold joint between the wall and the foundation. This behavior

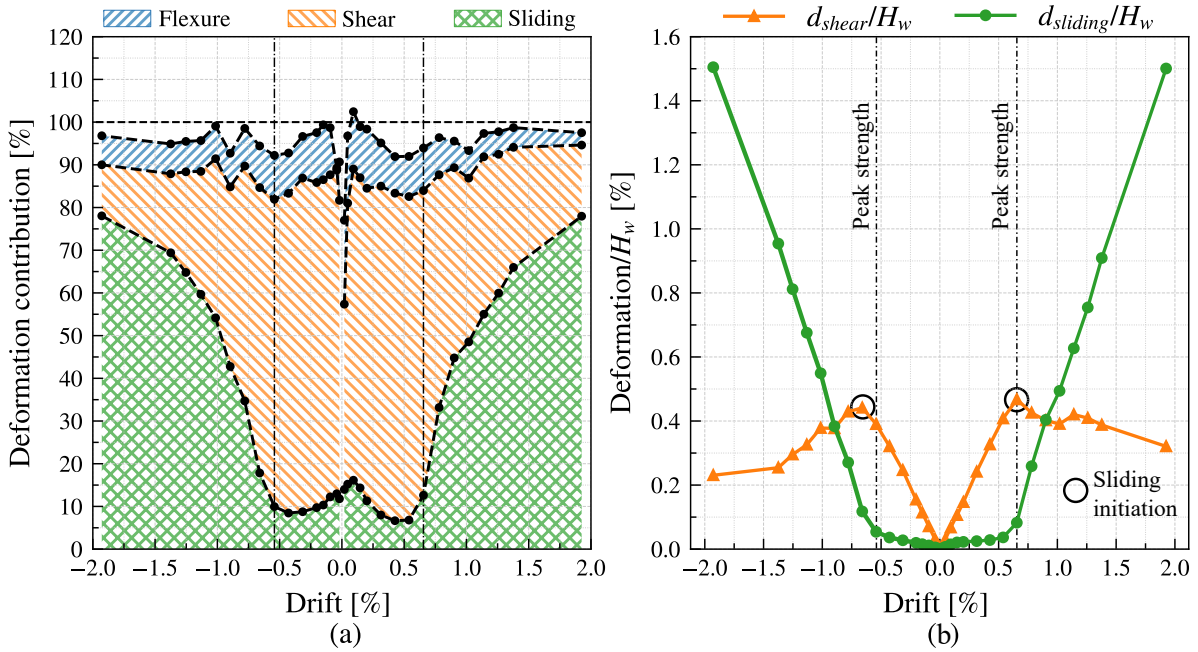

Figure 4.6: (a) Deformation contribution of flexure, diagonal shear and sliding shear of specimen SW01. (b) Diagonal hear and sliding shear deformation of specimen SW01.

mode transition was predicted accurately using the strength comparison approach [57] and the controlling behavior mode diagram in Figure 3.1.

4.3 Specimen SW02

Specimen SW02 had 10.53% of ALR, 0.53% of longitudinal and transverse reinforcement ratio and was in the shear zone of the controlling behavior mode interaction diagram (Figure 3.1). Figure 4.7 shows the lateral force-drift hysteresis and Table 4.2 presents the values of forces and shear-span ratio obtained at the peak of each cycle.

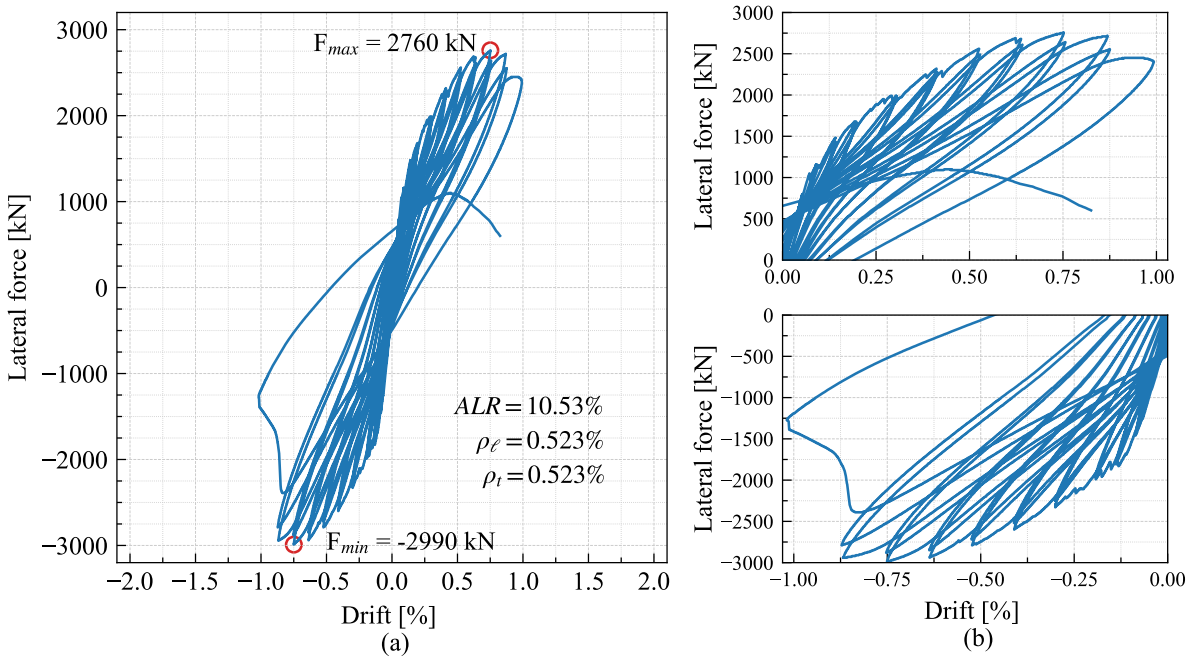

Figure 4.7: Lateral force-drift hysteresis of specimen SW02.

Specimen SW02 remained uncracked and responded in essentially linear flexure and diagonal shear during the force-controlled cycles, with an initial stiffness of 674 kN/mm. The first diagonal crack formed at 0.07% and -0.08% drift ratios with load resistances of 1050 kN and -1460 kN, respectively (Table 4.1). The diagonal cracks spread with each increase in displacement: the new cracks can be identified in the lateral force-drift hysteresis as a subtle drop in the resistance of the specimen with increasing displacement. The crack pattern was fully developed at 0.61% and -0.55% drift ratio. The crack pattern (Figure 4.8) was characterized by diagonal cracks inclined in 65^o in the positive direction and 52.8^o in the negative direction, with an average spacing between the main cracks of 200 mm. There were flexural cracks in the four corners of the specimen due to the fixed-fixed boundary conditions, and the widest flexural crack formed at the location of the splice of the boundary steel reinforcement bars. The width of the widest diagonal crack reached 1 mm at $\pm 0.5\%$ drift ratio, but after this point, the positive direction had a faster increase, reaching values of 2.7 mm at 0.90% drift ratio. In contrast, in the negative direction, the width was 1.56 mm at the same displacement. The wider cracks in the positive direction can be attributed to the large inclination of the main crack.

Specimen SW02 attained its peak strength of 2990 kN at a 0.75% drift ratio, and could practically attain the same resistance level at the next drift ratio of 0.90% in the test protocol. Up to this drift ratio, there was no concrete spalling in any zone of the wall panel, only mild wear in the diagonal cracks at 0.87%

Table 4.4: Lateral force resistance V and shear-span ratio M_{bot}/VL_w measured at the peak. The sub-index "1" and "2" refers to the first and second cycles of a given amplitude.

Δ	Positive cycles					Negative cycles				
	V_1 [kN]	$\frac{M_{bot1}}{VL_w}$	V_2 [kN]	$\frac{M_{bot2}}{VL_w}$	$\frac{V_2}{V_1}$	V_1 [kN]	$\frac{M_{bot1}}{VL_w}$	V_2 [kN]	$\frac{M_{bot2}}{VL_w}$	$\frac{V_2}{V_1}$
0.03	399	0.382	397	0.381	0.99	-399	0.390	-401	399	1.01
0.05	799	0.365	794	0.359	0.99	-796	0.392	-796	796	1.00
0.09	1160	0.304	1160	0.301	1.00	-1460	0.392	-1440	1460	0.99
0.14	1480	0.281	1430	0.279	0.97	-1810	0.377	-1790	1810	0.99
0.20	1680	0.297	1670	0.301	0.99	-1990	0.382	-1960	1990	0.98
0.30	1990	0.317	1980	0.318	0.99	-2300	0.407	-2250	2300	0.98
0.41	2320	0.347	2270	0.345	0.98	-2600	0.412	-2520	2600	0.97
0.53	2560	0.361	2490	0.360	0.97	-2790	0.412	-2720	2790	0.97
0.64	2680	0.370	2610	0.367	0.97	-2940	0.407	-2850	2940	0.97
0.75	2750	0.377	2640	0.373	0.96	-2980	0.407	-2880	2980	0.97
0.87	2710	0.381	2550	0.383	0.94	-2940	0.412	-2790	2940	0.95
0.99	2400	-0.394				-1270				

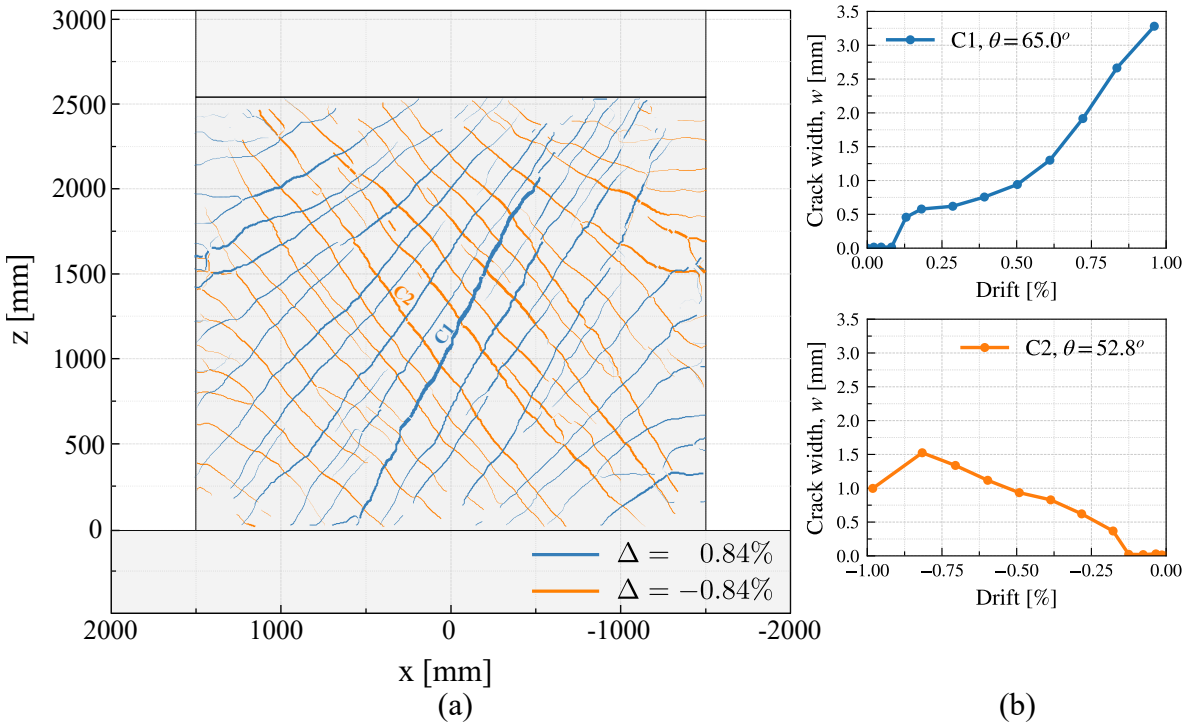

Figure 4.8: Crack pattern of specimen SW02

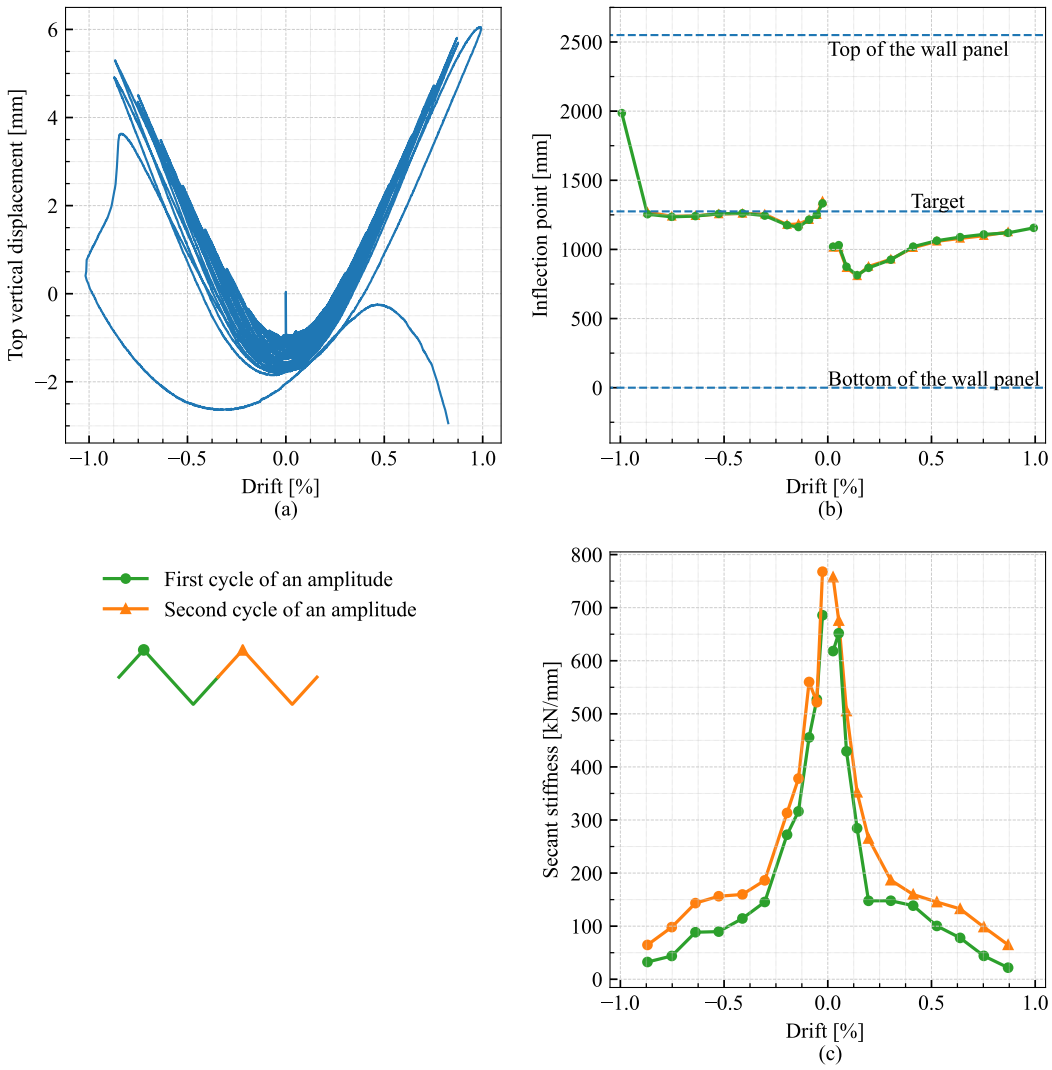

Figure 4.9: (a) Top growth of specimen SW01 (b) Position of the inflection point (c) Secant stiffness. The legend is valid for plots (b) and (c).

drift ratio (Figure 4.10), and the crack pattern was already fully developed (Figure 4.8). The resistance dropped by 12% from the positive direction's peak-strength of 2750 kN to 2400 kN during the cycles of 0.99% drift ratio, which was accompanied by mild concrete spalling at the top of the wall panel (Figure 4.10). During the first excursion to -0.99% drift ratio, the specimen experienced a sudden drop of lateral resistance at -0.82% drift ratio from -2390 kN to -1260 kN, but managed to hold the axial load at 1800 kN even with a sudden shortening of the specimen of 3.2 mm (Figure 4.9(a)). The loss of resistance and height from -0.82% to -0.99% drift ratio was associated with massive concrete spalling at the top of the wall panel, with large pieces of concrete spalling in rhomboidal pieces defined by the intersection of the diagonal shear cracks (Figure 4.10 (b)).

The MAST Facility was able to arrest this developing failure and bring the specimen back to a final cycle, which continued with the concrete spalling, and eventually, the specimen became vertically unstable and the test was stopped at a 0.82% drift ratio and 609 kN. The failure was sudden, in shear and compression along a significant portion of the upper half of the wall panel. Specimen SW02 could not hold its axial load, so that the MAST cross-head began moving rapidly downwards under load control. In the final

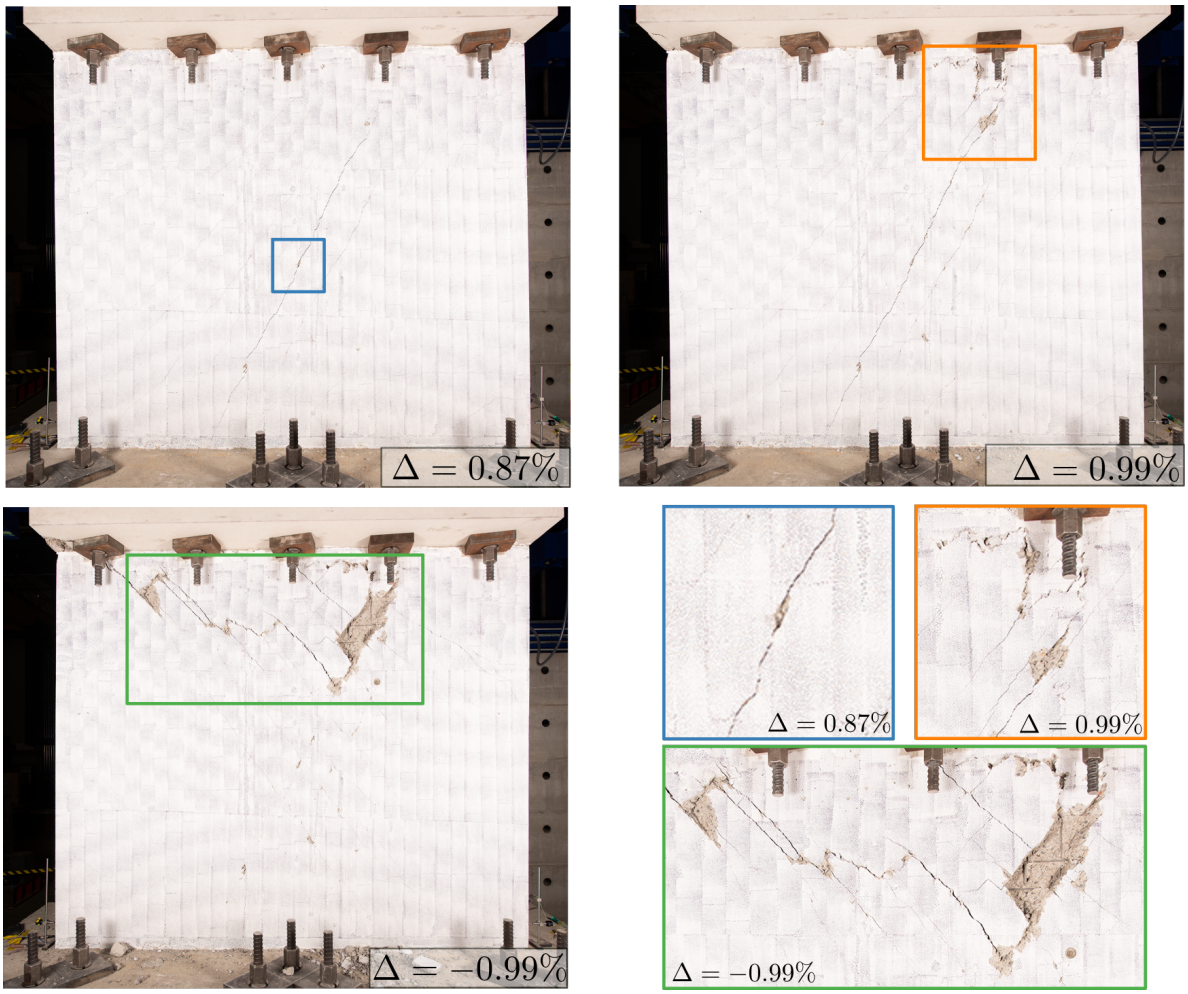

Figure 4.10: Damage progression of specimen SW02.

state of the specimen, it was possible to see through to it. This failure was identified as a brittle shear concrete crushing.

Figure 4.11 shows the final state of specimen SW02, which failed in diagonal shear, specifically in diagonal compression or concrete crushing. The final state is characterized by massive concrete spalling in the upper section of the wall and visible diagonal cracks in the web. The concrete spalled in rhomboidal pieces defined by the intersection of the diagonal cracks, exposing the distributed web reinforcement bars. When the loose concrete was removed, it was possible to see through the wall panel. There was no visible or trace of reinforcement bars fracture.

Specimen SW02 had considerable restoration capacities, with residual drift ratios below 0.1% and residual crack width below 0.5 mm for a drift ratio peak of 0.72% (Table 4.5). Only at the last cycle, when the failure was developing, the specimen had a larger increase in the residual drift ratio, where SW02 reached 0.49%. It also had residual crack widths larger than 0.5 mm after attaining their peak strength. FEMA 306 [51] assigns the damage for walls that had a diagonal shear failure in terms of crack widths: 1.6 mm (1/16 in) for insignificant and 3.2 mm (1/8 in) for moderate damage, values that underestimate the damage according to the result obtained in these tests. The order of magnitude of FEMA 306 is closer to the peak crack widths rather than the residual crack width.

The deformation decomposition of SW02 shows a diagonal shear-controlled behavior during the entire

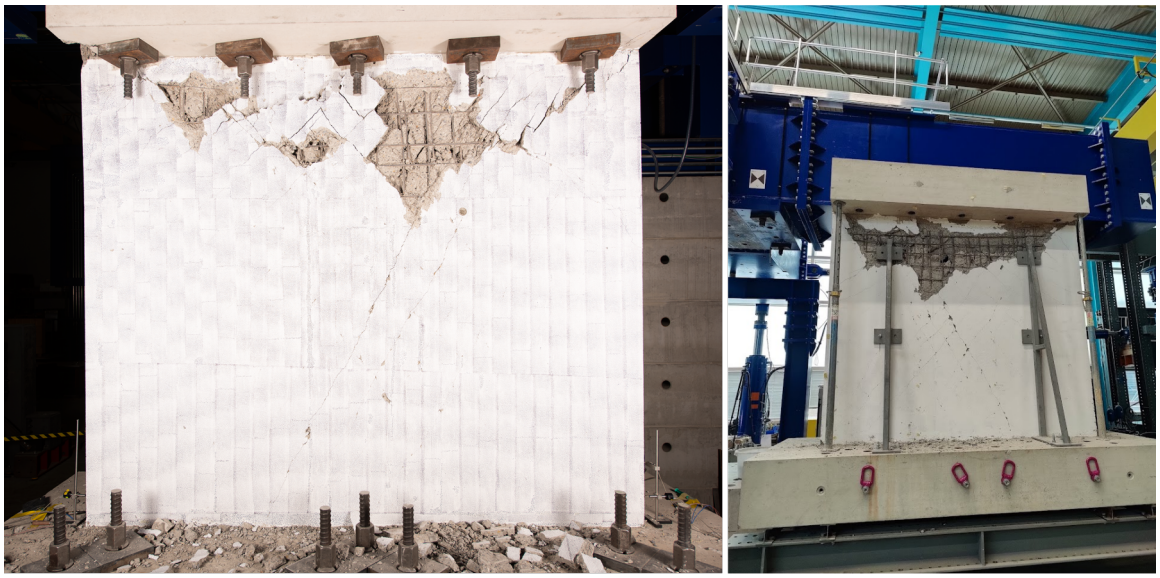

(a) (b)

Figure 4.11: Final state of specimen SW02 (a) At the end of the test. X positive direction points to the left (b) Specimen removed from the ETH MAST Facility. The x positive direction points to the right.

Table 4.5: The peak attained drift ratio Δ_{peak}, the residual top drift ratio (Δ_{res}) and residual crack width w_{res} (computed at zero force after each cycle peak) of the tested specimens in each test cycle. Only the positive drift values are shown. Rows in bold denote the test cycles when the peak strength of the respective specimen was attained.

Δ_{peak} [%]	Δ_{res} [%]	w_{res} [mm]	Δ_{peak} [%]	Δ_{res} [%]	w_{res} [mm]
0.08	0.02	-	0.5	0.06	0.24
0.13	0.02	-	0.61	0.07	0.36
0.18	0.03	0.15	**0.72**	**0.09**	**0.59**
0.29	0.04	0.11	0.84	0.12	0.91
0.39	0.05	0.16	0.96	0.19	-

test, consistent with the observations of the lateral force-drift hysteresis and damage progression. Diagonal shear deformations contributed around 80% of the top displacement, flexure deformations 10%, and sliding shear had a negligible contribution. A deeper look into the diagonal shear deformation reveals that they increased with the displacement, almost linear with the increase of deformation, and followed the path of the main diagonal crack width.

Notably, specimen SW02 did not transition from its pre-peak diagonal shear and flexure behavior after attaining its maximum resistance. Instead, it continued to respond in diagonal shear and flexure and developed brittle shear concrete crushing failure at drift ratios of approximately 1%. The lateral force-drift and the top vertical-displacement response of the specimen followed the path of a shear-behaved controlled specimen with a brittle behavior. This behavior mode was predicted accurately using the strength comparison approach and the controlling behavior mode diagram in Figure 3.1.

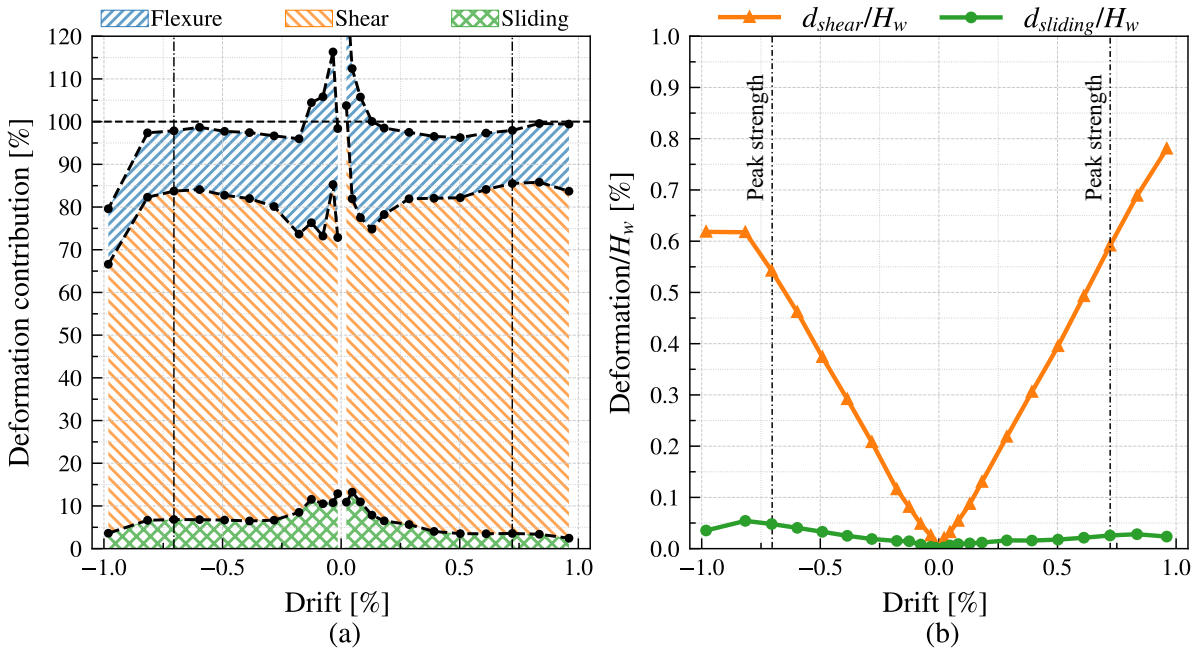

Figure 4.12: (a) Deformation contribution of flexure, shear and sliding of specimen SW02. (b) Shear deformation of specimen SW02

4.4 Specimen SW03

Specimen SW03 had the same geometry and axial load ratio as SW01, but the longitudinal and transverse reinforcement ratios were lowered from 0.53% (ϕ10@15) to 0.33% (ϕ8@15). According to the controlling behavior interaction diagram, specimen SW03 should have sliding-controlled behavior. Figure 4.13 (a) shows the lateral force-drift hysteresis curve obtained in the test.

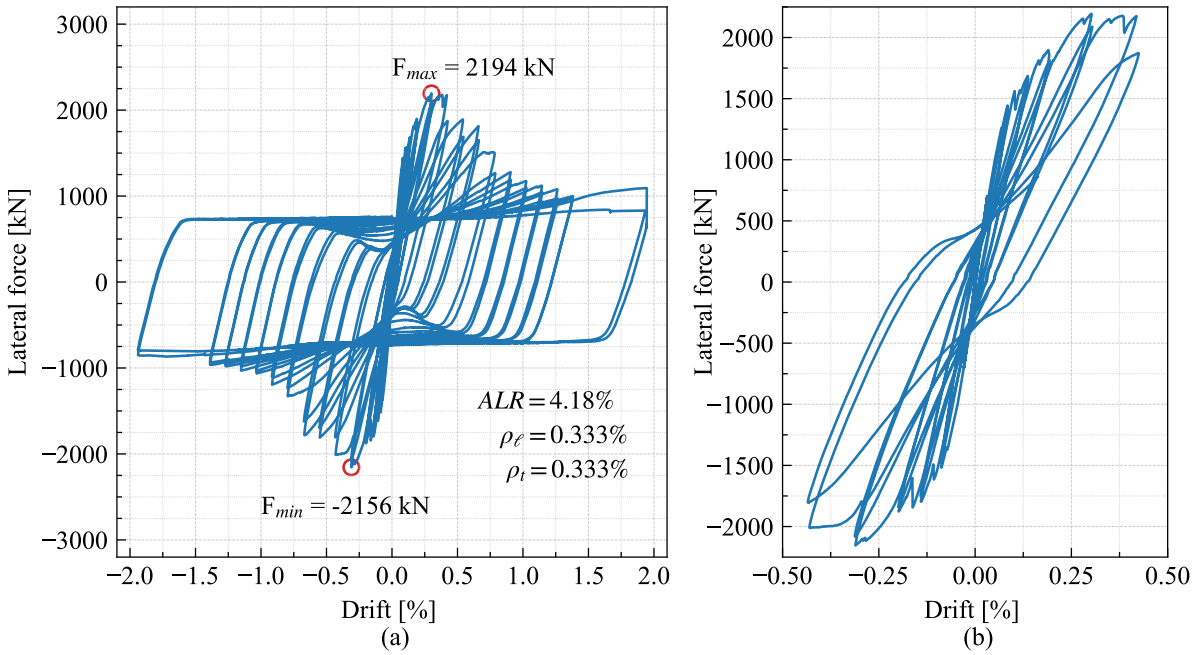

Figure 4.13: (a) Lateral force-drift hysteresis of specimen SW03 (b) Lateral force-drift hysteresis plotted until the sliding initiation.

Specimen SW03 had an uncracked behavior in the first two force-controlled cycles with an initial stiffness of 904 kN/mm. Between the start of the test and until a drift of ±0.30%, the wall had essentially a shear-controlled behavior, as shown in Figure 4.13(b), characterized by low pinching and low energy dissipation. The first diagonal cracks formed at 0.1% and -0.11% drift ratio with a load resistance of 1562 kN and -1615 kN, respectively. The diagonal cracks spread with each increase in displacement: the new cracks can be identified in the lateral force-drift hysteresis as a subtle drop in the resistance of the specimen with increasing displacement. The crack pattern was fully developed at ± 0.43% drift ratio (Figure 4.14). In the positive direction, the pattern is characterized by three concentrated diagonal cracks with 45^o inclination, but the one marked with "C1" was the first one to form, and flexural cracks in the border. It does not seem to have more shear cracks, as the ones in the corner start horizontally and then they change their inclination, typical of flexural cracks. The negative direction has one shear crack in the middle with 45^o inclination and two shear cracks spaced 620 mm from it, plus flexural cracks in the corners. The width of the main diagonal crack had a crescent behavior until 0.45% drift ratio. The diagonal crack width in the negative direction (1.77 mm) was larger than the positive (1.26 mm), which is attributed to the fact that in the positive direction, three cracks were taking the shear deformation, whereas in the negative only one crack does it.

The specimen attained its peak strength of 2194 kN and -2156 kN at ±0.30% drift ratio. It attained

Table 4.6: Lateral force resistance V and shear-span ratio M_{bot}/VL_w measured at the peak. The sub index "1" and "2" refers to the first and second cycle of a giving amplitude.

	Positive cycles					Negative cycles				
Δ	V_1 [kN]	$\frac{M_{bot1}}{VL_w}$	V_2 [kN]	$\frac{M_{bot2}}{VL_w}$	$\frac{V_2}{V_1}$	V_1 [kN]	$\frac{M_{bot1}}{VL_w}$	V_2 [kN]	$\frac{M_{bot2}}{VL_w}$	$\frac{V_2}{V_1}$
0.01	350	0.620	350	0.621	1.00	-350	0.407	-348	0.404	0.99
0.03	700	0.513	700	0.515	1.00	-700	0.433	-699	0.432	1.00
0.08	1437	0.424	1436	0.425	1.00	-1517	0.412	-1479	0.413	0.98
0.14	1685	0.392	1666	0.390	0.99	-1796	0.434	-1751	0.434	0.97
0.19	1861	0.410	1813	0.407	0.97	-1877	0.450	-1841	0.449	0.98
0.30	2189	0.398	2088	0.389	0.95	-2153	0.435	-2078	0.434	0.97
0.42	2174	0.375	1870	0.353	0.86	-2007	0.386	-1803	0.382	0.90
0.54	1885	0.330	1686	0.319	0.89	-1807	0.364	-1695	0.367	0.94
0.66	1812	0.312	1649	0.307	0.91	-1777	0.357	-1618	0.357	0.91
0.78	1495	0.282	1263	0.286	0.85	-1324	0.333	-1234	0.339	0.93
0.91	1278	0.289	1187	0.295	0.93	-1191	0.332	-1098	0.331	0.92
1.03	1171	0.291	1096	0.295	0.94	-1057	0.315	-1031	0.313	0.98
1.14	1114	0.287	1038	0.281	0.93	-1027	0.299	-977	0.294	0.95
1.26	1075	0.275	966	0.245	0.90	-975	0.280	-950	0.283	0.97
1.38	998	0.232	980	0.232	0.98	-962	0.277	-933	0.273	0.97
1.95	744	0.175	828	0.154	1.11	-848	0.213	-791	0.195	0.93

a similar force resistance of 2174 kN at 0.42%, but in the negative direction, it only attained 2007 kN, which represented a loss of 7% in resistance. Note that the crack pattern in the positive direction fully stabilized after attaining the peak strength, and the drop is clearly visible in the lateral force-drift hysteresis (Figure 4.13). At 0.42% drift ratio, there was no concrete spalling in any zone of the wall panel and the only visible damage were the diagonal and flexural cracks, plus a horizontal crack along the entire length of the wall-foundation cold construction joint. The pinching level at the peak-strength drifts was quite different, as the loss of strength was 3-5% at $\pm$0.30% drift ratio and 10-14% at $\pm$0.42% drift ratio. At the drift ratio of 0.42%, the specimen had low secant stiffness, which suggests that the specimen was close to its maximum diagonal shear/flexure capacity (Figure 4.15 (d)).

The drift ratio at 0.42% was the point considered as the initiation of the sliding shear mechanism at the wall-foundation interface, recognized by the high pinching level. The following cycles showed increasing and eventually considerable pinching of the lateral force-drift hysteresis (Figure 4.2). The post-peak resistance of Specimens SW03 decreased from 1880 kN, attained during the $\pm$0.42% drift cycles, to 1000 kN attained during the $\pm$1.38% drift cycles (Figure 4.13). At 1.38% drift ratio, the specimen had a low secant stiffness of 12 kN/mm, which means that the specimen reached its maximum shear strength and could have not increased its resistance if the force had continue to increase. Specimen SW03 reached a peak crack width of 1.25 mm in the positive direction, and 1.75 mm in the negative direction. After the peak strength, the crack width did not open further, and the maximum width

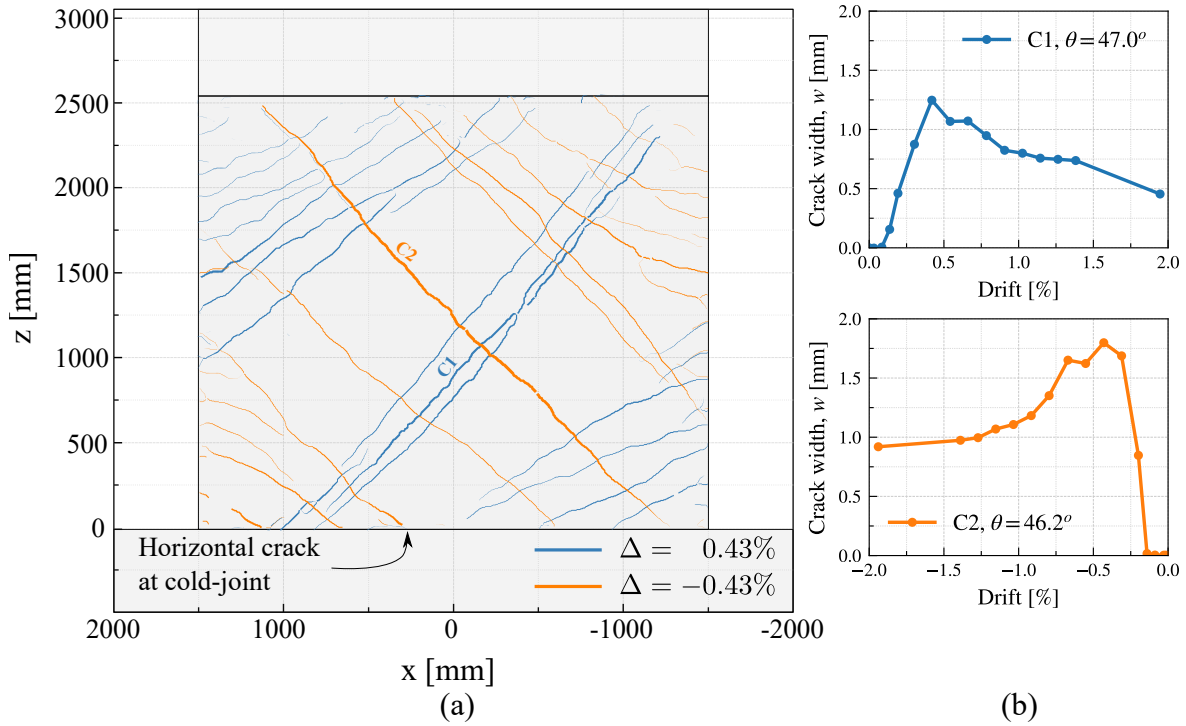

Figure 4.14: Crack pattern of specimen SW03

decreased within each cycle, going from 1.25 mm to 0.75 mm in the positive direction and from 1.75 mm to 0.98 mm in the negative direction, following the same effect as its lateral force-drift ratio response.

Specimen SW03 exhibited a resistance plateau of about 750 kN at a zero-displacement point during each post-peak-resistance test cycle (Figure 4.13 (a)), which is typical of a sliding-controlled behavior. During this plateau, the sliding displacements and damage in the cold joint occurred. This plateau is evident at the load reversal of ±0.54% drift ratio, where it reached force levels of 260 kN and, after each displacement increment, the force of the plateau increased until it stabilized at a force of 750 kN. With the increasing amount of cycles, the length of the sliding plateaus increased due to degradation of the cold joint. Figure 4.15 (c) shows the sliding displacement, where two effects can be observed: the sliding displacement increases with each increment of displacement, and the sliding contribution increases from the first to the second cycle of the same amplitude, a similar effect as specimen SW01.

Unloading of specimen SW03 upon the reversal of displacement direction in each post-peak cycle was practically linear-elastic, a consequence of the elastic rebound of the segment of the wall above the, now sliding, cold joint. The measured unloading stiffness was 240 kN/mm, which was invariant with the drift amplitude. The unloading branch had only flexure and shear deformations, and the specimen started to slide once again when they reached the sliding plateaus. The drifts at which the residual sliding shear resistance in the opposite direction was attained do not differ substantially from the test cycle amplitude (Figure 4.13 (a)), indicating that specimen SW03 had low displacement restoration capacities. Table 4.7 shows the values of residual sliding displacement, residual top displacement and residual crack width of the main diagonal crack. With an increasing number of cycles, the sliding residual displacement started to accumulate, reaching 1.83% drift ratio in SW03 after the last cycles. The increasing values of residual sliding displacements are due to the invariance of unloading stiffness: resistance force peaks had similar force levels, and with the same unloading stiffness the drift difference with the zero force

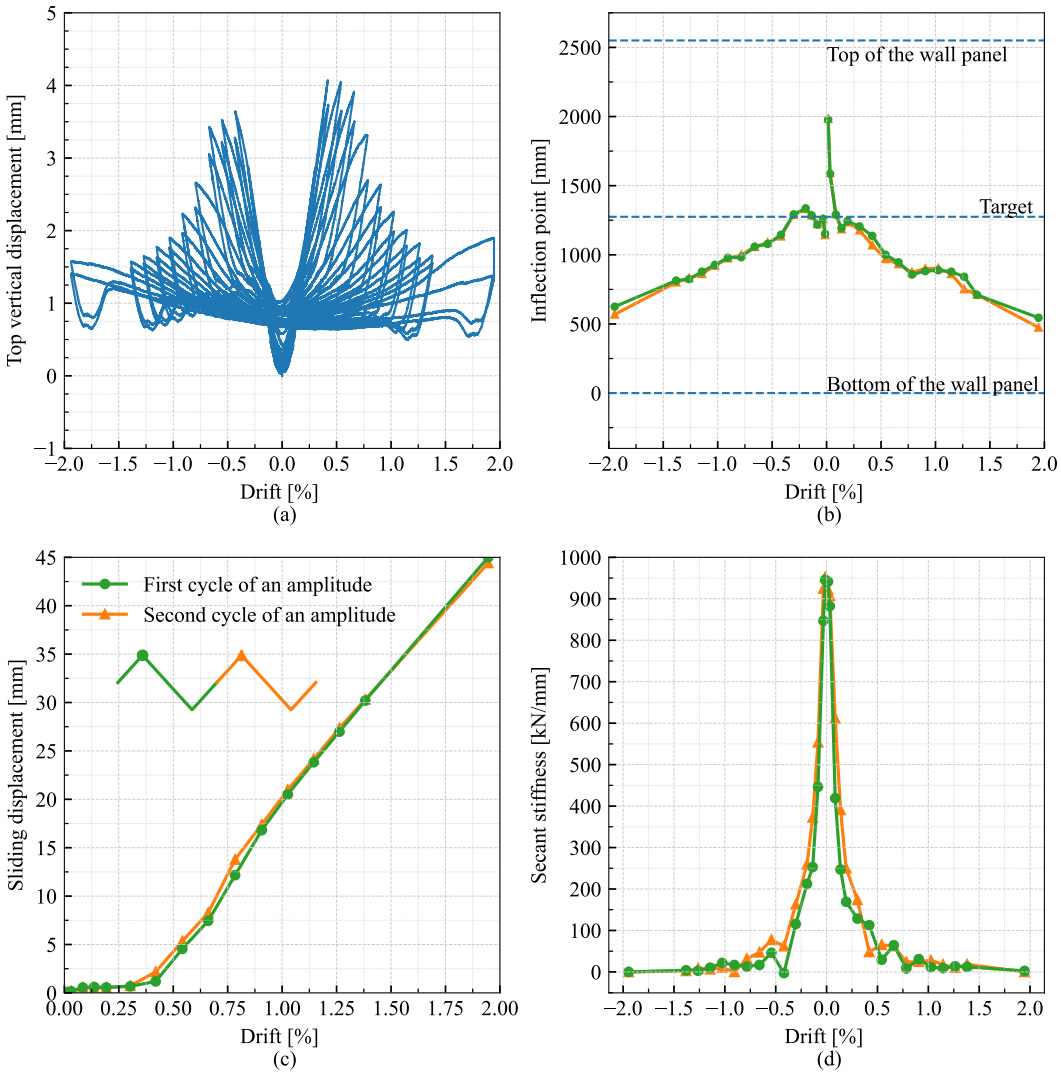

Figure 4.15: (a) Top growth of specimen SW03 (b) Position of the inflection point (c) Sliding displacement at the cold joint (d) Secant stiffness. The legend in plot (c) is valid for (b) and (d)

level is similar for each unloading branch. Note that the top residual displacement is relatively close to the sliding residual displacement, which indicates that there is a residual component of shear and flexure deformation, but mostly controlled by the previously attained sliding deformation during loading of the specimen. This can be seen in the hysteresis curves of SW03 (Figure 4.13). Gulec and Whittaker [54] assumed the failure drift of sliding walls to the one associated with a 0.5% residual drift ratio at the top of the specimen. Specimen SW03 exceeded this residual drift ratio when it was unloaded from 0.78% drift ratio.

The test of specimen SW03 was finished after the 1.93% drift ratio cycles because the specimen sliding behavior was repeatable. The specimen held the applied axial load throughout its test without showing any signs of impending axial instability or loss of axial load carrying capacity. The shape of the post-peak force-drift hysteresis curves of specimen SW03 resembles those of friction-sliding seismic isolation devices. Note that the peak residual resistance of this specimen depended on the damage induced at the wall-foundation interface, thus, indirectly, on the applied cyclic test protocol. Namely, the attained residual resistance is expected to be different if the test protocol with incrementally increasing symmetric

Table 4.7: The peak attained drift ratio Δ_{peak}, the residual sliding drift ratio Δ_{res}^{slid}, the residual top drift ratio (Δ_{res}) and residual crack width w_{res} (computed at zero force after each cycle peak) of the tested specimens in each test cycle. Only the positive drift values are shown. Rows in bold denote the test cycles when the peak strength of the respective specimen was attained.

Δ_{peak} [%]	Δ_{res}^{slid} [%]	Δ_{res} [%]	w_{res} [mm]	Δ_{peak} [%]	Δ_{res}^{slid} [%]	Δ_{res} [%]	w_{res} [mm]
0.09	0.01	0.01	-	0.78	0.46	0.53	0.42
0.14	0.01	0.02	0.05	0.91	0.65	0.7	0.36
0.19	0	0.03	0.19	1.03	0.79	0.84	0.3
0.30	**0.00**	**0.05**	**0.33**	1.14	0.92	0.97	0.33
0.42	0.02	0.09	0.66	1.26	1.05	1.09	0.33
0.54	0.16	0.24	0.39	1.38	1.17	1.22	0.31
0.66	0.28	0.36	0.41	1.95	1.76	1.83	0.23

amplitudes is changed after the specimen attains its peak resistance to a protocol with an asymmetric or monotonic amplitude pattern. Figure 4.16 shows the final state of specimen SW03 is characterized by damage focused at the bottom, and the diagonal cracks can be observed by the human eye. The vertical web steel reinforcement of specimen SW03 was fractured (4.16 (b)) and the boundary reinforcement buckled (4.16 (c)).

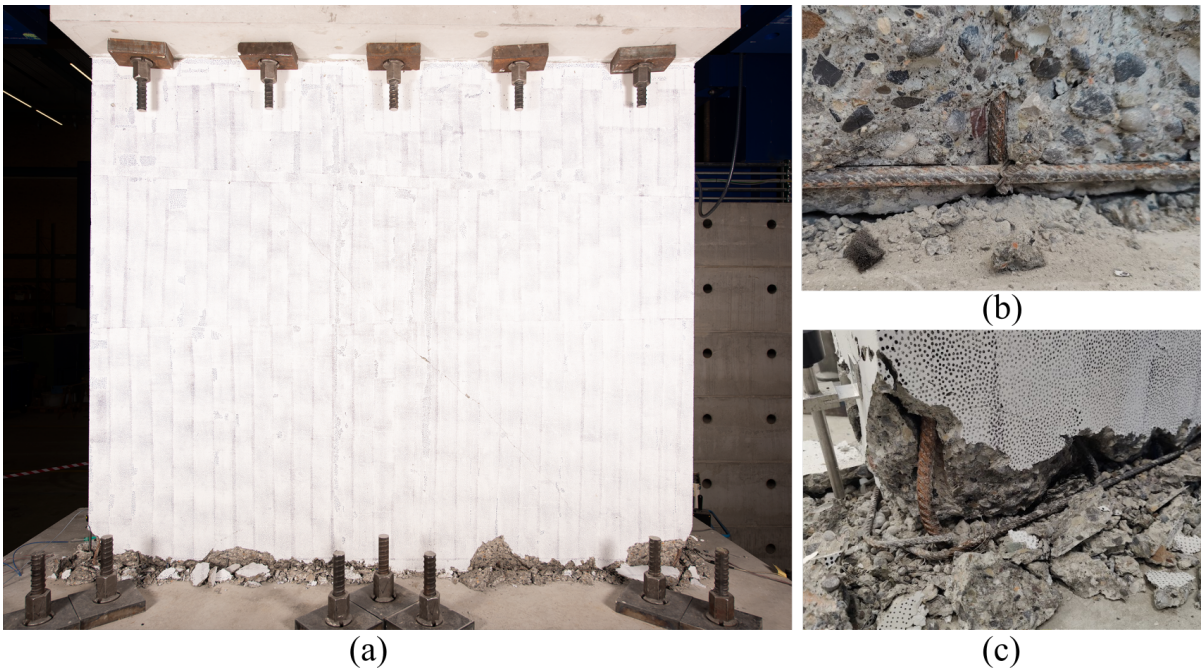

Figure 4.16: (a) Final state of specimen SW03. The X positive direction points to the left (b) Vertical reinforcement fracture at the cold joint (c) Buckled boundary reinforcement

Specimen SW03 had a diagonal shear-controlled behavior before it attained its peak resistance. Diagonal shear deformation controlled the majority (70% to 90%) of the top displacement until 0.35% drift ratio, and this level stayed until the sliding shear behavior was triggered. After this point, the sliding shear contribution increased up 80% to 90% of the total top displacement. A more detailed investigation into the absolute values of the shear contributions of these walls shows the evolution of diagonal shear and

sliding shear deformations (Figure 4.17). The shear deformations were computed at the same drift ratio as the deformation contribution, namely, only at the peaks of the first cycle of each amplitude. Post-peak diagonal shear deformations of SW03 reached values of $\approx 0.25\%$ in the peak of each cycle from 0.42% to 0.78%, and then it had a drop to 0.14% drift ratio at 0.91% drift ratio, which agrees with the drop in resistance (Figure 4.1 (a)) and crack width (Figure 4.2). This means that the specimen SW03 wall lost its diagonal shear resistance capacity, and therefore, in further cycles, it reached lower strength levels.

After the point of reaching its maximum resistance, specimen SW03 transitioned from a diagonal shear and flexure to a sliding shear-controlled behavior along the cold joint between the wall and the foundation. This behavior mode transition was predicted accurately using the strength comparison approach [57] and the controlling behavior mode diagram in Figure 3.1.

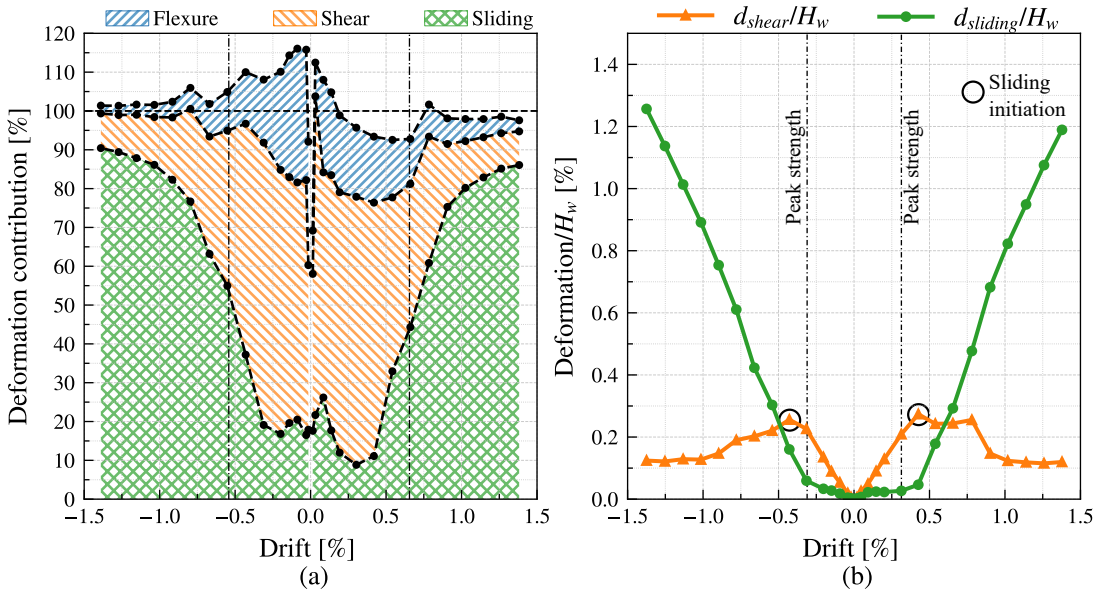

Figure 4.17: (a) Deformation contribution of flexure, diagonal shear and sliding shear of specimen SW03. (b) Shear deformation of specimen SW03

4.5 Specimen SW04

specimen SW04 had 4.72% of ALR, 0.53% of longitudinal reinforcement ratio and 0.39% of transverse reinforcement ratio. According to the interaction diagram (Figure 3.1) the specimen should have shear-controlled behavior. Specimen SW04 had reinforcement bars of ϕ10mm as in Specimen SW01, but the spacing of the transverse reinforcement was increased from 15 to 20 mm. The concrete strength was the largest of the rest of the specimens ($f'_c = 42.4$ MPa), and, therefore, the axial load was increased to 1200 kN to keep a similar axial load ratio level as SW01 and SW03. Fig. 4.18 shows the lateral force-drift hysteresis curve and Table 4.8 presents the values of forces and shear-span ratio obtained at the peak of each cycle.

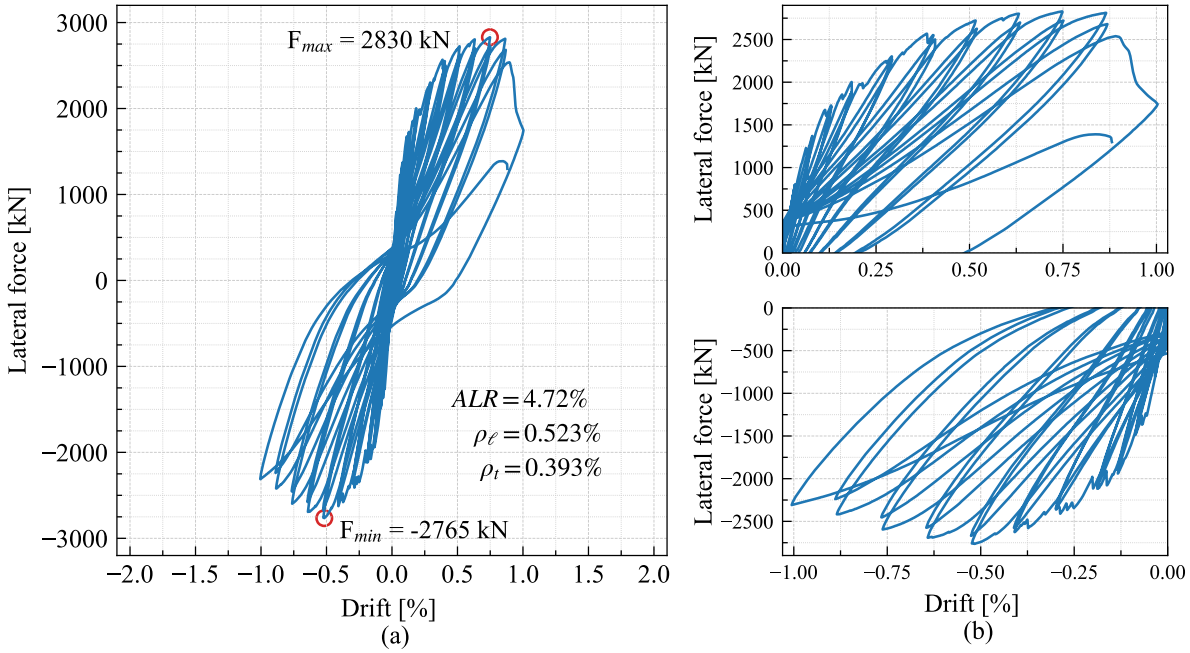

Figure 4.18: Lateral force-drift hysteresis of specimen SW04.

Specimen SW04 remained uncracked and responded in essentially linear flexure and shear during the force-controlled cycles, with an initial stiffness of 939 kN/mm. The first diagonal crack formed at 0.06% and -0.07% drift ratios with load resistances of 1229 kN and -1367 kN, respectively (Table 4.1). The diagonal cracks spread with each increase in displacement: the new cracks can be identified in the lateral force-displacement hysteresis as a subtle drop in the resistance of the specimen with increasing displacement. The crack pattern was fully developed at $\pm$0.64% drift ratio. The crack pattern (Figure 4.19) was characterized by diagonal cracks inclined at approximately 51^o with an average spacing between the main cracks of 200 mm. There were flexural cracks in the four corners of the specimen due to the fixed-fixed boundary conditions, and the widest flexural crack formed at the location of the splice of the boundary steel reinforcement bars. The main diagonal crack increased in width along with an increase in drift ratio, reaching values of up to 1.6 mm and 1.8 mm at 0.87% and -0.87% drift ratio, respectively.

Remarkably, specimen SW04 exhibited an asymmetric behavior (Figure 4.18). In the negative direction, the specimen attained its peak strength of -2765 kN at a -0.54% drift ratio (note that the resistance

Table 4.8: Lateral force resistance V and shear-span ratio M_{bot}/VL_w measured at the peak. The sub/-ndex "1" and "2" refers to the first and second cycles of a given amplitude.

Δ	Positive cycles					Negative cycles				
	V_1 [kN]	$\frac{M_{bot1}}{VL_w}$	V_2 [kN]	$\frac{M_{bot2}}{VL_w}$	$\frac{V_2}{V_1}$	V_1 [kN]	$\frac{M_{bot1}}{VL_w}$	V_2 [kN]	$\frac{M_{bot2}}{VL_w}$	$\frac{V_2}{V_1}$
0.02	397	0.560	398	0.561	1.00	-398	0.445	-401	0.445	1.01
0.03	799	0.492	799	0.489	1.00	-801	0.449	-801	0.447	1.00
0.08	1346	0.454	1370	0.459	1.02	-1488	0.433	-1464	0.432	0.98
0.13	1728	0.449	1712	0.450	0.99	-1940	0.426	-1900	0.427	0.98
0.19	1902	0.441	1882	0.445	0.99	-2117	0.457	-2089	0.457	0.99
0.29	2299	0.445	2265	0.447	0.99	-2362	0.442	-2349	0.444	0.99
0.40	2549	0.443	2455	0.440	0.96	-2624	0.439	-2575	0.441	0.98
0.52	2721	0.439	2626	0.435	0.96	-2759	0.430	-2669	0.429	0.97
0.63	2802	0.429	2698	0.426	0.96	-2691	0.406	-2574	0.404	0.96
0.75	2826	0.423	2721	0.422	0.96	-2593	0.381	-2452	0.378	0.95
0.87	2811	0.420	2679	0.418	0.95	-2418	0.359	-2239	0.358	0.93
1.00	1746	0.389				-2309	0.353			

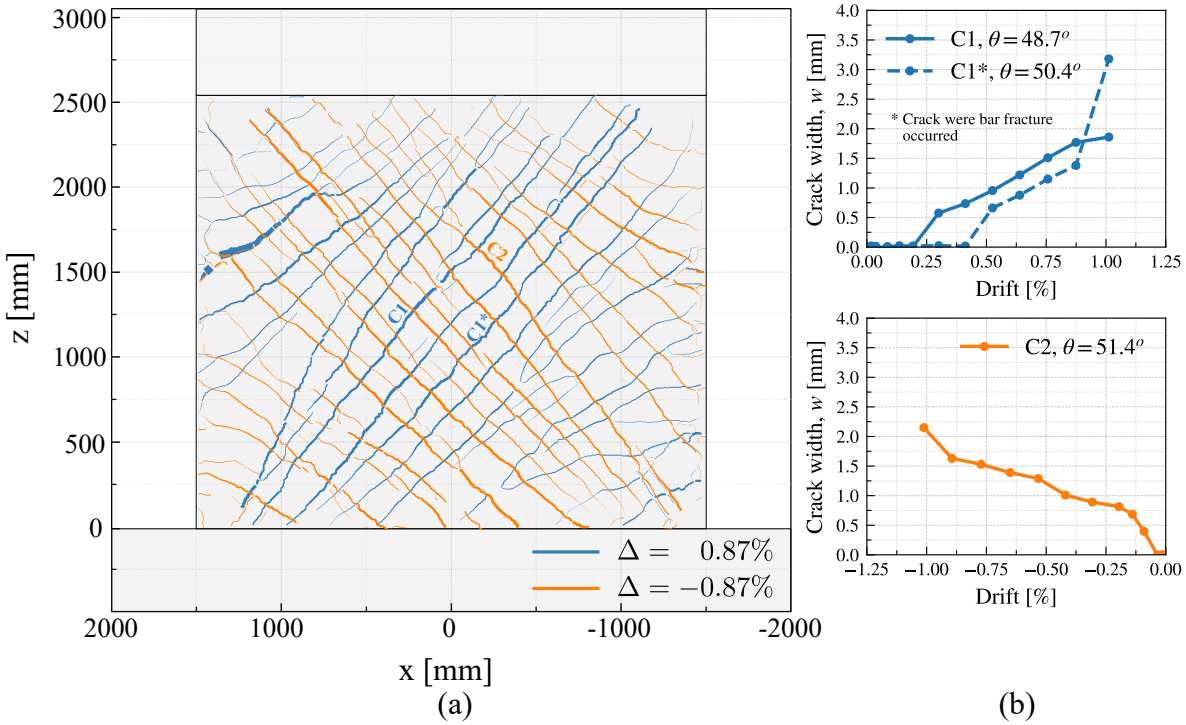

Figure 4.19: Crack pattern of specimen SW04

at the same drift ratio cycle in the positive direction was 2724 kN), and the resistance at the end of each subsequent cycle decreased until reaching -2309 kN at -1.00% drift ratio. There was a slight pinching increase between each par of cycles of a given amplitude with 3 to 7% of resistance loss. There was damage associated with sliding in the corner pushed by the sliding displacement (Figure 4.22), similar to SW01 and SW03 at their first set of sliding cycles. But unlike those specimens, the diagonal cracks continue to open from 1.4 mm at -0.51% to 2.2 mm at -0.83% drift ratio (Figure 4.19), which indicates that SW04 diagonal shear deformation in the negative direction was nevertheless increasing with displacement. Two other effects suggest that the sliding shear mechanism developed in the negative direction. First, the inflection point of the specimen was a bit above the mid-height of the wall panel in the cycles previous to 0.54% drift ratio, but once sliding started, the inflection point moved down. Second, the top vertical displacement-drift curve also shows and asymmetric behavior, having less vertical displacement than the positive direction, the unloading path does not follow the loading path, and there is an offset of the top vertical displacement peaks.

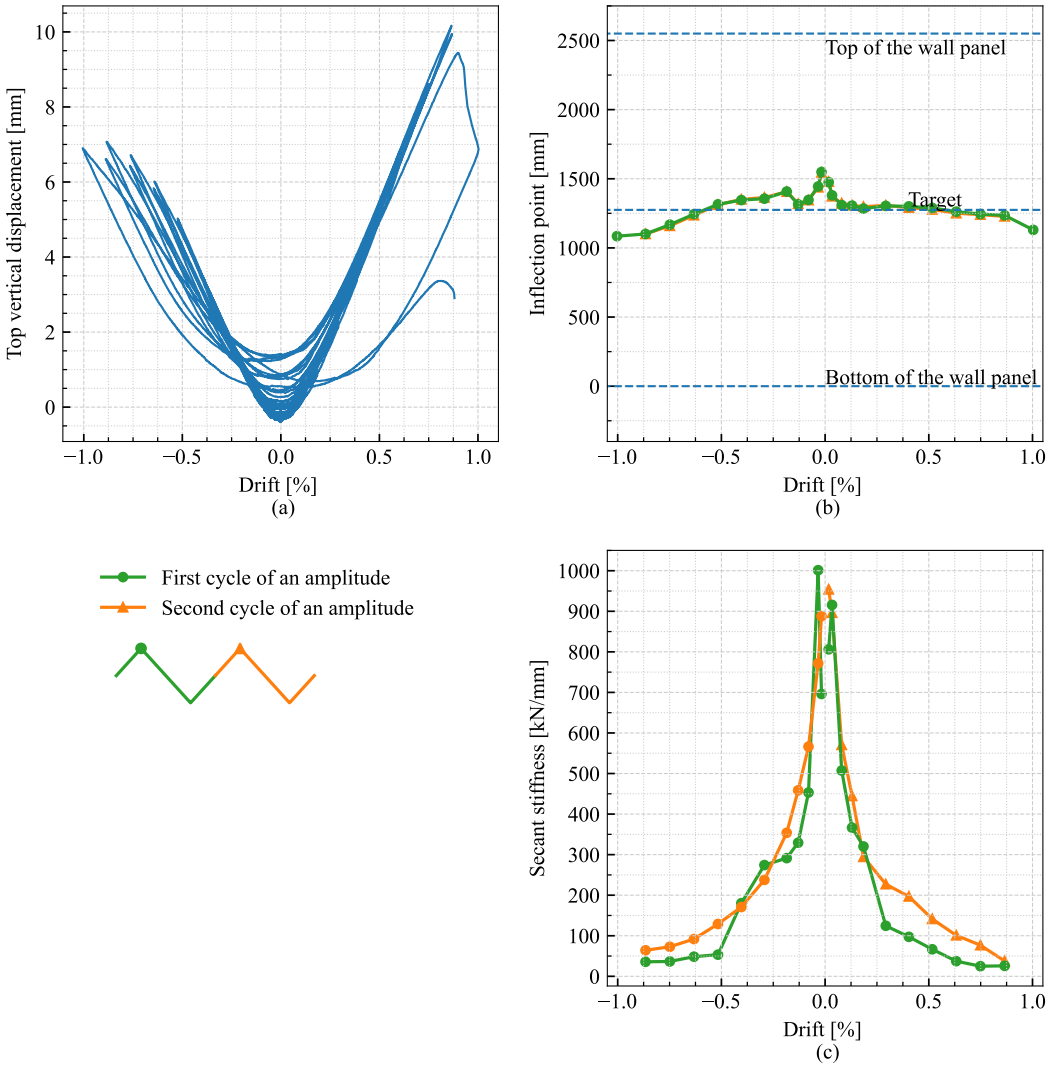

Figure 4.20: (a) Top growth of specimen SW04 (b) Position of the inflection point (c) Secant stiffness. The legend is valid for (b) and (c)

On the other side, the positive direction suggests a shear-controlled behavior. The peak resistance of 2830

KN was attained during the first positive direction cycle at the 0.78% drift ratio amplitude and there was practically no decrease of specimen resistance during the cycles to 0.86% drift ratio amplitude. During the 1.02% drift ratio cycles, the specimen had a sudden drop of resistance from 2530 kN at 0.91% drift ratio to 1742 kN at 1.00% drift ratio, which was accompanied by 2.46 mm shortening of the specimen (Figure 4.20 (a)) due to slipping along a diagonal crack. Figure 4.21 shows the state before and after the specimen slipped along the diagonal crack. The specimen moved to the negative direction and reached -1.00%, but a brittle failure ensued in the positive direction during the second cycle to 1.00% drift ratio at a 0.87% drift ratio and resistance of only 1330 kN. The failure was sudden, in shear and tension along a pronounced diagonal crack where the transverse reinforcement bars fractured (Figure 4.23. The specimen wall separated in two, with the upper portion sliding diagonally along the shear fracture zone, pushed down by the MAST cross-head in force control. The crack where the diagonal tension failure developed was not the first one to form. Figure 4.19 shows that the failed crack formed at a 0.41% drift ratio, and it only became the controlling crack at the first cycle of the 1.00% drift amplitude. The failed diagonal crack formed at a drift of 0.3% and had a large increase from 1.38 to 3.18 mm before the transverse reinforcement bars fractured. Specimen SW04 could not carry its axial load in a stable manner. The inflection point of the specimen was kept stable around mid-height of the wall panel in the positive direction during the test (Figure 4.20 (b)) which translates to a $M/VL_w \approx 0.425$.

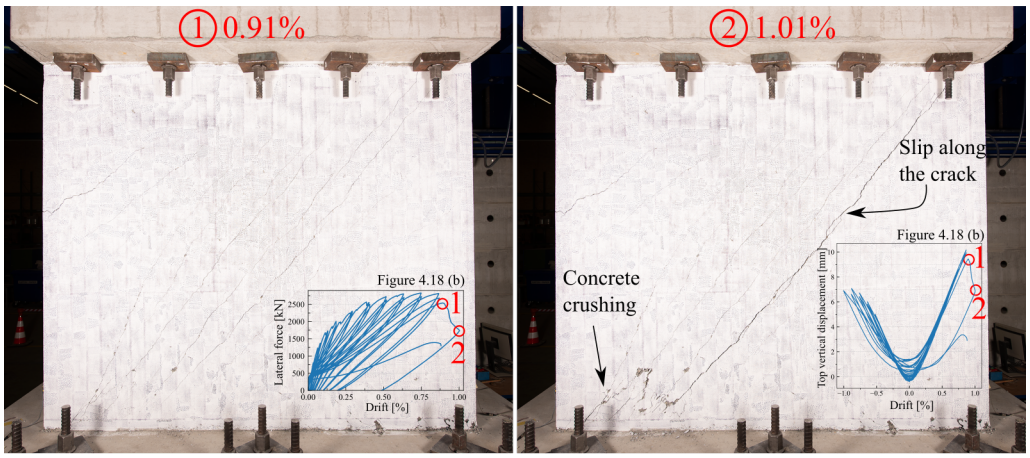

Figure 4.21: Specimen SW04 state during the 1.00% drift amplitude's first cycle (a) at 0.91% drift ratio and (b) at 1.00% drift ratio.

Figure 4.22 shows the final state of specimen SW04. The damage is characterized by a significant diagonal crack with a width larger than 30 mm. The transverse reinforcement bars crossing that crack were fractured, whereas the vertical ones did not. The rest of the diagonal cracks could be easily observed. Concrete spalling made the reinforcement bars visible in the bottom corner of the wall panel, where the fractured diagonal crack started.

Notably, specimen SW04 did not transition from its pre-peak diagonal shear and flexure behavior after attaining its maximum resistance. Instead, it continued to respond in diagonal shear and flexure and developed brittle shear failure in diagonal tension) at drift ratios of approximately 1%. This behavior mode was predicted accurately using the strength comparison approach and the controlling-behavior mode diagram in Figure 3.1.

(a) (b)

Figure 4.22: Final state of specimen SW04 (a) X positive direction points towards the left (b) X Positive direction points towards the right. Picture (b): Milan Rohrer

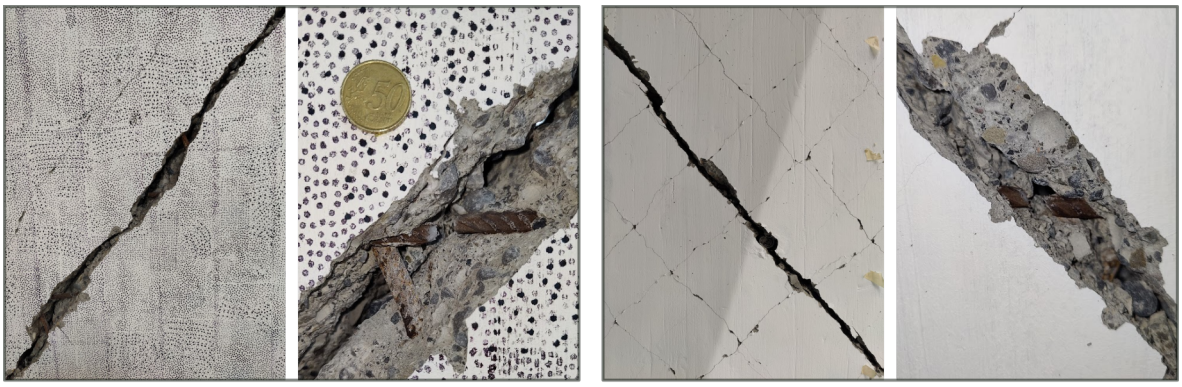

(a) (b)

Figure 4.23: Main crack damage (a) X positive direction points towards the left (b) X Positive direction points towards the right.

Specimen SW04 did have considerable restoration capacities, with residual drifts ratio below 0.1% and residual crack width below 0.5 mm for a drift ratio peak of 0.64% (Table 4.9). Only at the last cycle, when the failure was developing, the specimen had a larger increase in the residual drift ratio, where SW04 reached 0.49%. It also had residual crack widths larger than 0.5 mm after attaining their peak strength. FEMA 306 [51] assigns the damage for walls that had a diagonal shear failure in terms of crack widths: 1.6 mm (1/16 in) for insignificant and 3.2 mm (1/8 in) for moderate damage, values that underestimate the damage according to the result obtained in these tests. The order of magnitude of FEMA 306 is closer to the peak crack widths rather than the residual crack width, and the moderate damage crack width of FEMA is similar to the crack width at the final state of the specimen.

The deformation decomposition of specimen SW04 reaffirms the asymmetrical behavior previously described. In the positive direction, it showed a similar trend as specimen SW02 with diagonal shear contributions larger than 70% until failure, whereas in the negative direction, there was a considerable contribution of flexure, but shear still controlled the overall behavior. After the negative peak strength,

Table 4.9: The peak attained drift ratio Δ_{peak}, the residual top drift ratio (Δ_{res}) and residual crack width w_{res} (computed at zero force after each cycle peak) of the tested specimens in each test cycle. Only the positive drift values are shown. Rows in bold denote the test cycles when the peak strength of the respective specimen was attained.

Δ_{peak} [%]	Δ_{res} [%]	w_{res} [mm]	Δ_{peak} [%]	Δ_{res} [%]	w_{res} [mm]
0.09	0.01	-	0.53	0.07	0.2
0.14	0.02	-	0.64	0.1	0.33
0.19	0.03	0.01	**0.76**	**0.14**	**0.50**
0.3	0.04	0.21	0.87	0.19	0.6
0.41	0.06	0.22	1.01	0.49	-

the sliding shear contribution increased from 12% to 32%, and the specimen followed the trend of SW01 and SW03. Because the specimen failed in diagonal shear in the positive direction, the negative side could not transition from a diagonal shear to sliding shear controlled behavior. The diagonal shear deformations increased along with the displacement, even in the negative direction where sliding shear deformations increased its contributions.

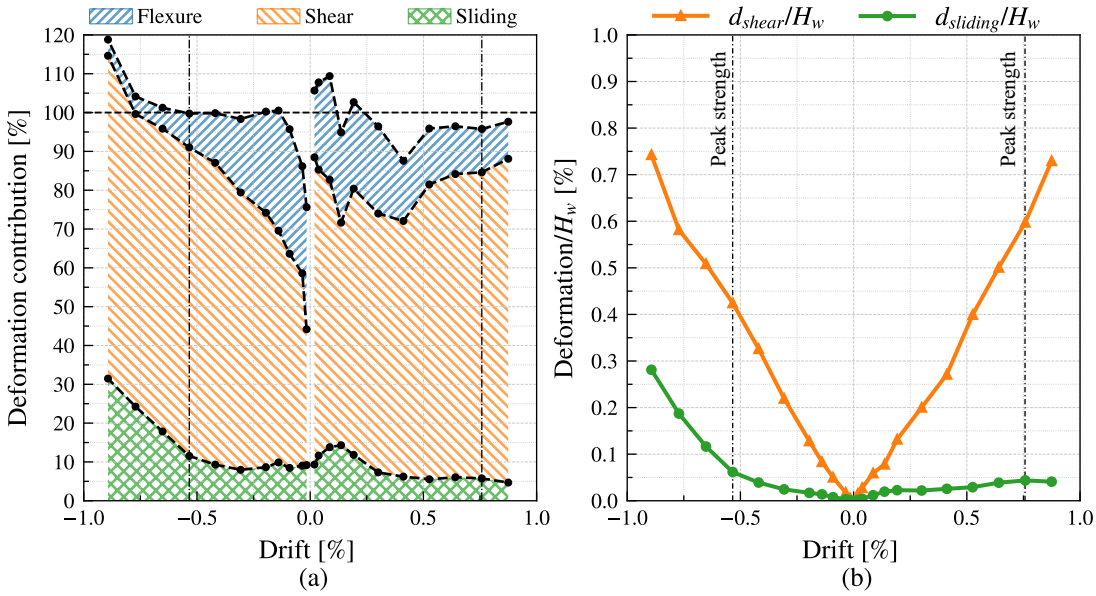

Figure 4.24: (a) Deformation contribution of flexure, diagonal shear and sliding shear of specimen SW04. (b) Shear deformation of specimen SW04

CHAPTER 5

HYBRID SIMULATION TESTS

This chapter presents the results of the hybrid simulation tests. First, Section 5.1 sets the context of the hybrid simulation by re-describing the hybrid system presented in Section 3.4.1. Section 5.2 describes the procedures and results to obtain the initial stiffness of the specimens and the damping contributed by the physical substructure, key elements to run the hybrid simulation, and validates them with an uncracked time history analysis.

The next two sections describe the results of the hybrid simulation tests with the scaled ground motion. Section 5.5 gives an overview of the results of the hybrid simulation by analyzing (1) the accuracy of the implementation described in Section 3.4, (2) describes the stop and restart of specimen HSW01 and its implications in the results and, (3) presents an energy balance analysis, in which the chosen viscous damping is discussed. Finally, Sections 5.5.1 and 5.5.2 describe the damage progression and hysteresis response of the specimens when subjected to the 1995 Kobe JMA scaled ground motion.

5.1 Hybrid system

The reference system corresponded to an in-plane single degree of freedom (DOF) structure (Fig. 5.1): a horizontal DOF u_1. The structure was fully fixed at the bottom, meaning that all the degrees of freedom were restrained, and the rotations and out-of-plane translations were restrained at the top. Such a model was selected to be consistent with the specimen boundary conditions imposed during the quasi-static cyclic tests. The system was subjected to a constant axial load P applied at the top (as specified by Table 3.1), and had a seismic mass m of 180 tons and an elastic/initial stiffness k of 780 kN/mm (estimated in Section 5.2). The system was subjected to a horizontal ground motion applied at the base.

The hybrid system divided the reference system into a physical and numerical part. The physical part consisted of the shear wall specimen, the boundary conditions at the top and bottom, the gravity loads, and the vertical degree of freedom. The numerical part consisted of the seismic mass and viscous damping ratio. The horizontal displacement of the top of the shear wall in its longitudinal direction u_1 was the controlled degree of freedom of the hybrid model and linked the numerical and physical substructures.

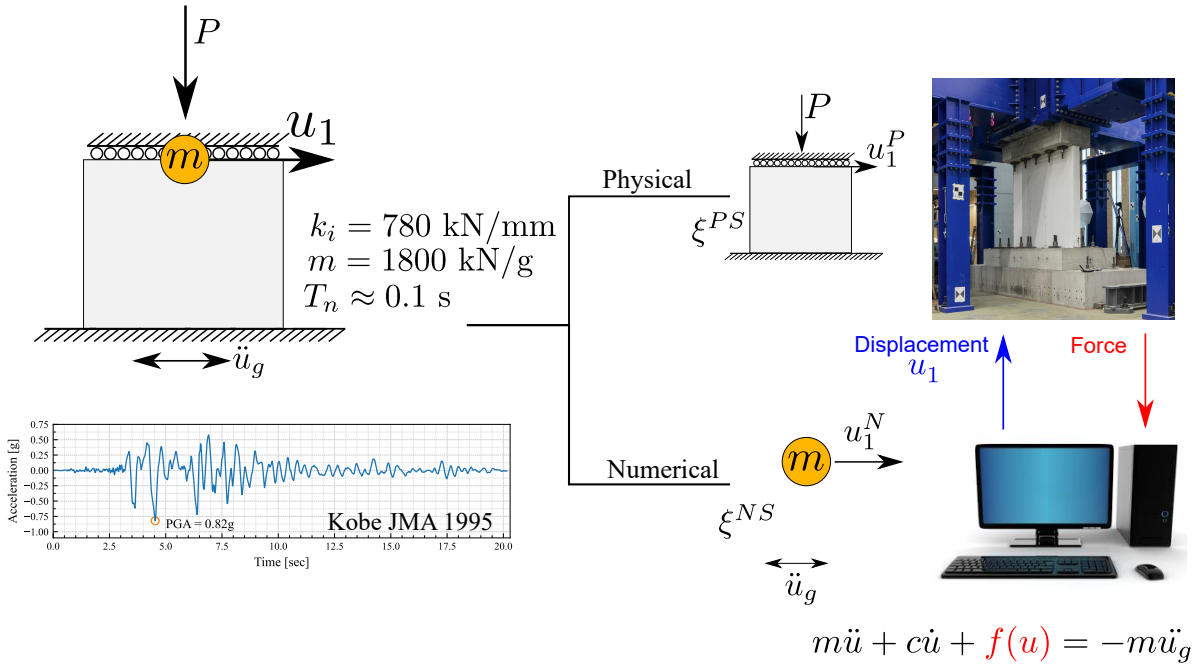

Figure 5.1: Hybrid simulation partitioned system

5.2 Initial stiffness

Both specimens were first subjected to two low displacement cycles to estimate their initial stiffness. After applying the vertical load P according to Table 3.1, Specimen HSW01 was subjected to two displacement-controlled cycles of 0.75 mm (0.03%), whereas Specimen HSW02 was subjected to two force-controlled cycles of 600 kN. The level of the cycles was selected such that the specimens did not have any damage before the full scaled ground motion tests, and to have enough displacement and force to have a good estimate of the initial stiffness. Figure 5.2 shows the lateral force-drift ratio hysteresis of these pre-tests. The measured initial stiffness was 760 kN/mm for Specimen HSW01 and 780 kN/mm for Specimen HSW02. With these initial stiffness values, the natural periods of both hybrid models were approximately 0.1 seconds.

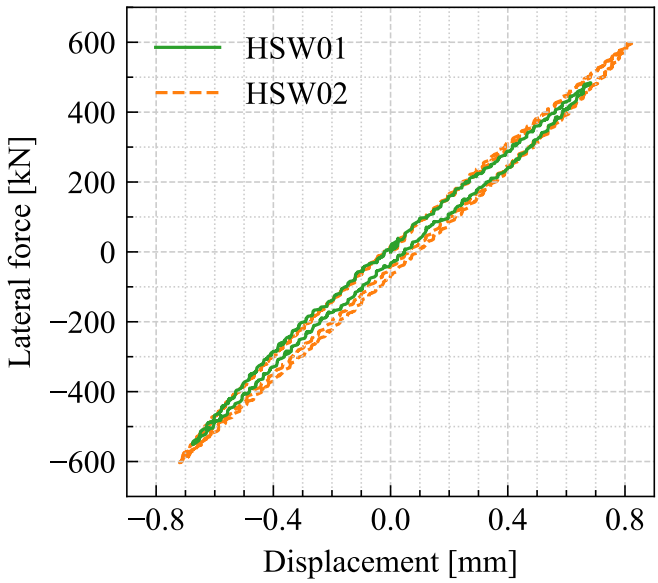

Figure 5.2: Lateral force-displacement response hysteresis during the elastic pre-tests of specimens HSW01 and HSW02

5.3 Damping

From a previous experimental campaign [102] conducted in the MAST, it was known that the MAST Facility contributes to the viscous damping of the system with a physical damping ξ^{PS}. The viscous damping associated with the physical substructure of the reference system ξ^{PS} for specimens HSW01 and HSW02 was determined by loading the specimens in one direction and letting them vibrate freely [103]. The specimens were subjected to a ground acceleration pulse shown in Figure 5.3 (a) and their response was evaluated using the ETH MAST hybrid simulation methodology. The top displacement response time history of specimen HSW02 is shown in Figure 5.3 (b). Using the decaying portion of the response after $t = 4.0$ s, the viscous damping damping can be estimated as,

$$\xi^{PS} = \ln \frac{\delta_k}{\delta_{k+1}} \cdot \frac{1}{2\pi} \tag{5.1}$$

Where δ_k and δ_{k+1} are subsequent local peaks of the displacement response in the free vibration phase (after $t = 4$ seconds).

The physical viscous damping ratios ξ^{PS} of specimens HSW01 and HSW02 were 2.5% and 2.0%, respectively. In order to keep the 3% total reference structure viscous damping ratio of the reference structure, the numerical damping ratios ξ^{NS} were set to 0.5% and 1.0% for specimens HSW01 and HSW02, respectively.

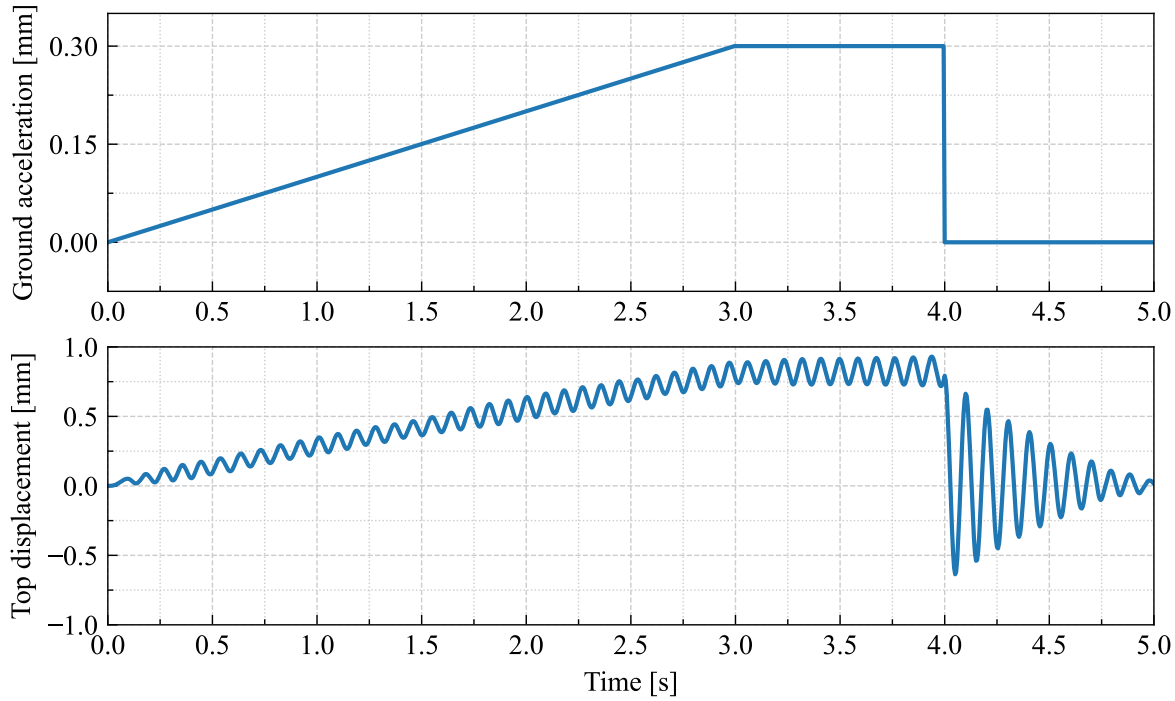

Figure 5.3: Free vibration test of specimen HSW02 to estimate the viscous damping contributed by the setup

The damping determination was conducted at a low-displacement level, lower than 1 mm, and was validated with a hybrid simulation in which the specimens were subjected to the Kobe JMA 1995 ground motion scaled by 0.3, which had displacements peaks lower than 1 mm. These time-history responses are analyzed in Section 5.4. However, the behavior of the damping was different when the systems where subjected to the Kobe JMA 1995 ground motion scaled by 1.75, where the specimens reached much larger displacements (Section 5.5).

These differences were identified during the post-processing of the results of the hybrid simulation tests, by conducting an energy balance analysis. The energy balance is an effective method to track the error of a hybrid simulation [104]. Each term of the equation of motion (Eq. 3.1) contributes to the energy dissipation of the reference systems: kinetic energy E_K, damping energy E_D, and strain energy E_S. In theory, the sum of them should be equal to the input energy E_I. Equation 5.2 shows the definition of each term, where $f(s)$ are the restoring forces, in this case, obtained from the physical substructure.

$$E_K = \int_o^u m\ddot{u}(t)du,\ E_D = \int_o^u c\dot{u}(t)du,\ E_s = \int_o^u f_s(u)du,\ E_I = -\int_o^u m\ddot{u}_g(t)du \tag{5.2}$$

Figure 5.4 shows the energy balance of the reference structure with specimen HSW01 and HSW02 subjected to the 1995 JMA Kobe ground motion scaled by 0.3 (the time-history responses are shown in Figure 5.6). Specimen HSW01 had $\xi^{NS} = 0.5\%$, and specimen HSW02 had $\xi^{NS} = 1.0\%$. By adding the measured physical viscous damping, the total viscous damping was 3% for both specimens and, therefore, that was the value used to calculate the damping energy E_D. By doing the energy balance, there is a good input/dissipation energy balance.

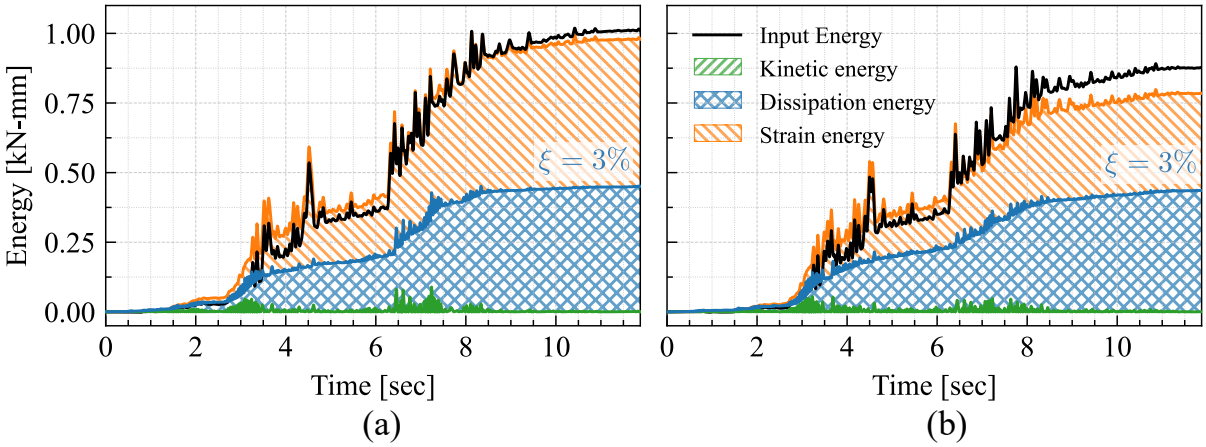

Figure 5.4: Energy balance of uncracked response of specimens (a) Specimen HWS01 (b) Specimen HWS02.

However, the energy balance of the hybrid simulation with the 1995 JMA Kobe ground motion scaled by 1.75 (Figure 5.5) showed that a better energy balance can be obtained by lowering the total viscous damping ratio of the reference system used to obtain E_D to $\xi = 0.5\%$, namely, keeping only the numerical viscous damping ratio ξ^{NS} of the reference system and setting the viscous damping ratio of the physical substructure ξ^{PS} to zero. If a damping of 3% is considered, the calculated energy balance is much larger than the input energy (dashed line in Figure 5.5). This suggests that the ETH MAST facility did not add significant physical damping at large displacements. This, in turn, means that the displacement responses of hybrid simulations with specimen HSW01 and HSW02 cannot be compared directly as they had different numerical substructure viscous damping ratios (0.5% and 1%, respectively). This observation shows that the energy dissipated by the physical substructure depends on its displacement amplitude. As a reminder, each subsequent section indicates the total damping considered in the hybrid simulation, as that would be the inherent damping needed to replicate the results with non-linear finite element models.

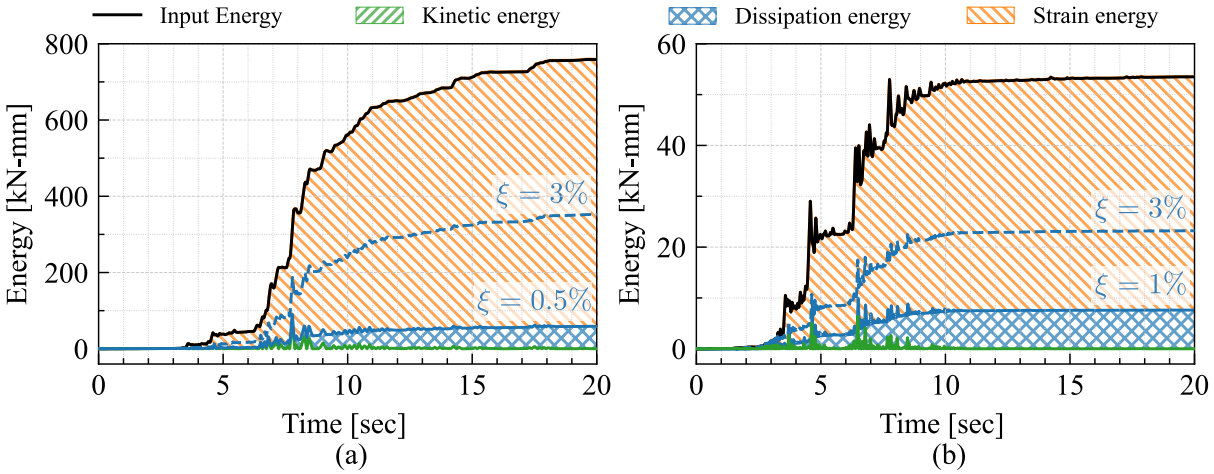

Figure 5.5: Energy balance of the response of the specimens under the 1995 Kobe JMA ground motion scaled by 1.75 (a) Specimen HWS01 and (b) Specimen HWS02.

5.4 Low-scaled ground motion response

The specimens were subjected to the seismic record scaled by 0.3 to have a response in the uncracked state and to validate the methodology, hybrid model and damping. The total damping considered in this simulations is $\xi = 3\%$. Fig. 5.6 shows the displacement history of the system, plotted against a time-history linear analysis with the exact parameters of the hybrid simulation ($m = 180$ tons and $\xi = 3\%$) and a stiffness of 760 kN/mm. The peak displacement of the specimens did not occur precisely at the same time but was very close: the maximum response of specimen HSW01 was 0.91 mm at 6.415 seconds, and of HSW02 was 0.84 mm at 6.405 seconds. The global maximum of the linear TH was 0.96 mm at 4.545 seconds, and the local maximum in the 6.2-6.5 seconds range was 0.86 mm.

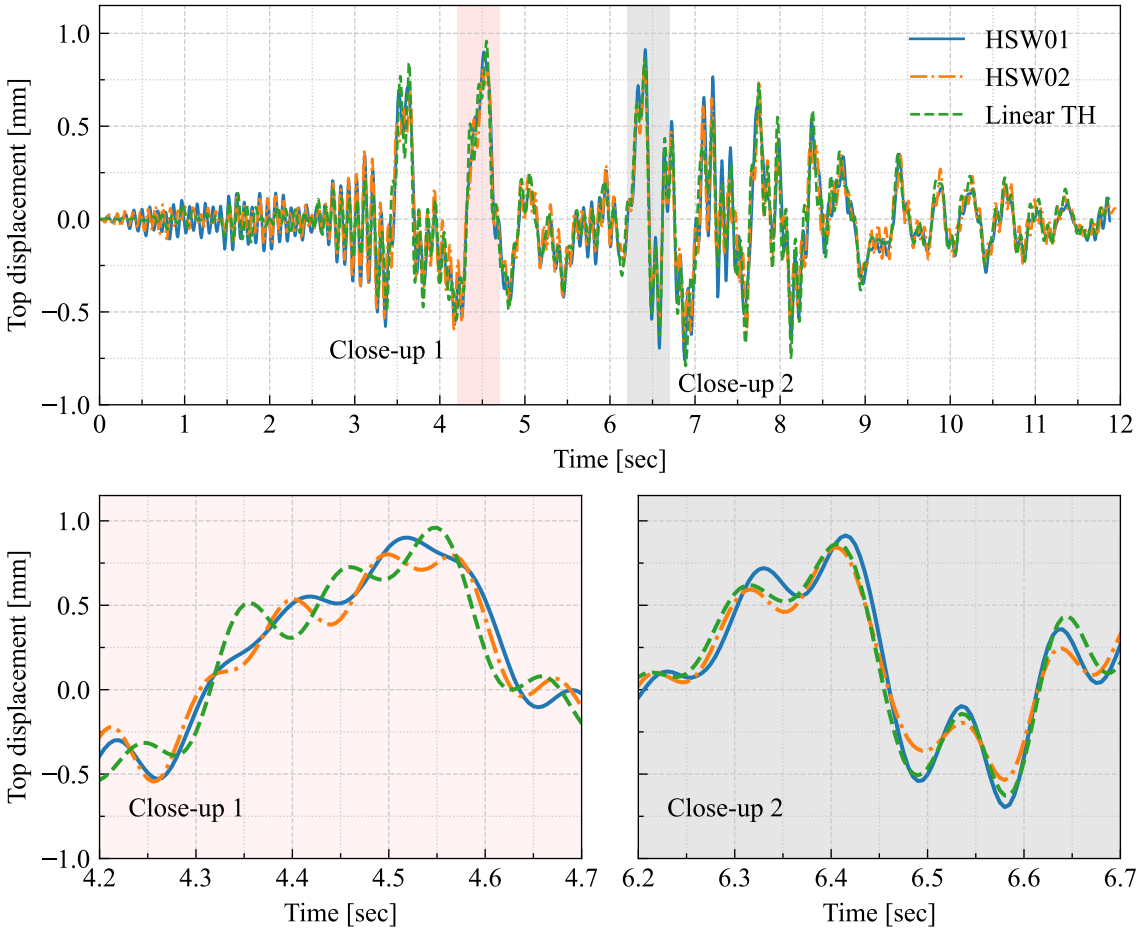

Figure 5.6: Displacement time-history of specimens HSW01, HSW02, and a SDOF elastic system. The ground motion was scaled by 0.3.

5.5 Overview of the hybrid simulation tests

5.5.1 Specimen HSW01

Figure 5.7 shows the displacement-history response of specimen HSW01 to the 1995 Kobe JMA ground motion scaled by 1.75. Important points are shown in the plots to track the specimen's behavior during this hybrid simulation. These points were time-wise numbered. The test was conducted in three stages, delimited by dashed lines in Figure 5.7.

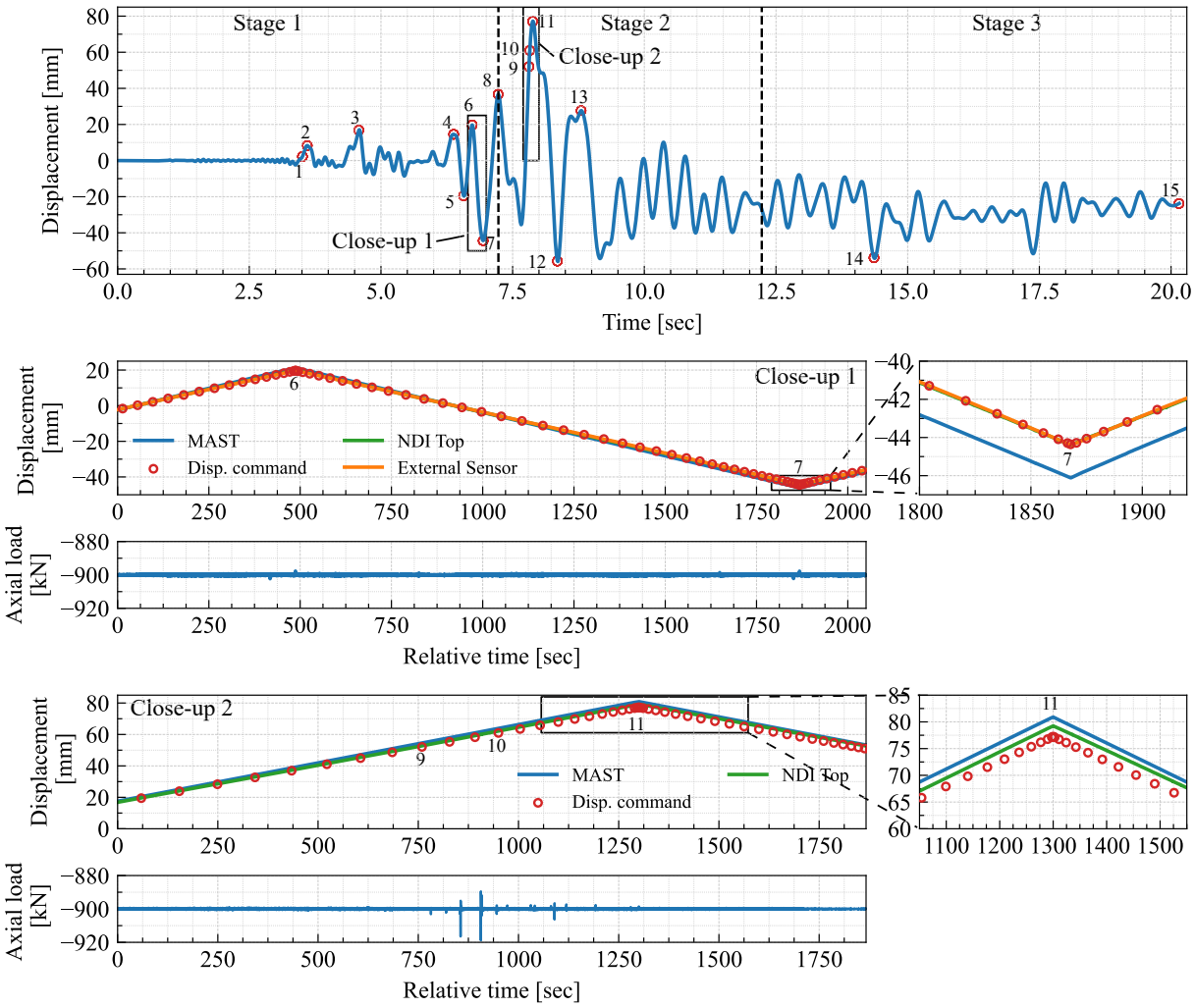

Figure 5.7: Displacement-history response of the hybrid model with specimen HSW01 to the 1995 Kobe JMA ground motion record scaled by 1.75. The close-ups show how the signals were sent and received from the host computer to the ETH MAST.

In the first stage, the simulation was controlled with the external sensor with the methodology explained in Section 3.4.3. Close-up 1 shows the signals sent and received from the host computer to the MAST. Each red dot of the displacement command corresponds to a time step in the numerical integration. The measurements at Point 7 show the accuracy of the implementation, where the displacement command, the measurement of the external sensor and the measurement of the NDI Optotrak cameras have similar displacements with negligible error. The displacement measured by the MAST has a larger value due to the flexibility of the crosshead. Overall, Stage 1 was conducted smoothly, as the Python script could control the lateral DOF u_1 and was stable even when diagonal cracks appeared, which are moments that

produce oscillations in the measurement instruments, and the specimen reached its peak strength in Stage 1.

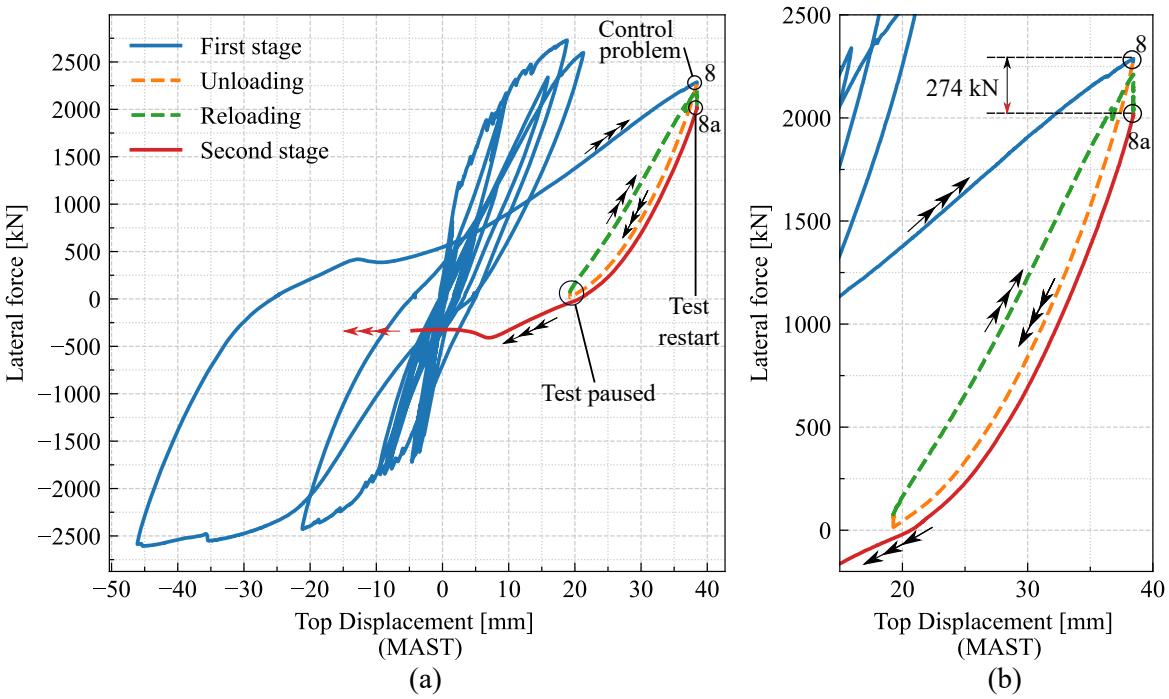

Figure 5.8: Part of the lateral force-displacement hysteresis response with the unloading and reloading branch of the test of specimen HSW01. The figure shows only a section of the second stage of the test.

The test had to be stopped and resumed at the load reversal from point 8, at 7.230 seconds of the hybrid simulation, situation illustrated in Figure 5.8. Due to a control problem, the specimen kept moving to the negative direction and the integration algorithm did not advance to the next step (unloading branch of Figure 5.8). The test was paused when it reached zero force to keep the specimen in a stable position, avoid relaxation of the actuators and give time to plan the restart of the test.

The horizontal displacement up to this point was larger than expected, and the specimen was about to exceed the maximum stroke of the magnetostrictive transducer (± 50 mm). Therefore, the next stages of the tests were conducted without the external sensor and using only the control of the MAST. To account for the crosshead's flexibility, an analysis of the results up to this point showed that the command displacements were close to 95% of the one measured by the MAST ($d_{\text{command}} = 0.95 d_{\text{MAST}}$), so that factor was used to transfer the command displacements from the numerical model to the MAST.

Once the Python script was updated to account for the control method and the restart of the test, the specimen was slowly reloaded to the same displacement that it had at 7.230 seconds (Figure 5.8), the last recorded time step. It reached the previous displacement of 36.71 mm with a force of 2175 kN, 5% lower than the force at the stop of the test. The test was not immediately restarted after reloading the specimen, and the actuators relaxed further to a total force of 2016 kN. The total loss of force in the process was 274 kN, which corresponds to 12% of the force before the restart (See Appendix B for an alternative restart solution, which avoids reloading). The test was then successfully restarted from Point 8a (Figure 5.8).

The test was stopped once more at late night and resumed the next day into Stage 3. It was paused at 12.230 seconds of the hybrid simulation, when the specimen had zero force to avoid unloading and a future reloading to restart the test.

Table 5.1: Difference between the hybrid simulation displacements (HS) and actual displacements measured with an NDI Led Target at the top of the wall panel. The points refer the enumeration of Figure 5.7.

	Top Displacement [mm]		Drift Ratio [%]			
Point	HS [mm]	NDI [mm]	HS [%]	NDI [%]	Error [%]	Comments
1	2.23	2.23	0.09	0.09	-0.34	
2	8.33	8.39	0.33	0.33	-0.74	
3	17.10	17.11	0.67	0.67	-0.06	
4	14.53	14.49	0.57	0.57	0.25	
5	-19.68	-19.60	-0.77	-0.77	0.40	
6	19.72	19.69	0.773	0.77	0.14	
7	-43.32	-43.09	-1.74	-1.69	0.52	
8	36.71	37.15	1.44	1.46	-1.17	Stop
8a	36.71	37.15	1.44	1.46	-1.17	Restart
9	52.09	52.49	2.16	2.06	-0.77	
10	60.97	61.92	2.391	2.43	-1.53	
11	77.25	79.02	3.03	3.10	-2.24	
12	-55.97	-58.30	-2.19	-2.29	-3.99	
13	27.68	27.85	1.09	1.09	-0.63	
14	-54.18	-56.69	-2.12	-2.22	-4.43	
15	-23.74	-25.45	-0.93	-1.00	-6.72	

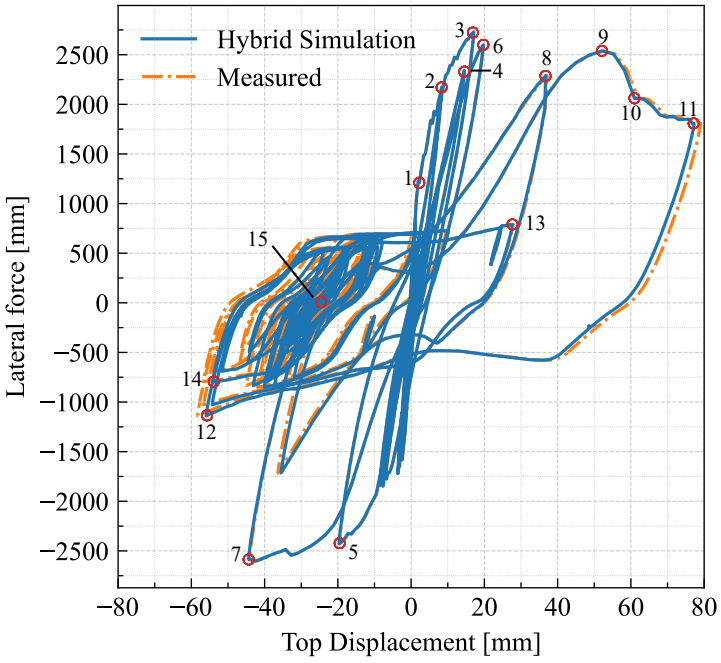

Figure 5.9: Lateral force-drift hysteresis of specimen HSW01 showing the error between the displacement commands and the actual displacements at the control point.

Close-up 2 of Figure 5.7 shows this stage of the hybrid simulation had a difference between the command-displacement (red dots) and the actual displacement at the top of the specimen, measured with the NDI Optotrak system. At points 9 and 10 there is good agreement, but Point 11 has a difference of 2.24% between the real displacement of the specimen against the commanded displacement. Table 5.1 shows the command displacements and drift ratios of the hybrid simulation, the displacements and drift ratios measured with the NDI Optotrak system, and the error between the commands and actual measurements at the selected points of Figure 5.7.

To keep the consistency of the results with the hybrid simulation tests, the displacements reported in Section 5.6, which describes the behavior of specimen HSW01 in the hybrid simulation, are given in terms of the command displacements, reported as HS in Table 5.1. This table serves as a reference to know the degree of error in the reported displacements. Most of the damage of specimen HSW01 occurred until Point 9, where the error is negligible. To graphically represent the differences reported, Figure 5.9 shows a comparison between the lateral force-drift hysteresis

5.5.2 Specimen HSW02

A total of three hybrid simulations were conducted with specimen HSW02. The 1995 JMA Kobe ground motion was scaled by 1.75 during the first hybrid simulation and in the second it was scaled by a factor of 2.0. The specimen failed only during the third hybrid simulation when the 1995 Kobe JMA ground motion record was scaled by 2.75. The first two simulations were run until the end of the seismic record. At the end of these tests, the specimen had zero residual force but it had residual displacements and thus, the second and third simulation started from the residual displacement of the respective previous test. The first two tests were run on the same day, and the third test was conducted on the following day.

Figure 5.10 shows the previously discussed displacements measured and calculated in the hybrid simulation test of specimen HSW02 under the 1995 Kobe JMA ground motion scaled by 2.0 (Figure 5.10 (b)). There is an additional displacement measured by an infra-red led target of an NDI system, d_{NDI}, to validate the measurements of the external sensor. The selected zone analyzed in Figure 5.10 (b) corresponds to the gray area in Figure 5.10 (a). At the peak shown in Figure 5.10 (b), the command displacement was 20.1067 mm, the reading of the external sensor was 20.1064 mm and the NDI-led target displacement was 20.104 mm. The error is negligible compared to the absolute displacement involved. Thus, the overall accuracy of the X-displacement control using the external high-precision sensor is validated. Upon load reversal, the measurement of the NDI-led target diverges, but by negligibly small values, indicating the error incurred during load reversals is also small. Note that the displacement of the ETH MAST controller always overestimates the real displacement of the control point because the applied flexibility compensation scheme did not totally eliminate the flexibility of the cross-head.

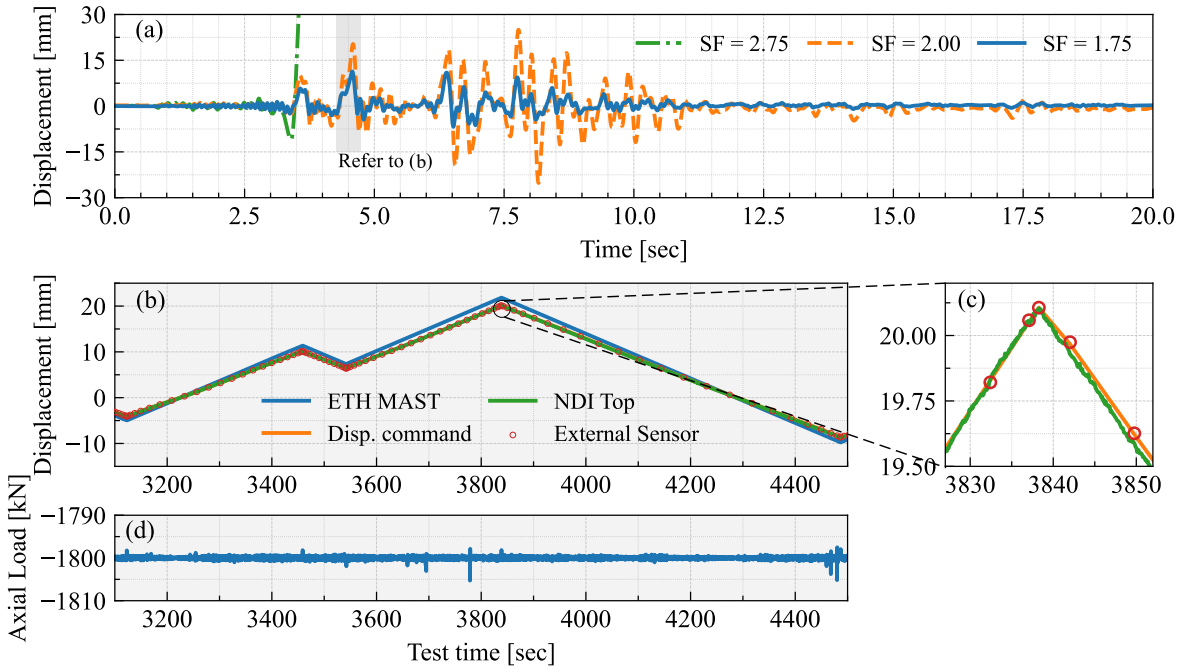

Figure 5.10: Results of the hybrid simulation of specimen HSW02. (a) Displacement history of the hybrid simulation (b) Commands sent to the ETH MAST and read by the external sensor and the NDI System of the simulation with the ground motion scaled by 2.0 (c) A zoom to the peak of (b) (d) Axial load measured during the simulation

5.6 Behavior of specimen HSW01

Figure 5.11 shows various aspects of the response of the hybrid model with Specimen HSW01 to the 1995 Kobe JMA ground motion record scaled by a factor of 1.75. A total of 15 important points in the response time history, listed in Table 5.2, are selected to describe the details of the observed response.

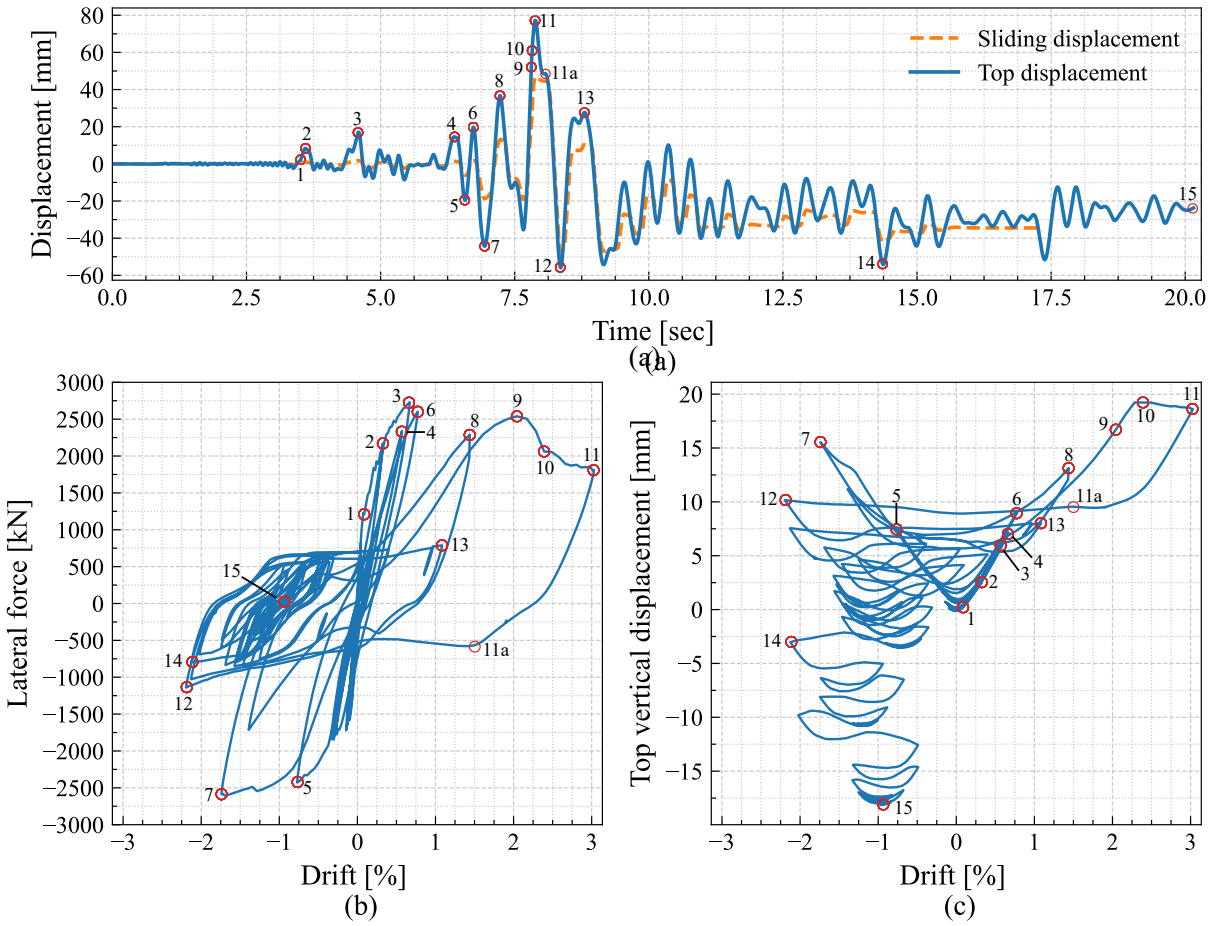

Figure 5.11: Responses of the hybrid model with specimen HSW01 to the 1995 Kobe JMA ground motion record scaled by 1.75: (a) displacement time-history; (b) horizontal force-drift ratio hysteresis curve; (c) vertical displacement vs. horizontal drift ratio curve. The sensor that measured the sliding displacements stopped working due to excessive concrete spalling of the specimen cold construction joint at the 17th second of the HS.

Specimen HSW01 remained uncracked and behaved in the essentially linear flexure and shear behavior mode until it reached Point 1, where the first diagonal crack appeared. The specimen remained in flexure and diagonal shear behavior mode and cracked further up to Point 2, where it reached 80% of its peak strength. At Point 3, the wall attained the peak lateral force of 2729 kN at a drift ratio of 0.67%, but the crack pattern in this positive displacement direction was not fully stabilized (Figure 5.12). The main shear cracks at this point reached a width of 0.93 mm (Figure 5.13), but the largest crack formed in flexure at the height of approximately 1500 mm where the vertical reinforcement originating in the top beam ends. Apart from the cracks, there was no additional damage to the wall.

Table 5.2: Important points in the response time history of the hybrid model with Specimen HSW01.

Point	Time [sec]	Δ [%]	Force [kN]	$\frac{M_{bot}}{VL_w}$	$\frac{h_{eff}}{H_w}$
1	3.510	0.09	1210	0.307	0.365
2	3.600	0.33	2171	0.385	0.456
3	4.590	0.67	2729	0.402	0.476
4	6.370	0.57	2329	0.397	0.471
5	6.575	-0.77	-2428	0.310	0.362
6	6.730	0.77	2600	0.376	0.445
7	6.920	-1.74	-2587	0.302	0.353
8	7.230	1.44	2290	0.318	0.377
9	7.810	2.16	2539	0.341	0.405
10	7.825	2.39	2061	0.254	0.302
11	7.885	3.03	1808	0.209	0.249
12	8.355	-2.19	-1140	0.217	0.253
13	8.805	1.09	789	0.183	0.221
14	14.370	-2.12	795	0.136	0.160
15	20.155	-0.93	28	-	-

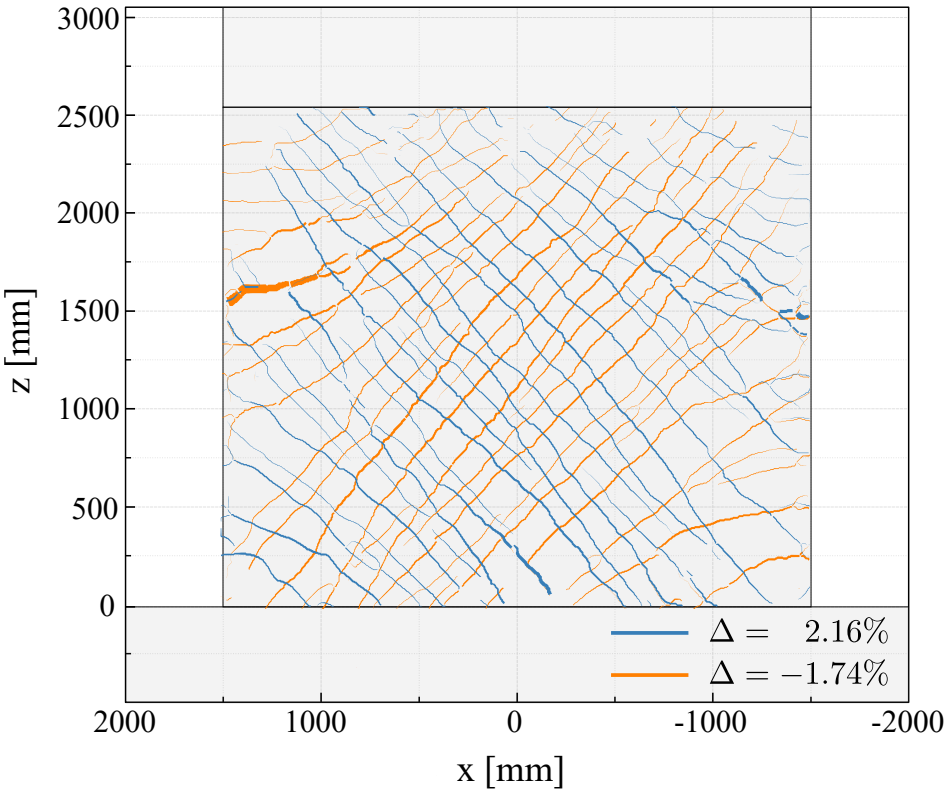

Figure 5.12: Specimen HSW01 crack pattern

The specimen attained considerable displacement levels at Point 4, with a 0.57% drift ratio and 2329 kN of lateral load. At load reversal, the specimen had considerable sliding displacements in the route to Point 5, where sliding contributed 26% to the total specimen displacement (Figure 5.14). This point was

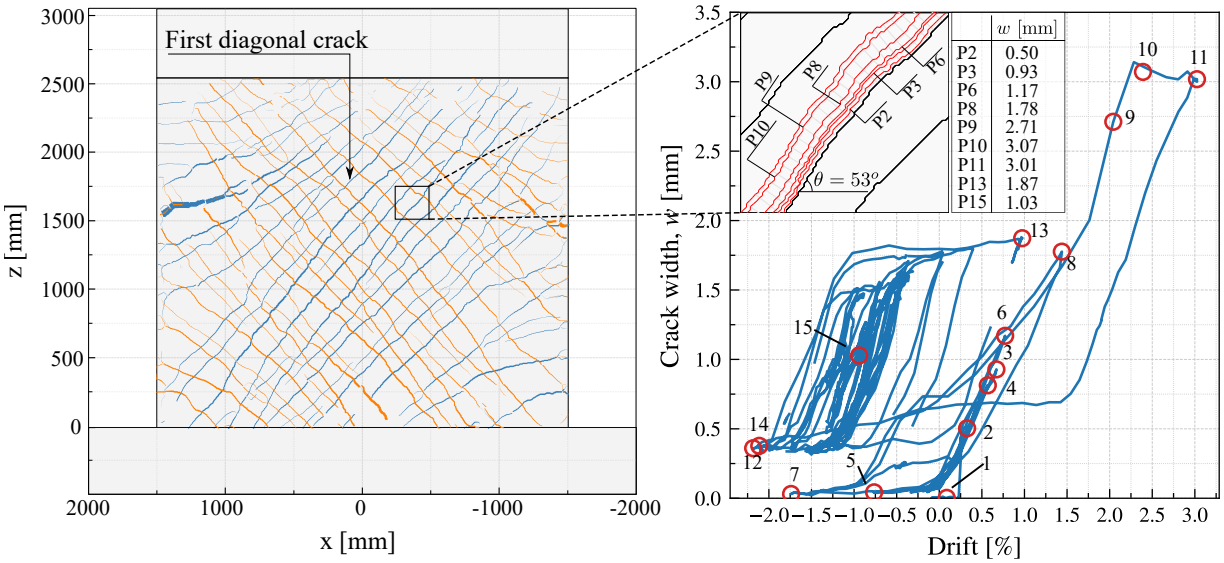

Figure 5.13: Specimen HSW01 crack pattern (a), with blue and red cracks developed in the positive and negative displacement directions, respectively. The crack opening response history (b) show the kinematics of the crack in a small region of the wall panel.

when specimen HSW01 started to change its behavior from diagonal shear to sliding shear. Pinching of the hysteresis loop associated with peak Point 6, compared to the absence of pinching in the Point 3 hysteresis loop, further indicates that the mode of specimen behavior changed. Sliding displacements occur mainly at a constant force level in a sliding plateau (see Specimen SW01 in Section 4.2), which in this specimen is evident in the hysteresis loop branch from Point 6 to Point 7 (Figure 5.11 (a)).

At Point 7, the specimen reached a -1.74 % drift ratio, the largest absolute displacement up to that time, with a significant sliding contribution of 38% (Figure 5.14) and fully developed its crack pattern in the negative direction (5.12). Then, en route to Point 8, the concrete at the cold joint mildly spalled due to sliding deformations. From this point on, concrete spalling was observed in the cold joint during each sliding excursion. The 16 mm corner reinforcing bars (Figure 5.15 (a)) buckled at the height where it was spliced, which caused a piece of concrete at that height to spall.

At Point 8, the hybrid simulation was stopped due to a problem with the ETH MAST controller but was successfully restarted following the guidelines of Terzic and Stojadinovic [105], as previously. Up to this point, the specimen reached a maximum displacement of -44.36 mm at Point 7, close to the maximum stroke of the external displacement sensor. Therefore, the external sensor was removed and the test was now controlled using the ETH MAST control point displacement. When the specimen was brought to the displacement of Point 8, it lost 274 kN in resistance due to relaxation, which explains the vertical drop in the force-drift ratio response curve. Once the hybrid simulation was restarted, the specimen displaced in the negative direction until a -1.14% drift ratio before going up to Point 9 in the positive direction. The sliding plateaus became quite long during the reversals between Points 7, 8 and 9, indicating an increasing contribution of sliding to the total specimen displacement (Figure 5.14 (a) and (b)).

The hysteresis loop associated with Points 9, 10 and 11 was the first loop during which Specimen HSW01 experienced a decrease in strength while being loaded in the same direction, with a decrease from 2505 kN to 2061 kN from points 9 to 10. Figure 5.14 (b) shows that the shear deformations between

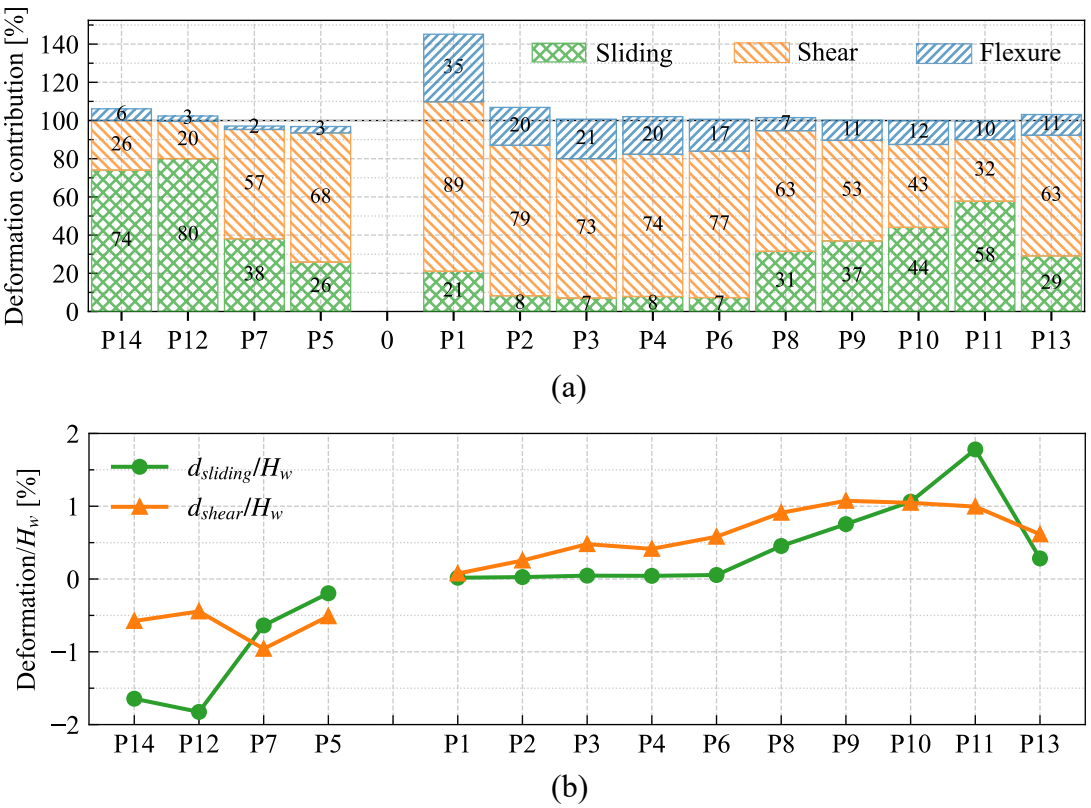

Figure 5.14: (a) Deformation contribution at points of Table 5.2. The numbers in the bar plot indicate the percentage that each deformation mode contributes. (b) Normalized sliding and shear deformation contributions at the selected points

points 9 and 11 did not increase, whereas the sliding deformations did. This event was associated with establishing a stable shear-resisting mechanism in the wall panel, capable of resisting the shear friction force at the cold joint of the wall.

After Point 10, the specimen behavior was controlled by sliding along the cold joint. The specimen reached the maximum lateral drift ratio, 3.03 %, at Point 11, with sliding contributing about 60% of the total displacement, while shear deformation and minor flexure deformation of the wall panel contributed the remainder. Right after the load reversal and on the route to Point 12, the specimen did not slide back immediately, which can be seen as in the sliding displacement time-history plot between Points 11 and 11a (Figure 5.11 (a)), but deformed in shear and bending. Once it reached the load level that triggered sliding on the cold joint in the negative displacement direction, at Point 11a, the wall slid again. That behavior can also be observed in the subsequent hysteresis loops, indicating that a shift of the behavior mode from shear to sliding was completed.

The subsequent hysteresis loops are shifted every time the system slides and have a trapezoid shape associated with the response of friction-dominated systems, as evident by Points 12 and 13. The peak forces attained in these loops indicate an equivalent sliding friction coefficient of 0.83. Points 12 and 14 have more sliding contributions and displacements than Point 13 (Figure 5.14 (a) and (b)) because the center of the deformation of the wall shifted: Points 12 and 14 are further away from 0% drift ratio because the have more sliding deformations, and Point 13 represents a re-centering of the specimen with less sliding deformations in relation to its initial position. Towards the end of the hybrid simulation, the height of specimen HSW01 started to decrease because of the excessive damage at the cold joint

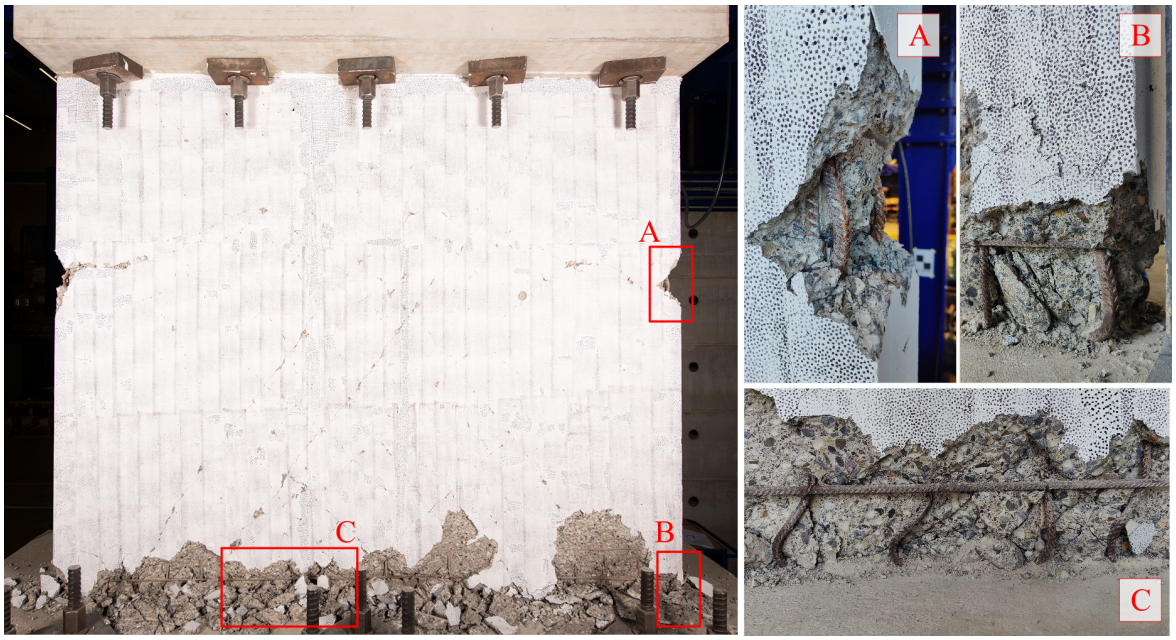

Figure 5.15: Final state of Specimen HSW01: (a) DIC side of the specimen; (b) Detailed view of areas A (end of vertical reinforcement bars originating in the top beam), B (bottom corner), and C (sliding zone at the wall-foundation cold joint).

due to sliding (Figure 5.11 (c)). At the end of the simulation, the wall shortened 18.1 mm from its initial configuration. Notably, specimen HSW01 was able to hold its axial load throughout the hybrid simulation and remained stable.

Figure 5.12 (b) shows the crack width-drift response of the widest diagonal shear crack of specimen HSW01 with the points of Table 5.2. Until Point 8, the crack width follows a diagonal shear-controlled curve. The largest crack width is 3.07 mm at Point 10 and did increase in Point 11, which suggests that the specimen lost the capacity to engage in diagonal shear strength, consistent with the lateral force-drift hysteresis. Furthermore, in the sliding shear-controlled zone of the response, the crack width is upper and lower limited by 1.87 mm and 0.38 mm. This shows that the sliding shear-controlled behavior of the specimen limited the diagonal shear deformations of the specimen that could have engaged in extra diagonal shear resistance.

Figure 5.15 shows the state of the specimen at the end of the hybrid simulation. The damage is characterized by heavy concrete spalling in the cold joint and numerous residual cracks in the wall panel. The distributed vertical shear reinforcement and the vertical corner bars were deformed and buckled, associated to the shortening of the specimen, but did not fracture. The specimen ended up with a residual top displacement of 23.74 mm, which corresponds to a 0.93% drift ratio. The residual width in the main diagonal crack was 1 mm (Point 15 in Figure 5.13).

5.7 Behavior of specimen HSW02

Fig. 5.16 shows the time history of the first hybrid simulation (scale factor 1.75) with the applied ground motion record and the specimen lateral force-drift and vertical-lateral drift response graphs. The lateral force-drift hysteresis loops are typical for the shear behavior mode, characterized by high strength and stiffness.

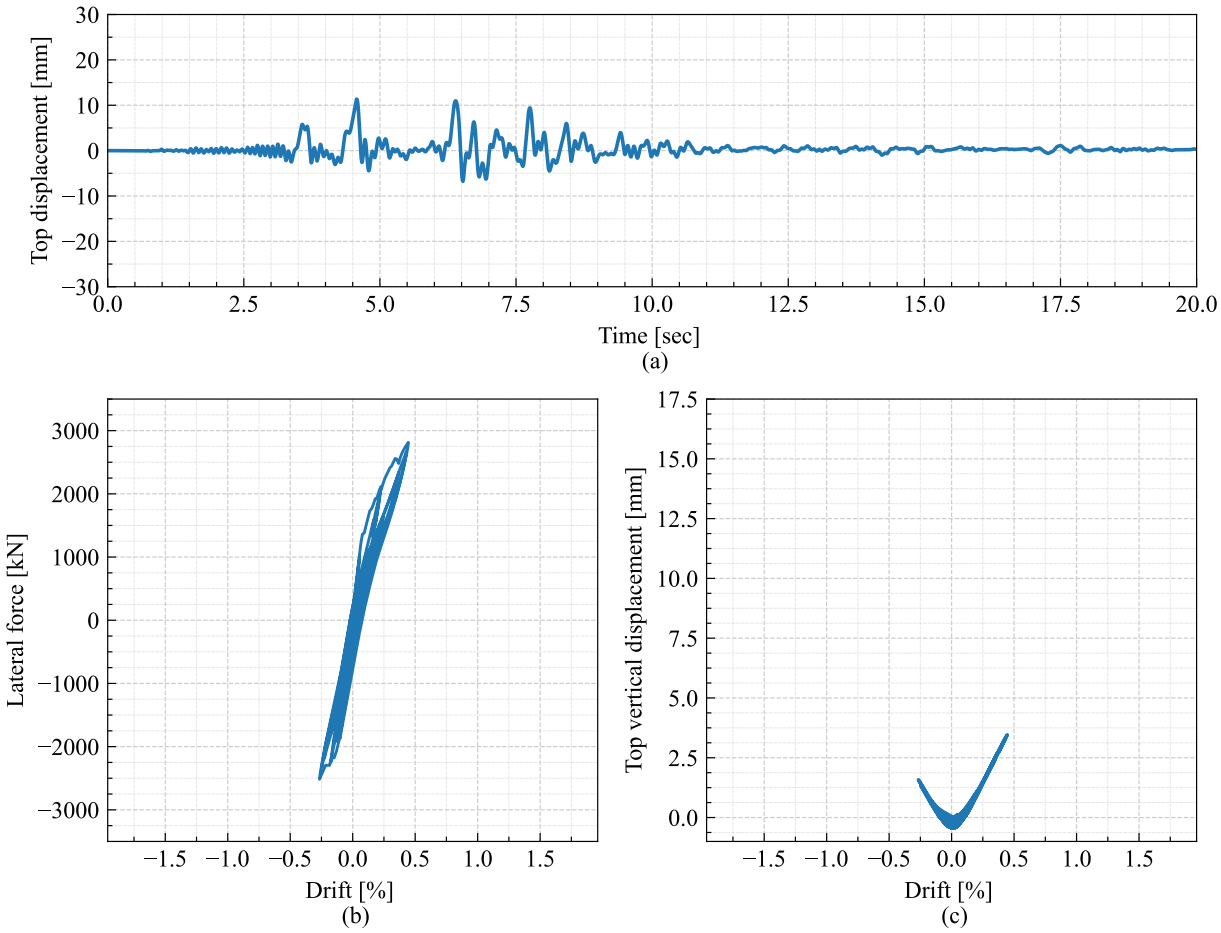

Figure 5.16: Responses of the hybrid model with specimen HSW02 to the 1995 Kobe JMA ground motion record scaled by 1.75: (a) displacement time-history; (b) horizontal force-drift ratio hysteresis curve; (c) vertical displacement vs. horizontal drift ratio curve.

In the first simulation, the specimen remained uncracked and essentially elastic until a 0.08% drift ratio and a lateral force of 1362 kN, when the first diagonal shear cracked formed. The peak strength during this hybrid simulation was 2814 kN at 0.45% drift ratio. The crack pattern at this peak response point, represented in Figure 5.17, was not yet fully developed, and the cracks reached a maximum width of 0.78 mm (Figure 5.17). In the negative direction, specimen HSW02 displaced to a 0.27% drift ratio and attained a peak load of 2516 kN. The specimen held the applied axial load throughout this hybrid simulation without problems while it moved up during the lateral displacement excursions consistent with the kinematics of the appearing shear cracks, as shown in (Figure 5.17). The response of specimen HSW02 during the first hybrid simulation was dominated by diagonal shear deformation, which contributed approximately 70% throughout the test, and minor contributions of flexure and sliding shear deformations (Figure 5.19).

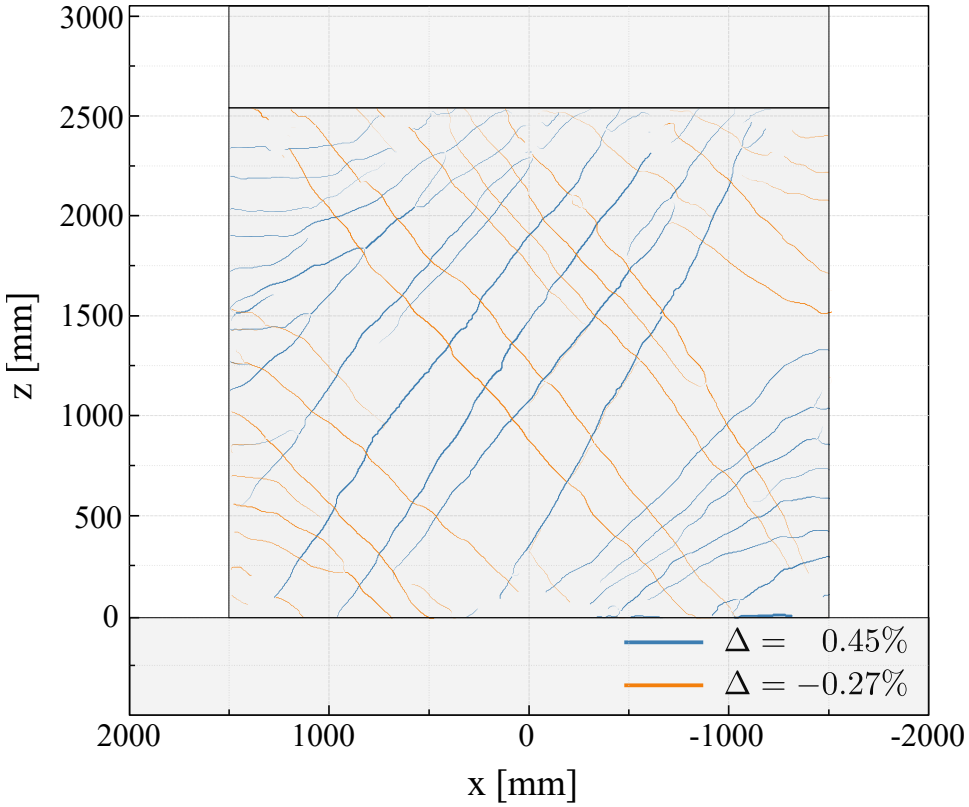

Figure 5.17: Crack pattern at peak loads of the first hybrid simulation

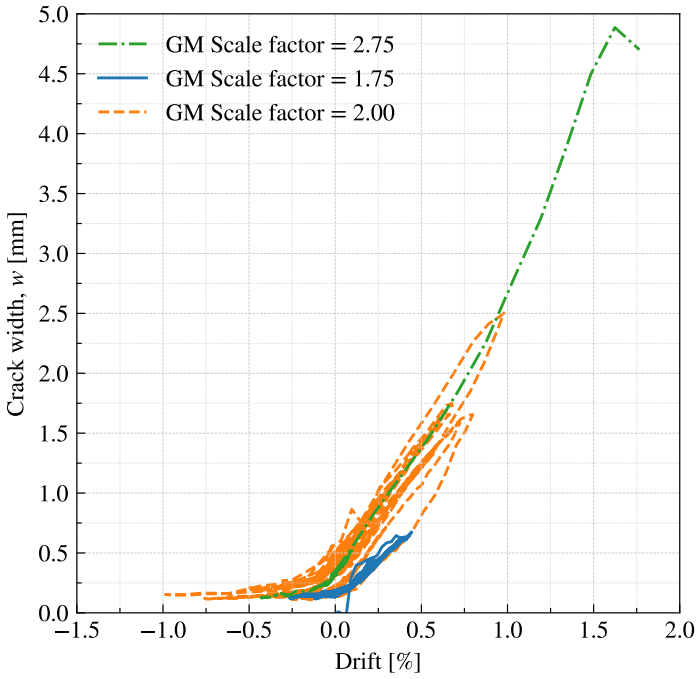

Figure 5.18: Crack width of the largest diagonal crack of specimen HSW02.

The specimen did not have considerable damage after the first simulation. There was no concrete spalling whatsoever, but the diagonal cracks could be observed with the help of a flashlight. The residual crack measured in the main diagonal crack obtained with the ACDM software was 0.134 mm, consistent with on-site measurements conducted with a crack width microscope. The top residual drift ratio was 0.01% (0.23 mm). This damage related to a peak force of 2814 kN, which was 83% of the maximum peak

strength, and a maximum drift ratio of 0.45%.

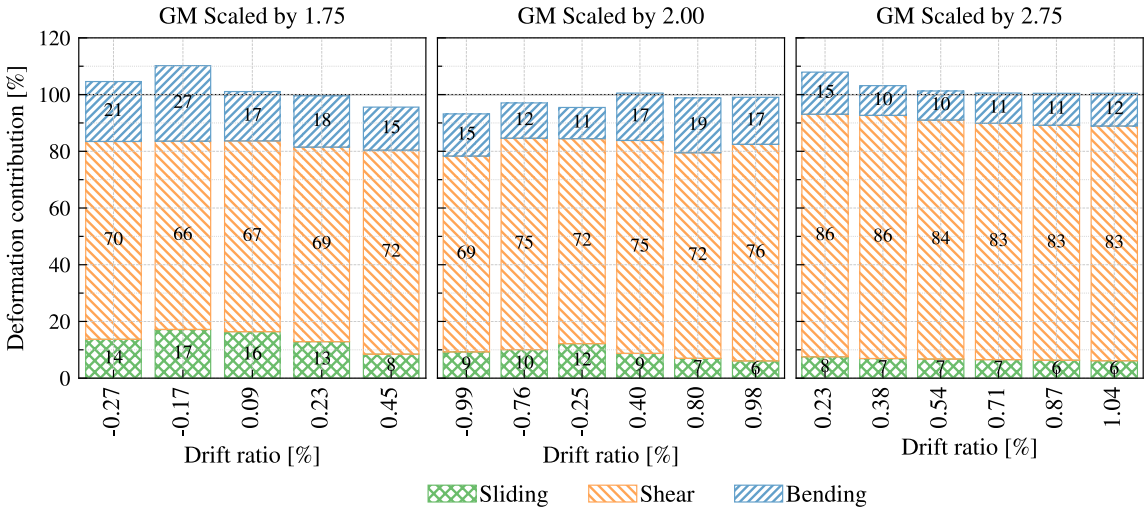

Figure 5.19: Deformation contribution of specimen HSW02 in the hybrid simulation tests

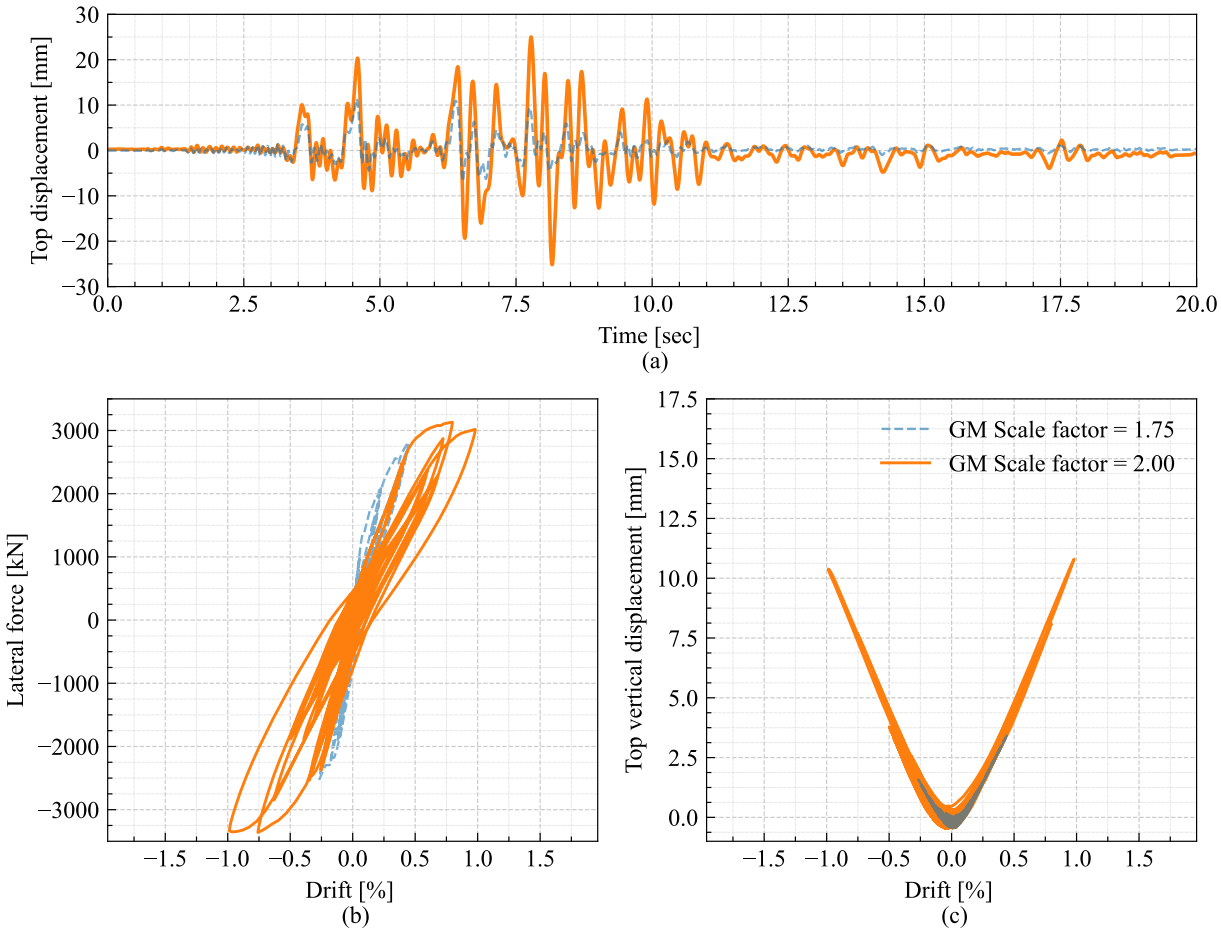

Figure 5.20: Responses of the hybrid model with specimen HSW02 to the 1995 Kobe JMA ground motion record scaled by 2.00: (a) displacement time-history; (b) horizontal force-drift ratio hysteresis curve; (c) vertical displacement vs. horizontal drift ratio curve.

The second hybrid simulation, with the 1995 Kobe JMA ground motion scaled by 2.0, started with an already cracked and slightly permanently displaced specimen HSW02. The cracked initial stiffness of the specimen was 650 kN/mm, 83% of that of the uncracked specimen. The second simulation started at

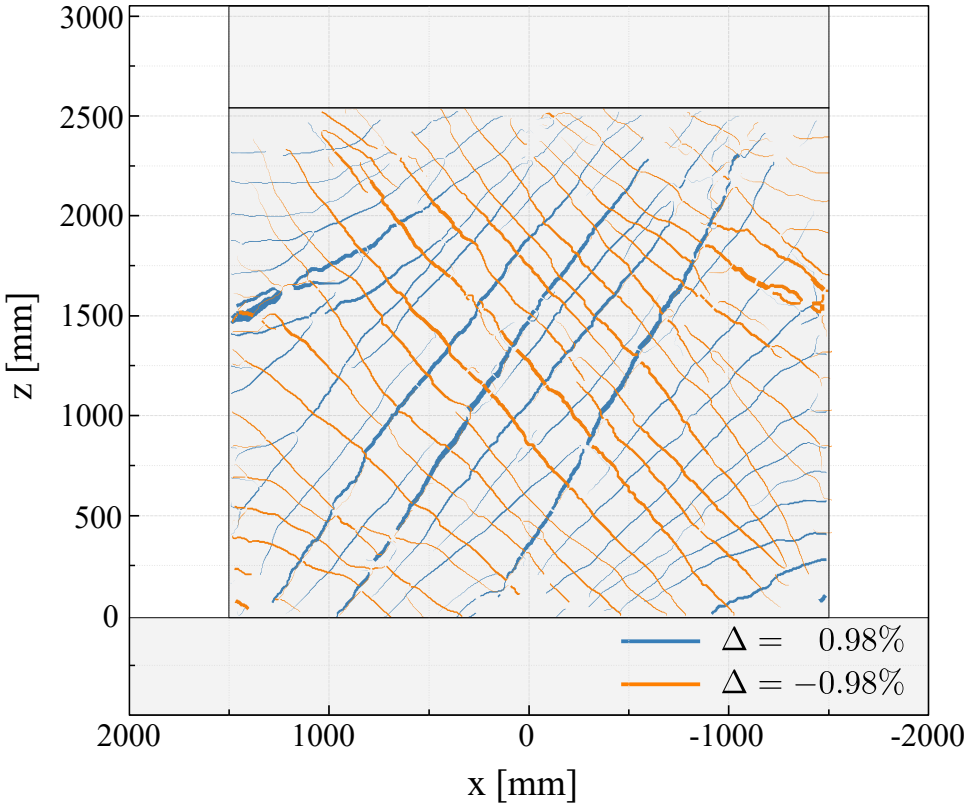

Figure 5.21: Crack pattern at peak loads of the second hybrid simulation

the residual displacement of the previous simulation and with zero lateral force. Throughout the second hybrid simulation, Specimen HSW02 remained in the shear behavior mode (Figure 5.20). The lateral force-drift hysteresis loops were somewhat wider than those recorded during the first hybrid simulation, indicating an increase in energy dissipation and, therefore, in damage. The shear crack pattern, shown in 5.21, developed fully. Notably, peak forces of 3250 kN and 3359 kN were reached at drift ratios of 0.78% and -0.78%, respectively. They were followed by excursions to maximum drift ratios of 0.94% and -0.98%, attained with smaller peak lateral forces of 3018 kN and 3350 kN, respectively. The principal diagonal crack reached a width of 1.65 mm at peak specimen strength and 2.50 mm at the peak specimen displacement in the positive direction (Figure 5.18). Notably, the crack continued to open further with an increase of 51% while the force attained at both cracks was practically the same, which indicates that the specimen developed its full strength and significant inelastic diagonal shear deformations. Meanwhile, the specimen held its axial load while moving up during lateral excursions, reflecting the motions at the shear cracks.

At the end of the second hybrid simulation, the principal diagonal crack had a residual crack width of 0.36 mm. The cracks were clearly visible. In addition, there was mild concrete spalling on some crack edges (Figure 5.23). The residual top drift ratio was 0.03% (-0.84 mm). This damage relates to a specimen that attained its maximum peak strength.

A third hybrid simulation, with the 1995 JMA Kobe ground motion scale factor of 2.75, was done to conclusively determine the failure mode of Specimen HSW02. The cracked initial stiffness of the specimen was 305 kN/mm, 39% of that of the uncracked specimen, and the simulation started at the residual displacement of the previous test. With the crack pattern stabilized and plenty of load

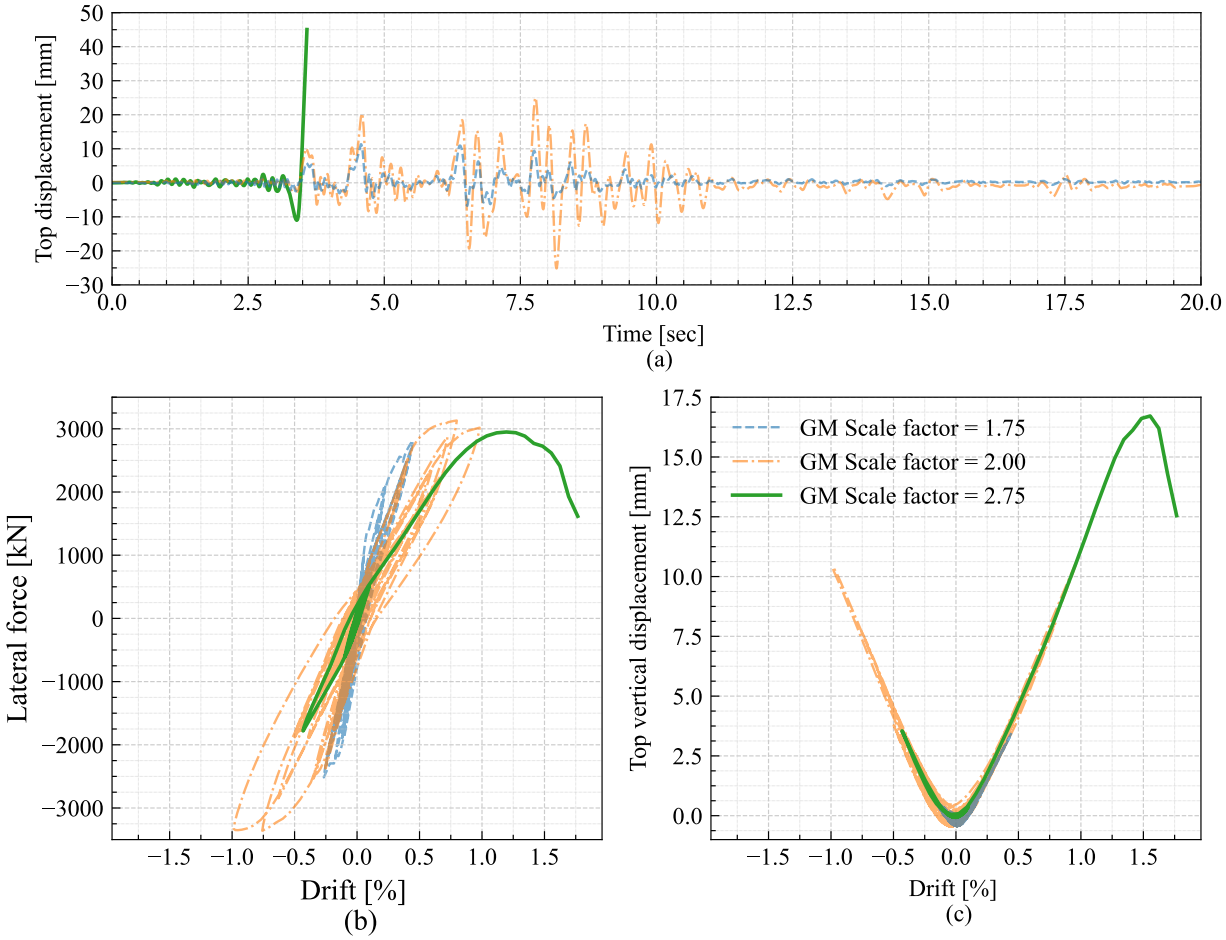

Figure 5.22: Responses of the hybrid model with specimen HSW02 to the 1995 Kobe JMA ground motion record scaled by 2.75: (a) displacement time-history; (b) horizontal force-drift ratio hysteresis curve; (c) vertical displacement vs. horizontal drift ratio curve.

cycles already applied, the specimen failed during the first significant lateral displacement excursion, approximately 3 seconds into the hybrid simulation. Thus, the lateral force-drift ratio response plot, shown in Figure 5.22, looks like a static pushover response plot. The peak lateral force was 2949 kN at 1.19% drift ratio, smaller than the previously attained peak loads.

The crack width followed the same path as during the second hybrid simulation, reaching a similar maximum width of 2.6 mm at a 1.0% drift ratio but at a lower force of 1653 kN. The crack continued to open further in the third simulation, reaching 3.29 mm width at the peak lateral force and opening up to 4.89 mm at 1.62% drift ratio when the specimen failed. Shear deformations controlled the entire test, with contributions close to 80% of the total deformation (Figure 5.19).

Shortly after Specimen HSW02 reached the peak strength in the third simulation, there was massive spalling and crushing of concrete in a relatively large region above the mid-height of the wall, clearly visible in Figure 5.23, which caused sudden drops in both the lateral and axial strengths of the wall with rapidly increasing lateral and downward motions of the ETH MAST cross-head. The failure mode of Specimen HSW02 was, therefore, shear diagonal compression. Notably, this hybrid simulation was done in mixed-mode control with the axial load controlled in force mode and the lateral displacement in displacement mode. Therefore, the observed behavior is consistent with a progressive catastrophic

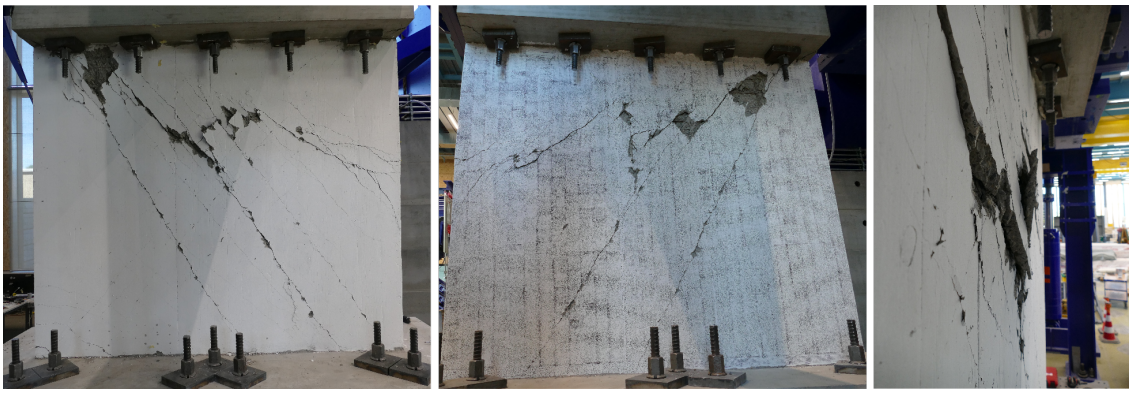

Figure 5.23: Final state of specimen HSW02 at the end of the hybrid simulation with 2.75 scale factor

failure of the specimen wall panel, characterized by simultaneous losses of its gravity and lateral load capacities. The third hybrid simulation was stopped at a 1.76% drift ratio (45 mm) to protect the ETH MAST facility.

CHAPTER 6

DISCUSSION

6.1 Effect of axial load ratio

A comparison between specimens SW01 and SW02 highlights the influence of the axial load ratio on peak strength, maximum drift, and behavior mode. Specimens SW01 and SW02 had axial load ratios of 4.41% and 10.71%, respectively, with the same transverse and longitudinal reinforcement ratio, geometry, and similar concrete strength. Both specimens attained their peak strengths in shear-controlled behavior. However, the peak strength of specimen SW02 was 24% larger than that of specimen SW01, which agrees with the known fact that a larger axial load ratio increases the peak shear strength [5]. The peak strength in specimen SW02, though, was attained at a 0.72% drift ratio, compared to 0.65% drift ratio when specimen SW01 developed its peak strength. This seems counter-intuitive until the behavior mode change is taken into account. Increasing the axial load ratio changed the failure mode of the specimens from sliding (SW01) to shear-compression concrete failure (SW02). A larger axial load ratio also triggered a catastrophic failure of specimen SW02 at 0.96% drift ratio, while specimen SW01 started to slide at 0.65% drift ratio, and continued to slide on the cold joint interface up to 1.93% drift ratio without losing its vertical load carrying capacity.

The axial load ratio affected the global response and behavior mode of the specimens tested under hybrid simulation. Specimen HSW01 had an axial load ratio of 4.02% and HSW02 had 8.00%, which corresponded to an axial load of 900 kN and 1800 kN, respectively. In the initial state, specimen HSW02 had an initial stiffness 2.5% larger than specimen HSW01, which could be considered equal in practical terms. The displacement response under the ground motion scaled by 0.3 (Figure 5.6) showed similar shear-controlled behavior in both specimens. Namely, the peaks occurred practically at the same time step with similar values, 0.91 mm for specimen HSW01 and 0.84 mm for specimen HSW02. The uncracked response of the specimens can be further compared with the crack displacements of the load-displacement curves, which was similar in displacement with 0.08% for both specimens, but with a load slightly larger in specimen HSW02 than in specimen HSW01.

Under up-scaled 1995 Kobe JMA ground motions, the peak strength of specimen HSW01 (2729 kN) was 23% lower than that of specimen HSW02 (3359 kN). This is consistent with the behavior prediction shown in Figure 3.1. The maximum strength of specimen HSW01 is associated with the start of the change of its behavior from shear of the wall panel to sliding on the wall-foundation cold construction joint. The equivalent friction coefficient at peak resistance computed using Equation 2.9 is $\mu = 1.00$. By applying the same friction coefficient to specimen HSW02, the equivalent sliding resistance is 3614 kN, larger than the peak shear strength of 3359 kN developed by its wall panel. Thus, specimen HSW02 retains it shear behavior until failure.

Once the sliding behavior was triggered, the hybrid model with specimen HSW01 behaved as a system

with a sliding base and a superstructure with shear and bending deformations. The maximum force such a system can develop depends on the friction at the cold joint. In the case of specimen HSW01, that friction force can be determined from the load-drift ratio hysteresis (Figure 5.11(b)) as the constant force of the plateau, estimated at 750 kN, corresponding to a sliding friction coefficient of about 0.8, which relates to the friction between concrete-concrete of the foundation and wall panel.

6.2 Effect of steel reinforcement

A comparison of specimens SW01 and SW03 shows the influence of the decrease in the transverse and longitudinal reinforcement ratios from 0.525% (specimen SW01) to 0.333% (specimen SW03). This was achieved by reducing the reinforcement bar diameter from ϕ10 mm (specimen SW01) to ϕ8 mm (specimen SW03). This steel reinforcement reduction did not change the behavior mode, as both specimens developed a sliding-controlled behavior, but it reduced the peak strength by 9%. The test outcomes indicate that the change of reinforcement affected the initiation of sliding, as it was triggered at a lower drift ratio in specimen SW03 (0.35%) than in specimen SW01 (0.65%). The earlier triggering of the sliding mechanism can be attributed to the smaller diameter of the vertical reinforcement bars, as both the dowel action resistance and the shear and kinking resistance are proportional to the bar diameter as the dowel action of the bars is proportional to the third power of the diameter (ϕ^3), and the kinking and shear to the second power (ϕ^2) [106]. The earlier sliding initiation of SW03 than of SW01 resulted in larger sliding displacement contributions at the same drift ratios, as shown in Figures 4.6 and 4.17.

The effect of reducing only the transverse reinforcement ratio is observed by comparing specimens SW01 and SW04. However, it is not conclusive in terms of the peak strength because of the larger nominal concrete strength of specimen SW04. Reducing the transverse reinforcement ratio changed the behavior mode from sliding to shear in diagonal tension, which resulted in a brittle failure of specimen SW04 compared to a the quasi-ductile sliding behavior of specimen SW01. While specimen SW04 reached it's peak strength at a larger drift ratio (0.76%) than specimen SW01 (0.65%), the sliding-controlled behavior allowed specimen SW01 to reach drift ratios of 1.93% without becoming unstable.

And finally, a comparison between specimens SW03 and SW04 shows the influence of increasing only the web longitudinal reinforcement. More longitudinal reinforcement increase the shear strength of specimen SW04, but this effect is masked by the increase of shear strength due to a significantly stronger concrete of specimen SW04. More longitudinal reinforcement together with an increase of the axial load (to maintain a similar ALR) prevented sliding to fully develop in Specimen SW04. Instead, it failed in diagonal tension at a smaller displacement.

The case of a specimen with a smaller longitudinal than transverse steel reinforcement ratio than longitudinal was not studied because section 18.10.4.3 of ACI 318-19 [26] requires that the longitudinal reinforcement ratio shall not be less than the transversal reinforcement ratio. With this requirement, the sliding behavior is restricted to specimens with equal transverse and longitudinal reinforcement ratios low boundary reinforcement, and walls are prone to be in the shear failure zone (Figure 3.1).

6.3 Effect of test protocol

By design of this ETH Zürich test campaign, specimens SW01 and HSW01 are nominally identical, as are specimens SW02 and HSW02. This makes it possible to directly compare the sliding and shear behavior and failure modes of the corresponding specimen pairs and identify the effect of different test protocols. The lateral force-drift hysteresis response plots for SW01-HSW01 and SW02-HSW02 specimen pairs are shown in Figure 6.1. The differences in specimen mechanical characteristics, and thus their load-deformation responses, are due to the different concrete strengths at the day of the test and the test protocols.

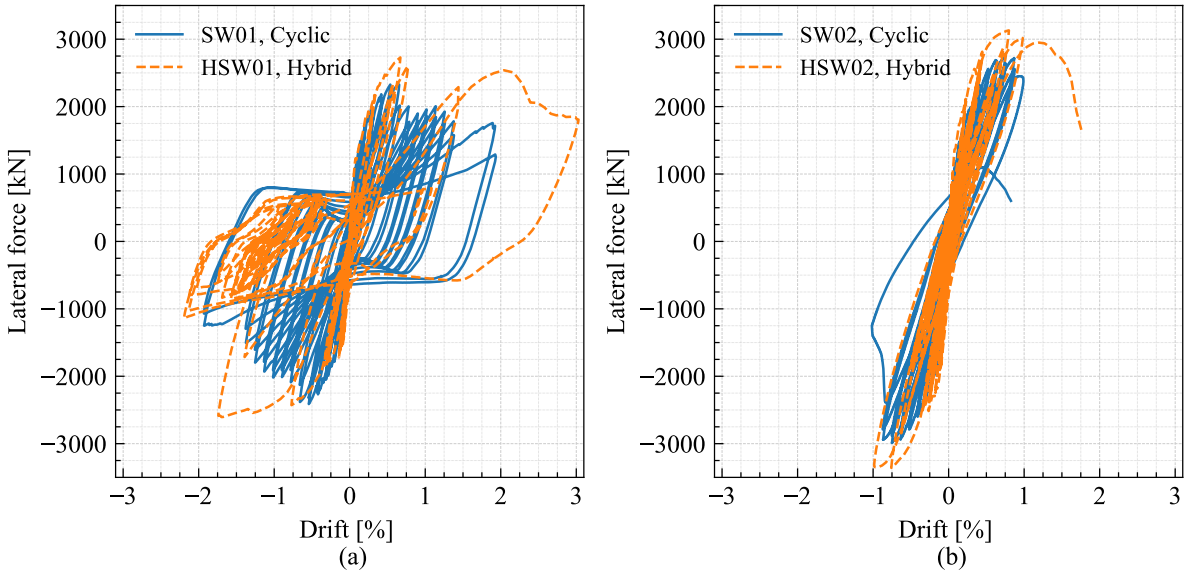

Figure 6.1: Comparison between the results of cyclic tests and hybrid simulation tests

The behavior of specimens SW01 and HSW01 was consistent (Figure 6.1 (a)) despite the very different quasi-static cyclic and hybrid simulation protocols. It was initially controlled by shear until the sliding initiation drift ratio, when the behavior mode changed to sliding on the cold joints between the wall panels and their foundations. The drift ratio of sliding initiation was 0.65% for the cyclically tested specimen SW01 and 0.77% for specimen HSW02 tested under hybrid simulation, which is a 18% difference. The considerable difference of this values agrees with the known fact that the cyclic test protocol underestimate the ultimate displacement of a wall [107], which could be in this case applied to sliding initiation.

A permanent sliding offset from the original wall centerline characterized subsequent displacement excursions of both specimens. The sliding resistance, evident in lateral load plateaus of the hysteresis loops, was approximately 700 kN, indicating that both specimens developed a similar cyclic sliding friction coefficient. The peak resistance of specimen SW01 was 12% smaller than that of specimen HSW01, consistent with the difference in their concrete strengths. Specimen SW01 could develop additional resistance in shear once its sliding motion was arrested by the compression diagonal engaging at the cold joint up to 1.93% drift ratio. Specimen HSW01 behaved similarly but experienced only one larger excursion, associated with Points 7 and 8 in Figure 6.1. Due to the numerous cycles,

specimen SW01 degraded in strength early and at large displacements only the cold joint contributed to the resistance, as shown by the plateau in the lateral force-drift response hysteresis. In contrast, the ground motion record drove specimen HSW01 and slid up to a displacement of 78 mm, which explains the difference in force levels at large drift ratios. Notably, both SW01 and HSW01 specimens carried the applied axial loads without problems.

The sliding initiation drift ratio correspond to the onset of the sliding deformations. Let's define a sliding ductility μ_{sl} as the ratio between a certain drift ratio and the sliding initiation drift ratio. The cyclically tested specimen SW01 reached a fully sliding-controlled behavior, with more than 50% of the total contribution (Figure 4.6 (a)) at 0.96% drift ratio ($\mu_{sl} = 1.48$), six fully reversed cycles after the sliding initiation drift ratio of 0.65%. On the other side, specimen HSW01 initiated sliding at 0.77%, and reached 50% of sliding contributions at 3.03% drift ratio ($\mu_{sl} = 3.94$). This means that is not possible to define a drift ratio limit which defines the moment when a wall will completely change to a sliding-controlled behavior, because it depends on the test protocol.

Specimen SW01 had shear residual strength after the sliding plateaus during the entire test, although the last two cycles of the 1.96% amplitude had considerable pinching between them. It never reached a situation similar to specimen HSW01, where its hysteresis had upper and lower limits defined by the friction coefficient between the concrete of the wall panel and foundation.

Specimens SW02 and HSW02 also behaved consistently (Figure 6.1(b)). From the outset, they behaved in shear. Specimen HSW02 was somewhat stronger and stiffer, consistent with the difference in concrete strength on the day of the tests. Interestingly, the number of load reversals imposed by the quasi-static loading on specimen SW02 is smaller than that imposed during the repeated hybrid simulations on specimen HSW02. Nevertheless, both specimens maintained a stable shear crack pattern and responded in shear until the critical shear diagonals failed in compression, leading to a sudden and potentially catastrophic loss of both lateral and axial strength. Thus, different test protocols do not seem to have influenced the outcome of the behavior or failure mode of these tests.

6.4 Energy dissipation

Sliding failure has been categorized with low energy dissipation capacities [33]. Therefore, this section analyses the tests results in terms of the energy dissipated per cycle and equivalent damping of the specimens tested under cyclic loading protocol. The energy dissipated per cycle, E_d, was calculated as the area inside the lateral force-displacement curve. This area is then normalized by the energy stored by an equivalent linear spring, E_s^+ and E_s^-. Figure 6.2 graphically represents the energy dissipated per cycle. The equivalent viscous damping ratio of each cycle can be calculated with Equation 6.1.

$$\xi_{eq} = \frac{E_d}{2\pi(|E_s^+| + |E_s^-|)} \tag{6.1}$$

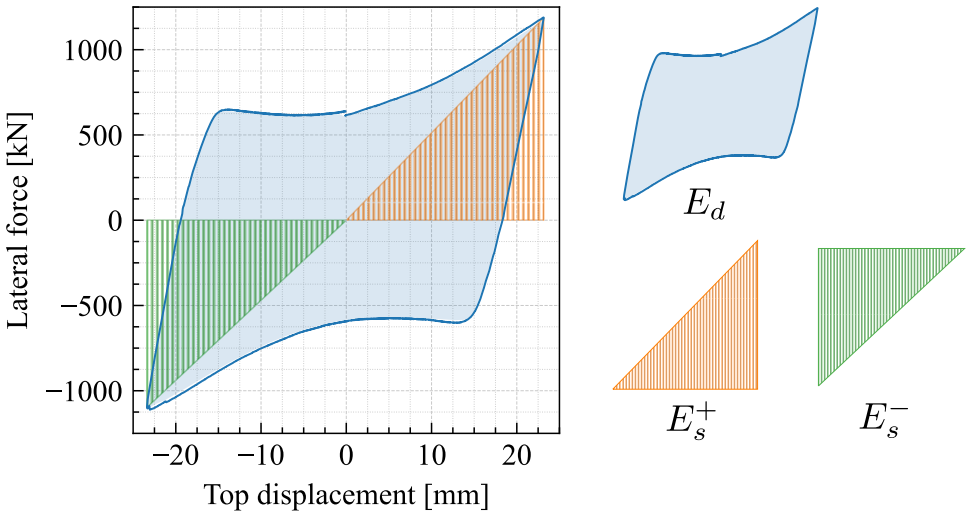

Figure 6.2: Areas representing the total energy dissipated per cycle E_d and the energy stored by an equivalent linear spring E_s^+ and E_s^-.

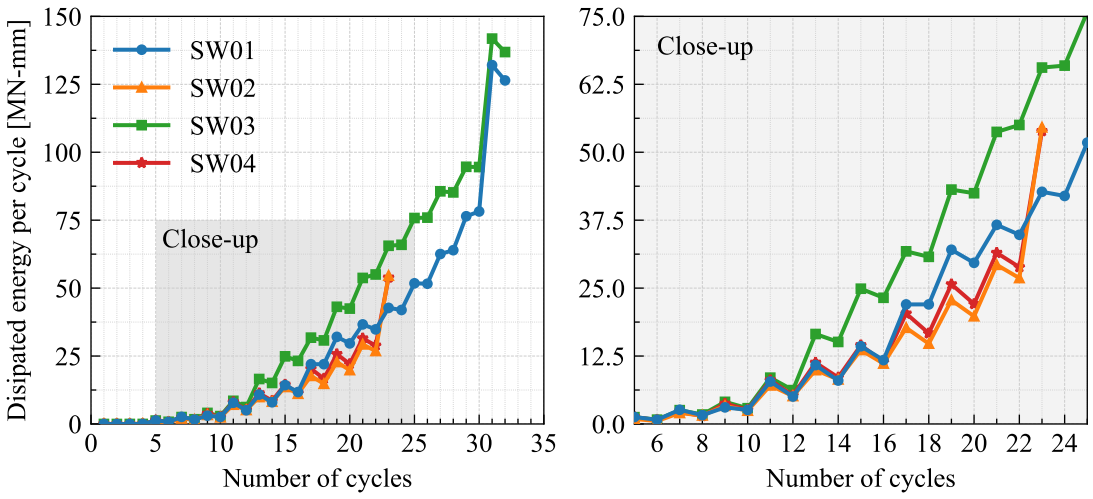

Figure 6.3: Energy dissipated per cycle of the specimens tested under cyclic testing.

Figure 6.3 shows the energy dissipated per cycle in the cyclically tested specimens. In a set of cycles of the same amplitude, the first cycles dissipates more energy than the second, which is expected because the

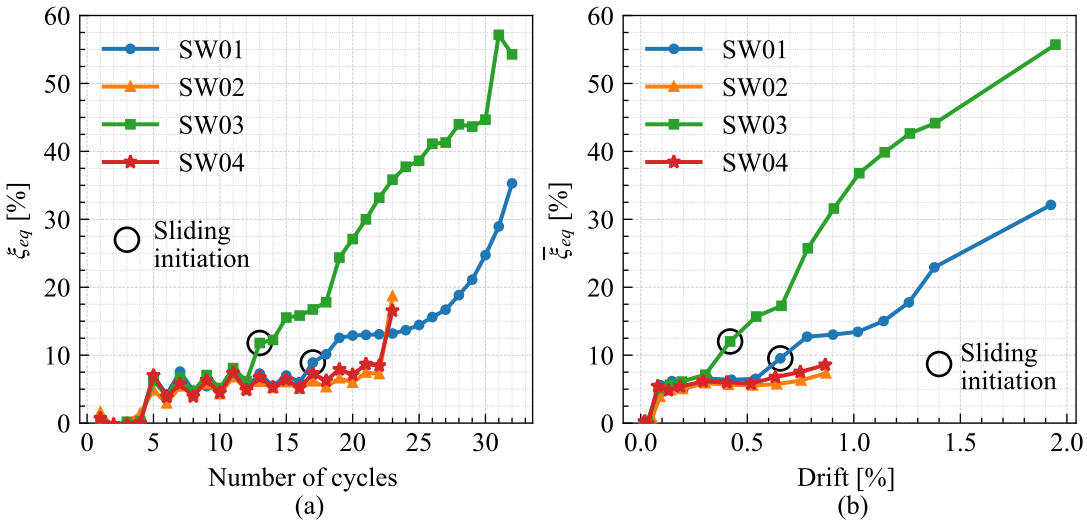

Figure 6.4: (a) Equivalent viscous damping per cycle of the specimens tested under cyclic testing. (b) Average equivalent viscous damping of the specimens, calculated as the average between the equivalent viscous damping obtained for the cycles of the same drift ratio amplitude.

first cycle generates cracks in the specimen and degrades the sliding crack interface, whereas the second cycle deforms an already a damaged specimen. This is clearly seen in the lateral force-drift hysteresis response plots, where the second cycle hysteresis always encloses a smaller area. The amount of energy dissipated increases with increasing displacements, as the damage increases and causes an increase in the area of each subsequent force-deformation hysteresis. Up to the 12th cycle, about ≈0.42%, all specimens dissipated a similar amount of energy. However, specimens SW01 and SW03 started to dissipate more energy than specimens SW02 and SW04 in cycles at drift ratios large than about 0.5% due to the initiation of sliding. Specifically, specimen SW03 began to dissipate more energy in 0.42% drift cycles, while specimen SW01 did so during the 0.65% drift cycles., but after that the point the amounts are larger in specimen SW03 because it started to change its behavior to sliding. The same effects happens in specimen SW01, but at 0.65% drift ratio.

Figure 6.4 (a) shows the equivalent viscous damping per cycle of the four specimens. In the shear-controlled behavior cycles in all four cyclic tests, the first cycle has a larger equivalent damping than the second, despite the different applied axial load ratio and reinforcement ratios. In the sliding-controlled behavior cycles of specimens SW01 and SW03, the second cycle has a larger equivalent viscous damping ratio than the first one: even though the energy dissipated is less in the second cycle than in the first one (Figure 6.3), the lower peak strength of the second cycle decreases the value of the equivalent viscous damping.

The average equivalent viscous damping ratio $\overline{\xi}_{eq}$ of specimens SW02 and SW04 is similar an oscillates between 5% and 6% from 0.14% to 0.63% drift ratio cycles. Specimens SW01 and SW03 had similar $\overline{\xi}_{eq}$ when they had a shear-controlled behavior, but when sliding triggered, there was a jump in the viscous damping ratio value. Specimen SW01 had an increase of 46% in $\overline{\xi}_{eq}$ from 0.54% to 0.65% drift ratio cycles, whereas SW03 had a 69% increase from 0.30% to 0.42% drift ratio test cycles. Then, the equivalent damping increased, attaining values of up to 30% in SW01 and 55% in SW03 in their last cycles. This results suggest that the equivalent viscous damping ratio might be a good indicator to

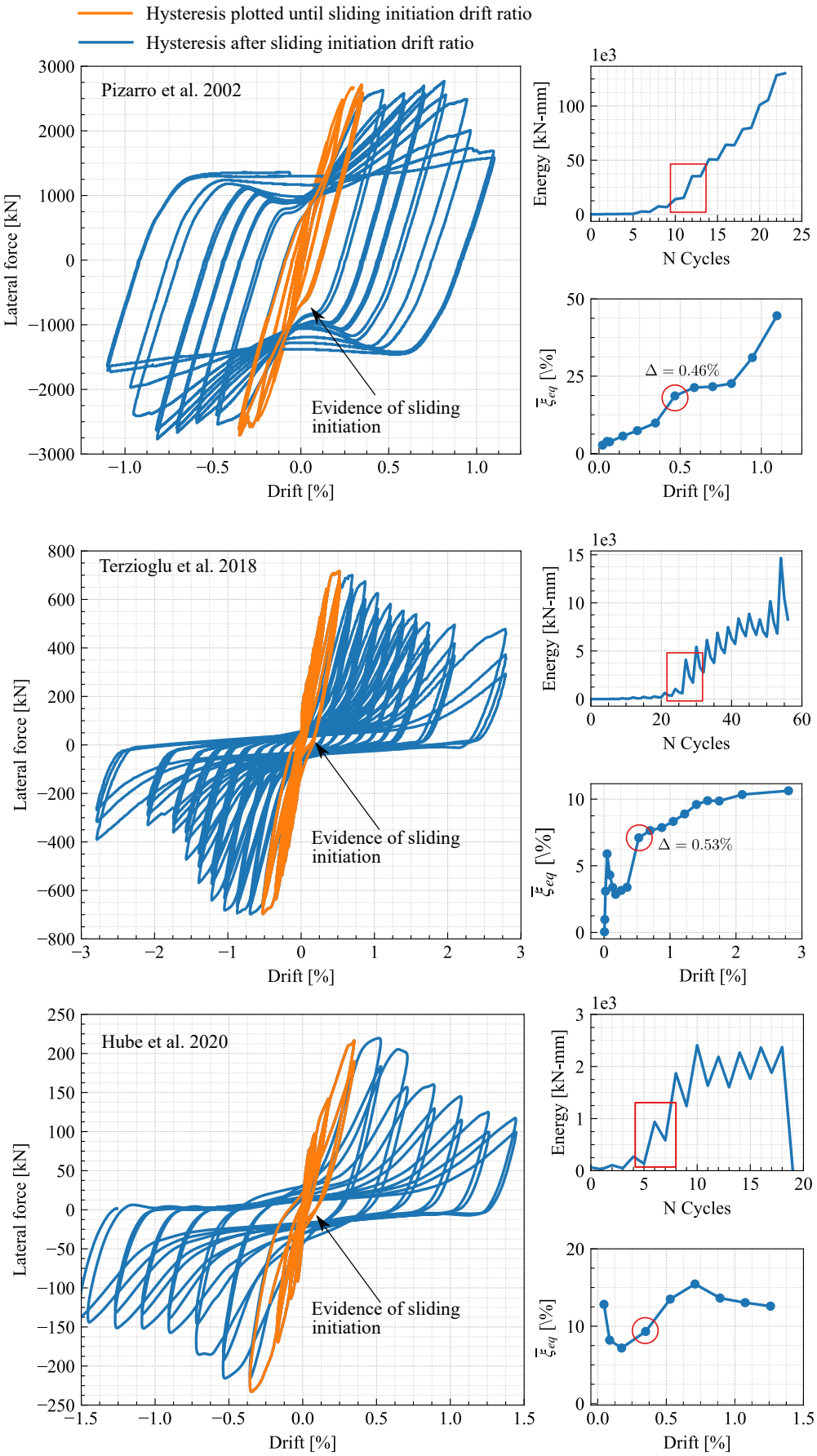

Figure 6.5: Lateral force-drift response hysteresis, energy dissipated per cycle, and average equivalent viscous damping of three specimens from other experimental campaigns.

identify the sliding initiation drift ratio.

To investigate if other specimens follow a similar trend in $\overline{\xi}_{eq}$ as specimens SW01 and SW03, three specimens with sliding-controlled behavior were selected. Figure 6.5 shows the lateral resistance-drift hysteresis, energy dissipated and average equivalent viscous damping of three shear walls, all of which had a sliding failure. The first specimen, from Pizarro et al [108], had an increase in the energy dissipated from the 11th to the 12th cycle, with $\overline{\xi}_{eq}$ increasing by 90% at 0.46% drift ratio. The specimen from Terzioglu et al. [42] had a jump in energy dissipated from the 24th to 25th cycle, and an increase of 110% in $\overline{\xi}_{eq}$ at 0.53% drift ratio. Finally, the specimen from Hube et al [43] had an increase in $\overline{\xi}_{eq}$ of 30% at 0.35%. The lateral force-drift hysteresis of the specimens show that upon load reversal from the drift ratios previously mentioned, there is evidence of sliding initiation as a mild softening of the specimen as it goes through zero drift ratio.

The sliding initiation of a specimen can be then identified in two steps, if the data of the lateral force-drift hysteresis is available. First, it has to be observed that final state of the specimen was dominated by a sliding-controlled behavior. Then, the average equivalent viscous damping has to be calculated for each drift ratio amplitude. The sliding initiation drift ratio can be identified as the one with an increase of more than 25% in $\overline{\xi}_{eq}$. The results would have to be further confirmed with the hysteresis loop.

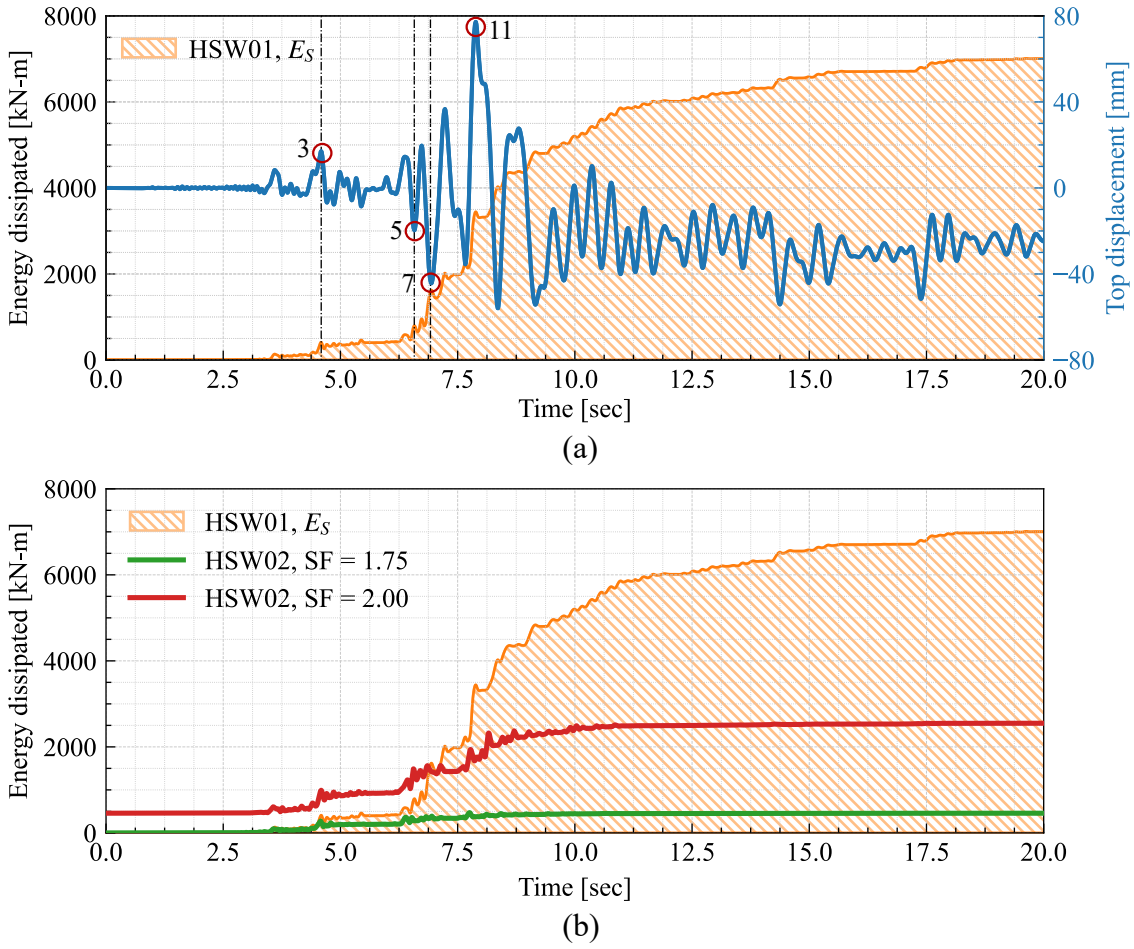

Figure 6.6: (a) Strain energy of specimen HSW01 (b) Comparison between strain energy dissipated by HSW01 and HSW02.

Although a similar equivalent viscous damping ratio analysis is not possible with the hybrid simulation

results, the energy balance, introduced in Chapter 5, can give insights in the relation between the sliding failure and energy dissipation. Figure 6.6 (a) shows the strain energy dissipated by the system with specimen HSW01 as the physical part, with its displacement response history overlapped. The first relevant increase in the strain energy is at the maximum peak-strength of at point 3 (Figure 5.11). Between points 5 and 7, the energy dissipated doubled (100% increase). Point 7 was previously identified as sliding initiation, which matches with the increase in energy. There is no relevant parameter in the hybrid simulation that could serve as a base to define the sliding failure, but by considering the sliding displacements measured during the test and the energy dissipated by the experimental specimen, the sliding initiation point can be identified. Figure 6.6 (b) compares the strain energy dissipated by HSW01 and HSW02. Even though the systems had different viscous damping ratio ξ in their respectives, the plot illustrates that the sliding-controlled behaved system dissipated more energy than the shear-controlled.

6.5 Peak shear estimation

6.5.1 Peak strength estimated with code provisions and proposed formulas

This section presents the shear strength of the six specimens calculated using different sets of equations: shear equation of Chapter 18 of ACI 318-19 (Equation 2.8), friction strength of Chapter 22 of ACI 318-19 with with two values of the friction coefficient, namely $\mu = 0.6$ and $\mu = 0.8$, and the equations proposed by Rojas-Leon et al (Equation 2.27), Moretti et al (Equation 2.20), and Gulec and Whittaker (Equation 2.19). Table 6.1 summarizes the results, and Figure 6.7 graphically represents them as a normalized strength with respect to the one obtained in the tests.

Table 6.1: Peak shear strength. Units in kN.

	Test	ACI 318-19	Rojas León et al	Moretti et al	Gulec	Sliding ACI 318-19 (Eq. 2.9)	
		Eq. 2.8	Eq. 2.27	Eq. 2.20	Eq. 2.19	$\mu = 0.8$	$\mu = 0.6$
SW01	2413	2237	2561	1771	1368	2524	1678
SW02	2990	2957	2722	1875	1717	2442	2218
SW03	2194	1812	2294	1507	1216	1950	1359
SW04	2830	2477	2754	1907	1440	2207	1858
HSW01	2729	2237	2657	1813	1386	2557	1678
HSW02	3359	2957	3027	2023	1781	2560	2218

The prediction with the ACI 318-19 provisions showed to be overall conservative but within a reasonable range. The closest prediction were for specimens SW01 and HSW01, which are similar specimens, with an error of 4.6% and -6.3%. The largest error was for specimens SW02, SW04 and HSW02, in the order of 20%, which agrees with the expected differences reported in the literature [55]. The equation proposed by Rojas-Leon et al. showed good agreement with the six specimens, and all the results are within $\pm 10\%$ of the measured peak strength. The equations of Moretti and Gulec proved to be quite conservative in relation to the other two equations, underestimating the peak strength in 40%. The equation of Rojas-León et al considered the most extensive data-set of the used equations, and it was obtained with a machine learning procedure.

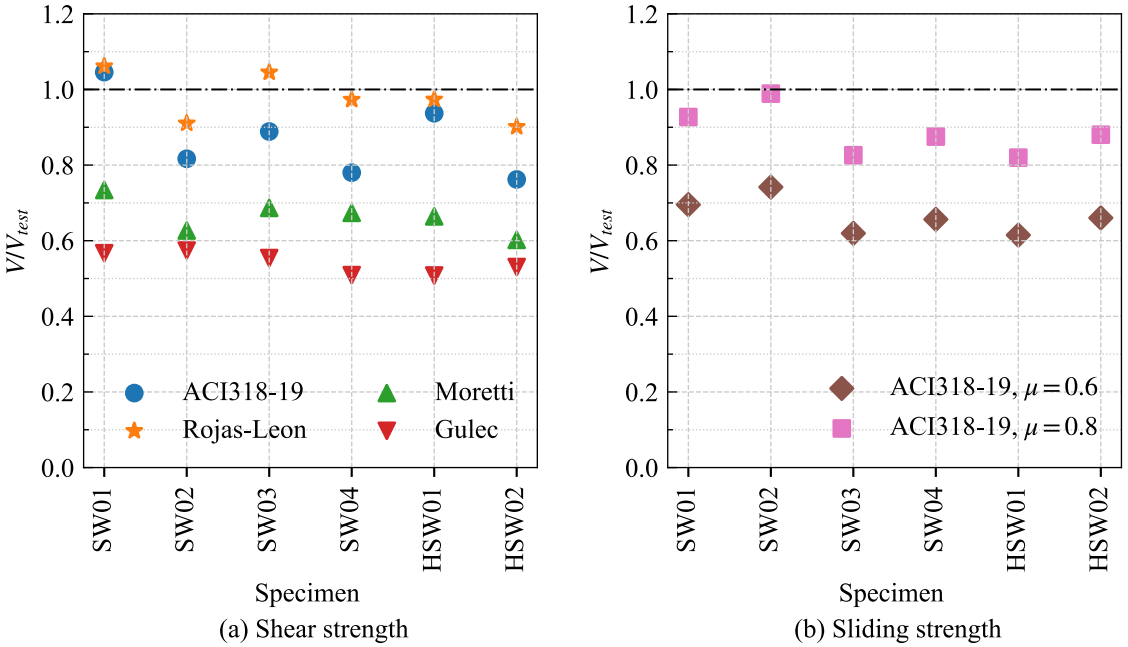

(a) Shear strength (b) Sliding strength

Figure 6.7: (a) Shear strength prediction (b) Sliding strength prediction with ACI 318-19

The sliding prediction of ACI 318-19 is highly dependant on the chosen friction coefficient, and for that reason, the predictions with two values are presented. According to Table 2.1, the friction coefficient of the tested specimens should be equal to 0.6, as the roughness of the cold joint does not reach 1/4 inch (6 mm). The prediction with $\mu = 0.6$ were in average, 64% of the measured strength of the specimens that failed in sliding (SW01, SW03 and HSW03). With a value of $\mu = 0.8$, used for the sliding nominal strength for the failure mode classification of the specimens (Figure 3.1), the accuracy increases to 85%. The ACI 318-19 friction coefficient of specimens SW01, SW03 and HSW01 can be estimated by replacing the total area of vertical steel reinforcement, axial load, yield strength and measured peak strength in Equation 2.9.

$$\mu = \frac{V_{test}}{A_{vf} f_y + P} \quad \Rightarrow \quad \begin{aligned} \mu_{SW01} &= 0.86 \\ \mu_{SW03} &= 0.98 \\ \mu_{HSW01} &= 0.98 \end{aligned} \tag{6.2}$$

The three specimens had the same treatment of the cold joint: it was cleaned and freed of laitance with high pressure jet water, but not mechanically roughened enough to reach the 1/4 inches. Nevertheless, the measured friction coefficient are 33% larger in SW01, and 63% larger in SW03 and HSW01 than the proposed $\mu = 0.6$ of the code. These results highlight that there is still a need to improve the friction coefficient of ACI 318-19.

6.5.2 Peak strength estimation with Vector2

The specimens were modeled in the software Vector2. These models were initially used to define the load protocol (Section), but were then updated with the measured concrete and steel properties. The specimens were modeled with rectangular elements of 100 mm x 98.1 mm, with smeared steel reinforcement as indicated in Table 3.1. The nodes at the bottom of the foundation were fixed in the

horizontal and vertical directions. The displacement protocol was applied as an equal displacement to all nodes of the top cap beam. In this way, the rotation is restricted as the nodes from the bottom and top of the top cap beam must have the same horizontal displacement. Vector2 does not have an element to model sliding in the surface, therefore, it is not expected to capture only the shear and flexure behavior modes. Figure 6.8 shows the model with the elements, and Figure 6.9 shows the lateral resistance-drift curves obtained with Vector2 plotted against the results of the cyclic tests.

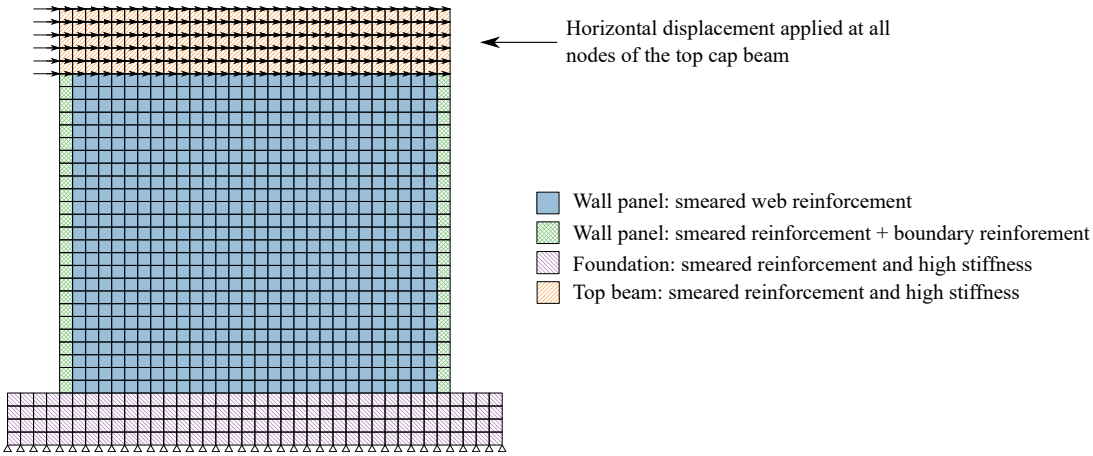

Figure 6.8: Vector2 model of the specimens

The models have a larger initial stiffness than the tests, and in all the specimens but in SW03, Vector2 attained the peak strengths at a lower drift ratio than the tests. The peak strength, though, had a good agreement with the results of the tests, with ratios of the strength obtained in vector against the tests of ≈ 0.97 for specimens SW02, SW03 and SW04, and 1.07 for specimen SW01. Even tough the the Vector2 models were stiffer than the tested specimens, they can give insights on the failure modes of the specimens. For instance, at the peak strength of specimen SW02, the compression strut had a larger principal compressive stress (f_2) than the maximum compression strength ($f_{2,max}$, adjusted with the compression softening factor), and the web reinforcement bars did not yield. This suggests that specimen SW02 would have a concrete crushing failure mode. On the other side, the transverse web reinforcement of specimen SW04 was fully yielded at the peak strength suggesting a diagonal tension failure.

Vector2 captured the crack pattern, inclination, and spacing well, but the crack widths were smaller due to the stiffer model. Figure 6.10 shows the crack inclination of specimens SW01 and SW03. The crack patterns are characterized by flexural cracks in the border and diagonal cracks in the web, consistent with those reported in Chapter 4. Specimen SW01 had a crack spacing of 273 mm in Vector2 against the 200 mm measured in the test. Vector2 calculated a crack spacing of 323 mm for specimen SW03, which in the test had a single single set of cracks (Figure 4.14). However, the results of Vector2 showed that the cracks of SW03 were quite focused in the mid-section of the web panel in a stripe of 300 mm width, meaning that only one crack could have formed, which agrees with the observed cracks of the test.

Although the sliding behavior mode was not captured by Vector 2, the crack width in the bottom corner subjected to tension of specimens SW01 (3.06 mm) and SW03 (3.05 mm) is larger than specimens SW02 (1.32 mm) and SW04 (2.00 mm), which is a hint that the cold joint of specimens SW01 and SW03 is opening and becoming more prone to sliding than specimens SW02 and SW04.

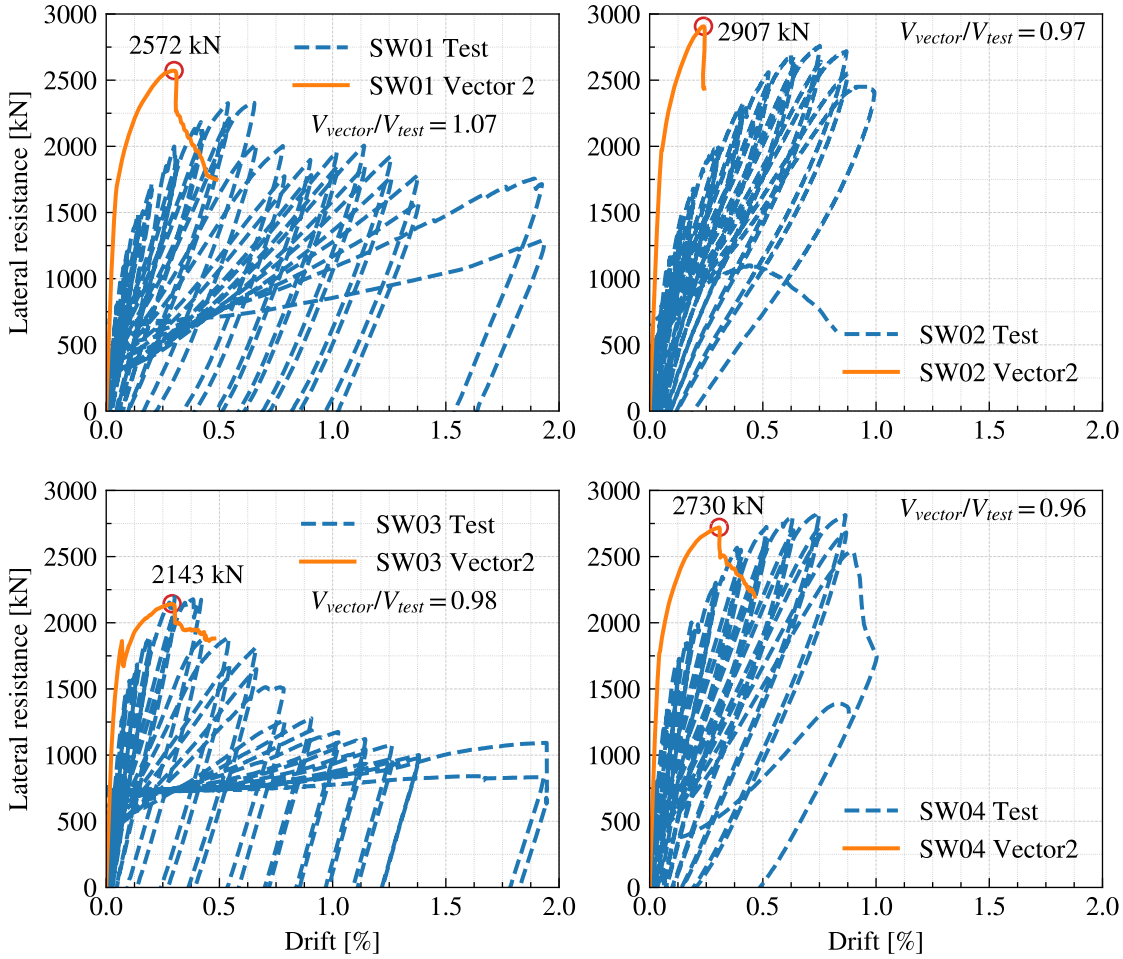

Figure 6.9: Comparison between the Vector2 and the experimental results of the cyclic specimens. The red points correspond to the obtained maximum peak strength.

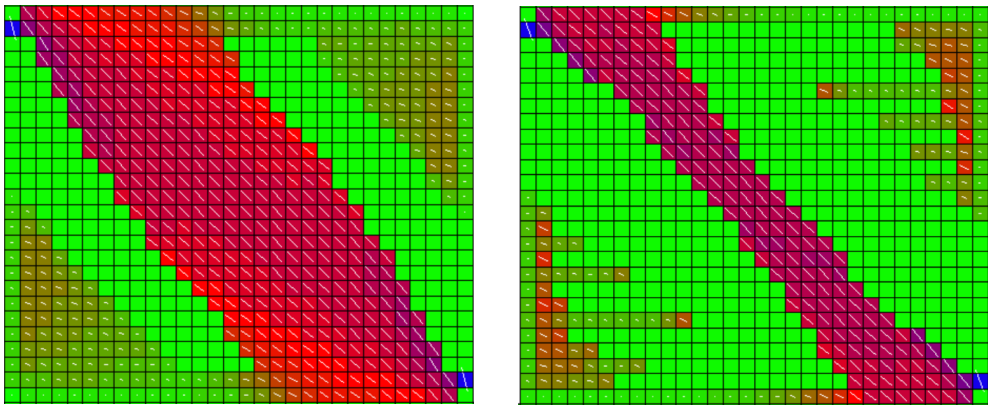

(a) Specimen SW01 (b) Specimen SW03

Figure 6.10: Cracks pattern and inclination obtained with Vector2 of specimens SW01 and SW03. Figures 4.2 and 4.14 shows the crack patterns of specimens SW01 and SW02, respectively.

6.6 Controlling behavior mode prediction

In recent years, there has been a growing interest in predicting the controlling behavior mode of the structures, as it is key information to determine the performance of a structure and to make decisions on seismic retrofit strategies. The main results of this experimental campaign were the behavior and failure modes, and the design parameters were selected such that the specimens were close to the transition between shear and sliding-controlled behavior modes. Therefore, two controlling behavior mode prediction methodologies will be analyzed and discussed regarding the experimental campaign results. These two methodologies had in common that they were calibrated with the failure mode of the specimen, namely, they assume that the controlling behavior mode of the test had the same source of deformation than the failure mode. These methods were previously presented in Section 2.5.

6.6.1 Behavior mode prediction of ACI 369-22

This was the methodology used to designed the specimens of this experimental campaign. It was proposed by Abdullah [57] and adopted by ACI 369-22 [8].

This methodology uses the friction strength formula of ACI 318-19 [26] to estimate the sliding nominal strength V_{sl}, which heavily relies on the friction coefficient μ. Figure 6.11 shows the controlling behavior mode prediction using friction coefficients of 0.6 and 0.8. The friction coefficient 0.6 is analyzed because the methodology was calibrated with that value and is the normative value for the tested specimens according to Table 2.1.

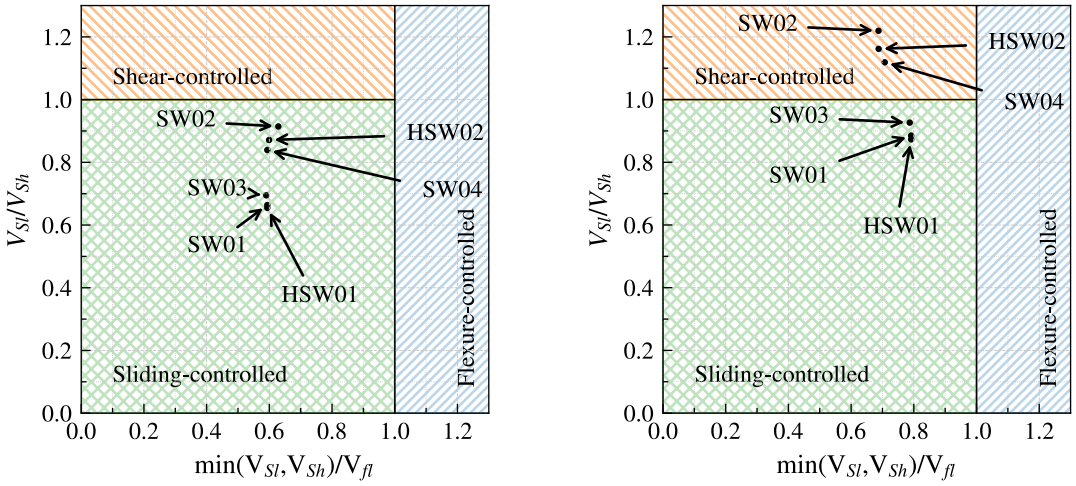

(a) $\mu = 0.6$ (b) $\mu = 0.8$

Figure 6.11: Controlling behavior mode interaction diagram (a) With $\mu = 0.6$ and (b) with $\mu = 0.8$

The friction coefficient of 0.6 underestimates the friction strength of the specimens and predicts sliding-controlled behavior mode for all of them. The experimental campaign was designed in two steps: first, specimens SW01 and SW02, and then SW03 and SW04. The first stage was designed considering $\mu = 0.6$, which assigned sliding-controlled behavior to specimens SW01 and SW02, but the latter was quite close to the shear-controlled boundary zone. After the tests, the friction was calibrated to 0.8 to design specimens SW03 and SW04, which shows good accuracy with all six tested specimens, as it correctly predicted the controlling behavior mode. This controlling behavior identification methodology

is simple and effective, and can give a good prediction if there is a good estimation of the friction coefficient.

The controlling behavior mode classification of Abdullah is, in a certain manner, deterministic; for instance, if a specimen has a $V_{sliding}/V_{shear} = 0.95$, the predicted controlling behavior mode is sliding. However, it does not account for any uncertainty even when the large scatter of the friction coefficient is known, and how difficult it is to predict it. With a value of $V_{sliding}/V_{shear} = 0.95$, it might not be correct to assume that the controlling behavior mode is sliding and not taking actions against shear behavior, which could lead to a brittle failure. An option to overcome this problem is to add a transition zone in terms of the friction coefficient, as shown in Figure 6.12. The diagram defines a transition zone between the sliding and shear behavior, defined by the boundaries with friction coefficients of 0.7 and 0.9, having 0.8 as the baseline. The lower bound of 0.7 was selected as it is recommended by ACI 369-22 to calculate the friction strength. The upper bound of 0.9 was defined as the base of the friction coefficient measured from these tests (Section 6.5). This transition zone acknowledges that specimens could have a combination of the behavior modes in that zone.

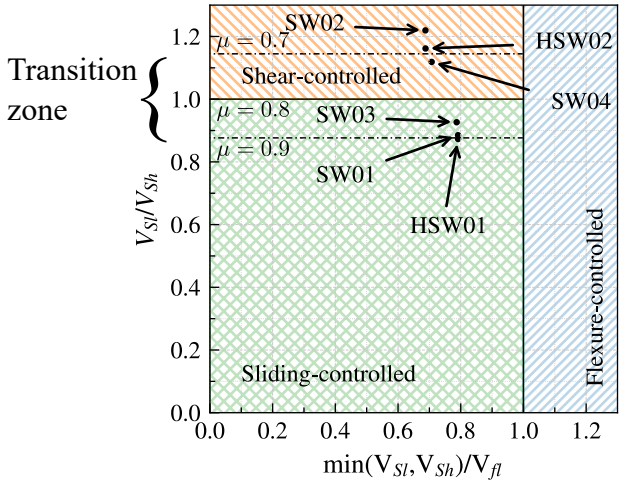

Figure 6.12: Failure mode interaction diagram with a transition zone.

The transition could be also defined for the shear and flexure-controlled zones, even though is out of the scope of this thesis. However, Abdullah [57] classified the specimens in four failure modes, flexure, shear, sliding, and flexure-shear, where the flexure-shear specimens were those scattered between $0.7 < V_n/V_{@Mn} < 1.3$, where V_n is the peak strength reported in the test, and those tests are shown in Figure 2.7. This transition is addressed in the failure mode of some tests, but it did not make it in the final version of the code as a transition between behavior modes.

6.6.2 Machine learning behavior mode prediction

Mangalathu et al. [32] used a machine learning approach to predict the failure mode of reinforced concrete shear walls. This section will use the model to evaluate if it can predict the specimens' controlling behavior mode with the script and database version provided in their publication. The published database has 392, of which 152 had flexure failure, 96 had flexure-shear failure, 122 had shear failure, and only 23 had sliding failure. The authors explored various machine learning techniques,

but this section uses Random Forest, which they reported gave better results. The training set comprised 70% of the specimens in the database, and the other 30% was the testing set.

Table 6.2: Failure mode prediction with the machine learning model of Mangalathu et al [32]

		Probability			
Specimen	Predicted failure mode	Flexure	Flexure-Shear	Shear	Sliding
SW01	Flexure-shear	0.305	0.425	0.170	0.100
SW02	Flexure-shear	0.235	0.470	0.140	0.155
SW03	Flexure-shear	0.235	0.610	0.125	0.030
SW04	Flexure-shear	0.310	0.545	0.100	0.045
HSW01	Flexure-shear	0.320	0.455	0.135	0.090
HSW02	Flexure-shear	0.250	0.545	0.115	0.090

The behavior mode prediction of the specimens is shown in Table 6.2, where the model predicted flexure-shear failure mode for the six specimens of this experimental campaign. The results were given deterministically as a single behavior mode, even though it was based on a statistical analysis. Therefore, it is worth deeply analyzing the algorithm's probabilities assigned to each behavior mode. The probabilities assigned to the sliding-controlling behavior are below 10% in all the specimens but in HSW01, to whom it was assigned 15.5%. The model decided between flexure and flexure-shear behaviors in all cases.

In the second stage, the specimens of this experimental campaign were added to the database. The test and train datasets were randomly selected, but for the interest of this thesis, the analysis were repeated until two or three of the specimens were in the training set. The results of the two studies are presented and shown in Table 6.3(a) and (b), where the specimens in bold were part of the testing set and the rest of the training set. In the first analysis (Table 6.3 (a)), the specimens SW02 (shear failure) and HSW01 (sliding failure) were part of the training set. The model only correctly predicted the sliding-controlling behavior mode of specimen SW01, to whom it assigned shear behavior as the second guess, consistent with the ACI 369-22 behavior mode classification. The first prediction in specimens SW03, SW04, and HSW02 was not correct, but the second highest probability is within the expected result. Even though the controlling behavior mode of specimen SW04 was flexure-shear, the second guess of sliding is close to what was observed during the negative direction of the test. The incorrect first prediction of HSW02 was not expected, as a similar cyclic specimen was part of the training set, and there were only mild differences in the axial load ratio and concrete strength.

In the second analysis (6.3 (b)), specimens SW02, SW04, and HSW01 were part of the training set. In this case, the prediction for SW01 is still sliding-controlled but the result was now closer to the sliding/shear boundary (45.5%/39.0%) than in the Table 6.3(a) (The same analysis works for specimen HSW02). The prediction of SW03, though, was shear with 43%, and the second highest probability was flexure-shear with 33%. The probability of shear failure was even less than in the previous analysis, with 20.5% against 23.5%.

The analysis of this experimental campaign's specimens motivated a closer look to the results of all the

Table 6.3: Failure mode prediction with the machine learning model of Mangalathu et al [32]. The specimens in bold were part of the testing set. (a) Four specimens were part of the testing set and two of the training set, and (b) Three specimens were part of the testing set and three of the training set

(a)			Probability			
Specimen	Failure Mode	Predicted failure mode	Flexure	Flexure-Shear	Shear	Sliding
SW01	**Sliding**	**Sliding**	**0.055**	**0.120**	**0.195**	**0.630**
SW02	Shear	Shear	0.075	0.105	0.685	0.135
SW03	**Sliding**	**Flexure-Shear**	**0.095**	**0.490**	**0.130**	**0.285**
SW04	**Shear**	**Flexure-Shear**	**0.150**	**0.380**	**0.125**	**0.345**
HSW01	Sliding	Sliding	0.065	0.140	0.120	0.675
HSW02	**Shear**	**Sliding**	**0.080**	**0.185**	**0.235**	**0.500**

(b)			Probability			
Specimen	Failure mode	Predicted failure mode	Flexure	Flexure-Shear	Shear	Sliding
SW01	**Sliding**	**Sliding**	**0.050**	**0.105**	**0.390**	**0.455**
SW02	Shear	Shear	0.060	0.155	0.710	0.095
SW03	**Sliding**	**Shear**	**0.035**	**0.330**	**0.430**	**0.205**
SW04	Shear	Shear	0.040	0.145	0.725	0.09
HSW01	Sliding	Sliding	0.030	0.095	0.295	0.580
HSW02	**Shear**	**Shear**	**0.045**	**0.175**	**0.430**	**0.350**

specimens considered in the dataset: How large was the probability of the predicted behavior mode? And if it did not predict correctly, was the second prediction correct? Figure 6.13(a) shows a bar plot with the two highest probabilities for each specimen, where each correct prediction is represented with a blue dot. The plotted first prediction does not differentiate behavior modes, and the presented results were obtained with the same training set as the analysis shown in Table 6.3 (b). The overall accuracy of the model was 83% (100 out of 120). The average highest probability in the correct guess is 80.5%, but nine of these specimens had a first failure mode with less than 50% chance. Of these nine specimens, five had a difference between the two highest probabilities of 0.1, which means that the model had to decide between two failure modes with similar probabilities. Note that two of these five specimens were SW01 and HSW02.

The 20 specimens with a wrong controlling behavior mode prediction are plotted separately in Figure 6.13 (b). Of these 20 specimens, there are 12 in which the model gave the second highest probability to the correct behavior mode. These results suggest that the model's accuracy could be improved (from 83% to 93%) by assuming that a specimen can have more than one failure mode, if the results are given with the corresponding probability. And finally, eight specimens did not have a correct guess with the two highest probabilities. In five of these eight specimens, the sum of the two largest probabilities was below 78%, which means that the model still had uncertainty in allocating the third the failure modes.

The remaining analysis would be to determine if the results of the two highest probabilities relate to the expected failure mode boundaries of the specimen. For instance, was the second highest probability

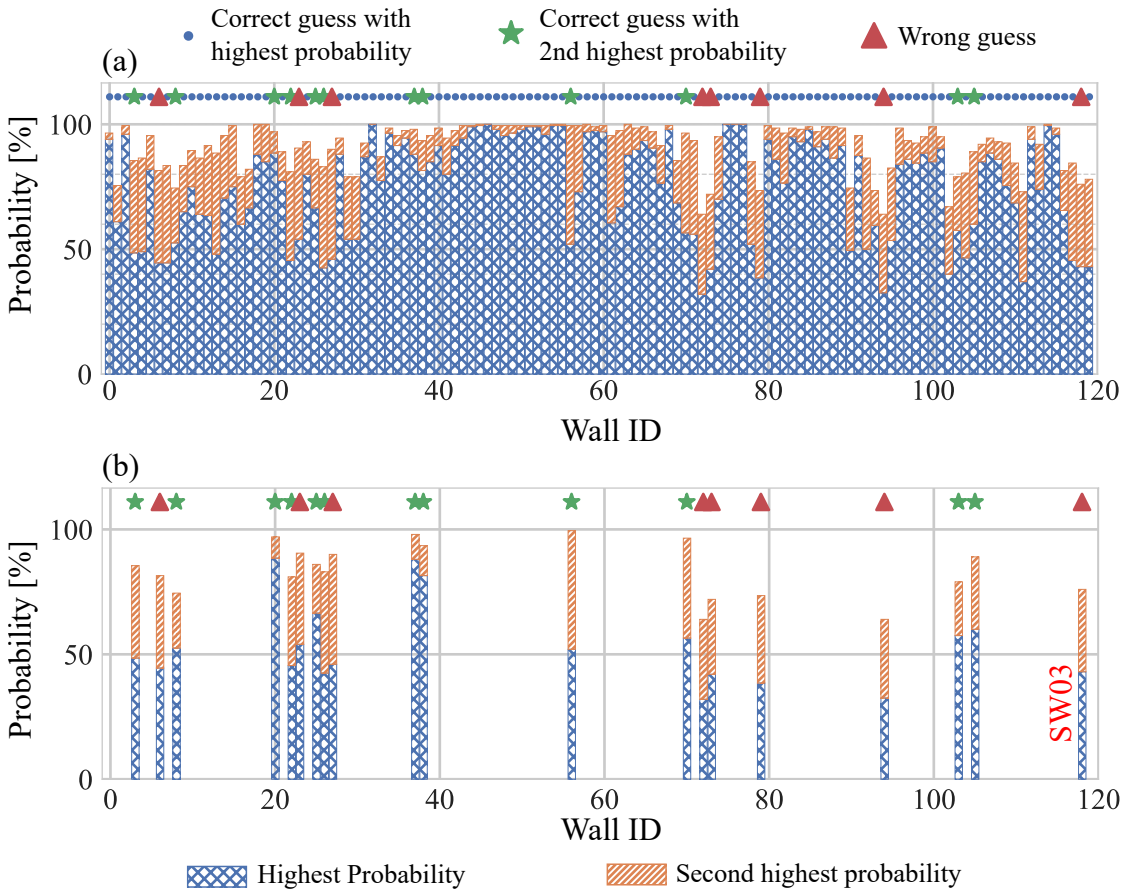

Figure 6.13: (a) Value of the two highest probabilities of the failure mode's prediction machine learning model (b) Specimens with the wrong prediction

a possible failure mode in the correct predictions? Or could the probability given by the model be associated with the actual probability of a wall failure mode? The answer to the second question is probably not with the amount of data, as the machine learning model is not mechanics-based but statistical.

The failure mode of a structural element should be considered probabilistic, especially for elements within the boundaries of two controlling behavior modes. Adding a transition zone to the ACI 369-22 behavior mode classification could clarify and help the engineers make decisions about retrofit, and in some sense, it is more honest in that it does not assume a fixed failure mode. Machine learning is a good and efficient way to predict the failure mode of a specimen. However, more data is still needed, especially in sliding failure, which is underrepresented in the database. It must be assumed that a shear wall database will never be large enough for a reliable machine learning model. Yet, the results and accuracy of the failure modes given by the machine learning algorithm could be improved and made more transparent if the results were given to the designer engineering in terms of probabilities rather than a fixed failure mode.

6.7 Sliding behavior mode

This experimental campaign has shown that specimens with sliding-controlled behavior can withstand larger displacement demands than those with shear-controlled behavior. The sliding behavior of reinforced concrete shear walls is less known to the community of structural engineers, and it has many uncertainties and unknowns. Thus, the sliding-controlled behavior is usually restricted or non-considered. In this section, I would like to address some of its paradigms.

The sliding initiation drift ratio (SIDR) is an important point in sliding-controlled walls. It defines the onset of the sliding deformations but does not relate to the drift ratio where sliding controls the global behavior. This research defined the cyclic value of SIDR in terms of the variation of the energy dissipated per cycle with respect to a previous cycle, and the hybrid simulation test had an energy jump in the dissipated strain energy in that could help to estimate the SIDR in a time-history response. Furthermore, the results of the presented tests showed that the SIDR depends on two factors: the web reinforcement ratio and the test protocol, and the latter is the one that gives more uncertainty to the response of a sliding-controlled specimen. It could be assumed that a lower limit estimation of the SIDR is the one provided by the cyclic tests and, on the contrary, that a monotonic pushover test protocol should not trigger a sliding but a shear-controlled specimen. There are still many unknowns on which parameter could be used to identify SIDR on a numerical model, but one that has been proposed is the crack width at the bottom [109]. In fact, specimens SW01 and SW03 started to slide after the base crack was wider than the maximum aggregate size. However, this accounts only for the crack width at one point of the bottom and does not consider the variation of crack width in the tension zone or the length of the compression zone.

It is difficult to determine when a wall will have a sliding-controlled behavior after its SIDR. The cyclically tested specimen reached more than 50% of sliding contributions at a much lower displacement than the hybrid simulation test, but with more fully reversed cycles. This means that the development of a sliding-controlled behavior is progressive, cumulative, and highly dependent on the test protocol or, in the case of a building, the type of earthquake. Furthermore, shear/flexure and sliding deformations do not always co-occur. For instance, consider a loading branch of specimen SW01 after the SIDR. In the beginning, the specimen will deform in shear and flexure. It will slide when it reaches the friction strength of the interface at the sliding plateau of 750 kN, and will not deform in shear or flexure until the friction force at the bottom can counterbalance the horizontal component of the diagonal strut. And when this happens, the wall deforms again in shear and flexure. Therefore, the contribution of sliding, shear, and flexure depends on the point where they are measured.

The controlling behavior mode diagram proposed by Abdullah [57] is a valuable and effective tool for design engineers as it makes possible to select behavior modes based on strength assessment (force method). But it does not account that the sliding behavior mode is preceded by shear and flexure deformations. Therefore, if during the evaluation of an existing structure a wall falls in the sliding-controlled behavior zone, the process should be done in a two-step procedure, first by identifying the SIDR and check if the considered ground motion intensity triggers sliding deformations. If it does, the

maximum displacement of the wall should account for sliding deformations plus the fact that it can re-engage in shear again. These effects are not considered in the ACI 369-22 code, but the main message is that a wall in the sliding-controlled behavior zone will have first a shear-controlled behavior, and the retrofit or repair interventions would have to address it.

A pushover analysis is one of the main methods used in practice to estimate the yield displacement and capacity of a structure, and including sliding deformation is the first step towards considering it as a design or evaluation behavior mode. The pushover analysis results can be used for displacement-based design methodologies such as the constant yield method approach [110]. The pushover analysis has been extensively used for flexure-controlled structures, and there are recommendations to consider shear deformations in reinforced concrete squat walls [111]. Schuler and Trost [112] proposed a model to estimate the sliding deformations and include them in such analysis. However, it considers only flexure and sliding deformations and does not account for test protocol effects. Neglecting shear deformations in squat walls underestimates the length of the compression zone at the base of the walls, as it ignores the impact of the compression strut that controlled the shear transfer. And on the other side, neglecting the test protocol does not consider that the wall could eventually engage in shear-behavior. Nevertheless, it gives a first step in incorporating sliding into practice analysis.

Sliding behavior mode will trigger in squat walls with a low shear-span ratio, which are usually part of the structural system of low and medium-rise buildings. These buildings have a complex array of floor plans, with walls acting simultaneously with columns, short beams, and other walls, which makes it hard to extrapolate the results of a single and planar specimen test when the potentially large displacement must be accommodated in a system of various structural elements. Many walls have L, C, T, or H-shaped sections, and the behavior of the flange still needs to be addressed in this study. A hint at how these will behave under sliding failure is given by Palermo and Vecchio [113] and Kim and Park [41], where their double T-shaped walls slid, but in tests that did not have an axial load. In particular, the tests from Kim and Park showed the specimens could reach drifts of up to 4% drift ratio, but the flanges had a pinching failure due to large sliding deformations of the web. The lateral resistance-force hysteresis displacement of those specimens is very consistent with the results of this study. However, due to the absence of axial load, it isn't easy to discuss the vertical stability of those specimens, but the final state of the flange suggests that they might have the ability to carry vertical loads. The T-shaped specimen of Kim and Park is interesting because in an actual building, the free corner of the web would have probably been confined due to the large amount of steel and concrete material in the flange. Eventually, the large compression due to flexure would affect the sliding behavior. However, the height of their specimens was 500 mm, which is not enough to consider effects due to the moment at the base. Nevertheless, these tests have shown that sliding can happen in T or H-shaped walls.

At the system level, it is important to identify where in a building the sliding-controlling behavior could develop. As a wall needs a low shear-span ratio, the most probable location would be at the cold joint with the foundations, or it can also develop at a zone with significant moment inversion, for instance, below the critical height of a building when the underground levels appear. As it needs a weak interface to develop, it would usually happen at the cold joint between the wall and foundation or at the bottom or

top connection of the slab (the latter was used as an example by Trost [28]). Once a wall starts to slide, the surrounding elements must be able to deform with it, either by sliding or by bending deformation. It is hard to imagine a wall sliding while the structural component next to it behaves in a shear-controlled behavior. But elements such as columns could accommodate that deformation in flexure, as it happened at the E-Defense 4-story building shaking table test [45]. This building had a simple floor plan, planar shear walls in one direction and frames in the other, but it provided a benchmark building with a sliding failure.

The design philosophy should always point towards structural components with ductile flexure-controlled behavior. However, in some cases, the structure geometry or other constraints will have elements prone to have a shear or sliding-controlled behavior. The designer could try to bring these elements towards the flexure-controlled zone, but in doing so, for instance by adding distributed vertical reinforcement, it could move them to the shear-controlled zone and have as a consequence a brittle failure mode. And if the element is close to the boundary of shear and sliding-controlled behavior, it might be a good idea to bring it to the sliding-controlled behavior zone.

CHAPTER 7

CONCLUSIONS AND OUTLOOK

7.1 Summary

Chapter 3 described how the experimental campaign was conceived, designed, and conducted. The experimental campaign studied the effect of the axial load ratio, steel reinforcement, and loading protocol on the specimens' failure mode. To this end, the specimens were designed to straddle between the boundaries of the sliding and shear failure modes according to the failure mode classification of Abdullah [57]. The set of specimens comprised a reference specimen named SW01, and the changes concerning that specimen were: SW02 had a double axial load ratio, SW03 had less transverse and longitudinal web reinforcement, and SW04 had the same longitudinal reinforcement but less transverse web reinforcement. Specimens HSW01 and HSW02 had identical geometry and reinforcement arrangement as SW01 and SW02 but were tested under hybrid simulation to evaluate the influence of the load protocol. The specimens were tested in the ETH MAST (Multi-Axis Sub-assemblage Testing) Facility. This computer-controlled machine can control the six degrees of freedom in force, displacement, or mixed mode control. The cyclic and hybrid simulation tests were implemented within the hybrid simulation architecture of the ETH MAST. The numerical integration and model of the hybrid simulation tests were coded and implemented in the host computer in a Python script. As the shear wall specimens were quite stiff, it was necessary to control the ETH MAST with an external sensor to accurately measure the specimen's top displacement, which was included in the hybrid simulation architecture at the Python script level.

Chapter 4 presented the results of cyclic tests of the four specimens. Specimens SW01 and SW03 had sliding failure. In the first instance, they had a shear-controlled behavior, but after attaining their peak strength, they changed to a sliding-controlled behavior at 0.65% and 0.42% drift ratios, respectively. Their post-peak sliding behavior was characterized by sliding plateaus in the lateral resistance-drift responses, in which the specimens slid with constant force until they could engage resistance again with shear and flexure deformations. The tests of specimens SW01 and SW03 were stopped at 2%, where they had considerable strength degradation; their response was primarily dominated by sliding deformations, but they never lost their axial load-carrying capacity. Specimens SW02 and SW04 had shear failures, specifically concrete crushing in the web and diagonal tension, respectively, and both had a shear-controlled behavior during the entire test. They reached a maximum drift ratio of 1.00%, where they developed their failures. Specimen SW02 had massive concrete spalling in the web, resulting in a sudden drop in resistance and height of the specimen. Specimen SW04 developed a large diagonal shear crack where the specimen slipped, which caused a sudden drop in height and lateral resistance. In the subsequent cycle, at a lower drift ratio, the reinforcement bars crossing the crack fractured. Specimens SW02 and SW04 failures were brittle, and the specimens lost their axial load-carrying capacity.

Chapter 5 presented the results of the hybrid simulation tests. The specimens were subjected to a cyclic test of low displacement to estimate their initial stiffness and a free vibration test to determine the damping contributed by the experimental facility. Specimen HSW01, identical to SW01, had a sliding failure after attaining its peak strength of 2729 kN. In the post-peak behavior, the specimen had similar sliding plateaus as the cyclic ones, and after reaching a 3.03% drift ratio, the wall lost its shear and flexural capacity beyond the friction resistance, and the behavior was purely sliding. Specimen HSW02 had a shear failure. It was first subjected to the same ground motion as HSW01, but it did not fail, attain the specimen peak strength, nor fully develop the crack pattern. The ground motion was scaled with a larger value, and in this simulation, the specimen attained the peak strength of 3300 kN, reached a drift ratio of 0.78%, and fully developed its crack pattern, but it did not fail. The ground motion scale factor was increased once again, where the specimen failed in shear, specifically in concrete crushing. The failure was brittle, and the specimen lost its capacity to carry vertical loads.

Chapter 6 discussed various issues in light of the results of the experiments. First, it discusses the effect of the axial load ratio and the steel reinforcement in the failure modes of the specimens. Because sliding failure has been catalogued with low dissipation capacities, an analysis of the equivalent viscous damping and its potential as a definition for sliding initiation was investigated. Then, this chapter evaluates two methodologies to predict failure mode of reinforced concrete shear walls. These two methodologies provide the result as a single failure mode, and it does not account for the fact that a specimen could be close to a failure mode boundary and, therefore, a proposal to account for a transition zone is proposed. And finally, it provides an analysis of the drawbacks and advantages of a sliding failure over a shear one, and what would be the possible effects of a sliding failure.

7.2 Conclusions

Sliding behavior mode

The results allowed to make key conclusions about the development of the sliding behavior mode. Three specimens of the experimental campaign had sliding-controlled behavior, with sliding deformations focused at the cold joint between the wall panel and the foundation.

- The sliding-controlled behavior triggers after cycles of displacements in shear-controlled behavior with negligible contributions of sliding deformation. The behavior mode changes after the drift ratio identified as "sliding initiation". But the transition develops incrementally, namely, the sliding deformation contribution to the total deformation increases after each cycle due to degradation of the cold joint.
- The sliding behavior mode showed to be stable during the entire tests as the specimens never lost their axial load carrying capacity. It can be considered a quasi-ductile behavior mode, as the specimens could reach considerable displacements after attaining their peak strength.
- The sliding initiation drift ratio can be identified with an equivalent damping approach. The friction mechanism has significant dissipation capacities, and when the sliding behavior is triggered, there is

a jump in the equivalent viscous damping which marks the difference between the shear and sliding behavior modes.

- The hybrid simulation tests showed that after the specimen reached its sliding initiation drift ratio at 0.77%, it still could reach 93% of its peak strength at a 2.16% drift ratio. This effect shows that it might not be necessary to fully replace a wall after it started to slide and that the sliding failure mode still needs a better numerical definition to define the drift associated to sliding initiation, which in this work is proposed in terms of the equivalent viscous damping in cyclic tests.
- The damage of a sliding failure focuses in an interface, which in these specimens was at the cold joint. The specimens pictures provided in this thesis allow to see the damage progression of an already triggered sliding behavior. At the early stages, the damage is minor and could be identified as small gap at the cold joint with minor concrete spalling or detachment of concrete in the corners, and with the increase of sliding deformations, the concrete will spall at the cold joint exposing the reinforcement bars.

Transitions between shear and sliding behavior modes

The experimental campaign revealed that in reinforced concrete shear walls which are close to the boundaries between the shear and sliding behavior modes, changes in the axial load ratio and steel reinforcement ratios could change the failure mode of the specimens, which would have important effects on their behavior. A comparison of specimens SW01, SW02, HSW01 and HSW02 showed that the axial load is a key parameter in determining the behavior and failure mode of the specimens: lightly loaded specimens changed their behavior from shear to sliding but continued to carry their axial load, whereas a heavily loaded wall had a shear controlled-behavior until failure by diagonal crushing compression of concrete. Therefore, it is key to have a good estimation of the axial load of a wall before and during an earthquake.

A comparison of specimens SW01, SW03 and SW04 revealed that the arrangement of the web steel reinforcement ratios affects the behavior mode of reinforced concrete shear walls, and each case must be analyzed independently. Specimen SW01, with equal longitudinal and transverse reinforcement ratios (0.523%) changed their behavior from shear to sliding-controlled. Specimen SW04 had less transverse reinforcement ratio (0.393%) than specimen SW01, and it had a shear controlled-behavior until failure by diagonal compression. And finally, specimen SW03, which had equal transverse and longitudinal reinforcement ratios but less than specimen SW01 (0.333%), had an initial shear-controlled behavior but changed to sliding.

The hybrid simulation tests showed that, in this experimental campaign, the loading protocol did not have an effect on the behavior and failure mode of the specimens. This was relevant because the cyclic loading protocols are very demanding, which could have degraded in excess the cold joint and favour a sliding failure, but it was shown that it could be triggered under a real ground motion excitation.

The specimens were designed by using the behavior mode classification of ACI369-22 guideline [8]. It correctly predicted the behavior modes observed in the four tests, but it showed to be quite sensitive to the selection of the friction coefficient μ, necessary estimate the sliding strength of the specimens. This

experimental campaign provides an independent validation of the classification, indicating that practicing engineers can use it to identify which behavior mode the shear walls they are designing are likely to develop and how to handle the consequences of that failure mode.

7.3 Future research

The work presented in this thesis was based on the results conducted in the experimental campaign, which was conducted in in-plane specimens under controlled boundary conditions, and it did not considered interaction with adjacent structural components.

The experimental research could include the testing of specimens with C, L, T or H shaped sections, which will help to understand the development of sliding failure in non-planar walls. Previous experiments showed that sliding can be triggered in H walls [41], but the specimens were not real scale and did not have axial load. The hybrid simulation conducted in this thesis considered the mass, damping and ground motion part to have consistency and the ability to compare with the set of cyclic tests. The next step would be to considered a full structure with the specimen as the physical substructure, which could account for the redistribution of vertical load due to the shortening of the specimens. Some studies have demonstrated that it can be done in three dimensional structures [81,82], but they were conducted in columns which have a very low stiffness when compared to a shear wall. The challenges to conduct such a hybrid simulation with stiff specimens has been addressed by Xiao et al. [114], and the characteristics of the ETH MAST facility could make that possible.

There are no models that could capture the sliding deformations of a shear wall considering shear-flexure interaction. The specimens of this experimental campaign provide a benchmark wall that could be model either in static cyclic loading or in a non linear time history analysis with the hybrid simulation. With a calibrated model, the study of the behavior of the system level when a wall fails in sliding could be addressed, and study which type of floor plan configurations could be prone to sliding, and fragility curves associated to the sliding failure could be obtained.

With a reliable model that can capture the sliding deformation a walls, the 2 DOF surrogate sliding-flexural model proposed by Silva [6] could be expanded to a sliding-shear surrogate for buildings with reinforced concrete shear walls. Her work considered a sliding interface with single friction pendulum isolators, which have their sliding plateau at their peak strength and do not which do no not engage in extra resistance after they start to slide, which differs with the sliding behavior that the specimens of this thesis had. With the model adopted to the shear walls, the maximum displacement of a building that is prone develop sliding behavior could be estimated in a simple and effective manner.

APPENDIX A

SPECIMEN CONSTRUCTION DRAWINGS

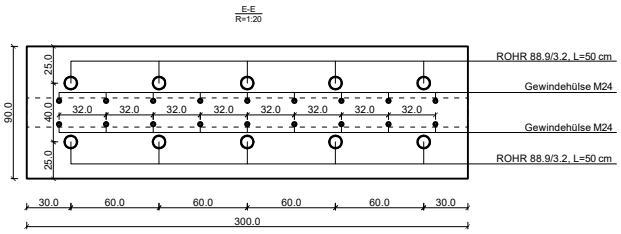

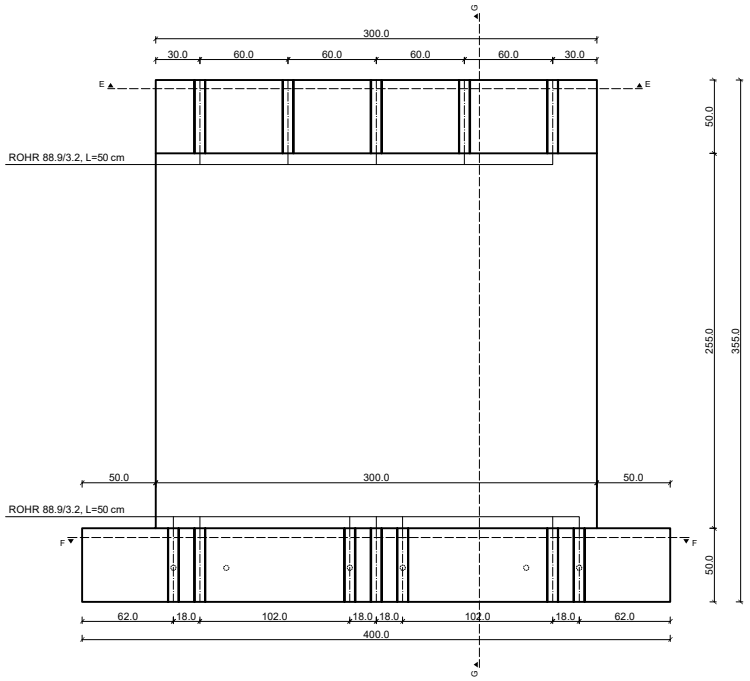

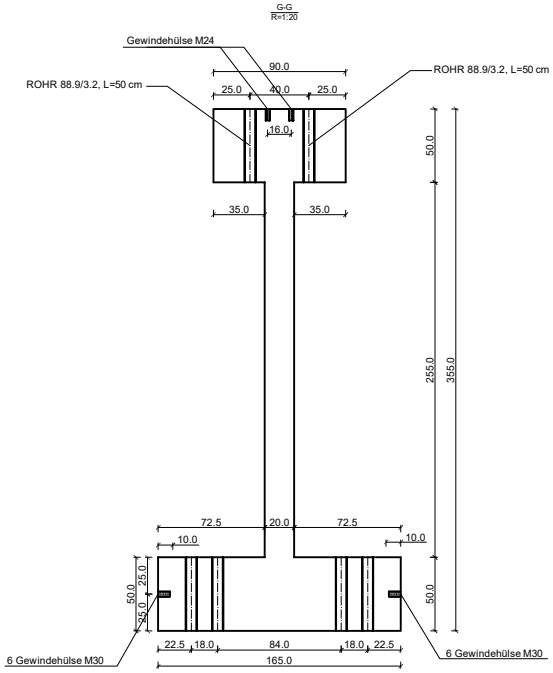

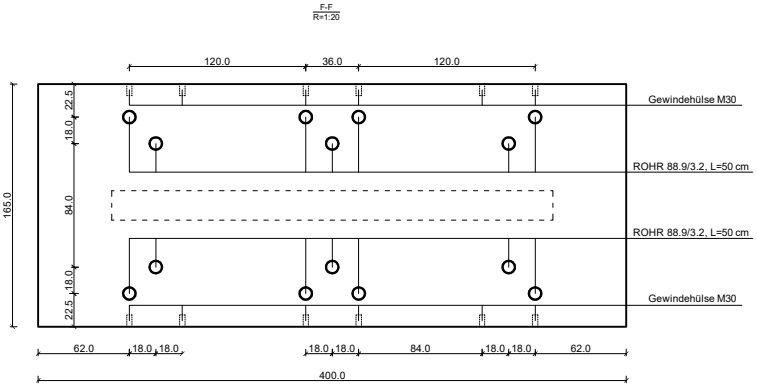

ETH Zürich Institut für Baustatik und Konstruktion	Datum	08.02.2023
	Bearbeitet	D. Pizarro
	Massstab	1:20
Benennung ETH MAST Versuchsanlage SW01, SW02, SW03, SW04, HSW01, HSW02	Blatt	A4
	Einheiten	cm
	Gewicht	16 t

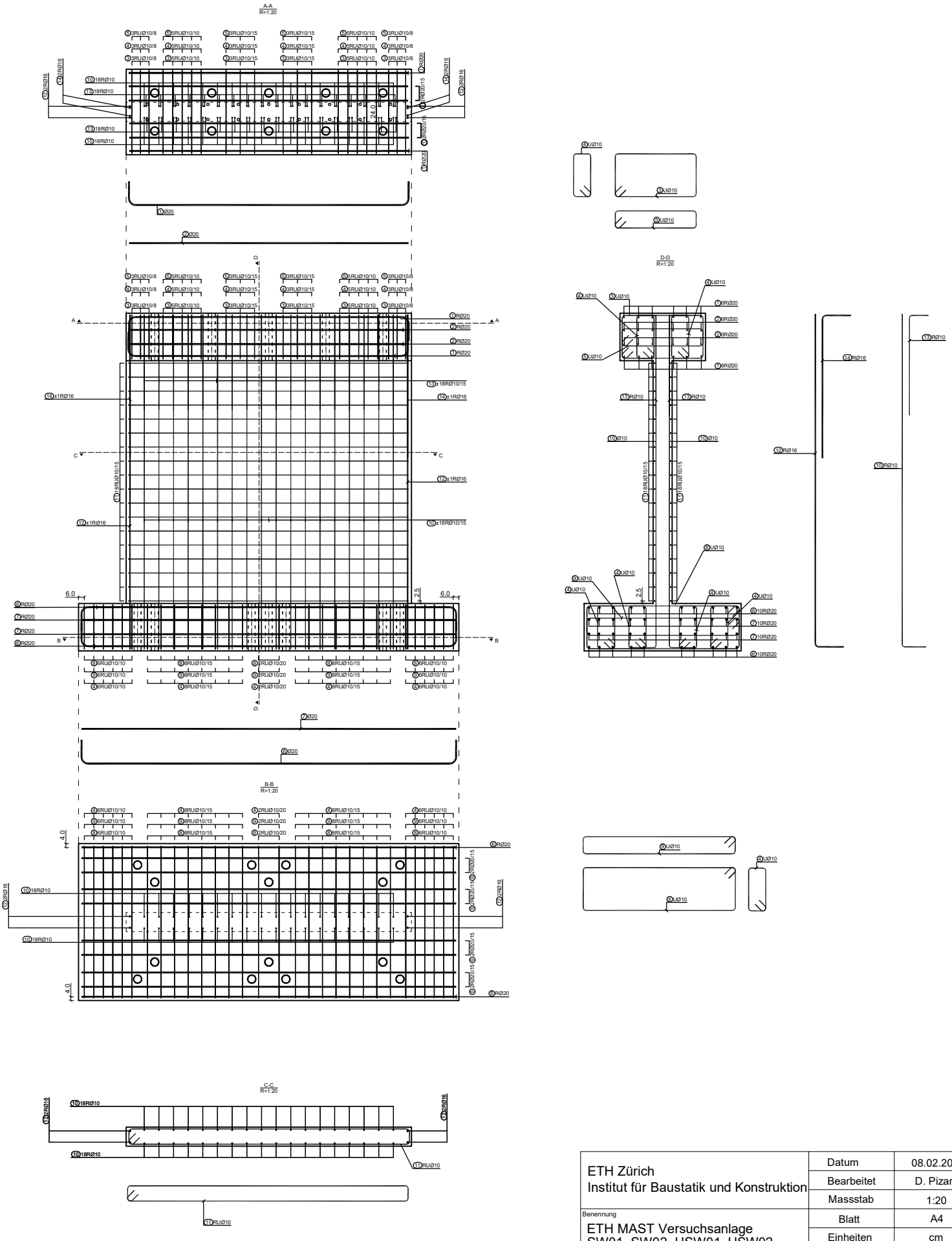

ETH Zürich Institut für Baustatik und Konstruktion	Datum	08.02.2023
	Bearbeitet	D. Pizarro
	Massstab	1:20
Benennung ETH MAST Versuchsanlage SW01, SW02, HSW01, HSW02	Blatt	A4
	Einheiten	cm
	Gewicht	16 t

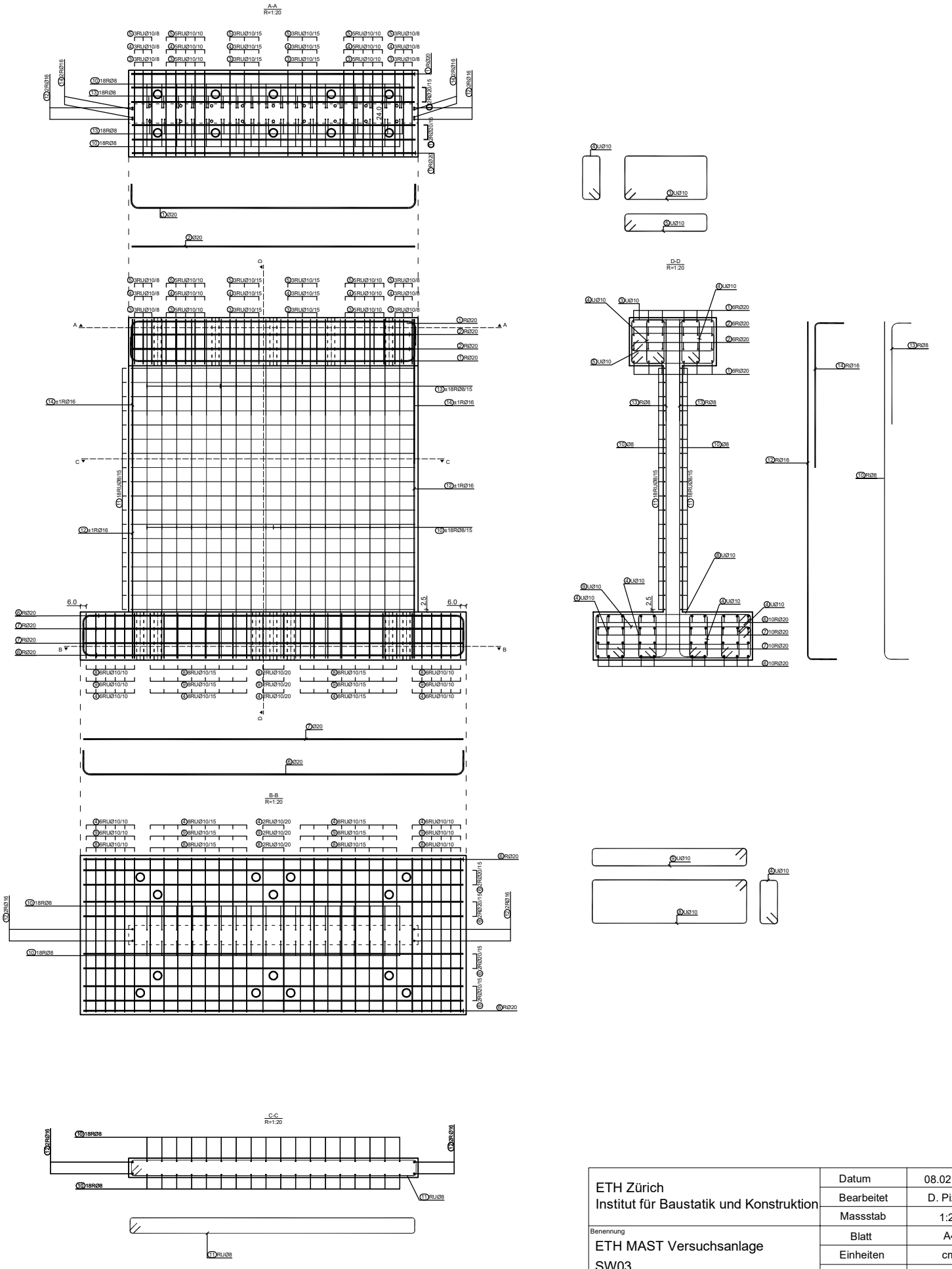

ETH Zürich Institut für Baustatik und Konstruktion	Datum	08.02.2023
	Bearbeitet	D. Pizarro
	Massstab	1:20
Benennung ETH MAST Versuchsanlage SW03	Blatt	A4
	Einheiten	cm
	Gewicht	16 t

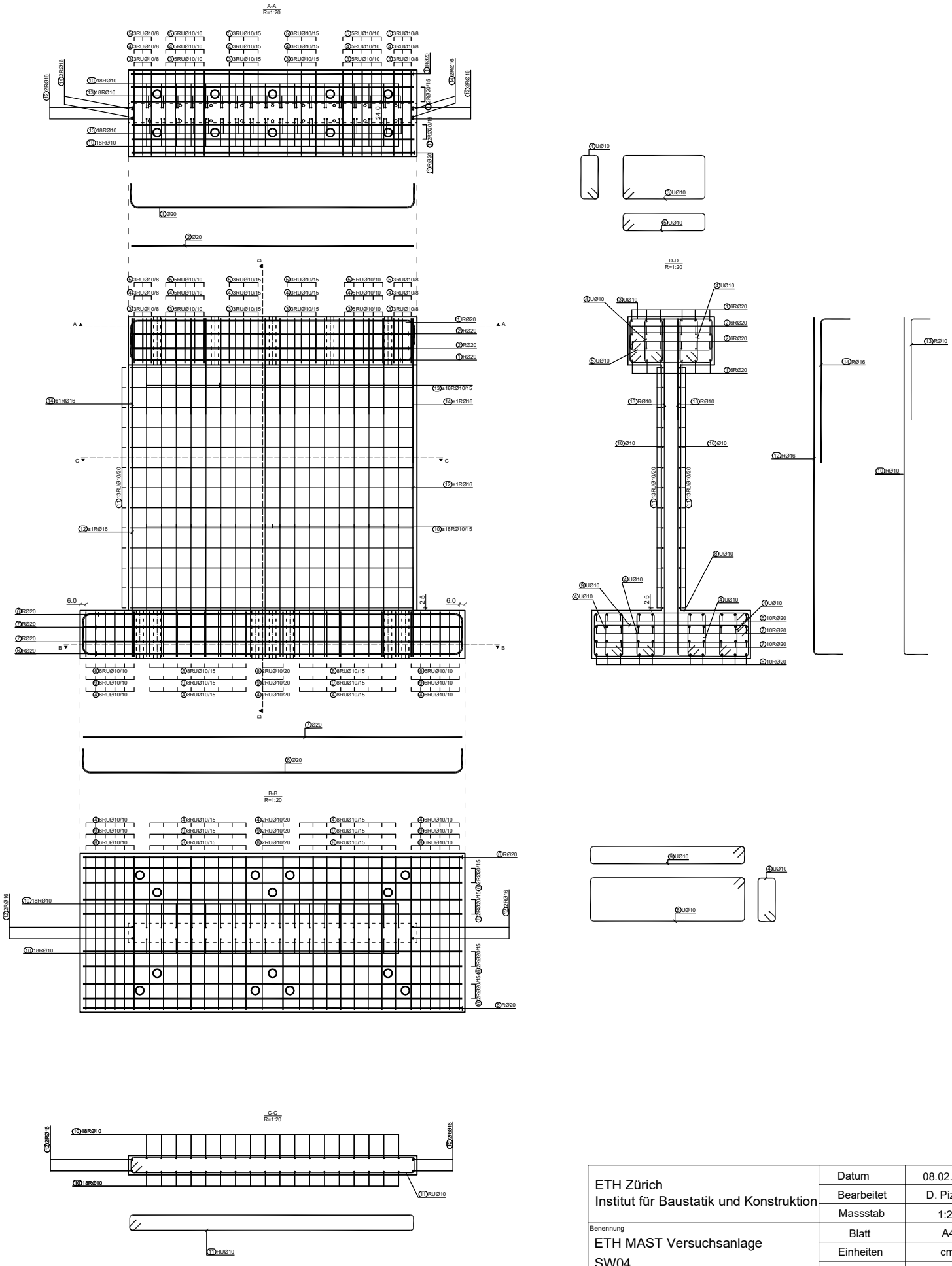

ETH Zürich Institut für Baustatik und Konstruktion	Datum	08.02.2023
	Bearbeitet	D. Pizarro
	Massstab	1:20
Benennung ETH MAST Versuchsanlage SW04	Blatt	A4
	Einheiten	cm
	Gewicht	16 t

APPENDIX B

HYBRID RESTART: AN ALTERNATIVE SOLUTION

We had to interrupt the test of Specimen HSW01 because of a control problem. In Chapter 5, I explained how we resumed the test and the implications in the specimen's response. However, while I was writing and adding the plots to the thesis, I realized that reloading the specimen could have been avoided. At the time step where we stopped the test (point 8), the specimen had zero velocity and started to unload. However, there was a problem with the control, and the specimen did not stop at the target displacement sent by the host computer. It continued to unload at a constant speed, and we paused the test when the specimen reached zero force.

The last recording point at the host computer was at $t = 7.230$ seconds, with a displacement of 36.51 mm and a lateral load of 2289.582 kN. Figure B.1 illustrates the situation: the specimen's dashed unloading branch was in fact the unloading path that the hybrid simulation should have followed. The data of that unloading branch had the necessary displacements and forces to conduct a numerical analysis, and restart the simulation at force 0 kN.

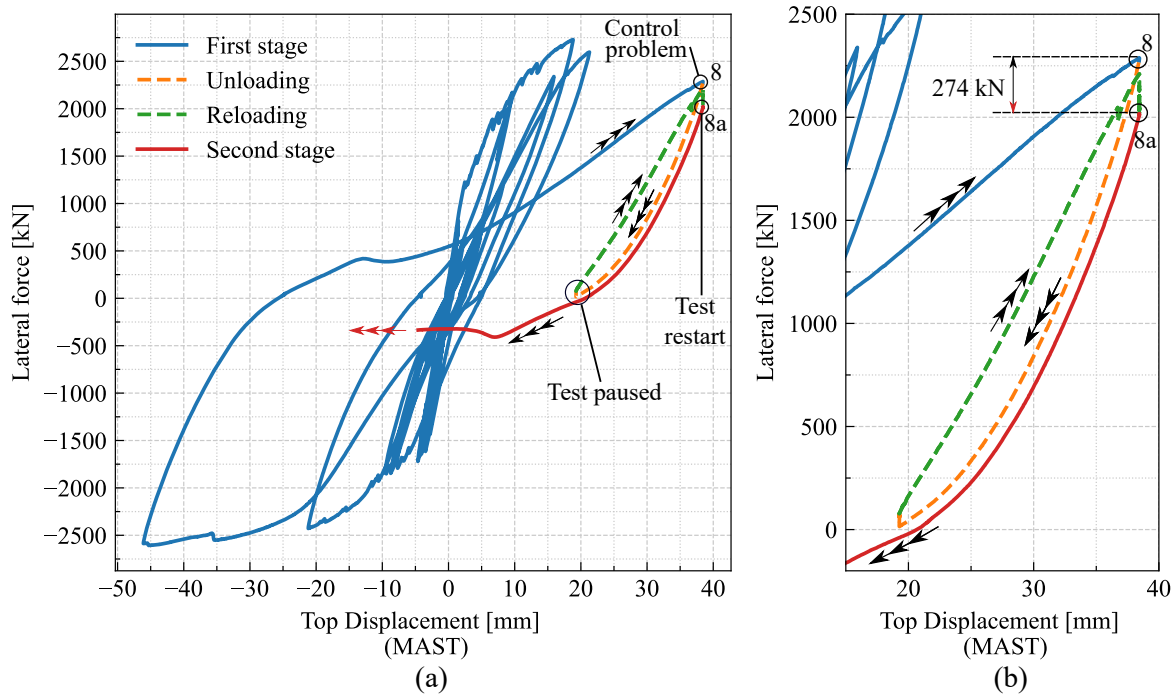

Figure B.1: Load-displacement curves during the restart of the test. Note that the displacements correspond to the one measured by the controller of the MAST, not the external sensor, and therefore they are larger than the measured in the top of the wall

A better solution than reloading the specimen would have been to numerically do the following integration steps until the displacement was close to the rest state of the specimen (zero load and 19.27 mm of top displacement) and obtain the restoring forces from the unloading branch. The unloading branch of Figure B.1 is in terms of the displacements measured by the MAST (which are overestimated), and as the external sensor did not record displacements in the unloading branch, the

MAST measurements would need to be transformed to the external sensor domain. One way to estimate the displacement of the external sensor would have been to assume that at 0 kN, it measures the same displacement as the MAST controller, which is quite accurate because there are no large forces involved in the system, and when the test was stopped at point 8, the external sensor measured 36.51 mm (external sensor measurement) and the displacement measured by the MAST was 38.44 mm. Then, a linear interpolation could transform the unloading branch into the sensor coordinates (Figure B.2 (a)).

Table B.1 shows the hypothetical steps, which are shown with dots in Figure B.2 (b). The last recorded point was at 7.230 seconds, and from then on, every step receives the feedback force from the data of the load-displacement history adjusted to the external sensor. The test could have restarted at 7.295 seconds, which would not have required reloading of the specimen and could have avoided relaxation problems. Figure B.2 shows the time steps of Table B.1 in what would have been this alternative solution and compares it to how we restarted the hybrid simulation.

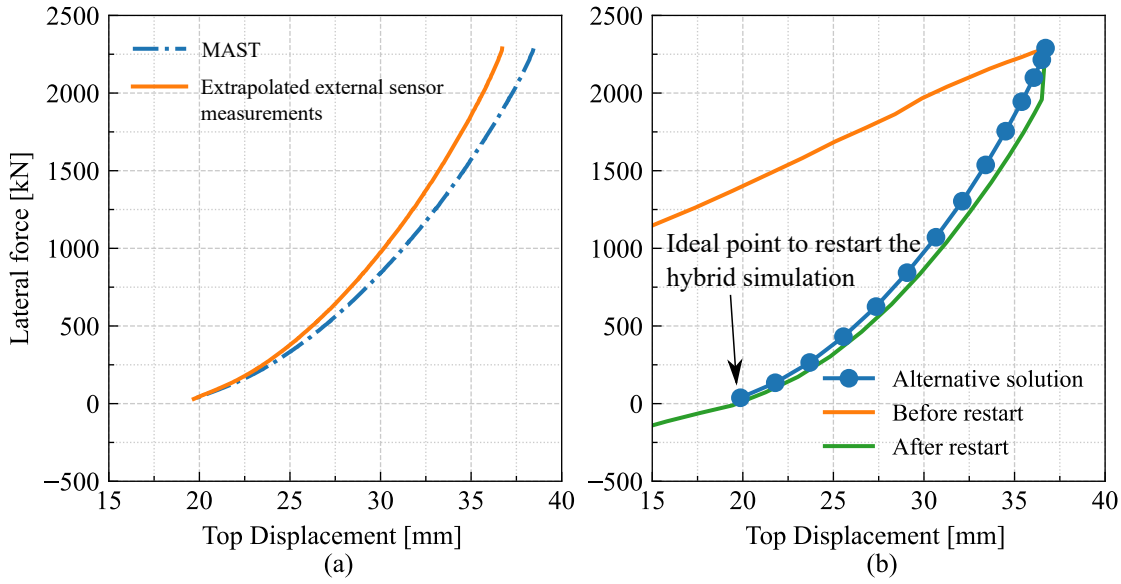

Figure B.2: (a) Estimation of actual displacement of the specimen from the measurements of the MAST (b) Integration points over the unloading branch of the specimens

Table B.1: Integration steps to restart the hybrid simulation test

Time [s]	$u1$ [mm]	$\dot{u}_1$ [mm/s]	$\ddot{u}_1$ [mm/s^2]	F [kN]	$\ddot{u}_g$ mm/s^2	Comment
7.225	36.687	26.294	-8630.169	2286.489	-3835.894	
7.23	36.711	-18.174	-9156.979	2289.582	-3296.926	Last point obtained during the test
7.235	36.506	-64.305	-9295.343	2214.766	-2721.148	Restart of the hybrid simulation
7.24	36.068	-110.574	-9212.440	2099.327	-2145.371	
7.245	35.400	-155.895	-8915.888	1944.534	-1569.594	
7.25	34.509	-199.254	-8427.977	1754.359	-993.816	
7.255	33.407	-239.192	-7546.970	1537.195	-666.422	
7.26	32.117	-274.506	-6578.873	1303.482	-339.028	
7.265	30.662	-305.011	-5622.782	1071.397	-11.634	
7.27	29.067	-330.798	-4692.219	843.437	315.759	
7.275	27.354	-351.305	-3510.585	624.806	337.846	
7.28	25.554	-366.253	-2468.425	431.126	359.933	
7.285	23.692	-376.370	-1578.410	264.812	382.020	
7.29	21.790	-382.531	-886.147	134.345	404.107	
7.295	19.867	-385.685	-375.271	37.755	421.178	After this point, restart the simulation

BIBLIOGRAPHY

[1] Massone L. M., Bonelli P., Lagos R., Lüders C., Moehle J., and Wallace J. W. Seismic design and construction practices for rc structural wall buildings. *Earthquake Spectra*, 2012, **28**(1_suppl1):245–256.

[2] Calderon J. *Update on structural system characteristics used in RC building construction in Chile (in Spanish).* Master thesis, Santiago de Chile, 2007.

[3] Lagos R., Lafontaine M., Bonelli P., Boroschek R., Guendelman T., Massone L. M., Saragoni R., Rojas F., and Yañez F. The quest for resilience: The chilean practice of seismic design for reinforced concrete buildings. *Earthquake Spectra*, 2021, **37**(1):26–45.

[4] Woods J. E., Lau D. T., and Erochko J. Evaluation by hybrid simulation of earthquake-damaged rc walls repaired for in-plane bending with single-sided cfrp sheets. *Journal of Composites for Construction*, 12 2020, 24:4020073.

[5] Moehle J. *Seismic design of reinforced concrete buildings.* McGraw-Hill Education, 2015.

[6] Silva A. H. *Performance-based seismic design framework for structures exhibiting response mode transitions.* Doctoral thesis, Zurich, 2024.

[7] Kovarbasic M. *Seismic behavior and performance of reinforced concrete shear walls with low to mid aspect ratios.* Doctoral thesis, Zurich, 2024.

[8] ACI (American Concrete Institute). *Seismic evaluation and retrofit of existing concrete buildings.* ACI369-22, 2022.

[9] Pizarro Pohl D., Kovarbasic M., and Stojadinovic B. Dataset: Hybrid simulation tests of real-scale squat reinforced concrete shear wall specimens, 2024-07-17. Available at https://doi.org/10.3929/ethz-b-000683348.

[10] Pizarro Pohl D., Kovarbasic M., and Stojadinovic B. Dataset: Cyclic tests on real-scale squat reinforced concrete shear walls, 2024-05-10. Available at https://doi.org/10.3929/ethz-b-000672199.

[11] Beck A. *Paradigms of shear in structural concrete: Theoretical and experimental investigation.* Doctoral thesis, ETH Zurich, Zurich, 2021.

[12] Walraven J. C. Aggregate interlock: a theoretical and experimental analysis. 1980.

[13] Walraven J. and Reinhardt H. Theory and experiments on the mechanical behavior of cracks in plain and reinforced concrete subjected to shear loading. *HERON*, 1981, 26:1–68.

[14] Vecchio F. J. and Collins M. P. The modified compression-field theory for reinforced concrete elements subjected to shear. *ACI J.*, 1986, **83**(2):219–231.

[15] CEN. *Eurocode 8: design of structures for earthquake resistance-part 1: general rules, seismic actions and rules for buildings.* 2004.

[16] fib (Federation internationale du beton). *FIB Model code for conctrete structures 2010.* ACI318-19, 2013.

[17] Gambarova P. and Karakoç C. A new approach to the analysis of the confinement role in regularly cracked concrete elements. 1983.

[18] Bažant Z. P. and Gambarova P. Rough cracks in reinforced concrete. *Journal of the Structural Division*, 1980, **106**(4):819–842.

[19] Li B., Maekawa K., and Okamura H. Contact density model for cracks in concrete. In *IABSE colloquium, Delft*, volume 1, pages 51–62, 1987.

[20] Beck A., Gehri N., Mata-Falcón J., and Kaufmann W. Cracked membrane model with fixed, interlocked cracks: numerical implementation and validation. *Journal of Structural Engineering*, 2020, **146**(2):04019193.

[21] Paulay T., Park R., and Phillips M. Horizontal construction joints in cast-in-place reinforced concrete. *Special Publication*, 1974, 42:599–616.

[22] Vintzēleou E. and Tassios T. Mathematical models for dowel action under monotonic and cyclic conditions. *Magazine of concrete research*, 1986, **38**(134):13–22.

[23] Mattock A. H. and Hawkins N. M. Shear transfer in reinforced concrete—recent research. *Pci Journal*, 1972, **17**(2):55–75.

[24] Mattock A. H., Johal L., and Chow H. Shear transfer in reinforced concrete with moment or tension acting across the shear plane. *PCI journal*, 1975, 77.

[25] Mattock A. H., Li W., and Wang T. Shear transfer in lightweight reinforced concrete. *PCI journal*, 1976, **21**(1):20–39.

[26] ACI (American Concrete Institute). *Building Code Requirements for Structural Concrete.* ACI318-19, 2019.

[27] Davaadorj O., Calvi P. M., and Stanton J. F. Shear stress transfer across concrete-to-concrete interfaces: Experimental evidence and available strength models. *PCI Journal*, 2020, **65**(4).

[28] Trost B. Interaction of sliding, shear and flexure in the seismic response of squat reinforced concrete shear walls. 2017.

[29] Calvi P. M., Bentz E. C., and Collins M. P. Reversed cyclic experiments on shear stress transfer across cracks in reinforced concrete elements. *ACI Structural Journal*, 2016, **113**(4).

[30] Abdullah S. A. and Wallace J. W. Drift capacity at axial failure of rc structural walls and wall piers. *Journal of Structural Engineering*, 6 2021, 147.

[31] Moretti M. L., Kono S., and Obara T. On the shear strength of reinforced concrete walls. *ACI Structural Journal*, 2020, 117.

[32] Mangalathu S., Hwang S.-H., and Jeon J.-S. Failure mode and effects analysis of rc members based on machine-learning-based shapley additive explanations (shap) approach. *Engineering Structures*, 2020, 219:110927.

[33] Paulay T., Priestley M. J. N., and Synge A. J. Ductility in earthquake resisting squat shearwalls. *Journal Proceedings*, 1982, 79:257–269.

[34] Salonikios T., Kappos A., Tegos I., and Penelis G. Cyclic load behavior of low-slenderness reinforced concrete walls: Design basis and test results. *ACI Structural Journal*, 1999, 96.

[35] Salonikios T., Kappos A., Tegos I., and Penelis G. Cyclic load behavior of low-slenderness reinforced concrete walls: Failure modes, strength and deformation analysis, and design implications. *ACI Structural Journal*, 2000, 97.

[36] Cheng M.-Y., Hung S.-C., Lequesne R. D., and Lepage A. Earthquake-resistant squat walls reinforced with high-strength steel. *ACI Structural Journal*, 9 2016, 113.

[37] Park H.-G., Baek J.-W., Lee J.-H., and Shin H.-M. Cyclic loading tests for shear strength of low-rise reinforced concrete walls with grade 550 mpa bars. *ACI Structural Journal*, 5 2015, 112.

[38] Baek J.-W., Park H.-G., Lee J.-H., and Bang C.-J. Cyclic loading test for walls of aspect ratio 1.0 and 0.5 with grade 550 mpa shear reinforcing bars. *ACI Structural Journal*, 7 2017, 114.

[39] Baek J.-W., Kim S.-H., Park H.-G., and Lee B.-S. Shear-friction strength of low-rise walls with 600 mpa reinforcing bars. *ACI Structural Journal*, 2020, 117.

[40] Kim J.-H. and Park H.-G. Shear and shear-friction strengths of squat walls with flanges. *ACI Structural Journal*, 2020.

[41] Kim S.-H. and Park H.-G. Shear-friction strength of reinforced concrete walls with 700 mpa reinforcing bars. *ACI Structural Journal*, 1 2023, 120.

[42] Terzioglu T., Orakcal K., and Massone L. M. Cyclic lateral load behavior of squat reinforced concrete walls. *Engineering Structures*, 4 2018, 160:147–160.

[43] Hube M. A., María H. S., Arroyo O., Vargas A., Almeida J., and López M. Seismic performance of squat thin reinforced concrete walls for low-rise constructions. *Earthquake Spectra*, 2020, 36:1074–1095.

[44] Barbachyn S. M., Devine R. D., Thrall A. P., and Kurama Y. C. Behavior of nuclear rc shear walls designed for similar lateral strengths using normal-strength versus high-strength materials. *Journal of Structural Engineering*, 11 2020, 146.

[45] Nagae T., Ghannoum W. M., Kwon J., Tahara K., Fukuyama K., Matsumori T., Shiohara H., Kabeyasawa T., Kono S., Nishiyama M., et al. Design implications of large-scale shake-table test on four-story reinforced concrete building. *ACI Structural Journal*, 2015, 112:135.

[46] Cook D., Sen A., Liel A., Basnet T., Creagh A., Koodiani H. K., Berkowitz R., Ghannoum W., Hortacsu A., Kim I., Lehman D., Lowes L., Matamoros A., Naeim F., Sattar S., and Smith R. Asce/sei 41 assessment of reinforced concrete buildings: Benchmarking nonlinear dynamic procedures with empirical damage observations. *Earthquake Spectra*, 8 2023, 39:1721–1754.

[47] ASCE (American Society of Civil Engineergs). *Seismic evaluation and retrofit of existing buildings.* ASCE 41-17, 2017.

[48] Wight J. and MacGregor J. *Reinforced Concrete: Mechanics and Design.* Pearson Prentice Hall, 2009.

[49] ASCE/SEI 41-23. *Seismic evaluation and retrofit of existing buildings.* Reston, VA: American Society of Civil Engineers, 2023.

[50] Federal Emergency Management Agency (FEMA). *NEHRP Recommended revisions to ASCE/SEI 41-17, Seismic Evaluation and retrofit of existing buildings (FEMA publication P-2208).* Washington, DC:FEMA, 2023.

[51] FEMA. *Evaluation of Earthquake Damaged Concrete and Masonry Wall Buildings: Basic Procedures Manual.* FEMA 306, 1988.

[52] FEMA. *Seismic performance assessment of buidings, Volume 3 - supporting electronic materials and background documentation, third edition.* FEMA P-58-3, 2018.

[53] Gulec C. K., Whittaker A. S., and Hooper J. D. *Damage states and fragility curves for low aspect ratio reinforced concrete walls (FEMA P-58/BD-3.8.8).* 2009.

[54] Gulec C. K., Whittaker A. S., and Hooper J. D. Fragility functions for low aspect ratio reinforced concrete walls. *Engineering Structures*, 2010, **32**(9):2894–2901.

[55] Gulec C. K. and Whittaker A. S. Empirical equations for peak shear strength of low aspect ratio reinforced concrete walls. *ACI Structural Journal*, 2011, **108**(1).

[56] Rojas-Leon M., Wallace J. W., Abdullah S. A., and Kolozvari K. New equations to estimate reinforced concrete wall shear strength derived from machine learning and statistical methods. *ACI Structural Journal*, 1 2024, 121:89–104.

[57] Abdullah S. A. Reinforced concrete structural walls: Test database and modeling parameters. 2019.

[58] Trost B., Schuler H., and Stojadinovic B. "sp-339-12: Interaction of sliding, shear, and flexure for earthquake design of reinforced concrete shear walls". volume 339, pages 196–216. American Concrete Institute, 2020.

[59] Mosalam K. M. and Günay S. Hybrid simulations: theory, applications, and future directions. *Advanced Materials Research*, 2013, 639:67–95.

[60] Nakashima M. Hybrid simulation: An early history. *Earthquake Engineering & Structural Dynamics*, 2020, **49**(10):949–962.

[61] Takanashi K., Udagawa K., Seki M., Okada T., and Tanaka H. Nonlinear earthquake response analysis of structures by a computer-actuator on-line system. *Bulletin of Earthquake Resistant Structure Research Center*, 1975, 8:1–17.

[62] Udagawa K., Takanashi K., and Tanaka H. Non-linear earthquake response analysis of structures by a computer actuator on-line system (part 2 response analysis of one bay-one story steel frames with inelastic beams. *Trans. of the Archi. Inst. of Japan*, 1978, 268:49–59.

[63] Tanaka H. A computer-actuator on-line system for non-linear earthquake response analysis of structures. *SEISAN-KENKYU, IIS, Univ. of Tokyo*, 1975, **27**(12):15–19.

[64] Takanashi K., Udagawa K., and Tanaka H. Non-linear earthquake response analysis of structures by a computer-actuator on-line system (part iii: Response analysis of 1-bay 2-story frames) trans. of the archi. *Inst. of Japan*, 1979, 288:115–124.

[65] Wight J. K. et al. Earthquake effects on reinforced concrete structures: Us-japan research. *(No Title)*, 1985.

[66] Shing P.-S. B. and Mahin S. A. Cumulative experimental errors in pseudodynamic tests. *Earthquake engineering & structural dynamics*, 1987, **15**(4):409–424.

[67] Shing P.-s. B. and Mahin S. A. Experimental error effects in pseudodynamic testing. *Journal of Engineering Mechanics*, 1990, **116**(4):805–821.

[68] Dermitzakis S. N. and Mahin S. A. *Development of substructuring techniques for on-line computer controlled seismic performance testing*. PhD thesis, University of California, Berkeley, 1985.

[69] Nakashima M., Kato H., and Takaoka E. Development of real-time pseudo dynamic testing. *Earthquake engineering & structural dynamics*, 1992, **21**(1):79–92.

[70] Schellenberg A., Kim H. K., Takahashi Y., Fenves G. L., and Mahin S. A. Openfresco command language manual. *University of California, Berkeley*, 2009.

[71] Huang X. and Kwon O.-S. A generalized numerical/experimental distributed simulation framework. *Journal of Earthquake Engineering*, 2020, **24**(4):682–703.

[72] Mazzoni S., McKenna F., Scott M. H., Fenves G. L., et al. Opensees command language manual.

[73] Stojadinovic B., Mosqueda G., and Mahin S. A. Event-driven control system for geographically distributed hybrid simulation. *Journal of Structural Engineering*, 2006, **132**(1):68–77.

[74] Najafi A., Fermandois G. A., Dyke S. J., and Spencer Jr B. F. Hybrid simulation with multiple actuators: A state-of-the-art review. *Engineering Structures*, 2023, 276:115284.

[75] Schellenberg A. H. *Advanced implementation of hybrid simulation*. University of California, Berkeley, 2008.

[76] French C. W., Schultz A. E., Hajjar J. F., Shield C. K., Ernie D. W., Dexter R. J., and Olson S. A. Multi-axial subassemblage testing (mast) system: Description and capabilities. In *Proceedings of the 13th World Conference on Earthquake Engineering.*, Vancouver, 2004.

[77] Al-Mahaidi R., Hashemi J., Kalfat R., Burnett G., and Wilson J. *State-of-the-Art System for Hybrid Simulation at Swinburne*, pages 19–42. Springer Singapore, Singapore, 2018.

[78] Imanpour A., Tremblay R., Leclerc M., Siguier R., Toutant G., Balazadeh Minouei Y., and You S. Development and application of multi-axis hybrid simulation for seismic stability of steel braced frames. *Engineering Structures*, 2022, 252:113646.

[79] Abbiati G., Whyte C., Dertimanis V., and Stojadinovic B. Hybrid simulation of large-scale structures at eth zürich: the new 8-actuator multi-axial subassemblage testing (mast) setup. 2017.

[80] Kim H., Whyte C., and Stojadinovic B. Force, mixed and switch degree-of-freedom control in hybrid simulation. In *Proceedings of the 9th US National and 10th Canadian Conference on Earthquake Engineering, Toronto*, 2010.

[81] Hashemi M. J., Al-Ogaidi Y., Al-Mahaidi R., Kalfat R., Tsang H.-H., and Wilson J. L. Application of hybrid simulation for collapse assessment of post-earthquake cfrp-repaired rc columns. *Journal of Structural Engineering*, 2017, **143**(1):04016149.

[82] Sepulveda C., Mosqueda G., Wang K.-J., Huang P.-C., Huang C.-W., Uang C.-M., and Chou C.-C. Hybrid simulation framework with mixed displacement and force control for fully compatible displacements. *Earthquake Engineering & Structural Dynamics*, 2024, **53**(2):838–855.

[83] Al-Attraqchi A. Y., Hashemi M. J., and Al-Mahaidi R. Hybrid simulation of bridges constructed with concrete-filled steel tube columns subjected to horizontal and vertical ground motions. *Bulletin of Earthquake Engineering*, 2020, 18:4453–4480.

[84] Whyte C. A. and Stojadinovic B. Effect of ground motion sequence on response of squat reinforced concrete shear walls. *Journal of Structural Engineering*, 2014, 140:A4014004.

[85] Whyte C. and Stojadinovic B. Use of a high-precision digital displacement encoder for hybrid simulation of seismic response of stiff specimens. *Experimental Techniques*, 4 2016, 40:677–688.

[86] Fatemi H., Paultre P., and Lamarche C.-P. Experimental evaluation of inelastic higher-mode effects on the seismic behavior of rc structural walls. *Journal of Structural Engineering*, 2020, **146**(4):04020016.

[87] Fatemi H., Lamarche C., and Paultre P. Hybrid testing of capacity designed rc structural walls for the determination of nonlinear seismic shear amplification. *Earthquake Engineering Structural Dynamics*, 10 2021, 50:3266–3287.

[88] Zhang X., Zhang S., Luo Y., and Wang L. Effects of interface orientations on bond strength between old conventional concrete and new self-consolidating concrete. *ACI Structural Journal*, 2020, 117.

[89] SIA. *Concrete Structures.* 2004.

[90] Campbell S. A system for simultaneous pseudodynamic testing of multiple substructures. 1998.

[91] ACI (American Concrete Institute). *Guide for testing reinforced concrete structural elements under slowly applied simulated seismic loads.* ACI3742.R-13, 2013.

[92] Wong P., Vecchio F. J., and Trommels H. Vector2 and formworks user's manual. *Department of Civil Engineering, University of Toronto*, 2002.

[93] Japan Meteorological Agency. Strong-motion seismic waveform (1995 hyogo-ken nanbu earthquake), Dec. 5, 1994 1995.

[94] Abbiati G., Covi P., Tondini N., Bursi O. S., and Stojadinović B. A real-time hybrid fire simulation method based on dynamic relaxation and partitioned time integration. *Journal of Engineering Mechanics*, 9 2020, 146:4020104.

[95] Gravouil A. and Combescure A. Multi-time-step explicit–implicit method for non-linear structural dynamics. *International Journal for Numerical Methods in Engineering*, 2001, **50**(1):199–225.

[96] Park K., Felippa C. A., and Gumaste U. A localized version of the method of lagrange multipliers and its applications. *Computational Mechanics*, 2000, **24**(6):476–490.

[97] TR Electronic GmbH. Compact linear position sensors for standard applications. Tube-types up to 3 m stroke - LMR_27. 2021.

[98] Gehri N., Mata-Falcón J., and Kaufmann W. Automated crack detection and measurement based on digital image correlation. *Construction and Building Materials*, 2020, 256:119383.

[99] Gehri N., Mata-Falcón J., and Kaufmann W. Refined extraction of crack characteristics in large-scale concrete experiments based on digital image correlation. *Engineering Structures*, 2022, 251:113486.

[100] Hiraishi H. Evaluation of shear and flexural deformations of flexural type shear walls. *Bulletin of the New Zealand Society for Earthquake Engineering*, 1984, 17:135–144.

[101] Massone L. M. and Wallace J. W. Load-deformation responses of slender reinforced concrete walls. *ACI Structural Journal*, 2004, 101:103–113.

[102] Kovarbasic M. *Seismic Behavior, Performance and Design of Reinforced Concrete Shear Walls with Low to Medium Aspect Ratios.* PhD thesis, ETHZ Zurich, 2024.

[103] Molina F. J., Magonette G., Pegon P., and Zapico B. Monitoring damping in pseudo-dynamic tests. *Journal of Earthquake Engineering*, 2011, **15**(6):877–900.

[104] Ahmadizadeh M. and Mosqueda G. Online energy-based error indicator for the assessment of numerical and experimental errors in a hybrid simulation. *Engineering structures*, 2009, **31**(9):1987–1996.

[105] Terzic V. and Stojadinovic B. Procedure to restart an interrupted hybrid simulation: Addendum to peer report 2010/103. *PEER Report*, 2012, 2012.

[106] Jeli I., Pavlović M., and Kotsovos M. A study of dowel action in reinforced concrete beams. *Magazine of Concrete Research*, 1999, **51**(2):131–141.

[107] Moscoso J. F., Hube M. A., and María H. S. Residual seismic capacity of reinforced concrete walls with unconfined boundaries. *ACI Structural Journal*, 9 2021, 118:205–220.

[108] Pizarro D., Kovarbasic M., and Stojadinovic B. Experimental investigation of the sliding failure mode in full-scale squat reinforced concrete shear wall specimen. pages 938 – 944. Editura Conspress, 2022.

[109] Trost B., Schuler H., and Stojadinovic B. Sliding in compression zones of reinforced concrete shear walls: Behavior and modeling. *ACI Structural Journal*, 2019, **116**(5).

[110] Silva A. H. d., Tsiavos A., and Stojadinović B. Ductility-strength and strength-ductility relations for a constant yield displacement seismic design procedure. *Bulletin of Earthquake Engineering*, 2023, **21**(9):4449–4479.

[111] Krolicki J., Maffei J., and Calvi G. Shear strength of reinforced concrete walls subjected to cyclic loading. *Journal of Earthquake Engineering*, 2011, **15**(S1):30–71.

[112] Schuler H. and Trost B. Sliding shear resistance of squat walls under reverse loading: mechanical model and parametric study. *ACI Structural Journal*, 2016, **113**(4):711–722.

[113] Palermo D. and Vecchio F. J. Behavior of three-dimensional reinforced concrete shear walls. *ACI structural journal*, 2002, **99**(1):81–89.

[114] Xiao J., Kwon O.-S., Bentz E., and Kwon T.-H. Preliminary study on multi-axial hybrid simulation of a shear wall in the auxiliary building of apr1400-type npp subjected to lateral force. 2022.